POLITECNICO DI MILANO

Facoltà di Ingegneria Industriale

Corso di Laurea in
Ingegneria Aeronautica

Turbulent drag reduction at moderate Reynolds numbers via spanwise velocity waves

Relatore: Prof: Maurizio QUADRIO

Tesi di laurea di:
Davide GATTI Matr.740405

Anno Accademico 2010/2011

Contents

List of Figures

List of Tables

Abstract

The effects of high Reynolds numbers, up to 73000, on turbulent drag-reduction (DR) effectiveness of streamwise-traveling waves of spanwise velocity are addressed by direct numerical simulations (DNS). The effectiveness of the traveling waves in reducing turbulent drag has been observed to be mildly weakened by increasing the value of the Reynolds number. To increase Re while keeping the computational costs affordable, we have employed DNS within computational domains of reduced extension. Though they are much larger than the MFU, the Minimal Flow Unit that guarantees a self-sustained turbulence, their limited size requires special care to interpret results that are indeed slightly dependent upon the box size. Space-averaged quantities shows large fluctuations in time when the domain size is reduced, due to the smaller averaging area, and require longer averaging times to converge. We aim at finding a suitable compromise between space- and time-average, leading to reliable measurements of DR with affordable computational effort. Two special procedures have been developed to instrument the DNS results with an error bar, that is related to the finite averaging time. Significant DR is still observed at Re=73000. The maximum DR is proportional to $Re_\tau^{-0.217}$ in the Reynolds range investigated. Our results suggest the possible existence of a potential net power saving at high Reyolds number and wave frequencies far away from the optimal value, where the power required for the control decreases more rapidly with Re than DR.

Keywords: drag reduction, predetermined control, traveling waves, oscillating wall, minimal flow unit, channel flow, net power save.

Sommario

Gli effetti di elevati numeri di Reynolds, fino a 73000, sull'efficacia nella riduzione di resistenza (DR) delle onde viaggianti sono studiati attraverso simulazione numeriche dirette di un canale piano. E'stato dimostrato che l'efficacia nella riduzione della resistenza delle onde viaggianti è indebolita dal crescere del numero di Reynolds e con i dati a disposizione, che derivano sopratutto da studi numerici e di laboratorio a basso Reynolds, si possono fare solo congetture sulla possibilità di raggiungere alte riduzioni di resistenza a altro Re. Per raggiungere numeri di Reynolds elevati mantenendo ragionevoli costi computazionali, abbiamo adottato domini di calcolo di estensione ridetto rispetto alle usuali DNS. Sebbene siano molto più ampi della MFU, la Minimal Flow Unit che garantisce la sostentazione della turbolenza, la loro dimensione richiede particolare cura nell'interpretare i risultati che sono infatti debolmente dipendenti dalla dimensione del dominio. Le quantità mediate nello spazio mostrano fluttuazioni nel tempo quando il dominio viene ridotto e richiedono tempi d'integrazione più lunghi. Abbiamo cercato un compromesso adatto tra media spaziale e temporale, che portasse a misure affidabili di riduzione di resistenza e contenessero lo sforzo computazionale. Due procedure spaciali sono state sviluppate per dotare i risultati di barre di errore, dovute al tempo di media finito. Persino a Re=73000 è stata ottenuta una significativa riduzione di resistenza e la massima riduzione è proporzionale a $Re_\tau^{-0.217}$ nell'intervallo Re studiati. Suggeriamo inoltre la possibilità di raggiungere elevati risparmi netti di potenza a alti Re e frequenze di forzamento distanti da quella ottimale, qui la potenza spesa per il controllo decresce con Reynolds molto più rapidamente della DR.

Parole chiave: drag reduction, predetermined control, traveling waves, oscillating wall, minimal flow unit, channel flow, net power save.

A Giancarlo

Chapter 1

Introduction

The next great era of awakening of human intellect may well produce a method of understanding the qualitative content of equations. Today we cannot. Today we cannot see that the water flow equations contain such things as the barber pole structure of turbulence that one sees between rotating cylinders. Today we cannot see whether Schroedinger's equation contains frogs, musical composers or morality or whether it does not. We cannot say whether something beyond it like God is needed, or not. And so we can all hold strong opinions either way.

R.P.Feynman (1964)

The deep comprehension of Turbulent Flows is still nowadays a great unresolved problem of classical physics and fluid dynamics The difficulty to state a simple and unique definition of turbulence and of its features gives an idea of its complexity. In spite of the ubiquitous nature of turbulence, it remains a critical branch of fluid dynamics, where a lot of research effort has to be done yet. Developing analysis tools for turbulent flows, either experimental, theoretical or numerical can be very hard and limited the gain of new knowledges in the field.

The flow of a gas or liquid in a pipe, the flow around an airplane, the mixing processes that take place in engines, the boundary layers and wake around bluff bodies, atmospheric phenomena and blood flow in human body are some example of the great variety of everyday-life situations, industrial and practical processes, in which turbulent flows can be encountered. Turbulent flows are thus the rule, not the exception. Then, the interest of researchers in fluid dynamics and turbulence can be easily understood.

As of today, according to [35], three are the main fields of research in turbulence:

- Theoretical comprehension of properties and dynamics of turbulent flows, which allows further developments in turbulence modeling and prediction;
- Experimental campaigns, both numerical and practical which allows the discovery of qualitative and quantitative data on several turbulent flows;
- Flow control techniques, which allows the achievement of particular engineering goals through the change of particular flow characteristics.

The present work focuses on both the second and the third branch: a Direct Numerical Simulation of a plane channel flow, a particular and idealized flow described later, is computed

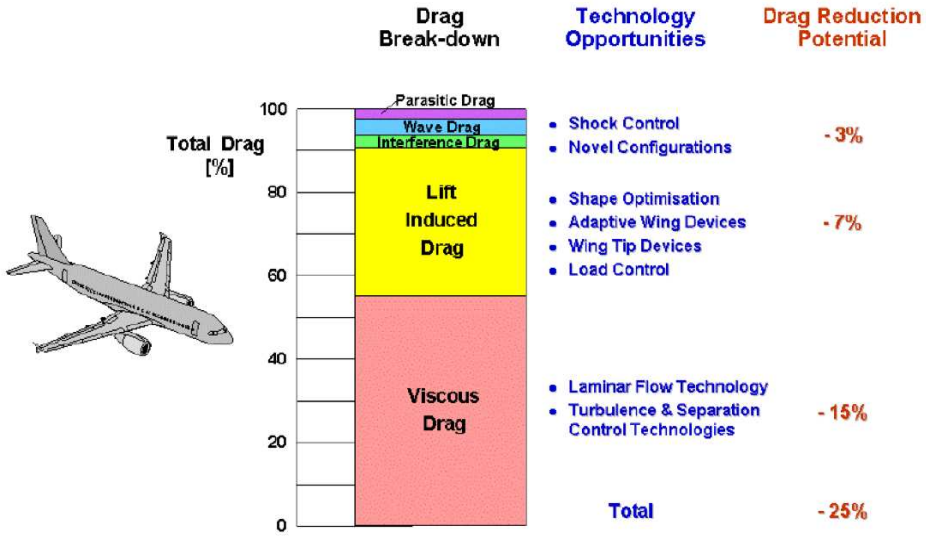

Figure 1.1: Different improvements that can lead to a sensible drag reduction [50]

in order to achieve new information about one of the most interesting flow control techniques, the streamwise-traveling waves of spanwise wall velocity.

Flow Control for turbulent drag reduction

The possibility of manipulating a flow field in order to obtain a desired objective is of immense technological importance and this surely accounts for the subject being more hotly pursued by scientists and engineers than any other topic in fluid mechanics. It is sufficient to think that the potential benefits arising from the implementation of efficient flow control systems range from saving billion of dollars in annual fuel costs for land, air and sea vehicles, thus reducing pollutants and environment impact, to achieving more competitive industrial processes involving turbulent fluid flows

In this context, flow control may play a key role in developing several technical advantages, such as:

- Reduction of drag
- Increase of lift
- Increase of mixing of mass
- Reduction of flow-induced noise

Among the above, the most pursued aim, we try to reach in this work at moderate Reynolds numbers and for a particular flow control technique, is the reduction of drag. An idea of how friction drag can be very influent is given by a recent study [50] by Airbus: turbulence control could reduce the drag of a civil aircraft up to 15%, as shown in figure 1.1, resulting in more than 15 billion dollar saving per year for shipping industry.

Control techniques are typically divided in two large groups:

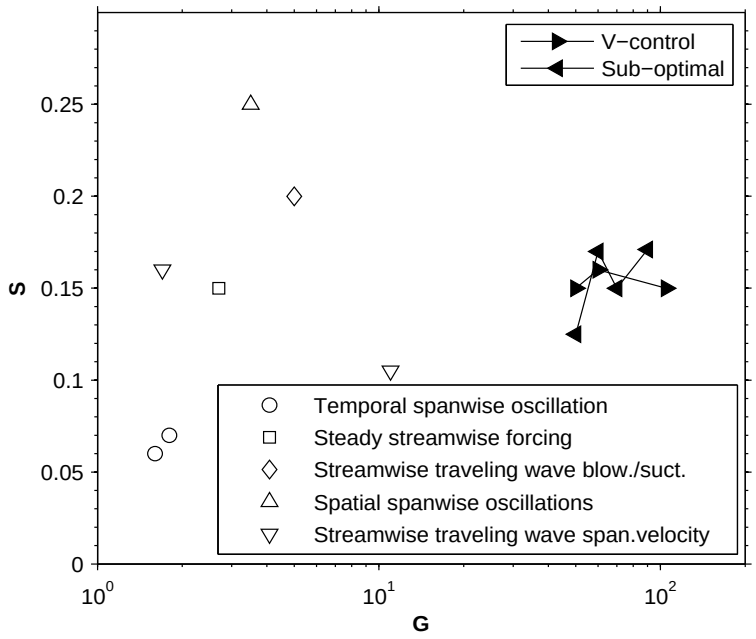

Figure 1.2: Net Power Saving S versus control Gain G for several open-loop (bank symbols) and closed-loop (black symbols) controls, data taken from [18].

- Active control, which do require external energy to be introduced into the system;
- Passive control, which does not.

The flow control technique studied in this work is active, since it implies the wall of a channel to be moved in the spanwise direction. This movement can be possible only if an external power source introduce energy to oppose to the spanwise friction drag.

Active control techniques can be considered useful only whether the reduction in power required to drive the flow is greater than the power needed to actuate the control, in other words, whether a net power saving can be achieved.

A clear-cut definition of net power saving, indicated as S, is given in the recent work [18], namely:

$$S = \{P_0 - (P + P_{sp})\} / P_0 \tag{1.1}$$

where P_0 and P are the powers needed to drive the flow in the uncontrolled and controlled case respectively and P_{in} is the external power of the control, disregarding mechanical losses and the actuator efficiency.

Another important parameter, the gain, represents the power saving per unit input power, say:

$$G = (P_0 - P)/P_{sp} \tag{1.2}$$

which is greater than unity only if a net power budget is achieved by the control. The actuator of a control set-up should be at least $1/G$ efficient to obtain a net energy saving in a real implementation of the control.

A promising control technique has both high S and G, allowing to reach high net energy savings, even with significant mechanical losses.

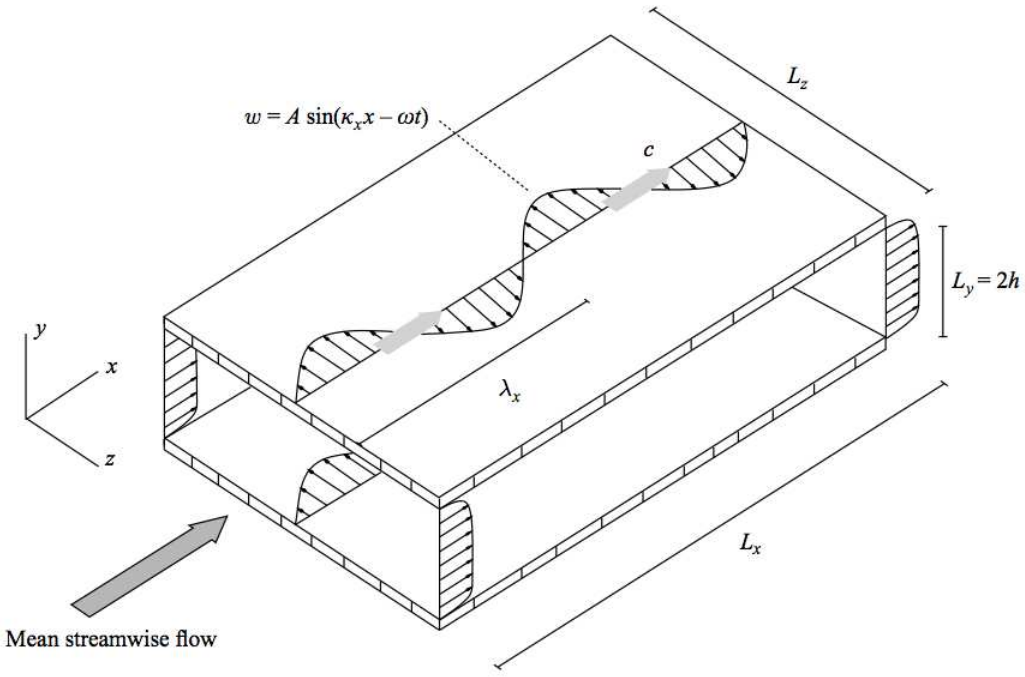

Figure 1.3: Graphical representation of the traveling waves of spanwise velocity

Another useful classification is between open-loop strategies, whose control law is predetermineds and do not require any measurement within the flow, and closed-loop, which require a control law with feedback. The former are simpler than the latter, which on the other hand minimize the external energy input, on average reaching higher Gains.

Figure 1.2, taken from [18], shows S and G for several control strategies: it is clear that simpler open-loop techniques (blank markers) can reach very high S but values of gain G are more than one order of magnitude smaller than closed-loop control (black markers). Predetermined control hence need very high theoretical energy saving S, in order to obtain a positive energy budget in real applications, due to the high energy input they require.

Nevertheless, predetermined control is very appealing due to its simplicity, complex sensors and actuators are not required and their effectiveness in reducing drag is proven.

This work is concerned with a particular kind of open-loop predetermined control technique, described in detail in chapter 2.3.

The streamwise-traveling waves

Among predetermined techniques, great interest is arisen by those involving in-plane wall motions, which may be very simple to realize practically and give very attractive results in reducing friction drag. Two of the reviews in the last decade ([17] and [36]) describe well the scenario.

In this work we deal with the most promising predetermined control technique, in terms of high net energy saving achievable: the streamwise traveling waves of spanwise wall velocity.

The walls of a channel are moved, cyclically in time and space, in the streamwise direction,

as in figure 1.3, according to the following law:

$$w_w(x,t) = A\,\sin(\kappa_x\,x - \omega\,t) \tag{1.3}$$

where w_w is the spanwise wall velocity, A is the wave amplitude, ω is the oscillation frequency, κ_x is the streamwise wavenumber, responsible of the streamwise modulation of the spanwise wall velocity, x is the streamwise coordinate and t is the time.

When the characteristics of the flow, say the Reynolds number, are chosen, a set of three (A, κ_x and ω) control parameters are still free to be chosen.

The effectiveness of streamwise-traveling waves of spanwise wall velocity in reducing friction drag and reaching a net power saving, up to $\approx 20\%$ at $Re_\tau \approx 200$, has been proved for the first time in [42]: a meticulous numerical campaign in the whole control parameter space, through which an optimal set of parameters has been found. Even laboratory experiments ([37] and [2]) confirmed the capabilities of the velocity waves.

A further comprehension of he mechanisms at the basis of drag reduction through spanwise wall motions has been reached in [41], where the spanwise boundary layer due to the motions is related to drag reduction.

What happens at high Re?

In spite of the great expectation on traveling waves, a significant issue bridles their development and practical application.

Traveling waves effectiveness in reducing drag has been proven to be mildly weakened by an increase in Reynolds number. The trend has been observed in various types of controls, either predetermined or closed-loop, especially when the flow is controlled through modifications of wall turbulence.

A still unanswered question arises:

> Can significant Drag Reduction be obtained even at very high Reynolds numbers, comparable to those of real applications? [42] [36]

Answering this question, either numerically or experimentally, is a true challenge and would have significant consequences.

Figure 1.4 show only few numerical (blank symbols) or experimental (filled symbols) results from literature. The decrease of friction reduction with Re can be appreciated and two scenarios (solid lines) are possible, both consistent with available evidence. One possibility is that drag reduction eventually drops before reaching application-level Re. The alternative is that the observed weak decrease in performance as a *low*-Re effect, which is deemed to disappear at reasonably high values of Re. This view is supported by numerical experiments of [14], who considered a virtual active control system capable of suppressing near wall fluctuations in the near-wall layer. The outcome is that drag reduction indeed decreases at low-Re but then becomes almost constant while increasing Re.

The race to develop special high-efficiency actuators, suited to traveling-waves of spanwise wall velocity has already begun, though the theoretical effectiveness of this technique at high Reynolds numbers has not been proven yet. Obviously this is risky, nonetheless most of the research centres and companies accept the risk, thanks to the great profit they would have if the technology revealed so effective even in real applications.

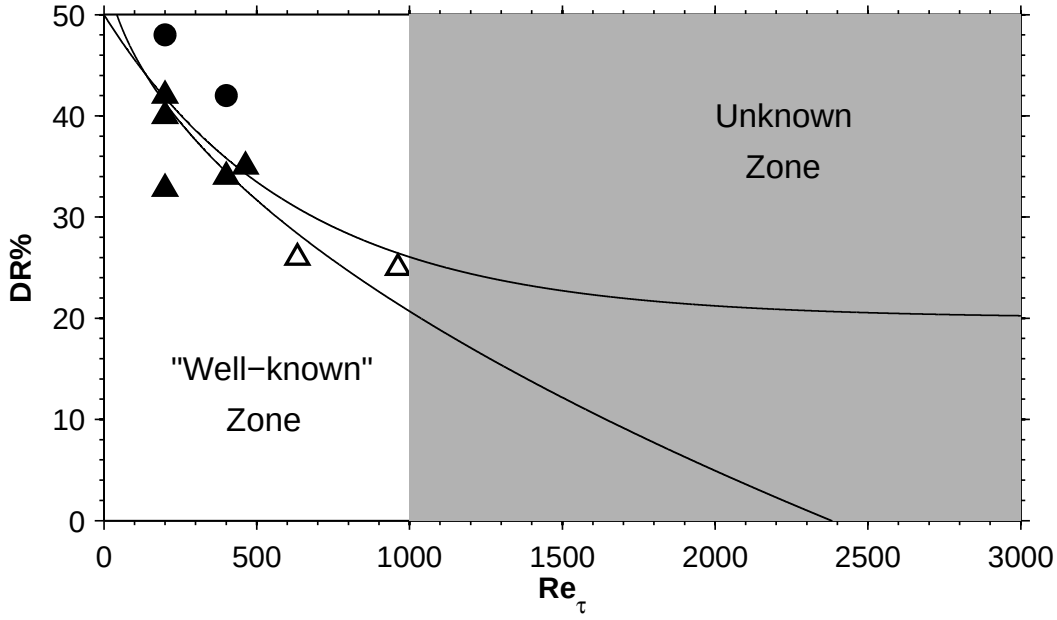

Figure 1.4: Drag Reduction as a function of the Reynolds number Re_τ for few experimental (filled symbols) or numerical (blank symbols) studies from literature. Solid lines represent two possible trend of DR against Re.

Unfortunately, the two main research tools used to investigate the effects of traveling waves, i.e. Direct Numerical Simulation and experiments, make it difficult to reach Reynolds number near those typical of applications.

All the available numerical information on spanwise wall forcing to date concerns flow at very low values of Re, with most of the DNS being at $Re_\tau = 100 - 200$ and only a few reaching $Re_\tau = 400$. Such limited value of Reynolds numbers are mainly due to the huge computational costs at increasing Re, which may be considered prohibitive even for the most recent supercomputers.

The main trouble studying the behavior of traveling waves with DNS is the wide extent of the control parameters space: in order to obtain rich information, the whole (A, κ_x, ω) space should be investigated at each Reynolds number. The DNS at the highest Re available in literature are those of [12], where $Re_\tau = 2003$ at constant flow rate is reached after 6×10^6 processor hours on 2048 processors, for a total of 122 wall clock days. A hundred simulations would be necessary to sweep the whole (κ_x, ω) plane, requiring more than 33 years at $Re_\tau = 2000$, if the per-simulation runtime of [12] applies.

Theoretically, computational costs could be reduced and Re increased if RANS turbulence models or LES were preferred to DNS. Unfortunately, only well-resolved DNS can give such an high reliability on results and the most common turbulence models misrepresent the effect of traveling waves, disclosing that physics of drag reduction still escapes our modeling ability.

Laboratory experiments could in principle allow the achievement of drag reduction measures at higher Reynolds number than DNS, yet some drawbacks make the task difficult.

First of all, most of numerical data are obtained through simulations of plane channel flow, which is an idealized flow that extends in the streamwise and spanwise direction infinitely,

and it can not be reproduced in laboratory, where pipe flows are used. Thus, comparison between the two, while qualitatively subsist, is not quantitatively valid.

A more complex phenomenon is the initial transient. In numerical simulations, after the initial transient, which runs out in a finite time, the whole domain reaches a statistically steady state. In laboratory experiments, initial transient turns out to be a spatial transient, which takes a finite length to end, requiring long pipe to obtain correct measurements.

Then, applying streamwise traveling waves at walls is not always easy but is important to compare well numerical and laboratory results. In [2], the correct waveform is discretized in the spatial direction through a piecewise-constant approximation. A Fourier analysis of the discrete waveform revealed that several harmonics other than κ_x have a relevant energetic content and affect drag reduction result significantly.

Finally, the wavelength $\lambda_x = 2\,\pi/\kappa_x$ should shorten as Reynolds increases, if the hypothesis of viscous length scaling were valid, at $Re_\tau \approx 10^5$ the wavelength is 500 times shorter than at $Re_\tau = 200$.

Present work

We intend to (try to) answer the Reynolds-effect question, reaching up to $Re_\tau = 2000$, thus entering what is represented in figure 1.4 as the "unknown zone". Direct Numerical Simulations of channel flow controlled by streamwise traveling waves are conducted, comprising the special case of steady wave and oscillating wall. Our heavy numerical campaign sweeps the most interesting part of the (κ_x, ω) plane, where highest friction reduction rates are obtained, in order to obtain useful information on both the effect of Reynolds on maximum drag reduction and on the optimal set of control parameters.

Moderate Reynolds number are reached through simulations of channel flows on domains of reduced extension, in order to keep the computational cost affordable. Space-averaged quantities, such as wall shear, which we are interested in, shows wider fluctuations when the domain size is reduced, due to the smaller averaging area. To obtain reliable measurements and control their uncertainty, a longer time average is needed. We try to find a good compromise between space- and time-average, which allow to reduce the computational effort and can lead to reliable drag reduction measurements.

The finite-average time requires special procedures to give the DNS results an error-bar, which gives information on the uncertainty of the measurements due to randomness of the measured variable. Systematic errors,i.e. biases of the results due to slight dependency upon the box size, are estimated by the comparison with available data.

When evaluating the power needed for the control, the collaborative effect has been studied methodically for the first time in this work. It is the amount of energy that can be saved if the actuator could be sensitive to those portion of the wall the flow drives instead of slowing.

The work is structured as follows:

- CHAPTER 1: INTRODUCTION

- CHAPTER 2: TURBULENCE AND FLOW CONTROL
  A brief introduction on turbulence and main flow control techniques, presenting those concepts recalled many times in the work, is followed by a detail description of the streamwise traveling waves of spanwise wall velocity, the type of control object of this study, and of the parameters used to judge control performances.

- CHAPTER 3: DIRECT NUMERICAL SIMULATION OF A CHANNEL FLOW
  A description of the set of equations that govern the flow in a channel and of the numerical strategy adopted to solve it, focusing on the choice of simulating a narrow channel, i.e. Minimal Flow Unit, on what this choice implies and on the minimal box that can be used.

- CHAPTER 4: MINIMAL FLOW UNIT FOR DRAG REDUCTION ESTIMATE
  Minimal flow unit is used to evaluate control performance at moderate Reynolds number. The minimal domain that leads to a good esteem of drag reduction is presented and two error-estimation strategies are described and compared.

- CHAPTER 5: OSCILLATING WALL
  Results concerning a particular case of traveling wave, the spanwise oscillating wall, are presented. In particular, the attention is focused on drag reduction, power spent and net power saving. A study of initial transient and uncertainty scaling is led, as well as of the effect of the box size on the drag reduction. Spectra of the space-averaged streamwise wall shear are also studied.

- CHAPTER 6: TRAVELING WAVES
  Results concerning traveling waves are presented. In particular, the attention is focused on drag reduction, power spent and net power saving. A study of initial transient and uncertainty scaling is led, as well as of the space-averaged and punctual streamwise wall shear.

- CHAPTER 7: CONCLUSIONS AND FUTURE DEVELOPMENTS

- APPENDIX A : ERROR-ESTIMATION STRATEGIES The two error-estimation strategies used in this work are discussed in detail and compared.

- APPENDIX B : FURTHER RESULTS Further results, equally interesting but not strictly related to the effect of Re on DR are presented in this appendix, focusing on initial transient length, uncertainty and their scaling. A brief study of space-averaged and punctual wall-shear spectra is presented.

Chapter 2

Turbulence and Flow Control

Turbulence is a very challenging field of classical physics and fluid dynamics. Despite its ubiquitous nature, even a simple and unique definition of turbulence can not be easily stated. Moreover, the solution of the well-posed set of PDEs that govern turbulent flows is yet unknown. Their solution can be attempted mainly in two ways: through Direct Numerical Simulation or Turbulence Models. While its numerical solution through Direct Numerical Simulation costs a lot in terms of computational resources, the development of turbulence models based on averaged equations leads to a systems with more unknowns than equations and a closure problem arises. Within the approach, the advantage of a reduced computational cost is counterweighted by an increased analytical effort, by the need of empirical laws of closure and the low reliability of results. This chapter is intended to give the reader an outlook on this evolving panorama, by concisely discussing the most widely accepted concepts in turbulence theory, in order to better understand the main mechanisms of the near wall turbulence and thus various mean available for its control.

2.1 Fundamentals of Turbulence

Without going deep into the description of mechanisms of turbulence, this section introduces the reader to some concepts that are recalled frequently in this work.

The Turbulent Regime In a famous paper dated 1883 [44], Osborne Reynolds describes the results of an experiment that was as simple as important. He proved what happened to thin streaks of highly coloured water when they enter a tube filled with flowing clear water. He wrote in the original paper:

> When the velocities were sufficiently low, the streak of colour extended in a beautiful straight line through the tube. If the water in the tank had not quite settled to rest, at sufficiently low velocities, the streak would shift about the tube, but there was no appearance of sinuosity. As the velocity was increased by small stages, at some point in the tube, always at a considerable distance from the trumpet or intake, the colour band would all at once mix up with the surrounding water, and fill the rest of the tube with a mass of coloured water.

This experiment demonstrates that some flow and fluid characteristics can be related to the presence or absence of turbulence and those features typical of turbulent flows. In particular,

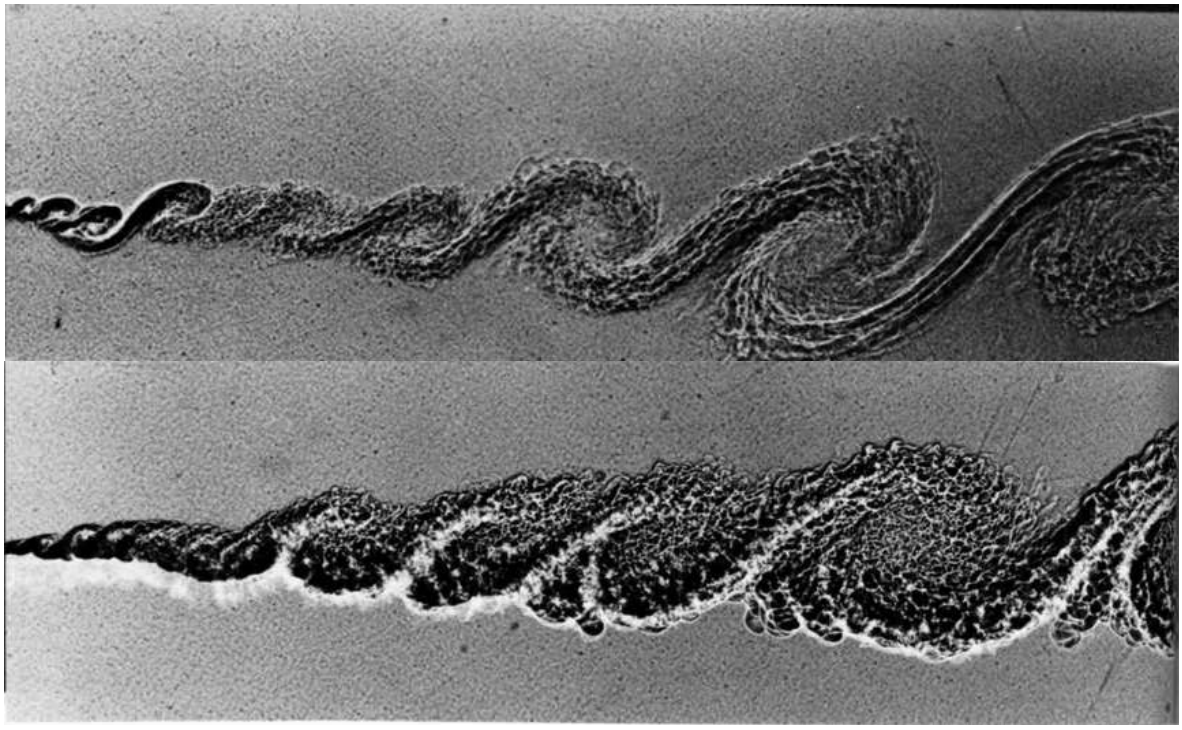

Figure 2.1: Structures of different scales in a turbulent mixing layer. In the figure below Reynolds number is twice as above. Picture taken from Van Dyke's *Album of Fluid Motion* [8].

he discovered that turbulent features begin to appear at particular values of an nondimensional number, nowadays called *Reynolds number*, defined:

$$Re = \frac{U\,L}{\nu} \tag{2.1}$$

where U and L are typical velocity and length scale of the flow, while ν is the cinematic viscosity of the fluid.

The energy cascade The concept of *energy cascade* was first introduced by L.F.Richardson in 1922. Turbulent flows can be considered as made up of a random superposition of *eddies* of various size. As can be shown in figure 2.1, the size of the smallest eddies depends on the Reynolds number of the flow. Increasing Reynolds number also increase the ratio between the dimension of largest and smallest eddies.

Defining a Reynolds number based on velocity u of a particular eddy of size l, one of the largest eddies has a big chance, due to its high Reynolds number, to become *unstable* and *break up* into smaller eddies. In this way the turbulent kinetic energy contained in the largest eddies is transferred to lesser eddies and thus, to smaller scales. This energy cascade continues until the eddy Reynolds number tends to unity, when the viscous phenomena dissipate energy.

Cinematic considerations One of the consequences of the existance of the energy cascade can be proved through a simple dimensional analysis. Recalling the definition of the second-

order *rate of strain* tensor, defined as:

$$S_{ij} = \frac{1}{2}\left(\frac{\partial u}{\partial x_i} + \frac{\partial u}{\partial x_j}\right) \tag{2.2}$$

the *dissipation rate* of kinetic energy per unit mass can be defined, using Einstein's notation:

$$\epsilon = 2\nu S_{ij} S_{ij} \tag{2.3}$$

where ν is the cinematic viscosity. Using dissipation rate and cinematic viscosity alone, a length, time and velocity scales can be defined. These scales, called *Kolmogorov scales*, in honour to Andrej N.Kolmogorov who first introduced them, are:

$$\eta \equiv \left(\frac{\nu^3}{\epsilon}\right)^{1/4} \qquad u_\eta \equiv (\nu\epsilon)^{1/4} \qquad \tau_\eta \equiv \left(\frac{\nu}{\epsilon}\right)^{1/2} \tag{2.4}$$

Handling the three equation above, the ratio between Kolmogorov scales and the integral scales U, L and $\tau_0 = \mathrm{L/U}$ can be expressed in terms of powers of Reynolds number, obtaining:

$$\frac{\eta}{L} \sim Re^{-3/4} \qquad \frac{u_\eta}{U} \sim Re^{-1/4} \qquad \frac{\tau_\eta}{\tau_0} \sim Re^{-1/2} \tag{2.5}$$

The ratio between integral and Kolmogorov length scales increases with Re, while the dynamic of Kolmogorov scales becomes faster if compared to the integral timescale. This consideration and the observation that the Reynolds number based on Kolmogorov scales takes the value of unity, suggest that Kolmogorov scales are those dissipative scales dominated by viscous dissipation situated at one end of the energy cascade.

This is the basis of Kolmogorov *hypotesis of local isotropy*: observing a turbulent high Reynold number flow at its small scales, directional information is lost and thus flow statistic can supposed to be *isotropic*. Due to their fast dynamic and small length, the small scales are suggested to be universal.

A flow with mean shear: plane channel flow The flow studied in the present work is a wall bounded flow called plane channel flow. In this type of flow a fluid is pressure-driven between two parallel semi-infinite smooth walls, placed at a distance 2h. In wall flows, the phenomenon of dissipation through the energy cascade takes place mainly in the very neighbourhood of the wall. The thickness δ of this region provides a good measure of the largest eddies in the flow, while the smallest scales, the viscous wall units, are of the order of Kolmogorov scales.

Since in the near-wall region viscous effects dominate over inertia, the streamwise shear stress τ is mainly represented by its viscous component. Furthermore, since no-slip boundary condition imposes null velocity at the wall, the inertial stresses due to turbulent velocity fluctuations, also called Reynolds stresses, are zero and the shear stress at the wall can be written as:

$$\tau_w = \rho\nu \frac{\partial \langle U \rangle}{\partial y}\bigg|_w - \rho \langle uv \rangle |_w = \rho\nu \frac{\partial \langle U \rangle}{\partial y}\bigg|_w \tag{2.6}$$

where the operator $\langle\cdot\rangle$ is the expected value, u and v are streamwise and spanwise fluctuations of velocity, respectively, and y denotes the wall-normal direction. In the very near wall region,

an inner scaling can be defined by using cinematic viscosity ν and the wall shear stress τ_w, leading to the following:

$$u_\tau = \sqrt{\tau_w/\rho} \qquad \delta_\nu = \nu/u_\tau \qquad t_\nu = \left(\frac{\partial \langle U \rangle}{\partial y}\bigg|_w \right)^{-1} \tag{2.7}$$

where u_τ, δ_ν and t_ν are a velocity-, length- and time-scale respectively. Near-wall flow can be represented using dimensionless wall units, usually denoted with a + superscript, obtained after scaling flow variables with the inner scales defined above. Hence, the nondimensional distance from wall is:

$$y^+ = y/\delta_\nu = y\, u_\tau/\nu \tag{2.8}$$

Then, depending on y^+, different regions, or layer, are defined in the near-wall flows. We define the *viscous wall region* as the region for $0 < y^+ < 50$, while the region $y^+ > 50$ is called the *outer layer*. Furthermore, within the viscous wall region, we define the *viscous sublayer*, where $y^+ < 5$, in which Reynolds shear stresses are negligible with respect to viscous shear stresses. Finally, the transition region between the viscosity-dominated and the inertia-dominated part of the flow, i.e. $5 < y^+ < 30$, is called *the buffer layer*.

Coherent structures (CS) Starting from this well-accepted framework, fluid dynamicists have long sought to understand how boundary-layer turbulence is generated and dissipated. Since boundary-layer flows are technical driver for several engineering applications, lots of financial and human resources have been brought to bear on the problem over many decades of studies. The progress made, however, has not been commensurated with the effort expended, reflecting the intrinsic complexity of turbulence phenomena and the difficulty that must be faced when trying to reproduce turbulent processes in a controlled framework. For this reason, most of turbulence knowledge has resulted from investigations at low Reynolds numbers, where effective flow visualizations and Direct Numerical Simulations (DNS) are possible.

In this context, it has been possible the identification of coherent structures. Historically, fundamental studies can be found in [49] [55] and nowadays, even if with some controversy, they are quite universally considered as reference works. Despite this, no generally accepted definition of what is meant by coherent motion has arisen. Actually, in physics coherence stands for a well-defined phase relationship. As for turbulence, we can accept Robinson's definition *"a coherent motion is a three dimensional region of the flow over which at least one fundamental flow variable exhibits significant correlation with itself or with another variable over a range of space and/or time that is significantly larger than the smallest local scales of the flow"* [47]. The major motivations for investigating coherent structures in turbulent boundary layers are:

- to aid predictive modelling of the gross statistics of turbulent flows
- to understand the dynamical processes responsible for statistical properties in order to predict them through an appropriate modelling
- to guide alteration and control of turbulence

The third reason, in particular, concerns the main issues addressed in the present work.

In the description of coherent structures we refer to the simple model of a turbulent boundary layer over a flat plate with no pressure gradient imposed and no heat transfer. In this case the most important and widely recognised CS are:

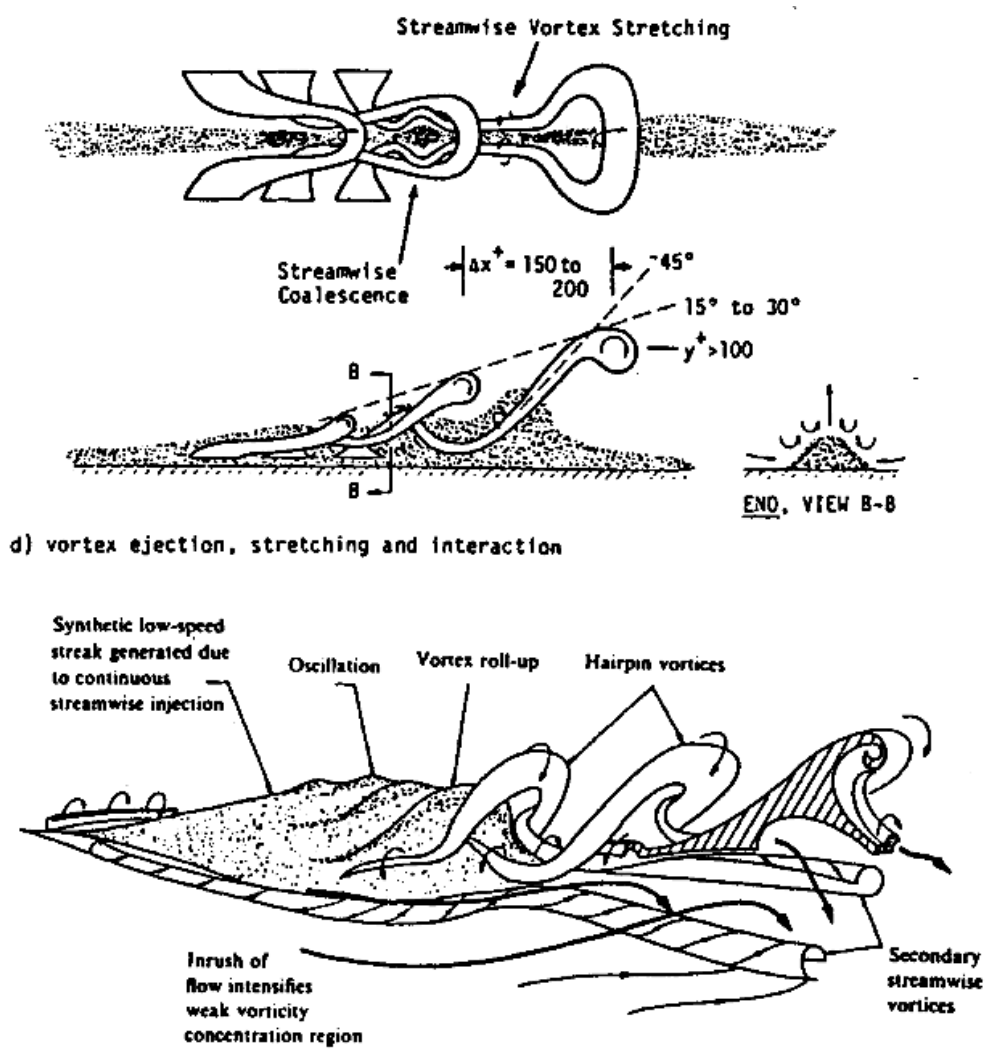

Figure 2.2: Quasi-streamwise vortices and Low Speed Streaks interaction during the wall cycle [1]

- Low Speed Streaks (LSS) in the viscous sublayer
- Ejections of near wall low-speed fluid
- Sweeps of high-speed fluid towards the wall
- Quasi-streamwise vortices and other vortices
- Inclined shear layers

Most of these CS show a strong interaction and contribute heavily to the turbulence generation and conservation mechanisms at the wall. One of this mechanisms has been investigated during the last decades and is called *Wall cycle*.

During the wall cycle, in the near wall region, violent ejections of low-speed fluid and inrushes of high-speed fluid have been observed experimentally and numerically. This in-

termittent quasi-cyclic sequence of intense events have been collectively termed the *bursting* phenomenon. The name is due to the early conditional sampling techniques used to investigate the wall cycle events. This process begins with elongated counter-rotating quasi-streamwise vortices, which induce low- and high-speed streaks between them. Then, the low-speed region grows downstream, lift up and develop instantaneous inflectional velocity profiles. At approximately the same time, the interface between low- and high-speed fluid begins to oscillate. Hence the low-speed region lifts up away from the wall as the oscillation amplitude increases and then the flow rapidly breaks up into a completely chaotic motion. This phase is followed by a large-scale motion of upstream fluid that emanates from the outer region and sweeps the wall region. This sweep event seems to have a stabilizing effect on the bursting site, since it prepares the wall region for a new cycle, thus determining a self-sustaining regime.

The relationship between coherent structures in the outer region and near-wall cycle is still not completely understood, even though strong evidence of this interaction has been provided in recent works [13] [11]. The existence of interaction between the wall and the outer region actually implies a residual dependence of wall statistics from Reynolds number based on integral scales.

2.2 Control of turbulence

The possibility of manipulating a flow field in order to obtain a desired objective is of immense technological importance and this surely accounts for the subject being more hotly pursued by scientists and engineers than any other topic in fluid mechanics. It is sufficient to think that the potential benefits arising from the implementation of efficient flow control systems range from saving billion of dollars in annual fuel costs for land, air and sea vehicles, to achieving more competitive industrial processes involving fluid flows.

In this context, flow control may play a key role in developing several technical advantages, such as:

- Reduction of drag
- Increase of lift
- Increase of mixing of mass
- Reduction of flow-induced noise

To achieve these results the transition from laminar to turbulent regime may be advanced or delayed, flow separation may either have to be provoked or prevented, and finally turbulence level may have to be either enhanced or reduced. The aim of the engineer is to achieve the desired objective adopting simple devices, inexpensive to build as well as to operate, so that the expense for flow manipulation would result in a significant net positive power saving.

Unfortunately, all these goals are difficult to be reached efficiently together and potential conflicts usually arise as one tries to reach a particular control goal only to affect adversely another goal. Thus, an ideal method that is simple, inexpensive to build and operate, and that does not have any trade-offs does not exist and the skilled engineer has to make compromises.

In order to give an exhaustive view of the flow control methods, we have to remark that flow control techniques are usually divided into categories, as shown in figure 2.3. One of

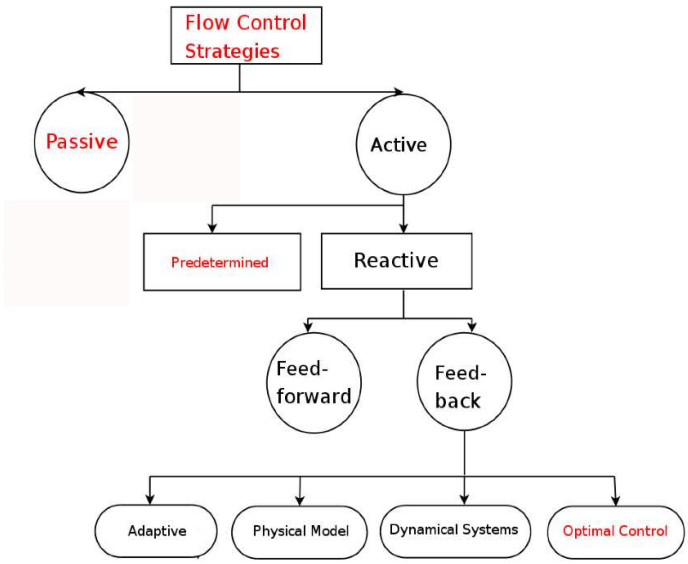

Figure 2.3: Various classifications of flow control

these is to consider whether the technique is applied at the wall or away from it. The control at the wall has been experimented after the observation that most of turbulence is produced near the wall. The flow may be altered through wall control by modifying significant surface parameters, like curvature, rigid-wall motions, compliance, temperature and porosity. Even wall heating or cooling can influence the flow. Mass transfer is possible via blowing/suction through a porous wall.

Another way for classifying flow control methods involves energy expenditure and the control loop involved. A control device can be passive, thus requiring no auxiliary power and no control loop, the net power saving being equal to power saved due to drag reduction, or active, hence requiring some energy expenditure, thus the net power saving being equal to the power saved minus the power spent to apply the control.

Moreover, active control requires a control law and is further divided into predetermined or reactive. Predetermined control is an open-loop control that does not require any measure of the state of the flow, being independent from it. Reactive control depends on the sate of the flow, the control action is continuously adjusted based on measurements of some kind.

Reactive control can be feedback or feedforward. In reactive feedforward control, measured and controlled variables differ, while feedback control necessitates the controlled variable to be measured, fed back and compared with a target input.

In the following a brief review of the state-of-the-art control strategies is given, according to the approach adopted and, after that, an introductory discussion will describe the most up-to-date sensors and actuators which have been used in experimental tests regarding flow control.

2.2.1 Passive control

Compliant coatings

Among passive techniques for boundary layer manipulation, compliant coatings represent one of the simplest solutions, not requiring slots, ducts or internal equipment of any kind. Aside from reducing drag, other reasons for studying compliant coatings are their many other useful applications, for example as sound-absorbent material in noisy flow-carrying ducts in aero-engines and as flexible surfaces to coat naval vessels for the purpose of shielding their sonar arrays from the sound generated by the boundary layer pressure fluctuations.

The idea of adopting compliant coatings for drag reduction came out from studying dolphins' surprising swimming skill. As a matter of fact, bottlenose dolphins have been clocked swimming at speed exceeding $10m/s$ for periods over $7s$, but assuming that the power output of cetaceans is equal to that of other mammals ($\approx 35W/kg$ of body weight), then such speeds are reached under turbulent conditions only if dolphins can expend several times more power than their muscles can generate. More specifically, it can be demonstrated, on the basis of energy considerations, that dolphins can not exceed the speed of $6m/s$ for periods grater than $2h$. The only explanation is that dolphins have a lower skin friction drag level than expected due to their complex epidermis, winch acts as a compliant coating optimized over each portion for the appropriate range of local Reynolds number. However, replicating Nature's perfection has represented an arduous task and only after many decades of contradictory results, this technique has been proved to achieve some results in delaying flow transition from laminar to turbulent condition caused by Tollmien-Schlichting instabilities. For an exhaustive description of this phenomenon the interested reader is referred to [48].

The mechanism through which compliant coatings works is strictly related to the hydroelastical coupling of fluid and solid which causes an irreversible energy transfer from the former to the latter. However, for long time it has been deemed impractical to clearly demonstrate its effectiveness and the first significant results appeared for the first time in Lee's wind tunnel experiments [25]. The coating used for the tests was made by a mixing 91% by weight of $100mm^2/s$ silicon oil with 9% of silicone elastomer. Results showed that, as compared to the rigid wall, the single layer, isotropic, viscoelastic compliant coating significantly suppressed the root-mean-square (rms) amplitude of the artificially generated Tollmien-Schlichting waves across the entire boundary layer for a range of Reynolds numbers.

Another promising technique to exploit compliant coating, but not yet thoroughly tested in turbulent regime, is the transegrity fabric, studied by Luo and Bewley [31]. Trasegrity fabric is a structure of bars and tendons that, differently from viscoelastic compliant coating, can be tuned to improve compliant properties.

Introduction of additives

Turbulent skin-friction drag can be reduced by the addiction of several substances, such as long-chain molecules and micro bubbles in liquid flows. The addiction of these substances leads to a suppression of the Reynolds stress production in the buffer zone. As demonstrated by Lumley [30] [29], the addiction of polymers acts in particular on the buffer layer, where velocity fluctuations extend polymer chains, increasing the viscosity. Consequently the viscous length scale increases, leading to an increase in the buffer layer thickness.

Among the possible techniques for drag reduction, solutions of micromolecules is perhaps the more mature technology. It has been proved that the addition of less than $100ppm$ of

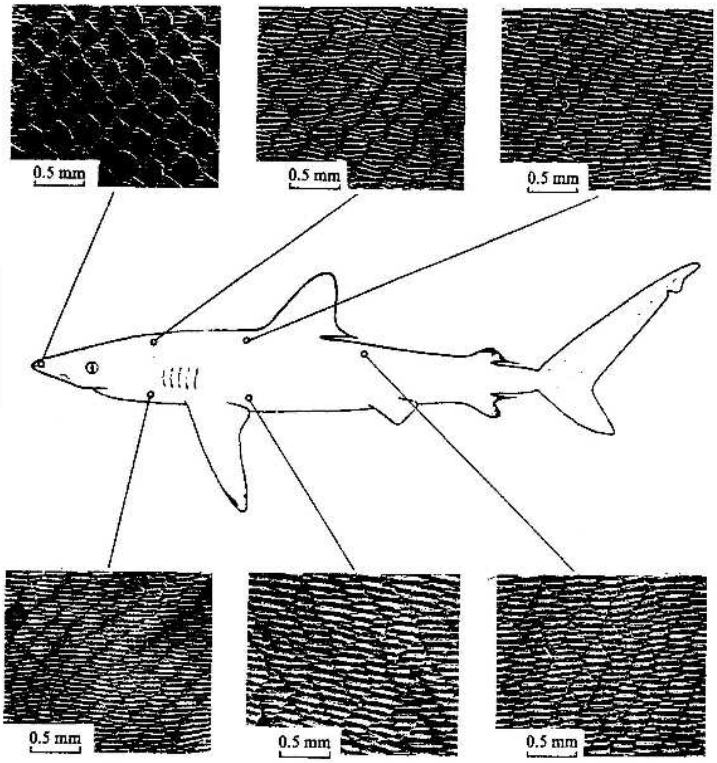

FIGURE 1. Silky shark, *Carcharhinus falciformis*, 2.27 m length.

Figure 2.4: Natural grooves on a silky shark skin.

polymethil methacrylate to a turbulent pipe flow of monochlorobenzene can lead to a skin-friction reduction up to 80% in both external and internal flows. Nevertheless the application can be very cost-effective: oil companies, for example, appear to have concluded that the use of polymers for supertankers is just at the break-even point, economically speaking.

Riblets

Another interesting geometrical modification is represented by riblets, which are particular wall grooves aligned with the freestream. Small longitudinal striations in the surface interacting favourably with the near-wall structures in a turbulent boundary layer can produce a modest drag reduction in spite of the increase in net wetted area. This feature of riblets has been observed even in silky sharks (*Carcharhinus falciformis*, Fig.2.4), whose skin shows striations of different size and shape according to the portion of their body.

The main effect of riblets is to stabilize QSV structures, decreasing the production of turbulent kinetic energy and thus to inhibit the wall cycle. The optimal spacing and height of riblets have been found to be $15\delta_\nu$ [27]. The presence of riblets affects the flow, modifying the boundary condition with respect to the solid wall case. In the case of riblets with sinusoidal shape, two virtual planes, placed at a different distance from an arbitrary reference point, acts as solid walls, requiring a homogeneous boundary condition for the longitudinal and transverse velocity respectively. We call the distance between the solid wall and the virtual

wall *protrusion height*. This is the main parameter that affect the efficiency in reducing friction drag.

2.2.2 Active Control

Predetermined control

Predetermined control mainly involves introducing waves into the flow through actuations or wall movement. Since this is the flow control method adopted in this work, we discuss it more in detail in the next chapter.

Spanwise wall oscillation Wall-bounded turbulent flows, both in the planar and cylindrical geometry, exhibit interesting modifications when cyclic surface motions are imposed in the spanwise direction. Perhaps the most interesting and practically appealing among the effects of the oscillating wall on turbulent flows is the significant reduction of the mean streamwise wall friction, first reported by [5]. A sensible drag reduction can be achieved with a wall moving sinusoidally in spanwise direction with a period T, according to the following law:

$$w_w(t) = A\sin(\omega t) \tag{2.9}$$

where w_w denotes the spanwise velocity at the wall and $\omega = \frac{2\pi}{T}$. In [40] this control law has been studied, through parametric investigation over Direct Numerical Simulation of turbulent channel flow, concluding that an optimal frequency ω_{opt} for drag reduction exists and such a reduction can be as high as 34% if $A = 12u_\tau$ and $Re_\tau = 200$.

The effect of Reynolds number on Drag Reduction it is not yet clear, but the evidence shows that the effect of the wall oscillation is reduced when Re is increased. One of the challenging questions we try to answer with this work is whether a significant drag reduction is achievable even at higher Reynolds number.

Travelling waves of spanwise velocity Travelling waves of spanwise velocity are a more complex and promising wall forcing that has proven to be very effective in reducing drag. Differently from oscillating wall, where the imposed spanwise velocity is homogeneous in stream- and spanwise directions, here the spanwise velocity has the following law:

$$w_w(t) = A\sin(\kappa_x\, x - \omega\, t) \tag{2.10}$$

where x is the streamwise coordinate and $\kappa_x = \frac{2\,\pi}{\lambda_x}$ is the streamwise wavenumber. With this motion law, which is graphically represented in Figure 2.5, waves of streamwise velocity moves in the streamwise direction with a speed:

$$c = \frac{\omega}{\kappa_x} \tag{2.11}$$

In [42] this wall motion law has then been tested through parametric DNS for an array of frequencies ω and wavenumbers α in order to find the optimum set $(\omega_{opt}, \alpha_{opt})$ achieving the maximum drag reduction and net power saving. A peak value of 48% of Drag Reduction has been found, when $A = 12u_\tau$ and $Re_\tau = 200$.

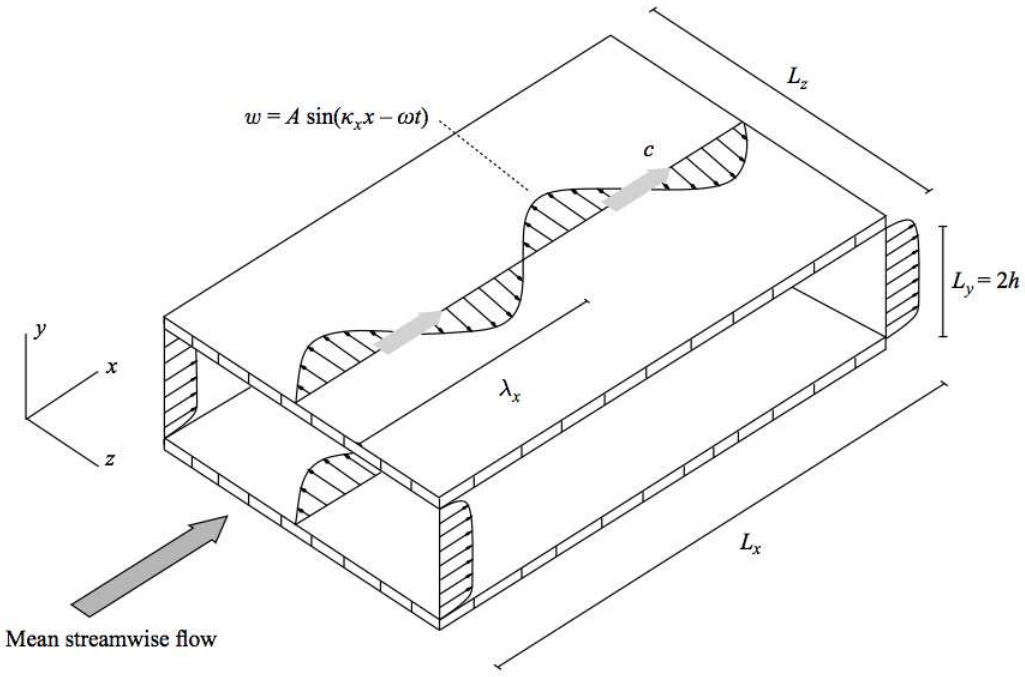

Figure 2.5: Graphical representation of the travelling waves of spanwise velocity

Feedforward control

The most popular feedforward strategy for controlling turbulent channel flows is the opposition control strategy firstly presented in [5]. With this approach, a detection plane for one of the velocity component is introduced in the flow at a distance $y+ \approx 10$. The detected velocity is then applied phase-shifted by $-\pi$ as a boundary condition at the wall. Whit this method, DNSs have shown a drag reduction of around 20% using wall-normal velocity and 30% using spanwise velocity.

Another meaningful attempt to introduce feedforward control, using this time a control law based on analytical model, is the one proposed in [3], which concerns the application of a receding-horizon model-predictive control to reduce drag in a turbulent channel flow. With this strategy, the evolution of the system is considered over a finite interval and control inputs are optimized over this finite interval using an iterative gradient-based strategy. Once optimized, control inputs are applied to the evolving flow system, then the procedure is applied to the following interval. It has been made possible thereby to fully relaminarize a turbulent channel flow at a low Reynolds number, indicatively $Re = 1500$.

Feedback control

Feedback control is the branch of reactive control that has received the greatest attention due to its solid theoretical background. In this context, the standard scenario considers channel flow with skin friction and pressure sensors at walls to provide system measurements, while zero-net-mass flux blowing/suction actuators continuously distributed over the walls are used to manipulate the flow inner structure.

One of the first approaches of this kind, before the introduction of linear system theory to flow control, has been presented in [23], where a neural network has been presented in order to adaptively find a feedback law for the local wall shear stress, achieving about 20% drag reduction. A linear feedback based on classical control theory has then appeared in [16], in which it was used to stabilize a turbulent wall flow in a two-dimensional channel using blowing/suction at walls, coordinated with measurements of wall shear stress. Afterwards, modern control theory has been introduced in [22], followed by the extension of the previously developed two dimensional controller to a three dimensional one. An exhaustive discussion on the application of linear quadratic feedback control to three dimensional channel flows has appeared for the first time in [24]. This strong theoretical framework has received further refinements in [4] and then applied for the first time for delaying laminar-to-turbulent transition. Also LQR control has been tested to achieve net drag reduction [33] for higher Reynolds numbers. Results showed that, as for other types of control, the net power saving decrease with Re, but a net saving is possible even at $Re = 6500$.

2.3 Streamwise traveling waves of spanwise wall velocity

In this section we are going to revise more in detail spanwise velocity waves as a flow control technique, main subject of this work. Firstly a description of both oscillating wall and travelling waves of spanwise velocity is given, introducing the main parameters of the predetermined control and those used to evaluate its effectiveness.

Then, results from main literature references are presented and briefly discussed.

Finally the main wall-flow interaction mechanism is described, focusing on the scaling factors for Drag Reduction (DR).

2.3.1 Description

Travelling waves The imposition of a non-zero spanwise velocity at walls of a channel flow influences deeply the flow and interacts strongly with the wall cycle, differently from a streamwise wall movement.

If some particular spanwise motions at walls are imposed, this interaction becomes favourable and produces, among others, the interesting and practical-appealing effect of reducing longitudinal friction drag.

On this study we focus on the streamwise-travelling wave of spanwise wall velocity, a particular wall motion that, in its most general formulation, for walls oscillating with period T and a spatial sinusoidal distribution of spanwise velocity over a wavelength λ_x, takes the form:

$$w_w(x,t) = A\sin(\kappa_x x - \omega t) \tag{2.12}$$

where w_w is the spanwise velocity of the wall, x is the streamwise coordinate, t is time, A is the oscillation amplitude, $\omega = \frac{2\pi}{T}$ is the frequency and $\kappa_x = \frac{2\pi}{\lambda_x}$ is the wavenumber. In 2.12, the wave of spanwise velocity moves (backward or forward) in the streamwise direction, and its phase speed is

$$c = \frac{\omega}{\kappa_x} \tag{2.13}$$

Oscillating wall and stationary waves The law 2.12 contains two more simple wall motions. In the case of $\kappa_x = 0$ spatial dependency from the coordinate x is lost and, disregarding the phase angle, the simple condition of walls that oscillate with a period T with the following law is obtained

$$w_w(t) = A\sin(\omega t) \tag{2.14}$$

On the contrary, if $\omega = 0$ a steady wave is obtained, the spanwise velocity of walls varies in the streamwise direction with a wavelength λ_x, according to the following law

$$w_w(x) = A\sin(\kappa_x x) \tag{2.15}$$

The time dependence of 2.14 is converted into a relatively unsteady interaction between the steady wall motion and the convecting near-wall turbulence. At first appearance this conversion is similar to the Taylor's frozen turbulence hypothesis, for which the velocity scale is the mean streamwise velocity. Indeed, a difference from the frozen turbulence hypothesis exists. With steady waves the mean velocity is zero at the wall, the turbulence keeps a strongly convective character ([21]; [19]), with elongated space-time correlations ([38]). The velocity scale for space-time conversion is therefore the convection velocity $\mathcal{U}$ of the turbulent fluctuations, which almost coincides with the mean velocity along with the wall-normal span of the channel, except for a thin near-wall layer, say $y^+ < 10$, where it is constant at $\mathcal{U}_w^+ \approx 10$. [46] have shown that the optimal frequency ω_{opt} for 2.14 translates into an optimal wavenumber $\kappa_{x,opt}$ for 2.15 through the relation

$$\kappa_{opt} = \frac{\omega_{opt}}{\mathcal{U}_w} \tag{2.16}$$

The bulk skin friction coefficient The streamwise shear stress is defined as

$$\tau = \rho\nu\frac{\mathrm{d} < u >}{\mathrm{d}y} - \rho < uv > \tag{2.17}$$

where $< \cdot >$ is the expected value operator. The wall-shear stress of a single wall, due to the homogeneous condition for u and v components of velocity, reduces to the following expression:

$$\tilde{\tau_w} = \rho\nu\frac{\mathrm{d} < u >}{\mathrm{d}y}\bigg|_w \tag{2.18}$$

Since a top and a bottom wall are present we have two wall shear stresses, $\tau_{w,t}$ and $\tau_{w,b}$, respectively. The average of stremwise shear stresses of the two walls is the significant quantity to measure the total mean streamwise wall stress:

$$\tau_w = \frac{\tau_{w,t} + \tau_{w,b}}{2} \tag{2.19}$$

Equally, the bulk skin friction coefficient of a single wall can be written as

$$\tilde{C_f} = \frac{2\tilde{\tau_w}}{\rho U_b^2} \tag{2.20}$$

while the skin friction coefficient of the two walls together is:

$$C_f = \frac{2\tau_w}{\rho U_b^2} = \frac{C_{f,t} + C_{f_b}}{2} \tag{2.21}$$

where $C_{f,t}$ and $C_{f,b}$ are the skin frictions of the top and bottom walls respectively.

Measure of Drag Reduction In order to give a clear-cut definition of Drag Reduction we define the input power that is necessary to drive the flow as:

$$P = \left\langle Q \frac{\partial p}{\partial x} \right\rangle \tag{2.22}$$

where $\partial p/\partial x$ is the streamwise pressure gradient and Q is the volume flow rate. Thus, the Power saved after the imposition of the predetermined control is

$$R = \frac{P_0 - P}{P} \tag{2.23}$$

where P_0 is the input drive power for the channel flow in the uncontrolled case.

To better understand how the coefficient R can be a measure of Drag Reduction, on should consider the two usual choices of running a channel flow simulation imposing the constant Q or constant $\partial p/\partial x$ condition.

In the first case, recalling Eq.2.21, it is trivial to verify that R reduces to:

$$R = DR = \frac{C_{f,0} - C_f}{C_{f,0}} \tag{2.24}$$

that is the relative change in skin friction coefficient, between the uncontrolled $C_{f,0}$ and the controlled C_f case. It is usual to express these coefficient in percentage, leading to

$$DR\% = 100 \frac{C_{f,0} - C_f}{C_{f,0}} \tag{2.25}$$

On the other hand, in the case of a constant P_x simulation, it can be observed an increase of Q (and hence of pumping power P), when a Drag Reducing control is applied. This counter-intuitive result is only apparent because, in this context, drag reduction means that the increase in pumping power required to support the larger flow rate is actually less than what would be necessary if the control were not used.

The skin friction coefficient actually decreases in both constant-Q and constant-p_x cases, when drag decrease.

Power required The imposition of a wall motion require the introduction of energy into the system. In order to evaluate the effectiveness of a DR technique, the power saving have to be compared with the energy spent for the control imposition. The actual device for wall oscillation can be complex, and it is not our aim to describe it. In the global power budget, we then disregard mechanical losses, which are unavoidable in a real-world implementation. However, the power that an ideal device dissipates against the viscous stresses provides an upper bound for the performance of the control strategy. We express this power as a percentage of the power spent to drive the fluid along the streamwise direction in the fixed-wall configuration:

$$P_{sp}\% = \frac{100}{(\mathrm{d} < u > /\mathrm{d}y)|_0 U_b} \frac{1}{L_x L_z} \int_0^{L_x} \int_0^{L_z} \left\langle w_w \frac{\partial w}{\partial y}\bigg|_w \right\rangle \mathrm{d}x \mathrm{d}z \tag{2.26}$$

where the subscript 0 stands for reference uncontrolled case quantities. In computations, the expected value operator $< \cdot >$ is substituted by its best estimate, that is the following time average:

$$< \cdot > = \frac{1}{T_{sim}} \int_0^{T_{sim}} \cdot \, \mathrm{d}t \tag{2.27}$$

where T_{sim} is the simulation time on which we average a specific quantity.

During the wall motions, fluctuations of spanwise wall shear can produce regions where the flow pull the wall, collaborating instead of opposing to its movement. With the space-average of Eq. 2.26, both positive and negative contributions of the term $< w_w(\partial w/\partial y)|_w >$ to the power spent $P_{sp}\%$ are summed up. This means to consider that a reduction of Power spent can be obtained by exploiting those portions of walls where the shear stress favourably drive the wall, requiring less energy for the actuation.

Since such a sensitive actuation is not always possible and with the intent to quantify the positive contribution to the power spent, it is useful to separate positive $P_{sp}^{+}\%$ and negative $P_{sp}^{-}\%$ contributions to the power spent, as:

$$P_{sp}^{+}\% = \frac{100}{(\mathrm{d} < u > /\mathrm{d}y)|_0 U_b} \frac{1}{L_x L_z} \left\langle \int_0^{L_x} \int_0^{L_z} w \mathrm{d_y} w \, f(w \mathrm{d_y} w) \mathrm{d}x \mathrm{d}z \right\rangle$$

$$P_{sp}^{-}\% = \frac{100}{(\mathrm{d} < u > /\mathrm{d}y)|_0 U_b} \frac{1}{L_x L_z} \left\langle \int_0^{L_x} \int_0^{L_z} w \mathrm{d_y} w \, f(-w \mathrm{d_y} w) \mathrm{d}x \mathrm{d}z \right\rangle$$

where $w\mathrm{d_y}w$ is the shortened form of $< w_w(\partial w/\partial y)|_w >$, used to lighten the notation and $f(u)$ is the unit step function.

Measure of Net Power saving Even more important is to quantify the net energy saving, defined as the difference between the percentage power saved to drive the fluid along the streamwise direction (which coincides with the DR at constant Ub) and the percentage power spent defined above, namely

$$P_{sav}\% = DR\% - P_{sp}\% \tag{2.28}$$

A more precise definition of Net Power Saving that can be used for constant-p_x, constant-Q or constant P channel flows, rely on the definition of pumping power P, as shown in the following:

$$S = \frac{P_0 - P + P_{sp}}{P_0} \tag{2.29}$$

Gain With gain we mean the saving per energy input, defined as:

$$G = \frac{P_0 - P}{P_{con}} \tag{2.30}$$

A big gain means that high pumping power (Drag Reduction) savings can be achieved through a small power input. A negative gain means that drag has increased, while if $|G| < 1$ the power input is greater than the pumping power saving, leading to a $S < 0$.

Generally speaking, a good control system should have G and S as great as possible.

2.3.2 Available Results

A meticulous numerical campaign has been conducted in [42] [40]. A large range of ω and κ_x have been spanned and both $DR\%$ and P_{net} computed. Figure 2.6 describes the effects of the travelling waves in terms of the percentage change in friction drag as a function of ω and κ_x for $A = 0.5$ and $Re_P = 4760$. Only the upper half of the $\omega - \kappa_x$ plane is shown, since 2.12 yields symmetric results upon exchanging the pair ω, κ_x with -ω, -κ_x. (This has been explicitly verified for a few points).

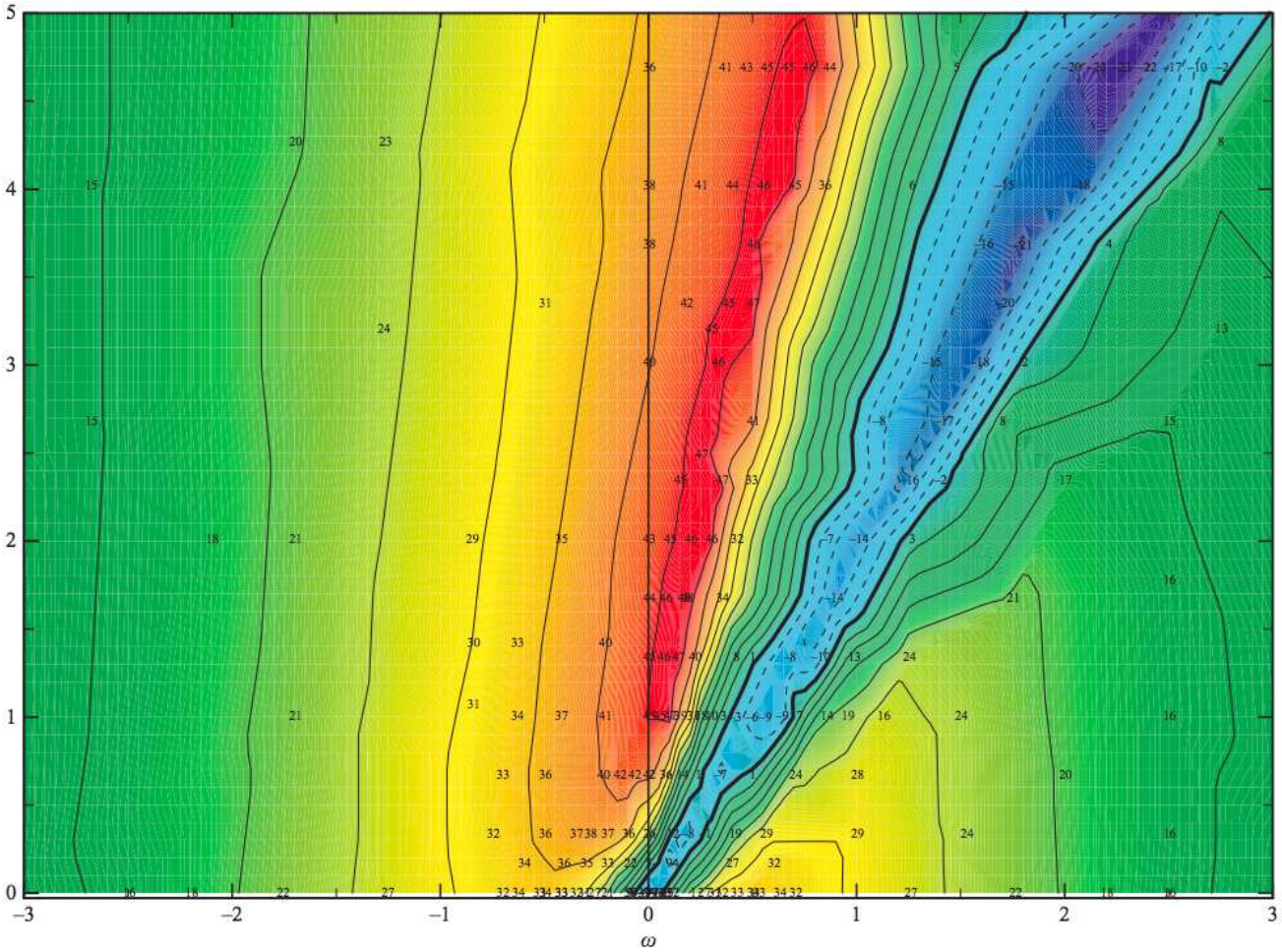

Figure 2.6: Map of friction $DR\%$ in the $\omega - \kappa_x$ plane for $A = 0.5$ and $Re = 4760$. Contours are spaced by 5% intervals, loci of zero DR are indicated by thick lines and negative values are represented by dashed lines. The numbers indicate percentage DR at measured points [42].

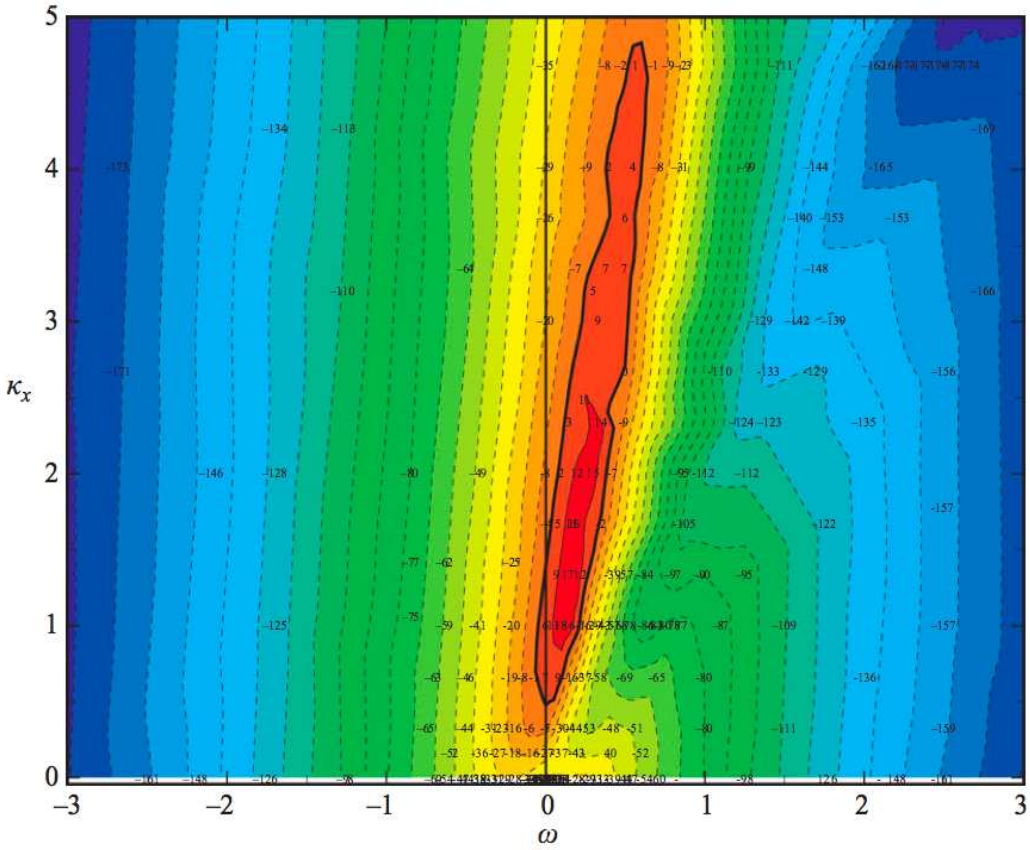

Figure 2.7: Map of net power saving $P_{net}\%$ in the $\omega - \kappa_x$ plane for $A = 0.5$ and $Re = 4760$. Contours are spaced by 10% intervals, locus of zero $P_{net}\%$ is indicated by thick line and negative values are represented by dashed lines. The numbers indicate $P_{net}\%$ at measured points [42].

The phase speed c is interpreted graphically as the inverse of the slope of straight lines passing through the origin. In the first quadrant, the waves move forward in the direction of the mean flow ($c > 0$), while the second quadrant corresponds to backward-travelling waves ($c < 0$).

On the horizontal ω-axis, 2.12 reduces to the oscillating wall case 2.14: our data agree with those by Quadrio and Ricco (2004), who used the same Re and slightly different discretization parameters. On the vertical κ_x-axis, 2.12 reduces to the steady wave case 2.15. DR behaves very similarly on the two axes, once frequency is converted into wavenumber through 2.16, reaching its maximum at $\omega = \omega_{opt} \approx 0.5$, and at $\kappa_x = \kappa_{x,opt} \approx 1$, with ω_{opt} and $k_{x,opt}$ related by $\mathcal{U}_w = 0.5$.

Figure 2.7 shows that $P_{net}\%$ is positive mainly for slow forward-travelling waves, and that 18% of maximum net is measured for $\omega \approx 0.15$, $\kappa_x \approx 1$ (which is also the optimum pair for minimum P_{sp}). This benefit is noteworthy when compared with the negative net balance of the oscillating wall at this value of A, and the small net gain of 5% obtained by the steady waves.

Figure 2.8 shows that $DR\%$ increases monotonically with A and reaches nearly 60% when

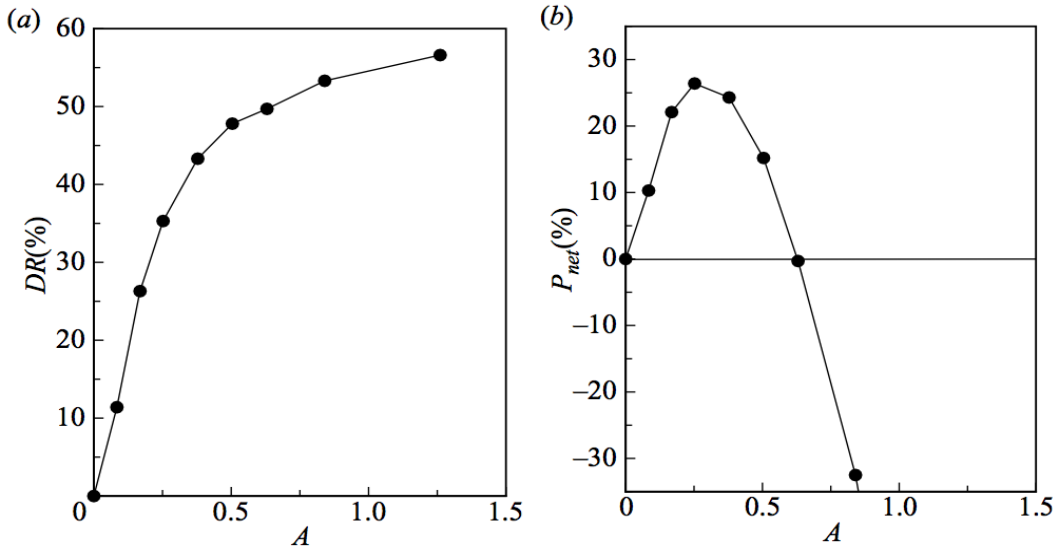

Figure 2.8: Percentage DR (a) and net power saving (b) as functions of forcing amplitude A. The forcing conditions are $\omega = 0.16$, $\kappa_x = 1.66$, which produce the maximum DR at $A = 0.5$ and $Re = 4760$ [42].

A is slightly larger than the flow centreline velocity. In the plot on the right, P_{net} grows significantly at lower amplitude, which is expected as the power spent to impose the travelling waves decreases quadratically with A, and is larger than 26% for $A = 0.25$. Both results are consistent with (but quantitatively much better than) the oscillating wall scenario.

An experimental campaign on travelling waves in a circular pipe flow has been led by [2]. Without getting to the heart of the experimental setup description, a circular pipe has been divided in several independently rotating slices. In this way the sinusoidal modulation of the wall velocity has been transformed into a piecewise-constant approximation of a sine wave, as shown in Figure 2.9b. Parameter, although not identical, are comparable to those of [42]. The DR obtained at two different sections of the pipe, namely the third $s = 3$ and sixth $s = 6$ slices, are reported in Figure 2.9b. It can be easily observed that main qualitative differences exists compared with the DNS results of 2.6, i.e.:

- The maximum drag reduction observed in the experiment is lower than that reported in the numerical simulations 33% versus 48%
- Although there is a clear indication that drag reduction due to waves drops when their phase speed is near $c+ \approx 12$, the increase of friction drag above that of the reference flow reported in the numerical simulations is not observed experimentally.
- The experimental curves present marked wiggles, which are stronger for the case at $s = 3$ and that are not observed in the numerical simulations.

These differences are maybe due to the different types of flow, channel flow in DNS and pipe flow in the experiment, and to the intrinsic transient of an experimental setup which differs from the idealized situation simulated by a DNS. Another big difference is the piecewise-constant approximation of the waveform, which introduces steps in wall velocity between

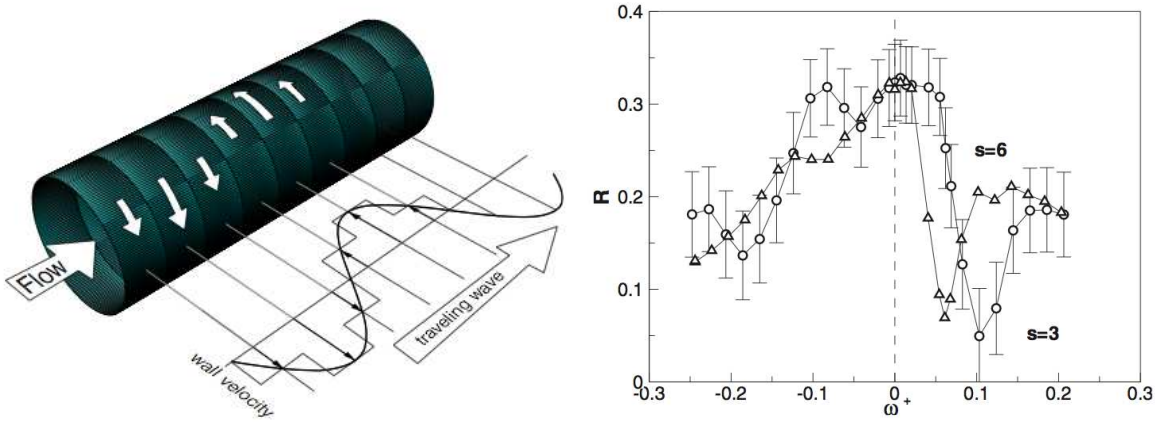

(a) (b)

Figure 2.9: On the left the experimental setup of [2]. On the right drag reduction rate as a function of the oscillation frequency, for $s = 3$ (circles) and $s = 6$ (triangles).

consecutive slices of the pipe. We know that the Fourier transform of the step function has a broad frequency content distributed over the spectrum. Thus, the actual forcing includes spurious wavenumbers that influences the result.

This astonishing decrease of DR between experiment and DNS has been observed also in other analogous experiments with oscillating wall technique [7] [53].

2.3.3 Mechanism of interaction: Generalized Stokes Layer

The first drag reduction results came before a rough comprehension of how spanwise velocity waves at the wall can influence turbulence and the wall-cycle. Even nowadays this interaction presents some obscure aspects.

A first step forward in comprehension of this phenomena pass through the description of the spanwise flow induced by streamwise travelling waves of spanwise velocity, as done in [41]. This flow is a thin, unsteady and streamwise-modulated boundary layer called the Generalized Stokes Layer (GSL). When the streamwise is laminar, there is the possibility to find the analytical solution for the laminar GSL. When the streamwise flow is turbulent, the laminar generalized Stokes layer solution describes well the space-averaged turbulent spanwise flow, provided that the phase speed of the waves is sufficiently different from the turbulent convection velocity, and that the time scale of the forcing is smaller than the life time of the near-wall turbulent structures. Under these conditions, the drag reduction is found to scale with the Stokes layer thickness, which renders the laminar solution instrumental for the analysis of the turbulent flow.

Thus, firstly we describe the main aspects of the procedure that leads to the analytical solution for the GSL, as presented in [41]. Then, the turbulent drag changes are correlated with the quantities computed through the GSL solution.

2.3.4 The laminar GSL

We consider a laminar incompressible flow driven by a *constant pressure gradient* in a channel flow domain. The flow is governed by the incompressible Navier-Stokes equations:

$$\frac{\partial \mathbf{u}}{\partial t} + (\mathbf{u} \cdot \nabla)\mathbf{u} + \frac{\nabla P}{\rho} = \nu \nabla^2 \mathbf{U} \tag{2.31}$$

$$\nabla \cdot \mathbf{u} = 0 \tag{2.32}$$

At the walls, i.e. at $y = 0$ and $y = 2h$, the spanwise velocity component takes the form of a travelling wave, so that the following boundary conditions are imposed:

$$u = v = 0 \qquad w = A\,\mathrm{Re}[e^{ik_x(x-ct)}] \tag{2.33}$$

where Re indicates the real part.

The system 2.31 and 2.32 can be simplified as follows. All terms involving the z derivatives are null because the non-homogeneous boundary condition 2.33 depends on the sole coordinate x and there is no pressure gradient along z. Analogously to the classical channel flow, from this simplification and the use of 2.31 it follows that the x- and y-momentum equations become independent of w. The streamwise flow is thus described by the steady parabolic velocity profile of the plane Poiseuille flow, $v = 0$ everywhere in the channel, and w satisfies the z-momentum equation.

$$\frac{\partial w}{\partial t} + u\frac{\partial w}{\partial x} = \nu \left(\frac{\partial^2 w}{\partial x^2} + \frac{\partial^2 w}{\partial y^2} \right) \tag{2.34}$$

This is equation resembles that one describing the second Stokes'problem.

Scaling and simplification of w-momentum equation Equation 2.34 is now non-dimensionalized and expressed in a simplified form. The problem involves two distinct length scales. The first one is $\lambda_x = 2\pi/\kappa_x$, the streamwise wavelength of the travelling wave. The second length scale is δ, a measure of the GSL thickness. The scaled streamwise coordinate is, therefore, $\tilde{x} = x/\lambda_x = O(1)$ and the scaled wall-normal coordinate is $\tilde{y} = y/\delta = O(1)$.

Analogously, two velocity scales exist in the boundary layer. The first one is related to the streamwise flow within the layer: it can be taken as the maximum streamwise velocity across the layer, i.e. the Poiseuille flow velocity at the edge of the GSL, we indicate it as $U_\delta = u(\delta)$. The stremwise velocity can be nondimensionalized through it, obtaining $u/\tilde{U}_\delta = O(1)$.

The assumption that

$$\delta \ll h \tag{2.35}$$

allow to express the velocity $u(y)$ through a Taylor expansion for small y.

$$u(y) = u(0) + \left.\frac{\mathrm{d}u}{\mathrm{d}y}\right|_{y=0} \tag{2.36}$$

where the first term on the right vanishes due to the homogeneous boundary condition for the streamwise velocity. The velocity scales then becomes:

$$U_\delta = \delta \tau_w \tag{2.37}$$

where τ_w is the wall shear stress $\mathrm{d}u/\mathrm{d}y|_w$. The nondimensionalized velocity $\tilde{u}(\tilde{y})$ becomes

$$\tilde{u}(\tilde{y}) = \tilde{y} \tag{2.38}$$

The Poiseuille velocity profiles becomes equivalent to the Couette laminar profile. Henceforth, $\tilde{u}$ can, therefore, be thought of as a Couette laminar flow bounded at $y = 0$ and unbounded as $y \to \infty$.

The spanwise velocity component scales with A, i.e. $\tilde{w} = w/A = O(1)$, and the time is scaled by the period of the wall motion, i.e. $\tilde{t} = tc/\lambda_x = O(1)$.

Substituting the scaled variables into 2.34 one obtains

$$\frac{\partial \tilde{w}}{\partial \tilde{t}} + \frac{U_\delta}{c}\tilde{y}\frac{\partial \tilde{w}}{\partial \tilde{x}} = \frac{\nu}{c\lambda_x}\frac{\partial^2 \tilde{w}}{\partial \tilde{x}^2} + \frac{\lambda_x \nu}{c\delta^2}\frac{\partial^2 \tilde{w}}{\partial \tilde{y}^2} \tag{2.39}$$

The boundary conditions are $\tilde{w} = \mathrm{Re}[e^{2\pi i(x-t)}]$ at $y = 0$ and $w = 0$ at $y \to \infty$. After the introduction of the similarity variable $\xi = \tilde{x} - \tilde{t}$ the equation 2.39 becomes:

$$\left(\tilde{y} - \frac{c}{U_\delta}\right)\frac{\partial \tilde{w}}{\partial \xi} = \frac{\nu}{c\lambda_x}\frac{\partial^2 \tilde{w}}{\partial \xi^2} + \frac{\lambda_x \nu}{c\delta^2}\frac{\partial^2 \tilde{w}}{\partial \tilde{y}^2} \tag{2.40}$$

and $\tilde{w}(\xi, y) = \mathrm{Re}(e^{2\pi i \xi})$ at $\tilde{y} = 0$

Three flow regimes After some dimensional considerations, an expression for the GSL thickness can be obtained in function of the parameters of the travelling waves.

Three flow regimes can be identified by considering the magnitude of the inertial terms in 2.40 with respect to the y-diffusion term.

In the limit

$$\delta \ll c/\tau \tag{2.41}$$

the balance between inertial and viscous effects gives:

$$\delta = O\left[\left(\frac{\lambda_x \nu}{c}\right)^{1/2}\right] \tag{2.42}$$

By inserting 2.42 in 2.41, a condition on the phase-speed velocity c is obtained: $c \gg (\lambda_x \nu)^{1/3}\tau^{2/3}$. The phase speed is so high that the convection is due solely to the unsteadiness and the flow induced by spatially uniform temporal wall oscillations is recovered.

In the limit

$$\delta \gg c/\tau \tag{2.43}$$

the balance between inertial and viscous effects leads to

$$\delta = O\left[\left(\frac{\lambda_x \nu}{\tau}\right)^{1/3}\right] \tag{2.44}$$

Again, substituting 2.44 into 2.43, the condition for the standing-wave regime is found: $c \ll (\lambda_x \nu)^{1/3}\tau^{2/3}$. The phase speed is so low that the convection is due solely to the streamwise modulation. The flow induced by stationary waves is obtained.

Travelling waves are the intermediate case, when the two inertia terms on the left side of 2.40 are comparable and the unsteadiness and the streamwise modulation both contribute to the convection. The boundary-layer balance is

$$\frac{\delta^3 \tau}{\lambda_x \nu} = O\left[\frac{\delta^2 c}{\lambda_x \nu}\right] = O(1) \tag{2.45}$$

A characteristic phase speed

$$c_c = (\lambda_x \nu)^{1/3} \tau^{2/3} \tag{2.46}$$

The speed c_c has the following physical interpretation. By substituting 2.42 and 2.44 into 2.37, one finds that $c_c \approx U_\delta$. This means that the characteristic phase speed is comparable with the streamwise velocity at the outer edge of GSL when the travelling-wave regime occurs.

The GSL thickness In summary, three GSL thickness for the three different regimes can be found.

In the oscillating-wall regime, δ is given by 2.42, or, equivalently, by $\delta = O[(\nu/\omega)^{1/2}]$, which is the classical Stokes layer result.

For the standing-wave regime, we recognize in 2.44 the $\lambda_x^{1/3}$ dependence of the steady SL thickness, which is due to the coupling with the streamwise flow.

In the travelling-wave regime, simplification of 2.45 shows that both expressions for δ, i.e. 2.42 for the oscillating-wall regime and 2.44 for the standing-wave regime, are valid.

Thin-layer assumption and Re_b The thin-layer assumption 2.35 can be expressed in a more convenient form in terms of the known quantities λ_x, h, ν and U_b by the use of the expressions for δ given in the previous paragraph. Use of 2.42, 2.44, 2.37 and the relation between wall-shear stress and $Re_b = 2U_b h/\nu$ for a laminar channel flow, shoes that 2.35 becomes

- For the standing-wave and the travelling-wave regimes, the thin layer approximation can be rewritten as

$$\frac{\lambda_x}{h} \ll Re_b \tag{2.47}$$

- For the oscillating-wave regime, it may be expressed as

$$\frac{\omega U_b^2}{h} \gg \frac{1}{Re_b} \tag{2.48}$$

For a streamwise turbulent flow, the wall friction and Re_b are related by an empirical relation found by Dean, i.e. $\nu\tau/U_b^2 \approx Re_b^\alpha$, with $\alpha = -0.25$. Equation 2.47 in case of turbulent flow, becomes:

$$\frac{\lambda_x}{h} \ll Re_b^{\alpha+2} \tag{2.49}$$

An analytical solution An analytical solution can be found for the laminar GSL that can be expressed in terms of the Airy function of the first kind, following the procedure given in [41]. For the interested reader we remand to the cited reference.

This analytical solution, found for the laminar streamwise flow, leads to the results that can describe well several turbulent turbulent statistics.

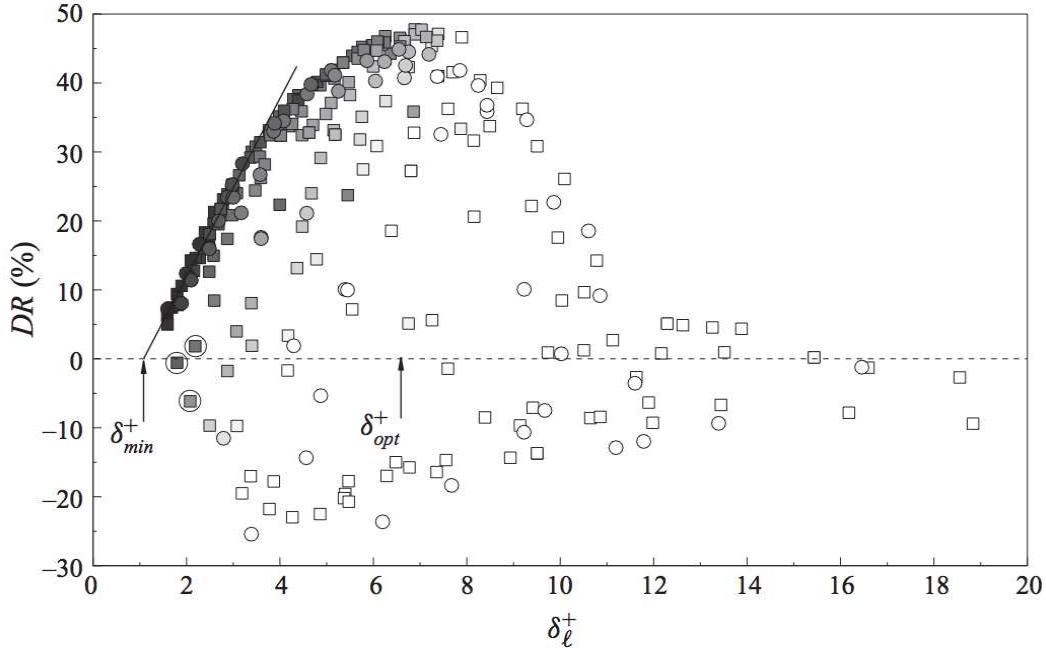

Figure 2.10: Drag reduction data as function of δ_l for constant-Q (squares) and constant-P_x (circles) simulations. The oblique straight line shows the linear correlation between DR and δ_l^+. The arrows indicate the minimal condition for drag reduction, $\delta_l^+ \approx 1 = \delta^+_{min}$, and the optimal GSL thickness, $\delta_l^+ \approx 6.5 = \delta^+_{opt}$. The colour changes on a linear scale from black at $T^+ = 0$ to white at $T^+ \geq T^+_{th} = 120$.

2.3.5 GSL and turbulent Drag Reduction

All this analytical effort has been intended to demonstrate the relation between the laminar GSL thickness δ and turbulent drag reduction.

The thickness of the laminar GSL is computed with the relation in [41], while for $\kappa_x = 0$ the Stokes layer is computed by $\delta_l^+ = \sqrt{2/\omega^+}$. In figure 2.10, the DR_P (DR in simulations at constant P_x data (circles) described in [41] and the DR_Q data by QRV09 (squares) are plotted as function of δ_l^+. Black and grey points correspond to small T^+, i.e. to a wall forcing which is unsteady with respect to the near-wall turbulence, $T^+ < T^+_{th} \approx 120$, and white points are for $T+ > T^+_{th}$. White points are extremely scattered, while black points collapse on a sharply-defined curve. At small T^+, when the GSL profile matches the mean spanwise turbulent profile, DR grows linearly with δ_l^+ and linearity holds up to $DR\% \approx 35$ and $\delta_l^+ \approx 4$. The maximum drag reduction occurs for $\delta^+ \approx 6.5 = \delta^+_{opt}$. It must be observed that a few dark points with small δ_l^+ do not correlate well: these point correspond to high value of κ_x^+, where the drag-increase region extends outside the strip $T^+ \leq T^+_{th}$. We thus conclude that DR is related to δ_l^+ as long as $T^+ \ll T^+_{th}$ and $|c - \mathcal{U}^+_w| \gg 0$. Under these conditions, the laminar solution can therefore be used effectively to predict DR.

Figure 2.11 represents $DR\%$ data versus $P_{req,l}$, the required input power (using the definition 2.26) computed for the laminar GSL solution. Data show a good correlation for dark symbols and worsens as T^+ increases. For the dark points, DR decreases monotonically as

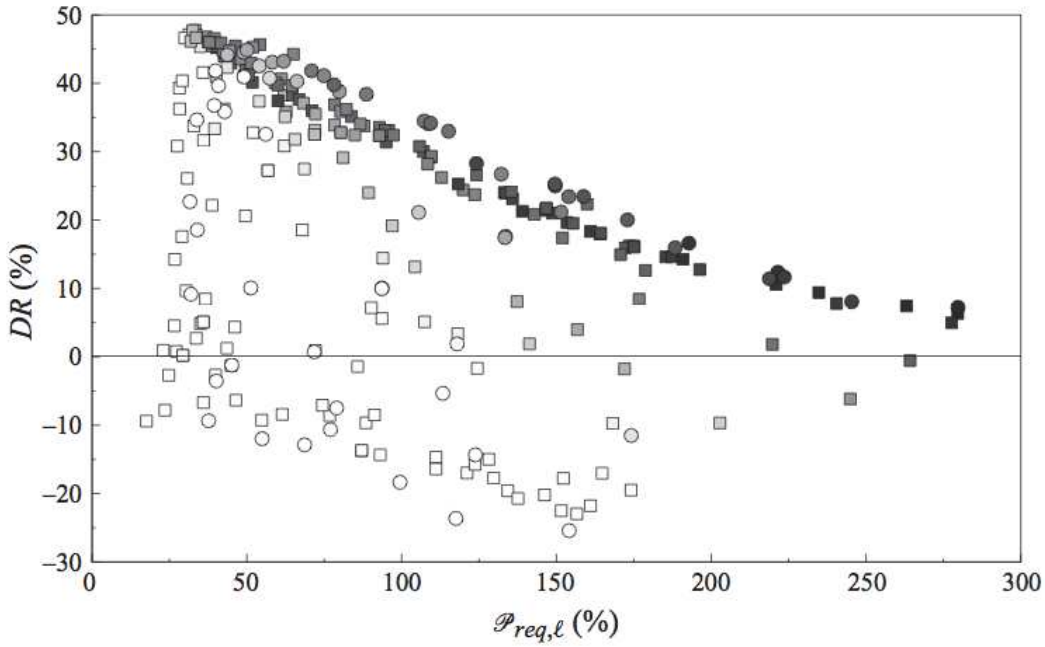

Figure 2.11: Drag reduction data as function of P_{req}% for constant-Q (squares) and constant-P_x (circles) simulations. Grey scale is as in figure 2.10.

$P_{req,l}$ increases, which is therefore minimum when DR is maximum. This correlation is of good omen, with the intent to reach the goal of a net power saving.

2.3.6 Four regimes for drag modification

In [41], two main parameters have found to be significant in the description of the possibly good interaction between the turbulent flow and the laminar GSL. The first is the forcing period T^+, scaled in viscous units. It is an index of the unsteadiness of the forcing in a frame moving at the (average) speed of the near-wall turbulence fluctuations U_w. Its ratio with T^+_{th} is the important parameter in the determination of the drag reduction regime. The other important parameter is the wave speed c^+, especially its relation with the convective velocity of main turbulent structures $\mathcal{U}_w$. According to the values taken by these two parameters, four regions for drag modification can be identified (Table 2.1).

According to table 2.1, in region 1, termed region of active drag reduction, the GSL thickness δ^+_l determines drag reduction. The success of GSL in reducing drag is due to the spanwise

$T^+ - T^+_{th}$ \ $c^+ - \mathcal{U}^+_w$	$\gg 0$	≈ 0
$\ll 0$	1 Active Drag Reduction	3 Weak Drag Increase
$\gg 0$	2 Weak Drag Reduction	4 Lock-in Drag increase

Table 2.1: Description of the four regimes for drag modification

viscous forces operating on a shorter time scale than the typical Lagrangian correlation time of near-wall structures, and through wall waves that travel slower than the turbulence structures. The laminar GSL thickness agrees well with the corresponding turbulent thickness, which makes the laminar analysis useful for predicting drag reduction.

Region 2, of weak drag reduction; a sharp drop of drag reduction occurs as T^+ increases beyond the optimum time scale T^+_{th}. The forcing is slow with respect to the turbulence, although the waves still travel faster than the structures. The GSL becomes thick and the near-wall turbulence is not efficiently altered because a typical structure loses its coherence before travelling a distance of one wavelength.

Region 3 is inside both the strip and the half-cone, and corresponds to high drag increase.

Region 4 of weak drag increase. The wave speed is comparable with the one of the near-wall structures, which cover only a small portion of one wavelength during their survival time. This occurs irrespectively of δ^+, which is consistent with the previous observation on figure 2.10 that the drag increase is not related to the GSL thickness.

Chapter 3

Direct Numerical Simulation of a channel flow

Channel flow at turbulent Reynolds number is a framework of particular interest in which developing and testing proper feedback control strategies. As a matter of fact, the symmetry and simplicity offered by the geometry of a plane channel flow lead to effective implementation in DNS code. What follows is an in-depth description of channel flow model and code used for numerical simulations.

3.1 A model problem

The channel flow is a flow between two parallel, infinite plates placed a distace $L_y = 2h$. As outlined in Figure 3.1, a Cartesian coordinate system is introduced, where x, y and z denote the streamwise, wall-normal and spanwise directions, respectively. The velocity field is composed by the streamwise, wall-normal and spanwise components u, v and w. The pressure field is denoted by p.

Due to the inifinite extent of walls, one can identify two statistically homogeneous direction, namely x and z, so that the Reynos-averaged streamwise velocity $< u >$ depends only on the wall-normal coordinate y. Thanks to this double homogeneity it is possible to take a finite-length doubly-periodic domain for computations. This means that the computational domain has a stream- and spanwise length of L_x and L_z with *periodic* boundary conditions on the unbunded portion of the domain, i.e.

$$u_j(L_x, y, z) = u_j(0, y, z) \qquad u_j(x, y, L_z) = u_j(x, y, 0) \qquad j = x, y, z \tag{3.1}$$

Several Reynolds number can be defined for a channel flow. One is based on the channel half-width h and the reference Bulk Velocity U_B as

$$Re_b = \frac{U_b h}{\nu} \tag{3.2}$$

while the reference bulk velocity is defined as

$$U_b = \frac{1}{2h} \int_0^{2h} < u > \mathrm{d}y \tag{3.3}$$

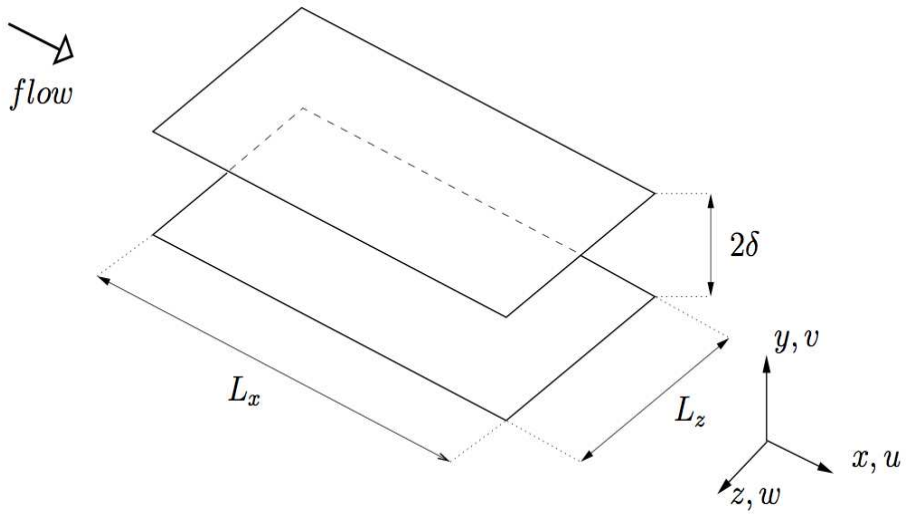

Figure 3.1: Computaonal domain of a turbulent channel flow

Where $< \cdot >$ is the expected-value operator. Moreover, a Reynolds number can be defined, based on the channel half-width and the velocity U_p, that is the centerline velocity of a Poiseuille flow with the same mass flow rate, obtaining

$$Re_p = \frac{U_p h}{\nu} \tag{3.4}$$

Recalling the parabolic law of a laminar Poiseuille flow and the definition 3.3, it is easy to observe that $U_b = \frac{2}{3}U_P$. Choosing the wall unit velocity u_τ as reference velocity, leads to the definition of another Reynolds number

$$Re_\tau = \frac{u_\tau h}{\nu} \tag{3.5}$$

The viscous velocity u_τ is proportional to the square root of the wall stress τ_w and thus Re_τ depends on the square-root of the derivative of the streamwise velocity at the wall.

In the present work, the channel half-height h is equal to unity, such that $L_y = 2$. The flow is driven by a time-varying streamwise pressure gradient, in order to keep a constant volume-flow rate (per unit surface) of $Q = 4/3$. The bulk velocity is hence also constant and equal to 2/3, while U_p is then 1. The Reynolds number Re_p based on U_p becomes a natural choice, since it is proportional to the inverse of cinematic viscosity ν, actually:

$$Re_p = \frac{U_p h}{\nu} = \frac{1}{\nu} \tag{3.6}$$

disregarding dimensons. The spanwise pressure gradient is kept constant and equal to zero, thus the mean spanwise flow rate will vary in time, oscillating around its null mean value. The number of terms in streamwise and spanwise Fourier expansions is adjusted to keep a constant relution in wall units of $\Delta x^+ = \Delta z^+ = 10$. The wall-normal resolution obeys to the more strict constraint of $\Delta y^+ = 4$, which is always satisfied taking a numer of collocation point in wall-normal direction equal to $n_y = Re_\tau/2$

3.2 Incompressible Navier-Stokes Equations

The equations that governs the flow are the incompressible Navier-Stokes equations (iNSEs) in cartesian coordinates

$$\begin{cases} \dfrac{\partial \mathbf{u}}{\partial t} + (\mathbf{u}\cdot\nabla)\mathbf{u} + \dfrac{\nabla P}{\rho} = \nu\nabla^2\mathbf{U} \\ \nabla\cdot\mathbf{u} = 0 \end{cases} \tag{3.7}$$

These equations are implemented in a easier to handle nondimensional parametric form by introducing the following nondimensional variables:

$$\tilde{\mathbf{u}} = \frac{\mathbf{u}}{U} \qquad \tilde{t} = \frac{t}{T_{ref}} \qquad \tilde{\mathbf{x}} = \frac{\mathbf{x}}{L} \tag{3.8}$$

After some algebra the equation set shows the parameter Re,

$$\begin{cases} \dfrac{\partial \tilde{u}}{\partial \tilde{t}} + \tilde{u}\dfrac{\partial \tilde{u}}{\partial \tilde{x}} + \tilde{v}\dfrac{\partial \tilde{u}}{\partial \tilde{y}} + \tilde{w}\dfrac{\partial \tilde{u}}{\partial \tilde{z}} + \dfrac{\partial \tilde{P}}{\partial \tilde{x}} = \dfrac{1}{Re}\nabla^2\tilde{u} \\ \dfrac{\partial \tilde{v}}{\partial \tilde{t}} + \tilde{u}\dfrac{\partial \tilde{v}}{\partial \tilde{x}} + \tilde{v}\dfrac{\partial \tilde{v}}{\partial \tilde{y}} + \tilde{w}\dfrac{\partial \tilde{v}}{\partial \tilde{z}} + \dfrac{\partial \tilde{P}}{\partial \tilde{y}} = \dfrac{1}{Re}\nabla^2\tilde{v} \\ \dfrac{\partial \tilde{w}}{\partial \tilde{t}} + \tilde{u}\dfrac{\partial \tilde{w}}{\partial \tilde{x}} + \tilde{v}\dfrac{\partial \tilde{w}}{\partial \tilde{y}} + \tilde{w}\dfrac{\partial \tilde{w}}{\partial \tilde{z}} + \dfrac{\partial \tilde{P}}{\partial \tilde{z}} = \dfrac{1}{Re}\nabla^2\tilde{w} \\ \dfrac{\partial \tilde{u}}{\partial \tilde{x}} + \dfrac{\partial \tilde{v}}{\partial \tilde{y}} + \dfrac{\partial \tilde{w}}{\partial \tilde{z}} = 0 \end{cases} \tag{3.9}$$

from now on, these equations and the nondimensionalized variables are used without superscript, to simplify the notation. The last of 3.9 is the continuity equation, while the other thee represent the conservation of momentum. Pressure does not have a state equation and appears only as a Lagrange multiplier in 3.9, needed to satisfy the continuity equation. Mass conservation is a non-evolutive equation and represent a cinematic constraint that needs to be satisfied everywhere at any time in the domain.

An equation for pressure can be determined by taking the divergence of momentum equation and using the continuity equation, giving the following result

$$\nabla^2 P = -\nabla\cdot(\mathbf{u}\cdot\nabla\mathbf{u}) \tag{3.10}$$

that is a Poisson equation for pressure. It can be used to recover pressure from a known flow field $\mathbf{u}$.

The problem is closed by assigning the following set of boundary and initial conditions

$$\begin{cases} \mathbf{u}(x,y,z,0) = \mathbf{u_0}(x,y,z) & \text{initial condition} \\ \mathbf{u}(x,\pm 1,z,t) = 0 & \text{noslip condition} \\ \left.\begin{array}{l} \mathbf{u}(x,y,L_z,t) = \mathbf{u}(x,y,0,t) \\ \mathbf{u}(L_x,y,z,t) = \mathbf{u}(0,y,z,t) \end{array}\right\} & \text{cyclic walls} \end{cases} \tag{3.11}$$

Initial and boundary conditions can not be freely chosen but have to respect three compatibility conditions, namely

$$\begin{cases} \nabla\cdot\mathbf{u_0} = 0 \\ \oint_S \hat{\mathbf{n}}\cdot\mathbf{u}\mathrm{d}S = 0 \\ \hat{\mathbf{n}}\cdot\mathbf{u_0}(\mathbf{x})|_S = \hat{\mathbf{n}}\cdot\mathbf{u}(\mathbf{x_0},0)|_S \end{cases} \tag{3.12}$$

where $\hat{\mathbf{n}}$ is the unity vector normal to each boundary surface S of the domain. The first of 3.12 requires a divergence-free initial condition, while the other are identically satisfied by the homogeneous boundary condition at walls and cyclic boundary condition at sides.

This scheme is the starting point for the implementation of the DNS. The code used in the present work is the one developed by Quadrio and Luchini, described in [28]. The programming language adopted has been written by Paolo Luchini and is called CPL, with which it is possible to exploit C, C++ and Fortran commands in the same environment.

3.2.1 iNSEs in $v - \eta$ formulation

Most of the problems connected to the solution of iNSEs are related to the impostion of the continuity equation, which request a divergence-free flow field. This problem could be solved, theoretically, projecting the iNSES in a divergence-free manifold. In this way one obtains a set of equations that automatically satisfies the continuity equation and loose the dependency from the lagrange multiplyer P. However this projection costs the change to a set of variables that are not the natural three cartesian velocity components and pressure.

Another drawback of this approach is the translation of the difficulty from the imposition of a divergence-free constraint to the determination of correct boundary and compatibility conditions, which is not always an easy task. Moreover, sometimes these conditions assume an integral form that it can not be easily implemented.

Fortunately, in the case of channel flow very simple domain this divergence-free projection leads to equations that take a form very suitable for numerical solution.

The four original iNSEs equation of system 3.9 are reduced to two scalar equations for the wall-normal velocity v and wall-normal vorticity η, which is defined as

$$\eta = \frac{\partial u}{\partial z} - \frac{\partial w}{\partial x} \tag{3.13}$$

The equation for the wall-normal vorticity can be easily obtained by taking the y-component of the curl of the momentum equation for v, leading to

$$\frac{\partial \eta}{\partial t} = h_\eta + \frac{1}{Re}\nabla^2 \eta \tag{3.14}$$

$$h_\eta = \frac{\partial}{\partial x}\left(u\frac{\partial w}{\partial x} + v\frac{\partial w}{\partial y} + w\frac{\partial w}{\partial z}\right) - \frac{\partial}{\partial z}\left(u\frac{\partial u}{\partial x} + v\frac{\partial u}{\partial y} + w\frac{\partial u}{\partial z}\right) \tag{3.15}$$

The equation for the wall-normal velocity can be obtained by taking the laplacian of the y-component of the momentum equation and substituting in it the Poisson equation for pressure, obtaining:

$$\frac{\partial \nabla^2 v}{\partial t} = h_v + \frac{1}{Re}\nabla^2\nabla^2 v \tag{3.16}$$

$$\begin{aligned} h_v = \frac{\partial}{\partial y}\Bigg[&\frac{\partial}{\partial x}\left(u\frac{\partial u}{\partial x} + v\frac{\partial u}{\partial y} + w\frac{\partial u}{\partial z}\right) + \\ &+\frac{\partial}{\partial z}\left(u\frac{\partial w}{\partial x} + v\frac{\partial w}{\partial y} + w\frac{\partial w}{\partial z}\right)\Bigg] + \\ -&\left(\frac{\partial^2}{\partial x^2} + \frac{\partial^2}{\partial z^2}\right)\left(u\frac{\partial v}{\partial x} + v\frac{\partial v}{\partial y} + w\frac{\partial v}{\partial z}\right) \end{aligned} \tag{3.17}$$

The two remaining velocity components u and w can be recovered through the continuity equation and the definition of η, solving the following system of equations:

$$\begin{cases} \dfrac{\partial u}{\partial x} + \dfrac{\partial w}{\partial z} = -\dfrac{\partial v}{\partial y} \\ \dfrac{\partial u}{\partial z} - \dfrac{\partial w}{\partial x} = -\eta \end{cases} \tag{3.18}$$

3.2.2 Boundary conditions

The $v-\eta$ formulation is made up of a fourth-order equation in v and a second-order equation in η, thus requiring six boundary condition, four for v and two for η, namely

$$v(x,\pm 1,z) = 0 \qquad \frac{\partial v}{\partial y}(x,\pm 1,z) = 0 \qquad \eta(x,\pm 1,z) = 0 \tag{3.19}$$

3.3 Route to discretization

The iNSEs in the $v-\eta$ formulation are now discretized in orded to be solved numerically, focusing on efficiency and reliability. The route to the discretized set of equations and boundary conditions begins with the Fourier expansion in the two homogeneous directions. Then time and spatial derivatives are discretized and the parallelization discussed.

3.3.1 Discrete Fourier Transform

The existence of two statistically homogeneous directions and the consequent imposition of cyclic boundary condition at sides of the domain, suggest the possibility to represent the solution $v(x,y,z,t)$ and $\eta(x,y,z,t)$ in terms of a complete expansion that automatically respects such a boundary condition.

The natural choice is the truncated Fourier series expansion in the two homogeneous directions x and z, leading to the following expressions for v and η:

$$v(x,y,z,t) = \sum_{h=-N_x/2}^{N_x/2} \sum_{l=-N_z/2}^{N_z/2} \hat{v}(\alpha,y,\beta,t) e^{j\alpha_0 h t} e^{j\beta_0 l t} \tag{3.20}$$

$$\eta(x,y,z,t) = \sum_{h=-N_x/2}^{N_x/2} \sum_{l=-N_z/2}^{N_z/2} \hat{\eta}(\alpha,y,\beta,t) e^{j\alpha_0 h t} e^{j\beta_0 l t} \tag{3.21}$$

where α_0 and β_0 are the fundamentals wavenumbers, defined as $\alpha_0 = 2\pi/L_x$ and $\beta_0 = 2\pi/L_z$, while N_x and N_z are the higher waenumbers at which the discrete fourier transform has been truncated, h and l are two integers that spans the Fourier space so that $\alpha = h\alpha_0$ and $\beta = l\beta_0$.

After the introduction of Fourier expansion the equation for wall normal vorticity 3.14 becomes

$$\frac{\partial \hat{\eta}}{\partial t} = \frac{1}{Re}\left[D_2(\hat{\eta} - k^2\hat{\eta})\right] + j\beta\hat{HU} - j\alpha\hat{HW} \tag{3.22}$$

where $D_n(\cdot)$ is the n-th order derivative operator in y direction and $k^2 = \alpha^2 + \beta^2$. The nonlinear terms, which come from Fourier-transforming the convective part of Navier-Stokes

equations, are grouped in the following definitions:

$$\begin{aligned}\widehat{HU} &= j\alpha\hat{u}\hat{u} + D_1(\hat{u}\hat{v}) + j\beta\hat{u}\hat{w}\\ \widehat{HV} &= j\alpha\hat{u}\hat{v} + D_1(\hat{v}\hat{v}) + j\beta\hat{v}\hat{w}\\ \widehat{HW} &= j\alpha\hat{u}\hat{w} + D_1(\hat{v}\hat{w}) + j\beta\hat{w}\hat{w}\end{aligned} \tag{3.23}$$

Equally the wall-normal velocity equation 3.16, after Fourier expansion in homogeneous direction, becomes:

$$\begin{aligned}\frac{\partial}{\partial t}\left[D_2(\hat{v}) - k^2(\hat{v})\right] =\\ \frac{1}{Re}\left[D_4(\hat{v}) - 2k^2 D_2(\hat{v}) + k^4\hat{v}\right] +\\ -k^2\widehat{HV} - D_1\left(j\alpha\widehat{HU} + j\beta\widehat{HW}\right)\end{aligned} \tag{3.24}$$

We can easily notice that Equations 3.24 and 3.22 are uncoupled if the nonlinear terms are known, e.g. by treating them explicitely in time discretization, keeping in mind that such a treatment will lead to a conditionally stable method. Thus, they can be solved separately to advance the solution in time. However, in order to compute the nonlinear terms, we need to compute $\hat{u}$ and $\hat{w}$. They can be computed by solving the Fourier-space counterpart of 3.18, namely

$$\begin{cases}\hat{u} = \dfrac{1}{k^2}\left[j\alpha D_1(\hat{v}) - j\beta\hat{\eta}\right]\\ \hat{w} = \dfrac{1}{k^2}\left[j\beta D_1(\hat{v}) + j\alpha\hat{\eta}\right]\end{cases} \tag{3.25}$$

This is a 2×2 algebraic system that can be solved very efficiently. One should observe that for the mean value of u and v, that is for $\alpha = \beta = 0$, the equations above become singular. This is a consequence of having obtained Eqns.3.24 and 3.22 from the initial differential system through a procedure involving spatial derivatives.

Let us introduce a plane-average operator:

$$\tilde{f} = \frac{1}{L_x L_z}\int_0^{L_x}\int_0^{L_z} f dz dx \tag{3.26}$$

The space-averaged streamwise velocity $\tilde{u} = \tilde{u}(y,t)$ is a function of wall-normal coordinate and time only, and in Fourier space it corresponds to the Fourier mode $k = 0$. The same argument is valid for the space averaged spanwise velocity $\tilde{w}$. The temporal average of $\tilde{u}$ is the streamwise mean velocty profile, while that of $\tilde{w}$ is zero. Nevertheless, they could take different values at a given time in a given point.

Two additional equations must be written to calculate $\tilde{u}$ and $\tilde{w}$; they can be worked out by applying the linear plane-average operator to the relevant components of the momentum equation:

$$\frac{\partial\tilde{u}}{\partial t} = \frac{1}{Re}D_2(\tilde{u}) - D_1(\tilde{u}\tilde{v}) + f_x \tag{3.27}$$

$$\frac{\partial\tilde{w}}{\partial t} = \frac{1}{Re}D_2(\tilde{w}) - D_1(\tilde{v}\tilde{w}) + f_z \tag{3.28}$$

In these expressions, f_x and f_z are the forcing terms needed to force the flow through the channel against the viscous resistence of the fluid. For the streamwise direction, f_x can be an

imposed mean pressure gradient, and in the simulation the flow rate through the channel will oscillate in time around its mean value. f_x can also be a time-dependent spatially uniform pressure gradient, that has to be chosen in such a way that the flow rate remains constant in time at an imposed value. The same distinction applies to the spanwise forcing term f_z: in this case however the imposed mean pressure gradient or the imposed mean flow rate is zero, while the other quantity will be zero only after time average.

The need for the imposition of inner variables suggest to perform simulations at constant-P_x, because in this way an inner scaling is uniquely defined. However, there are significant drawbacks with constant-P_x simulations, i.e.:

- Initial transient were very long and needed very long averaging time
- This need for long simulations reduce the advantage of MFU low computation cost
- Evaluation of statistics were made difficult by both the long initial transient and high-fluctuations due to the small MFU domain

All these practical reason made constant-Q simulations preferable.

The numerical evaluations of velocity products, needed to compute nonlinear terms 3.23, would require computationally expensive convolutions in wavenumber space, hence a more efficient way has been proposed, based on inverse Fourier-transforming the quantities of interest into physical domain, where convolution are replaced by products, thus re-transforming into wavenumber space, using Fast Fourier Transform (FFT) in both directions. In order to preserve spectral accuracy, a de-aliasing factor of 3/2 is introduced to expand the number of collocation points before transforming from wavenumber to physical space.

3.3.2 Time discretization

The following step involves time integration of equations 3.22 and 3.24 by adopting a semi-implicit method, paying some attention to memory requirements. The most stability-limiting part of the equations, i.e. the viscous part, is advanced with an implicit second-order Crank-Nicholson scheme. This relieves the constraint on the time-step size Δt, that is solely determined by the explicit third-order low-storage Runge-Kutta method used for advancing nonlinear terms, which can thus benefit from a higher precision. After time discretization, the equations for v and eta appear as follow:

$$\begin{aligned}
&\frac{\lambda}{\Delta t}\hat{\eta}_{hl}^{n+1} - \frac{1}{Re}\left[D_2(\hat{\eta}_{hl}^{n+1})\right] = \\
&= \frac{\lambda}{\Delta t}\hat{\eta}_{hl}^{n} - \left[D_2(\hat{\eta}_{hl}^{n}) - k^2\hat{\eta}_{hl}^{n}\right] + \\
&+\theta\left(j\beta_0 l\widehat{HU}_{hl} - j\alpha_0\widehat{HW}_{hl}\right)^n + \xi\left(j\beta_0 l\widehat{HU}_{hl} - j\alpha_0 h\widehat{HW}_{hl}\right)^{n-1}
\end{aligned} \tag{3.29}$$

$$\begin{aligned}
&\frac{\lambda}{\Delta t}\left(D_2(\hat{v}_{hl}^{n+1}) - k^2\hat{v}_{hl}^{n+1}\right) - \frac{1}{Re}\left[D_4(\hat{v}_{hl}^{n+1}) - 2k^2 D_2(\hat{v}_{hl}^{n+1}) + k^4\hat{v}_{hl}^{n+1}\right] = \\
&= \frac{\lambda}{\Delta t}\left(D_2(\hat{v}_{hl}^{n}) - k^2\hat{v}_{hl}^{n}\right) - \frac{1}{Re}\left[D_4(\hat{v}_{hl}^{n}) - 2k^2 D_2(\hat{v}_{hl}^{n}) + k^4\hat{v}_{hl}^{n}\right] + \\
&+\theta\left[-k^2\widehat{HV}_{hl} - D_1(j\alpha_0 h\widehat{HU}_{hl} + j\beta_0 l\widehat{HW}_{hl})\right]^n + \\
&+\theta\left[-k^2\widehat{HV}_{hl} - D_1(j\alpha_0 h\widehat{HU}_{hl} + j\beta_0 l\widehat{HW}_{hl})\right]^{n-1}
\end{aligned} \tag{3.30}$$

Coefficients λ, θ and ξ appearing in the equations, take different values according to integration scheme one can choose. As previously mentioned, velocity product appearing in nonlinear terms are computed through direct/inverse FFT. Then, for each wavenumber pairs (α, β), we need to solve a set of two ODEs derived from the implicit formulation of viscous terms. In order to provide a discrete solution of the resulting ODEs, a compact finite difference discretization has been introduced for wall-normal differential operators, so to guarantee spectral accuracy. Such discretization produces two linear systems with real banded matrices, whose solution gives $\hat{v}_{hl}^{n+1}$ and $\hat{\eta}_{hl}^{n+1}$, from which we can easily recover the other velocity components $\hat{u}_{hl}^{n+1}$ and $\hat{w}_{hl}^{n+1}$ from 3.25. Unlike the procedure used to build the RHS, this second step proceeds per wall-normal lines, since the simultaneous knowledge of the RHS in all y positions is required.

3.3.3 Spatial derivatives

The discretization of the spatial derivatives should have several good properties that make it suitable for turbulence DNSs, i.e. it should lead to a linear system that can be efficiently solved using parallelization and be adequately accurate. One of the most efficient code for the DNS of channel flows is the one implemented by Quadrio and Luchini on a dedicated Personal Supercomputer. The following description of the spatial derivatives discretization is freely taken from [28].

The discretization of the first, second and fourth wall-normal derivatives D_1, D_2 and D_4, required for the numerical solution of the present problem is performed through finite-differences (FD) compact schemes [26]. One important difference with [26] is that the compact schemes emplyed in the present work are at the same time explicit and at fourth-order accuracy. The computational molecule is composed of five arbitrarily spaced (with smooth stretching) grid points on a mesh of $ny+1$ points y_j, with $0 \leq j \leq ny$. We indicate here with $d_1^j(i)$, with i integer from -2 to 2, the five coefficients discretizing the exact operator D_1 over five adjacent grid points centered at y_j, i.e.:

$$D_1(f(y))|_{y_j} \simeq \sum_{i=-2}^{2} d_1^j(i) f(y_{j+1}) \tag{3.31}$$

where y_j is the y position on the computational mesh where the derivative has to be evaluated. The coefficients d^j change with the distance from the wall (i.e. with the integer index j) when a non-uniform mesh is employed.

Compact schemes are also known as implicit finite-differences schemes, because they typically require the inversion of a linear system for the actual calculation of a derivative [26],[32]: this increases the complexity and the computational cost of such an approach. For the present problem we are able however to determine explicitly the coefficients for compact, fourth-order accurate schemes, thanks to the absence of the D_3 operator from the present equations. This important simplification has been highlighted first in the original Gauss-Jackson-Noumerov compact formulation exploited in his seminal work by Thomas [52], concerning the numerical solution of the Orr-Sommerfeld equation.

To illustrate Thomas' method, let us consider a 4th-order ordinary differential equation (linear for simplicity) for a function $f(y)$ in the following conservation form:

$$D_4(a_4 f) + D_2(a_2 f) + D_1(a_1 f) + a_0 f = g \tag{3.32}$$

where the coefficients $a_i = a_i(y)$ are arbitrary functions of the independent variable y, and $g = g(y)$ is the known RHS. Let us moreover suppose that in frequency space a differential operator, for example D_4, is approximated as the ratio of two polynomials, say $\mathcal{D}_4$ and $\mathcal{D}_0$. Polynomials like $\mathcal{D}_4$ and $\mathcal{D}_0$ have their counterpart in physical space, and d_4 and d_0 are the corresponding FD operators. The key point is to impose that all the differential operators appearing in the example equation 3.32 admit a representation such as the preceding one, in which the polynomial $\mathcal{D}_0$ at the denominator remains the same. Eq.3.32 can thus be recast in the new, equivalent discretized form:

$$d_4(a_4 f) + d_2(a_2 f) + d_1(a_1 f) + d_0(a_0 f) = d_0(g) \tag{3.33}$$

and this allows us to use explicit FD schemes, provided the operator d_0 is applied to the RHS of the equation and to the terms not involving y derivatives. The overhead related to the use of implicit finite difference schemes disappears, while the advantage of using compact schemes is retained.

The actual computation of the coefficients d_0, d_1, d_2 and d_4 to obtain a formal accuracy of order 4 descends from the requirement that the error of the discrete operator $d_4 d_0^{-1}$ decreases with the step size according to a power law with the desired exponent -4. In practice, following a standard procedure in the theory of Pade' approximants, this can be enforced by choosing a set t_m of polynomials of y of increasing degree:

$$t_m(y) = 1, y, y^2, y^3, \ldots, y^m \tag{3.34}$$

by analytically calculating their derivatives $D_4(t_m)$, and by imposing that the discrete equation:

$$d_4(t_m) - d_0(D_4(t_m)) = 0 \tag{3.35}$$

is verified for the nine polynomials from $m = 0$ up to $m = 8$. Our computational stencil contains 5 grid points, so that the unknown coefficients d_0 and d_4 are 10. There is however a consistency condition, and we can write the equations in a form where for example:

$$\sum_{i=-2}^{2} d_0(i) = 1 \tag{3.36}$$

The other 9 conditions are given by Eqn. 3.35. We thus can set up, for each distance from the wall, a 10×10 linear system which can be easily solved for the unknown coefficients. The coefficients of the derivatives of lesser degree are derived from analogous relations, leading to two 5×5 linear systems once the d_0's are known.

We end up with FD operators which are altogether fourth-order accurate; the sole operator D_4 is discretized at sixth-order accuracy. The boundaries obviously require non-standard schemes to be designed to properly compute derivatives at the wall. For the boundary points we use non-centered schemes, whose coefficients can be computed following the same approach as the interior points, thus preserving by construction the formal accuracy of the method. Nevertheless the numerical error contributed by the boundary presumably carries a higher weight than interior points, albeit mitigated by the non-uniform discretization.

In the present code, the stretching function used to generate the mesh is

$$y = \frac{\tanh a\overline{y}}{a} \tag{3.37}$$

where a is an adjustable parameter used to modify the mesh deformation and $\overline{y}$ is a mesh grid with constant spacing coming from lower to upper wall.

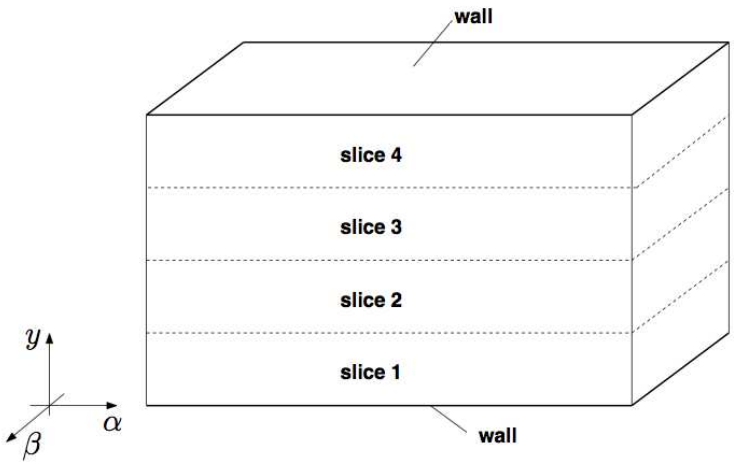

Figure 3.2: A schematic of computational domain division in slices between different machines

3.3.4 Parallel strategy

The approach previously outlined grants excellent parallelization performances, in that a compact difference discretization in wall-normal direction allows to distribute the variables in wall-parallel slices and perform direct and inverse FFTs locally at each machines. Moreover, thanks to the locality of compact difference operators, the communication required to compute wall-normal derivatives of velocity products is fairly small, since data transfer is needed only at the interface between contiguous slices. This is a major difference with respect to [20], where a fully spectral discretization was employed. Although spectral derivatives can benefit from higher accuracy, they have the significant drawback of being defined on the whole domain, thus a transposition of the whole dataset across the computing nodes is needed every time the numerical solution is advanced in time. It is worthless saying that this operation requires a large amount of computer communication, hence very fast networking system is needed to achieve good parallel performance, thus restricting DNS to be carried out only on very expensive computers only.

With compact differences scheme, transpose of the whole flow can be avoided if data are distributed in slide parallel to the walls and each one of the m machines representing our parallel system is assigned one of these slices. The arrangement is represented schematically represented in Figure 3.2: each machine holds all the streamwise and spanwise wavenumbers for n_y/m position, where n_y is the dimension of the mesh grid in y direction. In this way, a small amount of communications needed only at the interface between two contiguous slices, for the evaluation of RHSs.

The most critical task of the procedure lies in the second part of the time-step advancement, when we have to solve a set of two linear systems, one for each (h, l) pair, since data appear to spread over m machines. In this case we can avoid to perform a global transpose if we adopt a LU decomposition of the pentadiagonal distributed matrices and then apply a subsequent sweep of backsubstitution, which requires the transmission of only a few coefficients at the interface between neighbouring nodes. As the number of linear equations is very high, typically $(n_x + 1)(n_z + 1) \approx 10^4$ or bigger, the solution of the linear systems can be efficiently

pipelined as follows. When the LU decomposition of the matrix of the system for a given pair (h, l) is performed, there is a first loop from the top row of the matrix down to the bottom row, in order to eliminate the unknowns, then a second loop in the opposite direction. The machine owning the first slice performs the elimination in the local part of the matrix and then passes the boundary coefficients to the neighbouring machine, which starts the elimination. Instead of waiting for the elimination in the whole (k, l) system, the first machine can start working on the elimination in the matrix of the following system. A synchronization is needed only at the end of the elimination phase, then the whole procedures can be repeated for the backsubstitution phase. This effective pipelined-linear-system strategy allows a point-to-point communication, so that each computer has to exchange information only with adjacent CPUs, allowing to adopt mass-markeded CPUs instead of dedicated servers.

This structure has been realized at the University of Salerno and has been used to perform the most expensive simulations appearing in the present work. The particular technique adopted in the present work, which is based on the smallest domain that can lead to coherent results, allowed to use ordinary PCs and laptops to simulate channel flows at low Reynolds numbers.

3.4 Minimal Flow Unit

The Minimal Flow Unit (MFU) is the smallest doubly-periodic (in x and z directions) computational box that can sustain turbulence and lead to a good representation of near-wall structures and low-order statistics of a turbulent channel flow. Such a minimal flow can be very useful since it is made up of a minimal set of structures that are necessary to sustain a turbulent boundary layer. This simplified model represents a significantly simpler and more manageable 'laboratory' in which to study the mechanics of wall-bounded flows and in which to test turbulence control strategies.

In this section the results of the main work on this issue [15] are presented and a description of main features of MFU given.

3.4.1 Introduction

A Direct Numerical Simulation of a turbulent channel flow is very onerous in terms of computational cost and contains very detailed 'information' that sometimes may be unnecessary to a particular study.

The intrinsic doubly periodic nature of the DNS of a channel flow does not allow the existence of turbulent structures that extend over the streamwise and spanwise domain lengths, L_x and L_z respectively. A simulation of a doubly periodic small domain resolve only those scales that are big enough to be resolved with a particular grid resolution, yet enough small to fit into the domain. Only small-scale interaction can be predicted with the MFU, while large-scale interaction are definitely ignored. Thus, the whole complex scenario of a full developed channel flow is not obtained, but a simplified and more organized model of the flow, in which are contained only the main structures needed to sustain turbulence, in a periodic array. In this sense, MFU can be very useful to investigate the in dynamic mechanisms of the wall turbulence, in a simplified context.

Of course, the Minimal Flow Unit, especially with extremely small domains, can not reproduce well high other statistics, such as two-point correlation functions, but can predict with good accuracy low-order statistics of the near-wall turbulence.

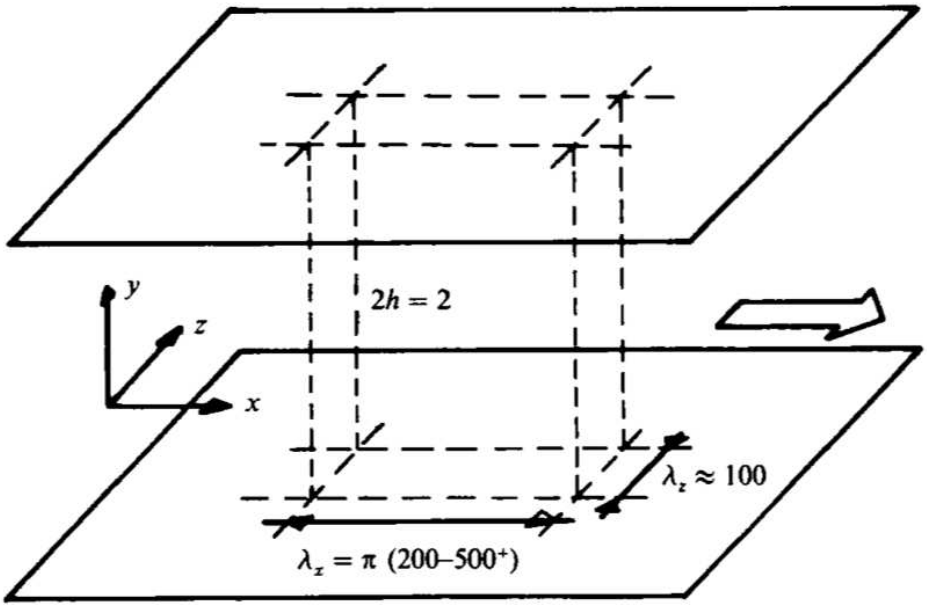

Figure 3.3: Geometry of the computational domain used in [15].

3.4.2 Box minimization

The DNS campaign conduced in [15] was intended to determine the smallest domain that can sustain turbulence, i.e. the Minimal Flow Unit. Simulation were ran at constant Q at three Reynolds number Re_P, namely 2000, 3000, 5000. Figure 3.3 represent a sketch of the computational doubly periodic domain. The channel height is $2h$, while the streamwise and spanwise length are varied, keeping an almost constant resolution, in wall units, of $\Delta z^+ = 5 - 10$ and $\Delta z^+ = 8 - 16$.

The spanwise length Firstly, a detailed fine-tuning of the spanwise dimension of the box was made at the constant streamwise length of πh. This first attempt value for the streamwise length has been chosen after a rough investigation that showed turbulence decay for as twice as shorter boxes and the presence of several structures for longer boxes.

For each Reynolds number in Figure 3.4, the spanwise dimension of the computational box, measured in wall units, is plotted against its value measured in outer units. The vertical lines mark the boundaries beyond which no turbulent flow could be maintained. It can be seen that the critical channel span varies for different Reynolds numbers when expressed in outer units but is roughly the same in wall units. The critical value is around $\lambda_z \approx 100$ or, more precisely, between 85 and 110. This is in very good agreement with the experimentally measured mean streak spacing in the viscous sublayer reported by [51]) who also found slightly lower spacings at higher Reynolds numbers.

The streamwise length In [15] less care has been put into the determination of the minimum streamwise length at each Reynolds number. This time, the spanwise length of the box has been kept constant and slightly greater than its minimum value for each Reynolds number. Figure 3.5 report a plot of λ_x^+ versus λ_x/h for each Reynolds number. The minimum

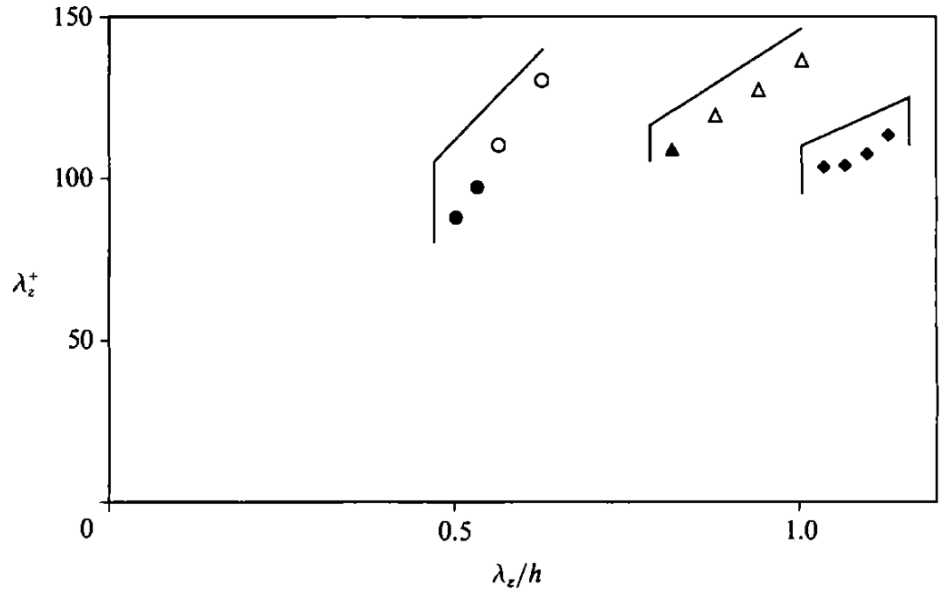

Figure 3.4: MFU box spanwise length in wall and absolute units. Vertical lines mark limits at which turbulence could not be sustained. $\diamond$ Re = 2000, $\triangle$ Re = 3000, $\circ$ Re = 5000. Open symbols indicate cases that sustained turbulence at both walls, filled symbols simulation that sustained turbulence at only one wall.[15]

streamwise length appears to be $\lambda_x^+ \approx 250 - 350$. . Apparently, this is the lower bound for the streamwise length of the eddies in the wall layer, or for the minimum streamwise spacing between eddies of dynamical significance.

The minimal box scaling Apparently the minimal box size seems to scale in viscous units $\delta = \nu/u_\tau$ but it exhibit a small Reynolds dependence. This is probably due to the presence of bigger turbulence structures in the logarithmic and buffer layer whose wall-normal extent, dependent on bulk Reynolds number, is constrained by the small spanwise and streamwise lengths. This means that a dependence on the dimension of these structure is retained. The result is a weak outer scaling and thus a dependence of the minimal box on bulk Reynolds number. The Reynolds dependence can be best seen in main statistics of the flow, which show significant non characteristic behaviour from the logarithmic region to the centreline.

3.4.3 Statistics

Two-point autocorrelation function Figures 3.6 and 3.7 show two-point spatial autocorrelation function for the velocity fields at $Re = 5000$. The correlation lack of a clear decay to zero for large separations. This is obviously due to the small size of the domain which is not large enough for distant points to be uncorrelated. This means that the flow is made up of an array of similar structures, each of which is relatively coherent in space.

Mean streamwise velocity Mean velocity, u^+,profiles for Reynolds numbers 3000 and 5000 are shown in Figure 3.8. The profile for the $Re = 3000$ case is in excellent agreement

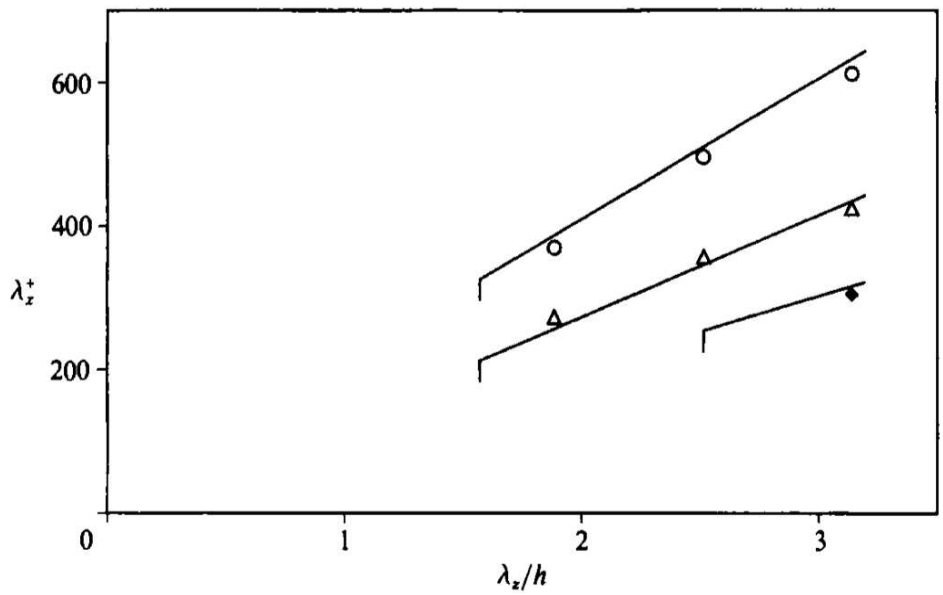

Figure 3.5: MFU box streamwise length in wall and absolute units. Vertical lines mark limits at which simulations could not be sustained. Symbols as in 3.5. Figure taken from [15]

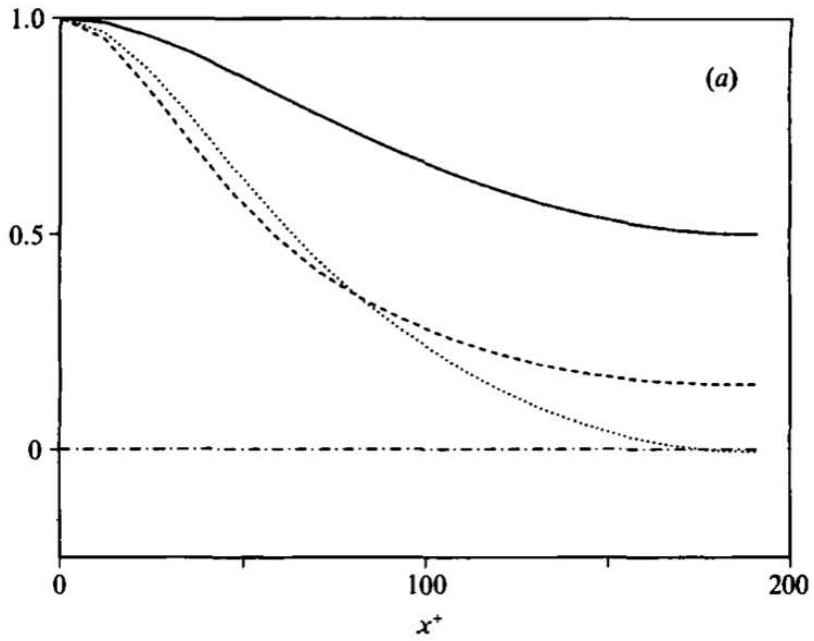

Figure 3.6: Two-point spatial autocorrelation function along x-axes, in the near-wall region ($y^+ = 7.2$); from [15]

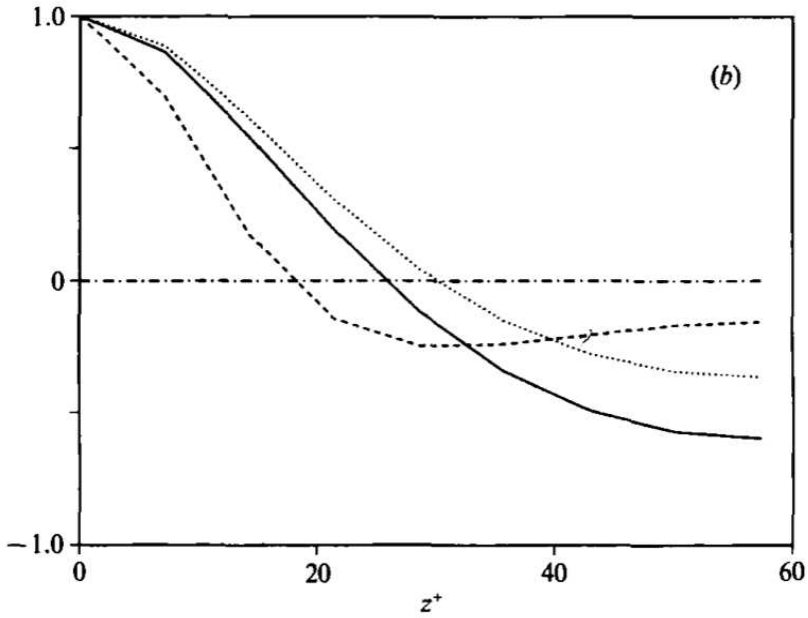

Figure 3.7: Two-point spatial autocorrelation function along z-axes, in the near-wall region ($y^+ = 7.2$); from [15]

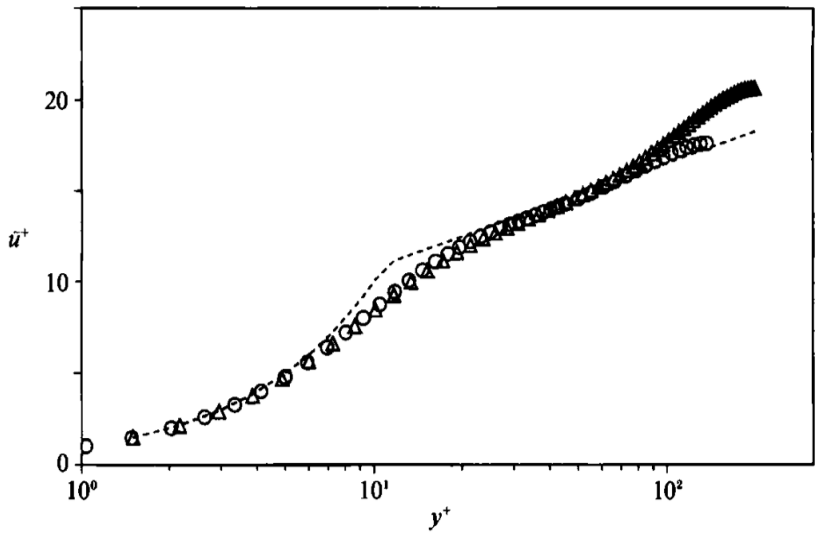

Figure 3.8: Mean streamwise velocity near the wall, symbols as in 3.5); from [15]

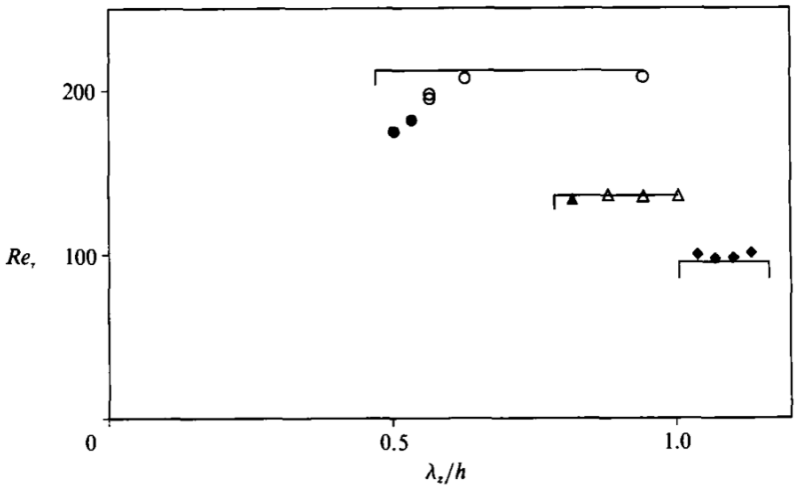

Figure 3.9: Time-averaged wall stress, measured as Re_τ, at different Reynolds numbers. Lines are from Dean's correlation while symbols are as in 3.5); from [15]

with the standard logarithmic law for turbulent channel flow, while the one for $Re = 5000$ is in good agreement in the inner region but exhibits only a minimal log layer and a wake region which is uncharacteristic of channels. At this last Reynolds number, the spanwise box width $\lambda_z^+ = 100$ correspond approximately to $\lambda_z/h = 0.5$. This is apparently too small to accommodate some of the large scale structures present in the outer layer and leads to this and other anormalities in this region of the flow.

Wall stress One of the standard measure of the adequacy of the simulated turbulent channel flow is its conformity to Dean's (1978) correlation. The dependency of Reynolds number based on shear velocity, Re_τ, on the spanwise box width is shown in figure 3.9. The lines are from Dean's formula, and symbols are the same of figure 3.5. Except for the three narrowest cases at the highest Reynolds number, $Re = 5000$,the numerical results are in remarkably good agreement with the experimental data. The cases that do not agree with Dean's correlation are those that lack a significant logarithmic layer in the mean velocity profile. In summary, low-order single-point turbulence statistics in the wall region are accurately predicted in the minimal channel simulations so long as at least the inner portion of the logarithmic layer is reproduced. The outer portion of the boundary layer does not appear to have significant influence on the inner-layer statistics.

3.4.4 Two peculiar phenomena

Intermittency Minimal Flow Unit can reproduce well some characteristics of turbulent flow especially in near-wall region. The small domain give the opportunity to analyse the flow in a simplified framework. Two are the main ingredients absent from MFU simulations. First, the small periodic domain turns the random occurrence in space of turbulent structures into a doubly periodic order. Second, the flow in the outer layer and its interaction with near-wall turbulence are not adequately modelled. The statistical results of the previous section suggest that the first is less important than the second, which turns out to be significant in

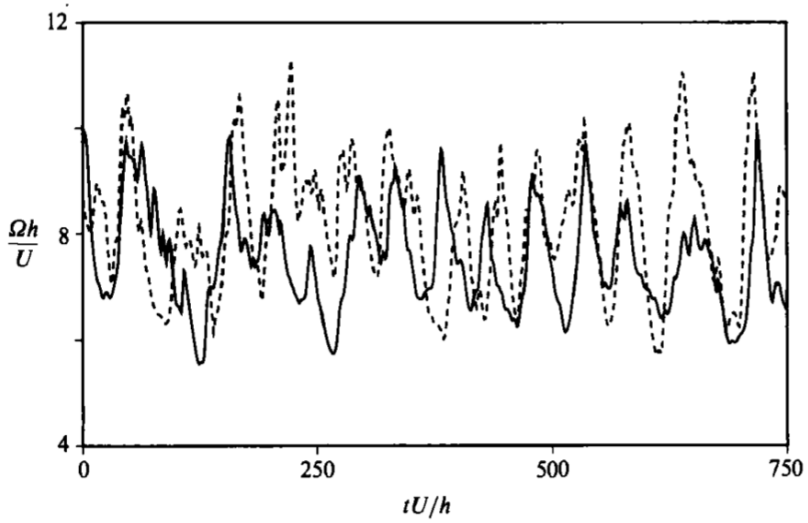

Figure 3.10: Instantaneous averaged wall-shear history for a minimal turbulent channel. Initial transients have been discarded. Only one wall is represented. Re = 5000. Solid line: $\lambda_x \times \lambda_z = \pi \times 0.18\pi$; Dashed line: $0.5\pi \times 0.18\pi$. From [15]

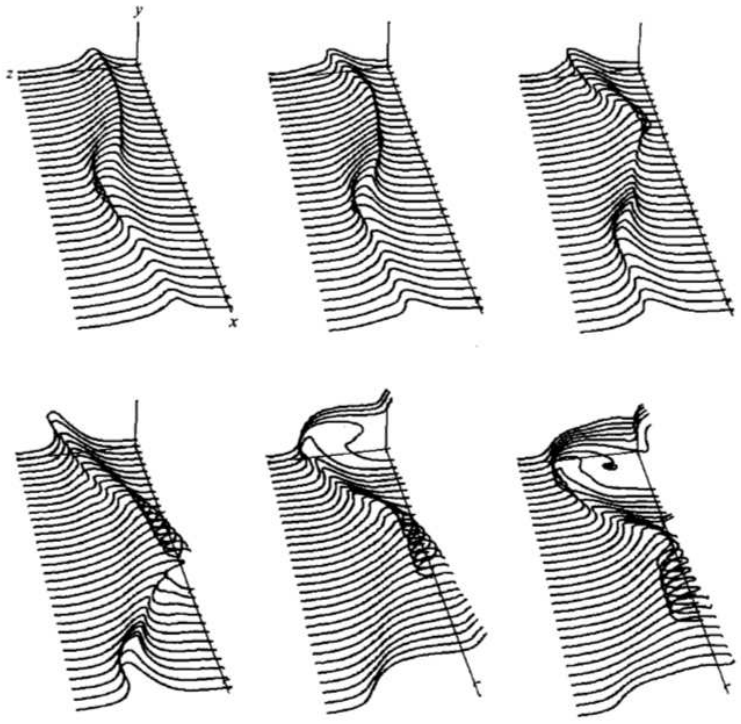

Figure 3.11: Time sequence of the evolution of the wall vorticity layer as it approaches the peak of the intermittency cycle. Flow coming out of the page. Time increases from left to right, top to bottom. From [15]

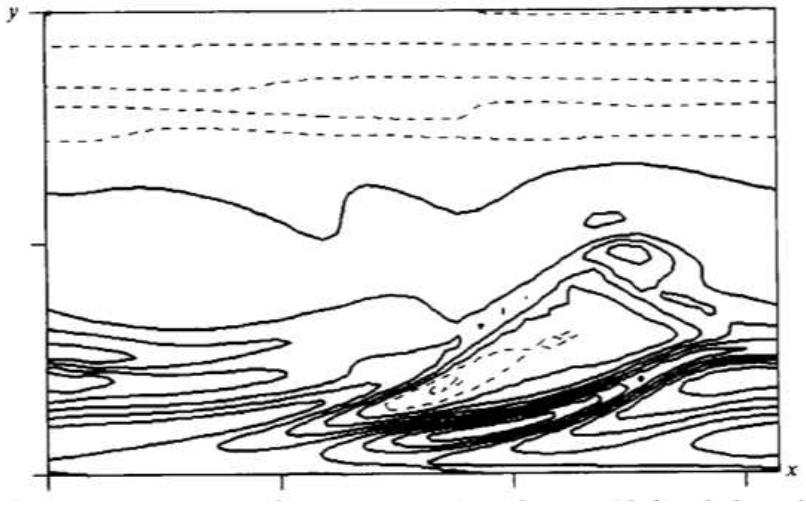

Figure 3.12: Instantaneous ω_z map for an (x, y) section of a one-sided turbulent channel. Note different levels of activity near both walls. Re = 2000. From [15]

the determination of wall shear stress and other statistics above $y^+ \approx 30$.

Time histories of wall-shear stress, as presented in figure 3.10, show an effect of he first point mentioned above. The presence of a small number of turbulent structures and their high order cause big oscillations in time histories of several quantities, such as wall shear stress and Reynolds stresses. They present also a random but quasi-periodic intermittency, which suggest the existence of period of high activity in near-wall turbulence.

Higher fluctuations of wall-averaged time histories is obviously due to the small domain, which offers a small surface for spatial averaging. The intermittent behaviour is not due to this, but [15] describes it as a consequence of modulation of bursting activity in time.

The intermittency period is $U_p T/h = O(100)$. Power spectra of the time series suggest the the this period increases with Re. This is a very long timescale, difficult to reconcile to any obvious property of the flow or of the simulation. In viscous wall units, the different value of intermittency period are more uniform, but ranges from $\mathrm{d} < u > /\mathrm{d}y|_w \approx 600$ to 1500.

An analysis of the flow velocity and vorticity fields has given a partial explanation to this intermittent phenomenon [15]. In figure 3.11 a time sequence of the evolution of the wall streamwise vorticity layer is given. The time interval considered is at the beginning of a peak in the wall shear stress, i.e. at the beginning of a high wall-activity period. A lift-up from the wall of the vortex layer can be easily seen. A vortex, that becomes wavy as the lift-up process take pale, extends in the streamwise direction and seems to brake at the end of the lift-up. Thus, it seems to exist a connection between the intermittency in wall-shear stress and the bursting activity in the wall-cycle. This is observed to a greater or lesser degree in all of the intermittency cycles of the MFU treated in [15].

One-sided turbulence One of the most interesting observations in [15] was the existence of stable states in the channel in which turbulent flow existed only near one wall. This was the predominant state for the three Reynolds numbers studied when the span of the computational box was near its minimal value, and it was the only state observed at Re =

2000.

Occasionally, the turbulent state was observed to shift from one wall to the other. When this happened, the "quiet" wall underwent transition and for a while both walls were turbulent. However, this state was not stable, and in a relatively short time turbulence at one of the walls decayed.

The switching of the active walls was a relatively rare event with a very long characteristic time ($tU_p/h \approx 1000$). Between those occasions, the flow remained essentially one sided. One-sided turbulent channels have never been observed experimentally. In an experiment, it is not possible to simulate the doubly periodic condition typical of MFU.

As measure of the activity of a wall [15] took the space-averaged histories of wall shear stress, as well as the instantaneous ω_z map for a (x, y) section of the minimal channel. In figure 3.12 we report from [15] only this latter case.

It should be observed from figure 3.9, that one-sided channels (closed symbols) predict well the averaged wall shear stress, except for two points at Re=5000.

3.4.5 Minimal box in the logarithmic layer

A more recent work [9], confirmed the result of [15]: a good description of the logarithmic layer is necessary to retrieve wall shear stresses in good agreement with full channel simulations and experiments. Long vorctical structures, which lie in the logarithmic and outer layer, becomes increasingly influent with Re in determining the wall shear. If the computational box is too small, long structures outside the inner layer do not fit the domain and their size is dictated by the box spanwise length, instead of by the distance from the wall. This leads to wrong statistics in the outer layer, such as the big wake region shown in 3.8, and slight biases in the wall shear.

The concept of Minimal Flow Unit is thus redefined. It does not exist a unique Minimal Flow Unit, but a hierarchy of minimal boxes exist. Each box, according to its spanwise fundamental wavelength, can represent turbulence correctly up to a certain distance y_d from the wall.

Florez and Jimenez [9] have found a roughly proportional law between the spanwise dimension and the limit of 'healthy' turbulence y_d:

$$y_d \approx 0.3 L_z \tag{3.38}$$

While the minimal streamwise limit, needed to reproduce a good logarithmic layer has been found to be

$$L_x^+ = 380 \approx h^+ \tag{3.39}$$

Taking in account for the aspect ratio of main vortex clusters contained in the outer region of the boundary layer (3:1:1.5), the minimal box for a given height y_d should be wide enough to contain at least an ejection from the wall and a sweep towards it, this yields to:

$$L_z = 3 y_d \tag{3.40}$$

Chapter 4

Minimal Flow Unit for Drag Reduction estimation

A narrower channel, than those typical of DNS, is used as a simplified laboratory for the estimate of Drag Reduction through streamwise-traveling waves of spanwise velocity. The smaller computational domain, on the one hand reduces the computational effort and allows to reach higher Reynolds numbers, up to 73000 in the present work; on the other requires particular care in the choice of simulation parameters and specific instrument to be developed in order to assess the result reliability.

Figure 4.1 shows two space-averaged wall-shear histories of a DNS and of a narrower channel: the former exhibits lower fluctuations, thanks to the wide averaging area. With the aim to obtain reliable results of mean wall-shear stress, a smaller averaging area turns into a longer averaging time. Thus, a narrow channel DNS advances more rapidly at each timestep, but a longer integration time is required, partially reducing its benefits.

The integration time is kept reasonably limited by the introduction of meticulous procedures to estimate the uncertainty on wall-shear stress: a given integration times and confidence level result into a particular confidence interval on the result.

In the first section of this chapter, the error estimation strategy is briefly discussed. Then, in the next two sections, the choice of the box size and integration time is discussed as well as their influence on skin-friction coefficient and drag reduction. Finally, the necessary condition for the quasi-laminar spanwise flow to stay laminar is found.

4.1 Uncertainty on wall shear

Two different kind of error are introduced by the small domain: systematic and random errors.

Systematic errors are repeatable biases in measurements, which cause a shift in the estimated expected value. They can not be predicted and do not disappear with averaging because affect all measures. In case of wall shear measurements with small domains, they turned out to be slight overestimations of the skin-friction coefficient, which increase for smaller domains. The only way to observe this errors and take them into account is the comparison with more accurate and reliable data.

Random errors are always present in turbulent flow measurements, because the measured variable, here the mean wall shear, is a random variable. Two different strategies to esteem

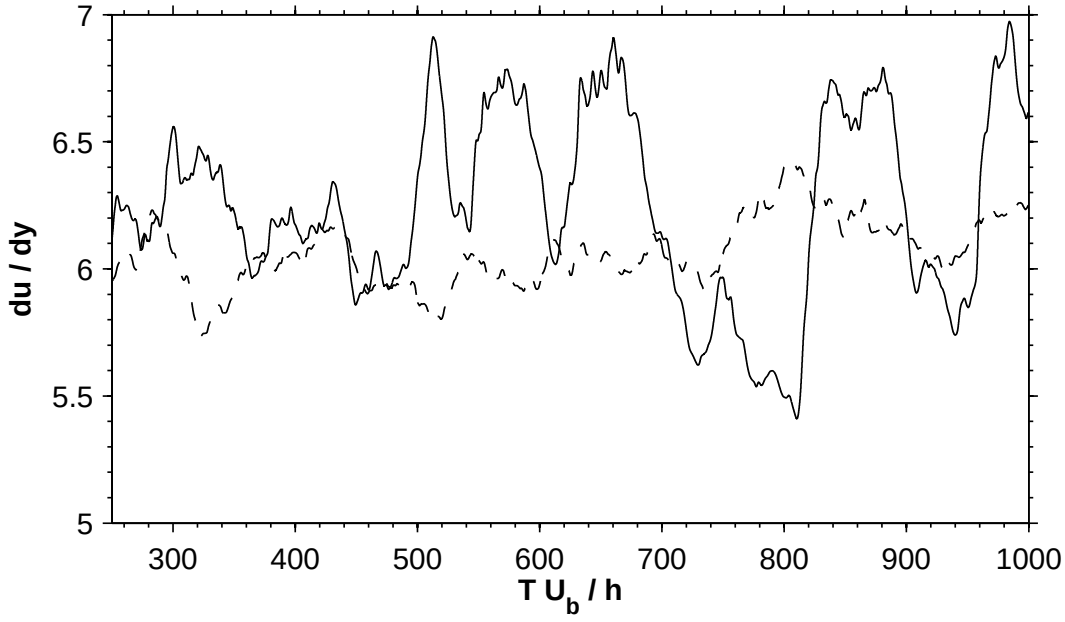

Figure 4.1: Comparison between two wall-shear time histories for two controlled case at $Re_p = 4760$ and similar DR. Dashed line: DNS from [42]; Solid line: MFU from the present work.

the random error, exhaustively described in appendix A, are adopted and compared in the present work. The first uses a integral timescale from the temporal autocorrelation function of the space-averaged wall shear to extend σ_ω, the sample standard deviation, to $\sigma_{\overline{\omega}}$, the standard error of the mean. The second partitions the signal into subsignal, in order to find the trend of the normalized random error ϵ with the averaging time, and compares it to the well-know behavior of white-noise with time, obtaining a upper bound for the standard error of the mean.

Regardless the method used, the standard deviation of the mean exhibit the following proportionality:

$$\sigma_{\overline{\Omega}} = C \, \frac{\sigma_\Omega}{\sqrt{T_{sim}}} \tag{4.1}$$

where Ω is the space-averaged wall shear, σ_Ω is its standard deviation, T_{sim} the total integration time and C a method-dependent coefficient, whose influence is proven to be limited.

Figure 4.2 shows the uncertainty on DR for different channel controlled by oscillating wall with a fixed simulation time T_{sim}. Uncertainty on DR, which differs from the standard error on the mean only by a multiplicative coefficient related to the desired confidence level, depends obviously on forcing parameters and on domain size. The bigger the domain, the wider is the area the wall shear is averaged on. This affects σ_Ω, the variance of longitudinal wall shear stress $\mathrm{d}u/\mathrm{d}y$, according to 4.1. A dependency of the DR-uncertainty on square root of the nondimensional box area $\sqrt{S^+}$ holds, being small discrepancies due to the coefficient C.

Thus, if the domain wall area is reduced by a factor 1/4, the time should be increased accordingly of a factor 4, so as to keep the same standard error of the mean, at least until systematic errors due to the small domain become significant.

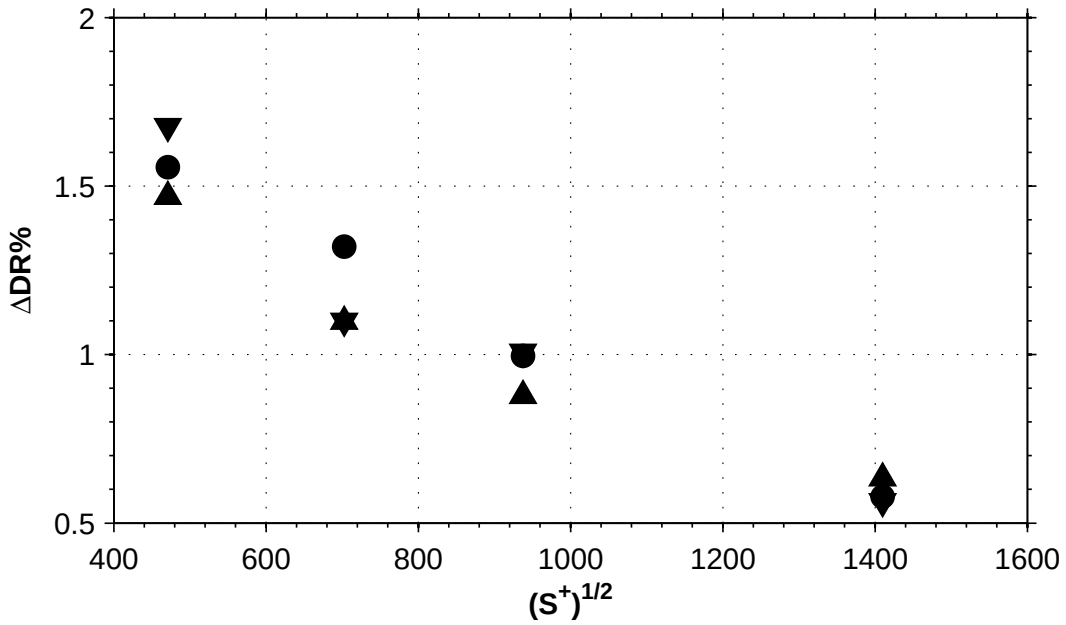

Figure 4.2: Uncertainty on DR at 95% confidence level versus square root of box nondimensional area $S^+ = L_z^+ \times L_z^+$ at $Re_p = 4760$. $\triangle$: $T^+ \approx 90$; $\bigcirc$: $T^+ \approx 100$; $\bigtriangledown$: $T^+ \approx 110$.

4.2 Box size

Differently from the minimization procedure led in [15], here there is no need to reach the minimal doubly periodic set of structures that can sustain turbulence. The computational box should obey the following qualitative requirements:

- it should be small enough to reach a suitable resolution with a moderate computational cost;
- it should be large enough to avoid one-sided turbulence;
- it should lead to consistent low-order statistics, such as wall shear stress;
- it should be large enough to contain wall shear fluctuations and thus the standard deviation of the wall shear;
- the streamwise length should be at least a fundamental wavelength λ_x of the forcing, or a multiple of it.

These qualitative requirements can be translated into specific quantitative conditions on box dimensions.

According to [15] and [9], the most critical quantity in the determination of the predictive-effectiveness of the MFU is its spanwise length L_z. Actually, turbulent near-wall structure size increases with the distance from the wall. The structures obviously extend along all the three dimensions of the channel. If the spanwise length is too small, it constraint the size of such structures, whose extent is no more dependent from the wall-distance. Thus, for a

Re_τ	Location of outer log-layer	$L^+_{z,min}$
200	$y^+ \approx 120$	360
1000	$y^+ \approx 170$	510
2000	$y^+ \approx 210$	630

Table 4.1: Minimal spanwise length to obtain a MFU that can resolve logarithmic layer velocity profile

Re_p	Case	L_z	L_x	L^+_z	L^+_x	$n_x \times n_y \times n_z$	$< \mathrm{d}u/\mathrm{d}y >$	Re_τ
4760	a	1.67	3.3	333	665	$64 \times 100 \times 32$	8.37	200
	b	2.5	5	497	993	$96 \times 100 \times 48$	8.29	200
	c	3.14	6.28	627	1253	$128 \times 100 \times 64$	8.36	200
	d	3.33	6.67	663	1326	$128 \times 100 \times 64$	8.31	200
	e	5	10	997	1994	$192 \times 100 \times 96$	8.36	200
29500	a	0.5	1	459	918	$96 \times 500 \times 48$	28.54	917
	b	0.66	1.32	627	1253	$128 \times 500 \times 64$	30.62	950
	c	0.68	1.36	644	1288	$128 \times 500 \times 64$	30.41	950
73000	a	0.63	1.28	1339	2678	$192 \times 1000 \times 96$	60.18	2096

Table 4.2: Computational domain size and friction Reynolds number Re_τ.

given small value of L_z, only turbulence below the wall-normal distance y_d will be correctly represented.

In [9], accounting for the aspect ratio of vortical structure in the logarithmic layer, the following law between L_z and y_d has been proposed:

$$L_z \approx 3y_d \tag{4.2}$$

In order to obtain good predictions for the wall shear stress, at least the inner part of the logarithmic layer in the mean velocity profile has to be resolved correctly [15]. Thus, L_z has been chosen in the upper part of the logarithmic layer, with the aim to obtain good prediction for $\mathrm{d} < u > /\mathrm{d}y$. For large Reynolds number logarithmic region spans from $y^+ \approx 20$ to $y/h \ll 0.1$. This condition can not be imposed due to the Reynolds number range of this study, except for the case $Re_\tau = 2000$, where it leads to a minimum spanwise dimension of $L^+_{z,min} \approx 630$. When Re is lower, say $Re_\tau = 200$, the availability of experimental and DNS data allowed us to put the logarithmic layer limit, conventionally, at $y^+ \approx 120$, which results in $L^+_{z,min} \approx 360$. At the intermediate Reynolds number of $Re_\tau = 1000$, a linear interpolation between $Re_\tau = 200$ and 2000 has been used. Table 4.1 summarizes the minimal spanwise length of the box, as required by 4.2, for the three Reynolds number of interest.

It should be observed that the property of a MFU to represent the logarithmic layer and hence to give a good estimate of the wall shear stress, does not imply necessarily its effectiveness in giving a good value of Drag Reduction, and vice versa.

The streamwise length of the computational box has been dictated by the fundamental wavelength λ_x of the wall forcing, or by the will to keep an $x - z$ aspect ratio of 2:1. In any case, the minimal limit [9] for a good description of the logarithmic layer $\lambda^+_x \approx h^+$ has been respected.

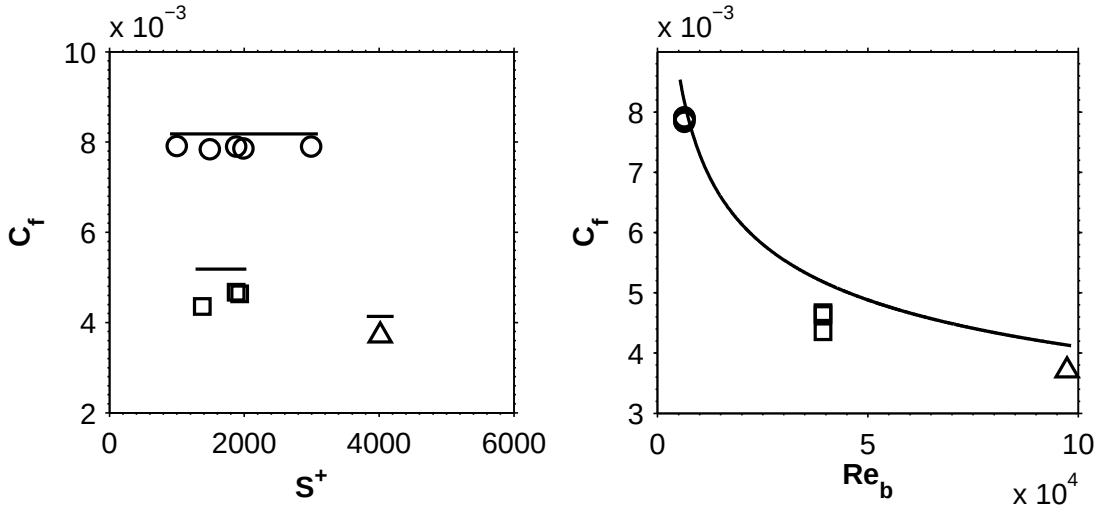

Figure 4.3: Skin friction coefficient in function of the domain area S^+ (left), and of Reynolds number based on bulk velocity U_b (right). $\circ$: $Re_p = 4760$, $\square$: $Re_p = 29500$ and $\triangle$: $Re_p = 73000$. Black lines show Dean's correlation for each Re_p.

4.2.1 Effects on fixed-wall skin friction

In table 4.2 a detailed description of domain size and mean wall shear are given for each uncontrolled case. At $Re_\tau = 200$, the change in domain size does not affect significantly the wall shear stress 4.3a, because minimal value of L_z are not reached. At $Re_p = 29500$, i.e. $Re_\tau \approx 1000$, the case (a) present a lower value of shear stress than the other two run (b) and (c). This is maybe due to its very small spanwise length L_z^+, which is smaller than the estimated $L_{z,min}^+$, the spanwise length at which the MFU can describe well the log-layer. Due to the high computational cost, only one domain size has been tested at $Re_p = 73000$. To reduce as much as possible MFU effects, the box size is much bigger than the minimal flow for the logarithmic layer.

In figure 4.3a Skin friction coefficient $C_f = 2\tau_w/(\rho U_b^2)$ is plotted against the computational box area L_z^+, in viscous wall units, for each value of Reynolds number. These values are compared to the C_f predicted by the Dean's correlation $C_f = 0.073 Re_b^{-0.25}$. The comparison of our measured C_f with results from Dean's correlation is not totally satisfying. It shows a 3% disagreement for circles at $Re_p = 4760$, but an identical disagreement is also present in Kim *et al.*'s results [20], and it may well be due to the non-optimal value predicted by the empirical correlation at low values of the Reynolds number.

Points at $Re_p = 29500$ (squares), in spite of their increased Reynolds number, show a 10% discrepancy from the empirical correlation. Nevertheless, two cases at $Re_p = 29500$ are agreed on a value of wall shear of ≈ 30, showing the repeatability of the measure, while only the leftmost one is influenced by the small spanwise box length. The case at $Re_p = 73000$ shows the same 10% disagreement 4.3b, even if its box dimensions are far from being minimal.

The box area S^+ is kept constant in viscous unit, except at $Re_p = 73000$ where it is 4 times wider, implying that the actual box area $S = S^+ \delta_\nu$ decreases with $\delta_\nu = 1/Re_\tau$, thus it reduces of a factor 1/5 when Re_τ is increased 5 times. Large-scale and very-large-scale turbulent structures, whose extension scales in outer units, affect wall turbulence at high

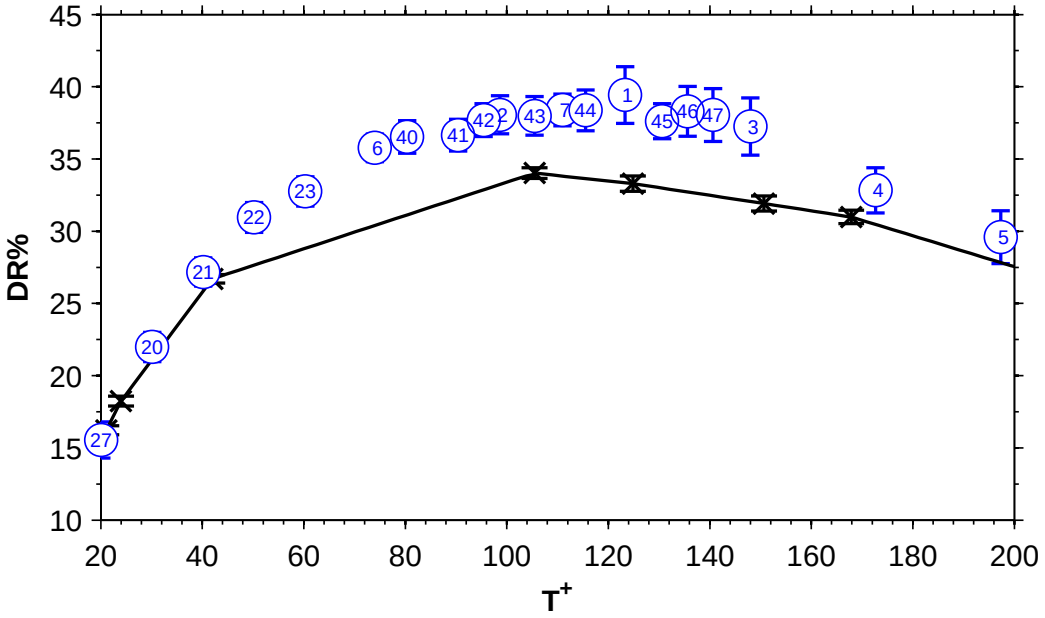

Figure 4.4: $DR\%$ versus T^+. Black solid line and $\times$: DNS Results at $Re_P = 4760$ from [40]; $\circ$: MFU at $Re_p = 4760$ and $L_z^+ = 497$.. Simulation numbers as in table 5.1.

Reynolds number [10] and influence the skin-friction coefficient. Our Minimal Flow Unit for DR estimation discards very large scales, which do not fit the small domain, and thus exhibits an increasing discrepancy in C_f at high Reynolds number 4.3b.

Minimal Flow Unit for DR could be a powerful mean for drag estimation if it predicted correct value of DR regardless in spite of the shift in the fixed-wall skin friction. The condition reveals to be true for a wide range of forcing parameters, except near the maximum of DR, where slight biases can be observed.

4.2.2 Effects on DR

The effects of box size on DR are not limited to the random error, i.e. to an increased σ_ω, but extends also to systematic errors, i.e. to overestimations of DR values.

By the comparison of the present results with those from [40], represented by the black solid line in figure 4.4, two remarks should be made:

- The $DR\%$ at $Re_\tau = 200$ is slightly overestimated for periods of oscillation ranging from $T^+ \approx 50$ to $T^+ \approx 180$, approximately when $DR\%$ exceeds the value of 30, that is near its maximum value.

- The point of maximum $DR\%$ at $Re_\tau = 200$ is shifted at larger T^+, from ≈ 105 to ≈ 125.

Both these effects could be related to the Minimal Flow Unit (MFU) but the lack of shift in the point of maximum $DR\%$ at $Re_\tau = 1000$ (see figure 5.1 in the next chapter) suggests that more complex phenomena are involved and a deeper analysis is needed.

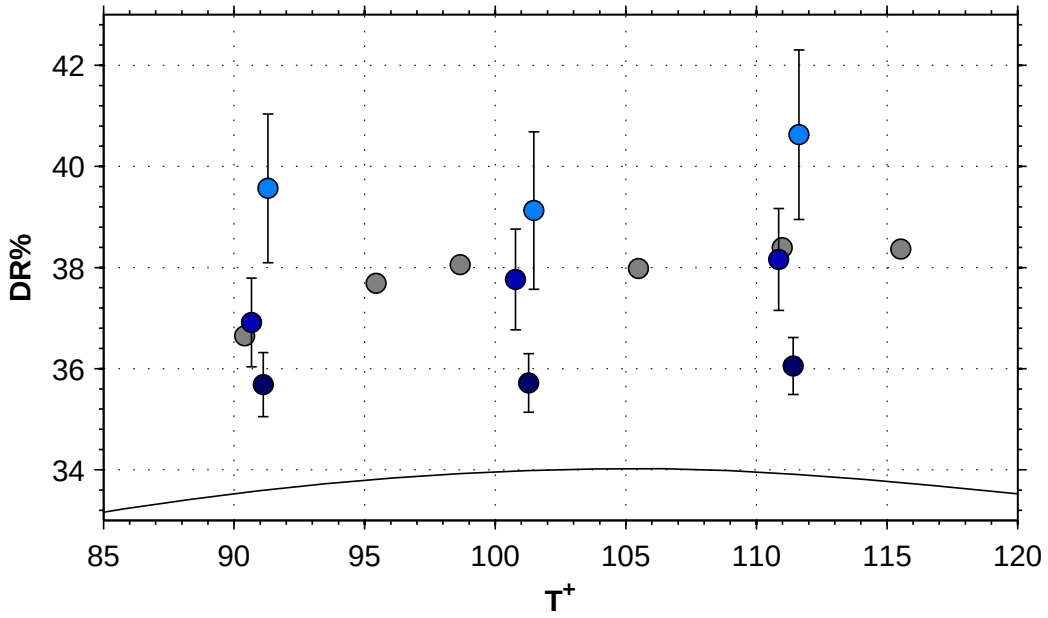

Figure 4.5: Drag Reduction $DR\%$ versus period of wall oscillation T^+ for various box sizes at $Re_p = 4760$. Light blue: $L_z^+ = 333$, Blue: $L_z^+ = 663$, Dark Blue: $L_z^+ = 997$, Gray: simulations at $L_z^+ = 497$, Black solid line: Full DNS.

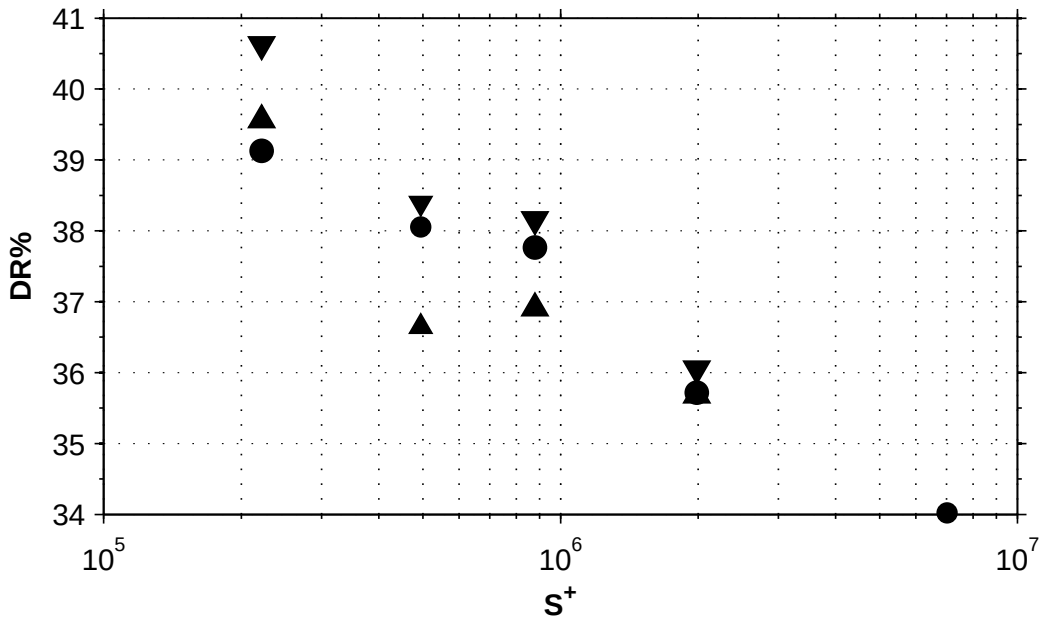

Figure 4.6: Drag Reduction $DR\%$ versus box area S^+ at $Re_p = 4760$. $\triangle$: $T^+ \approx 90$; $\bigcirc$: $T^+ \approx 100$; $\bigtriangledown$: $T^+ \approx 110$; the rightmost point is a DNS full channel from Quadrio's database [40].

Overestimation of DR%

Two hypothesis on the origin of $DR\%$ overestimation have been made.

Firstly, the domain spanwise length, expressed in wall units, changes if the actual viscous length $\delta_\nu = \nu/u_\tau$ of the controlled case, instead of the refence case, is used. In particular, it is reduced in case of DR and increased when a DI is obtained. It can be easily seen that the ratio $L^+_{z,\mathrm{act}}/L^+_{z,\mathrm{ref}}$ between the domain spanwise lengths expressed in reference $\delta_{\nu,\mathrm{ref}}$ and actual $\delta_{\nu,act}$ viscous units is proportional to $\sqrt{1-DR}$. Thus, the domain spanwise length of $L_z^+ \approx 500$, based on reference viscous units, reduces to ≈ 390 for Case 1 at $DR\% = 39.4$, if the viscous length based on actual wall shear is used. As the spanwise (and streamwise) length decreases, MFU effects become more influent and the portion of well-resolved turbulence apart from the wall becomes thinner [9]. A "too small" box leads to a overestimation of DR; while as the domain size is increased, the shear stress moves to more realistic values. At $Re_p = 4760$ a box can be considered "too small" to correctly predict DR if its *actual* spanwise and streamwise lengths decrease under $L^+_{z,\mathrm{act}} = 420$ and $L^+_{x,\mathrm{act}} = 840$. Actually the overestimation appears only when DR exceed the value of 30 (figure 4.4), to which corresponds an actual spanwise length of 420 wall units.

Higher value of DR (figure 4.5) are still present at $L_z^+ = 1000$, which correspond to $L^+_{z,act} \approx 800$, if scaled with *actual* viscous length. Anyway, the spanwise length that guarantees a correct prediction of DR near its maximum lies in the range $1000 \leq L_z^+ \leq 1800$, or $800 \leq L^+_{z,act} \leq 1400$ if actual viscous length is used. Even if this analysis has not been carried on, it can be supposed that the range of T^+ near T^+_{opt} that exhibit increase of DR, due to MFU effect, narrows when the domain size is enlarged. When the length $L_z^+ = 500$ is used, a maximum overesteem of 4%, based on the reference wall shear, is obtained in the whole T^+-range studied.

The issue could be overcome by imposing the inner scales *a priori* through constant-P_x simulations or by choosing a smaller maximum spanwise velocity, which leads to smaller DR and hence contains the change in domain size.

The DR overestimation could be also a Reynolds-dependent MFU effect. With low-Reynolds turbulence this effect is more significant and reduces as the switch to high-Reynolds turbulence is completed. This gives the hope of accurate DR prediction through MFU at high Reynolds number. In order to better understand this phenomenon, further simulation at even higher Reynolds number are needed,

Shift of Point of Maximum DR%

The shift of the point of maximum DR, very evident at $Re_p = 4760$ from figure 4.4, seems to be only apparent. The very flat maximum of the DR versus T^+ diagram does not help to locate the point of maximum precisely. DR reaches its highest values at $T^+ \approx 110$, then a region of higher uncertainty in DR from $T^+ \approx 120$ to $T^+ \approx 150$ appears. The higher scattering due to the increased uncertainty in this region causes the Case 1 to reach maximum DR. This post-maximum uncertainty raise seems to be the cause of the shift.

Differently, at $Re_p = 29500$ (figure 5.1) the point of maximum DR is nicely captured by MFU simulations and, in spite of the higher uncertainty compared to $Re_p = 4760$, the DR versus T^+ trend agree well with DNS prediction at $Re_p = 4760$.

This suggest, once again, that the shift could be a low-Reynolds related MFU effect, which disappears abruptly at higher Reynolds number.

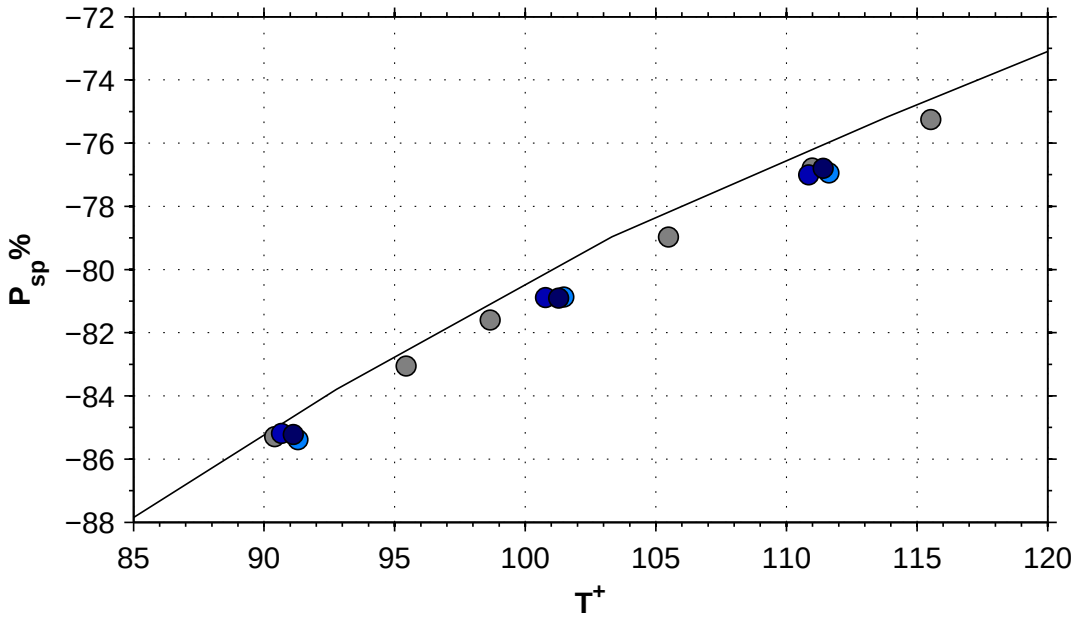

Figure 4.7: Power spent taking into account Regenerative Braking $P_{sp}\%$ versus period of wall oscillation T^+ for various box sizes at $Re_p = 4760$. Light blue: $L_z^+ = 333$, Blue: $L_z^+ = 663$, Dark Blue: $L_z^+ = 997$, Gray: previous simulations at $L_z^+ = 497$, Black solid line: Full DNS.

4.2.3 Effects on Power Spent

An interesting property of MFU is the capability to correctly predict power spent $P_{sp}\%$ even at high T^+ and very small boxes. No significant change in $P_{sp}\%$ can be shown in figure 4.7, even for boxes of $L_z^+ = 333$. The similarity of the spanwise turbulent flow, caused by wall movement, to the laminar GSL described in [41] explain such a good prediction even for narrow channels. The spanwise flow can be well described even with small boxes while it is the main streamwise flow and its turbulent structures that suffers from narrow boxes.

The scattering of figure 4.8 in $P_{sav}\%$ data at different T^+ for various box sizes is mainly due to the overestimation of DR rather than to bias errors in power spent, as we have already seen.

4.3 Simulation time

Simulation time affects directly the standard deviation of the mean of the space-averaged wall-shear stress (figure 4.9), which exhibits high fluctuations when Minimal Flow Unit is employed, due to its narrow averaging area.

While σ_Ω depends mainly upon the wall area and on Re_τ, simulation runtime can reduce the variance of the mean wall-shear and hence its uncertainty. The increase in σ_Ω is counterweighted by a an increase in T_{sim}, which is chosen in order to limit $\sigma_{\overline{\Omega}}$.

After various attempts, simulation were run over a time equal to $T_{sim}U_p/h = 1500$ at $Re_\tau = 200$, in viscous timescale $T_{sim}^+ = T_{sim}/t_\nu = 12500$. At $Re_\tau = 1000$ simulation time in viscous unit has been kept constant and equal to $T_{sim}^+ = 12500$, leading to a simulation time

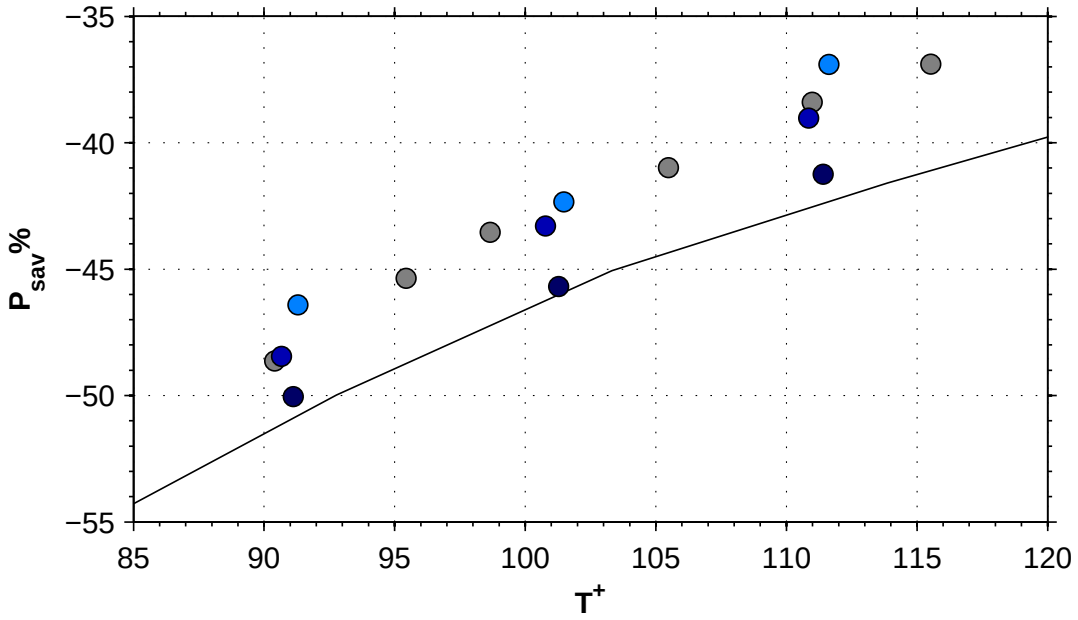

Figure 4.8: Power saved taking into account Regenerative Braking $P_{sav}\%$ versus period of wall oscillation T^+ for various box sizes at $Re_p = 4760$. Light blue: $L_z^+ = 333$, Blue: $L_z^+ = 663$, Dark Blue: $L_z^+ = 997$, Gray: previous simulations at $L_z^+ = 497$, Black solid line: Full DNS.

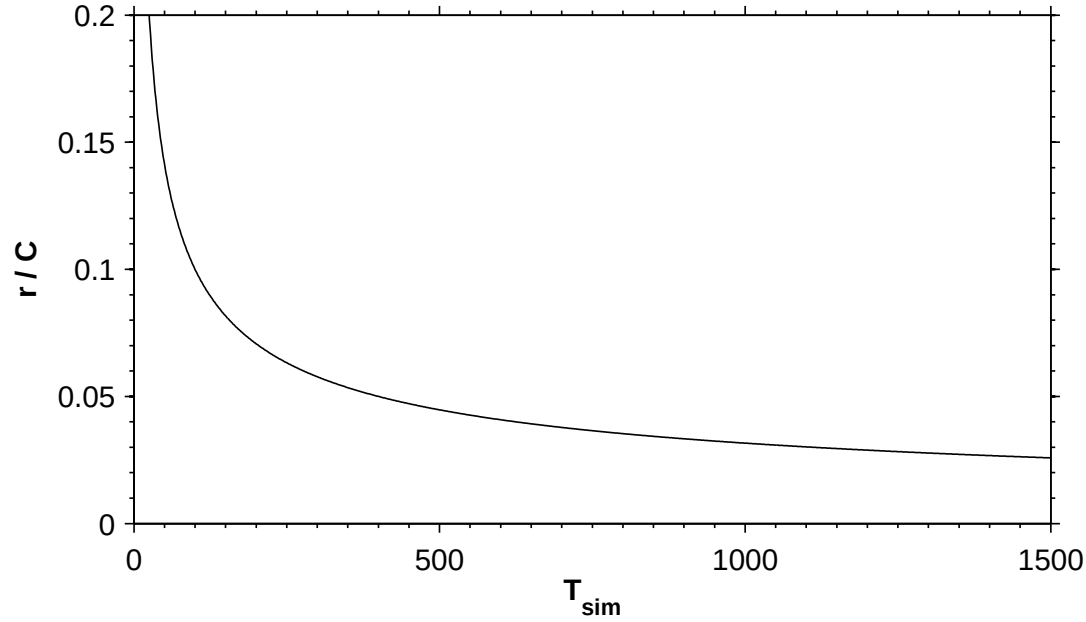

Figure 4.9: Influence of the simulation time on the mean wall shear average ratio $r = \sigma_{\overline{\Omega}}/\sigma_{\Omega}$.

of $T_{sim}U_p/h = 400$. At $Re_\tau = 2000$ a time of $T_{sim}U_p/h = 400$ has been kept, resulting in $T^+_{sim} = 24000$, in order to increase the reliability of the results.

The choice of inner scaling for the simulation runtime is justified by the scaling in viscous time of the initial transient and of the short-scale wall-shear fluctuations.

4.4 The quasi-laminar spanwise flow

The spanwise wall movement induces a thin spanwise flow near the wall, called generalized stokes layer (GSL), which interacts with the main turbulent flow. In order for the interaction to be effective, the induced spanwise flow has to be kept laminar.

The condition turns out to be a constraint on the Reynolds number based on the laminar GSL thickness δ_l, defined as:

$$Re_{\delta_l} = \frac{\delta_l A}{\nu} \tag{4.3}$$

where A is the spanwise velocity amplitude.

Namely, as documented by [54], the necessary condition for the spanwise flow to be laminar is:

$$Re_{\delta_l} < 120 \tag{4.4}$$

While [42] and [41] document that at $Re_p = 4769$, i.e. $Re_\tau \approx 200$, the spanwise Stokes layer keeps laminar for the optimal oscillating period for Drag Reduction of $T^+ \approx 120$, it is not known if this happens also at higher Re.

In case of oscillating wall, the boundary condition imposed at the wall is:

$$w_w(t) = A\sin(\omega t) \tag{4.5}$$

where $\omega = 2\pi/T$ is the frequency and T is the period. We indicate with the superscript $+$ the same quantities, but expressed in inner viscous units, i.e. $T^+ = T/t_\nu$, $\omega^+ = \omega\, t_\nu$ and $A^+ = A/u_\tau$.

In the hypothesis that the optimal value of ω (hence T) scale in viscous units, ω^+ and A^+ will be kept constant at higher Re. An estimate of the order of magnitude of Re_{δ_l} can be given. Actually, substituting in 4.3 the expression of δ_l, one obtains:

$$Re_{\delta_l} = \frac{A}{(\omega\nu)^{1/2}} \tag{4.6}$$

If we pick out the wall units, using $A = A^+u_\tau$ and $\omega = \omega^+/t_\nu$, and recall that $t_\nu = \nu/u_\tau^2$, then it turns out that:

$$Re_{\delta_l} = O\left(\frac{A^+}{\omega^+}\right) \tag{4.7}$$

This suggests that, if the oscillation parameters of 4.5 are kept constant in inner units, Re_{δ_l} should remain below its transitional-limit value. This gives the hope to reach high Reynolds number, maintaining a spanwise laminar Stokes layer. The hypothesis of inner scaling of optimal parameters for Drag Reduction is reasonable but not sure by now. Nevertheless, since Stokes Layer interacts favorably with wall-cycle when it is very thin ($\delta_{opt} \approx 6.5$ in order to give optimal Drag Reduction), it is more than reasonable to suppose that, even if there were discrepancies from the inner scaling, they would be small.

Therefore, simulations are conducted at increasing Re, assuming the inner scaling for the optimal value of the oscillating period T. Equally, inner scaling for the maximum spanwise velocity A has been taken.

In case of traveling waves, the condition 4.4 is fulfilled if the optimal wave speed c and wave amplitude A scale in viscous units.

We recall the spanwise wall velocity:

$$w_w(x,t) = A\sin(\kappa_x x - \omega t) \tag{4.8}$$

where $\kappa_x = 2\pi/\lambda_x$ is the streamwise wavenumber, λ_x its corresponding wavelength, $\omega = 2\pi/T$ the frequency and T its corresponding period. Eq. 4.8 represent a wave traveling in the streamwise direction with speed $c = \omega/\kappa_x$.

As reported in [41], the GSL thickness is proportional to $c\,t_\nu$. Substituting this expression in 4.3, one obtains:

$$Re_{\delta_l} = \frac{c\,t_\nu\,A}{\nu} \tag{4.9}$$

Expliciting wall units, $c = c^+u_\tau$ and $A = A^+u_\tau$. Recalling that $t_\nu = \nu/u_\tau^2$ 4.9 becomes:

$$Re_{\delta_l} = O(c^+A^+) \tag{4.10}$$

independent from u_τ and t_ν, as stated before. Thus, if c^+, hence ω^+ and κ^+, and A^+ are varied in a range that is kept constant at different Re, the condition for a laminar GSL is respected if the hypothesis of viscous units scaling holds.

Chapter 5

Oscillating Wall

Reynolds numbers up to $Re_p = 29500$ are reached in this chapter, where main results concerning wall oscillation as a predetermined flow-control technique are presented and discussed, making use of the parameters defined in the previous chapter to evaluate control effectiveness.

In the next sections, Drag Reduction $DR\%$ obtained at $Re_p = 4760$ and $Re_p = 29500$ is presented, as well as Power Required $P_{sp}\%$ to actuate the control and the Net Power budget $P_{sav}\%$.

In the last section the Reynolds effect is discussed.

Further results, equally interesting but not focused on the main topic of this work, the Reynolds effect, can be found in the Appendix B. The scaling of uncertainty and drag reduction is assessed and the effects of the control on the mean wall-shear spectrum are studied.

5.1 Drag Reduction

The whole set of simulations is documented in table 5.1 in terms of the parameters of the oscillation and the power budget for the two Reynolds numbers $Re_p = 4760$ and $Re_p = 29500$. Drag Reduction results from table 5.1 are represented in figure 5.1: only simulation with spanwise domain length $L_z^+ \approx 500$, based on viscous length δ_ν, are considered.

A maximum $DR\%$ of 39.4 has been achieved at $Re_\tau = 200$ (Case 1) with $T^+ = 123$ and $A^+ = 12$. At $Re_\tau = 1000$ the maximum $DR\%$ reaches the value of 34.2 (Case 32) when $T^+ = 103$ and $A^+ = 12$. This decreasing tendency of DR against Re_p is well documented in literature from very Reynolds number up to $Re_\tau = 400$. Our set of numerical experiment enriches the scenario, showing a modest DR at $Re_\tau = 1000$.

Comparing DNS data at $Re_p = 4760$ from [40] with MFU results at $Re_p = 29500$, no appreciable shift in the period T_{opt}^+ of maximum DR can be seen, when maximum wall displacement D_m^+ is left free to change. Thus, the scaling of T_{opt} with viscous time scale is suggested, at least at present moderate Reynolds number.

Case	D_m^+	T^+	P_{sp}	P_{sav}	$DR\%$	$\Delta DR\%$	Case	D_m^+	T^+	P_{sp}	P_{sav}	$DR\%$	$\Delta DR\%$
			$Re_p = 4760$							$Re_p = 29500$			
1	471	123	-72.9	-33.5	39.4	1.960	1	163	33	-190.6	-164.4	26.2	2.387
2	377	99	-81.6	-43.5	38.1	1.320	2	130	26	-213.8	-192.4	21.5	2.501
3	565	148	-66.2	-29.0	37.2	1.981	3	196	40	-173.5	-146.6	26.9	2.359
4	659	173	-60.9	-28.1	32.8	1.567	4	228	46	-160.8	-132.4	28.4	2.511
5	754	197	-56.5	-26.9	29.6	1.829	5	261	53	-149.9	-120.3	29.6	2.470
6	283	74	-94.5	-58.7	35.8	0.963	6	98	20	-248.2	-230.3	17.9	2.622
7	424	111	-76.8	-38.4	38.4	1.099	7	153	31	-196.8	-173.5	23.3	2.647
18	471	123	-73.0	-35.9	37.0	1.113	8	77	16	-280.4	-266.4	14.0	2.876
19	471	123	-72.8	-37.8	34.9	1.151	9	58	12	-326.8	-314.9	11.9	3.088
20	115	30	-149.9	-127.9	22.0	1.017	10	87	18	-263.7	-247.7	16.0	2.656
21	154	40	-129.2	-102.1	27.2	0.980	11	496	101	-107.9	-75.9	32.0	2.907
22	192	50	-115.3	-84.3	31.0	1.031	12	595	121	-97.9	-65.9	32.0	3.135
23	230	60	-104.9	-72.2	32.8	1.009	13	447	91	-113.8	-81.1	32.6	2.738
24	806	211	-54.6	-28.6	26.0	1.504	29	406	82	-119.6	-85.6	34.0	2.504
25	844	221	-53.4	-26.8	26.5	1.765	30	457	93	-112.7	-80.0	32.6	2.762
26	882	231	-52.5	-28.1	24.4	1.526	31	432	88	-116.0	-84.4	31.6	3.200
27	77	20	-185.3	-169.8	15.5	1.250	32	508	103	-106.9	-72.7	34.2	2.757
29	349	91	-85.4	-46.4	39.6	1.469	33	559	113	-101.5	-69.4	32.0	2.842
30	388	101	-80.9	-42.3	39.1	1.556	34	610	124	-96.9	-65.2	31.7	2.686
31	426	112	-76.9	-36.9	40.6	1.677	35	661	134	-92.9	-63.2	29.7	2.879
33	346	91	-85.2	-48.5	36.9	0.878	36	711	144	-89.4	-61.6	27.7	2.845
34	385	101	-80.9	-43.3	37.8	0.996	37	762	154	-86.1	-61.0	25.1	3.121
35	423	111	-77.0	-39.0	38.2	1.007	38	813	165	-83.3	-56.8	26.5	3.005
37	348	91	-85.2	-50.0	35.7	0.634	39	813	165	-83.4	-56.9	26.5	3.005
38	387	101	-80.9	-45.7	35.7	0.579	40	330	67	-133.0	-102.3	30.7	2.385
39	426	111	-76.8	-41.3	36.1	0.564	41	356	72	-128.1	-95.6	32.4	2.843
40	307	80	-90.7	-54.1	36.5	1.122							
41	345	90	-85.3	-48.6	36.6	1.099							
42	365	95	-83.1	-45.4	37.7	1.144							
43	403	105	-79.0	-41.0	38.0	1.335							
44	441	116	-75.3	-36.9	38.4	1.411							
45	499	131	-70.7	-33.1	37.6	1.212							
46	518	136	-69.5	-31.2	38.3	1.726							
47	537	141	-68.2	-30.1	38.0	1.824							
48	959	251	-50.1	-28.3	21.9	1.962							
49	38	10	-270.3	-264.3	6.0	1.398							

OSCILLATING WALL

Table 5.1: Power budget data for different oscillatory conditions, namely period T^+ and maximum wall displacement D_m^+ at $Re_p = 4760$ and $Re_p = 29500$.

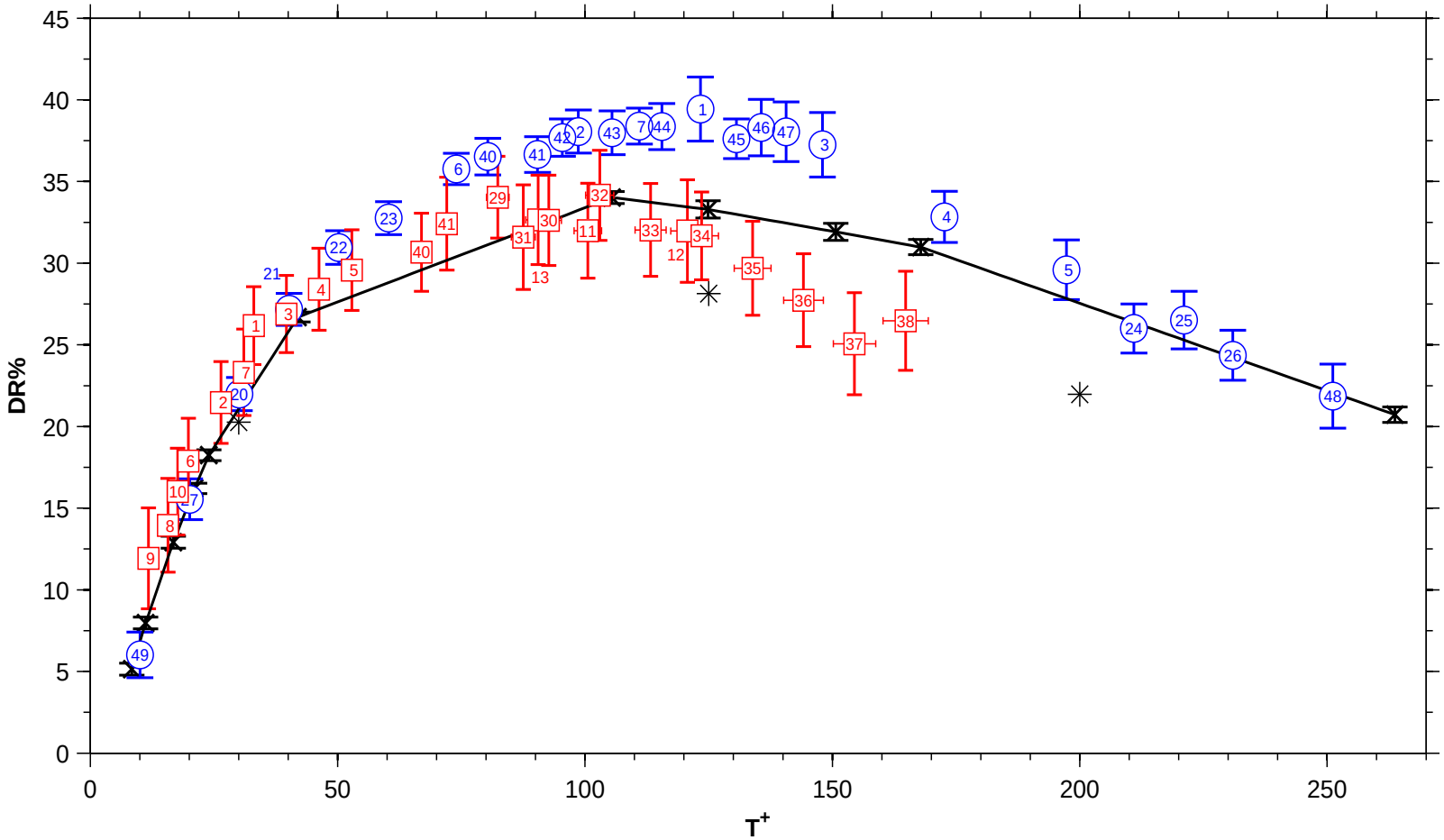

Figure 5.1: $DR\%$ versus T^+. Black solid line and $\times$: DNS Results at $Re_P = 4760$ from [40]; $*$: DNS results at $Re_p = 10500$ from [45]; $\circ$: MFU at $Re_p = 4760$ and $L_z^+ = 497$; $\square$: MFU at $Re_p = 29500$ and $L_z^+ = 459$. Error bars at 95% Confidence level.

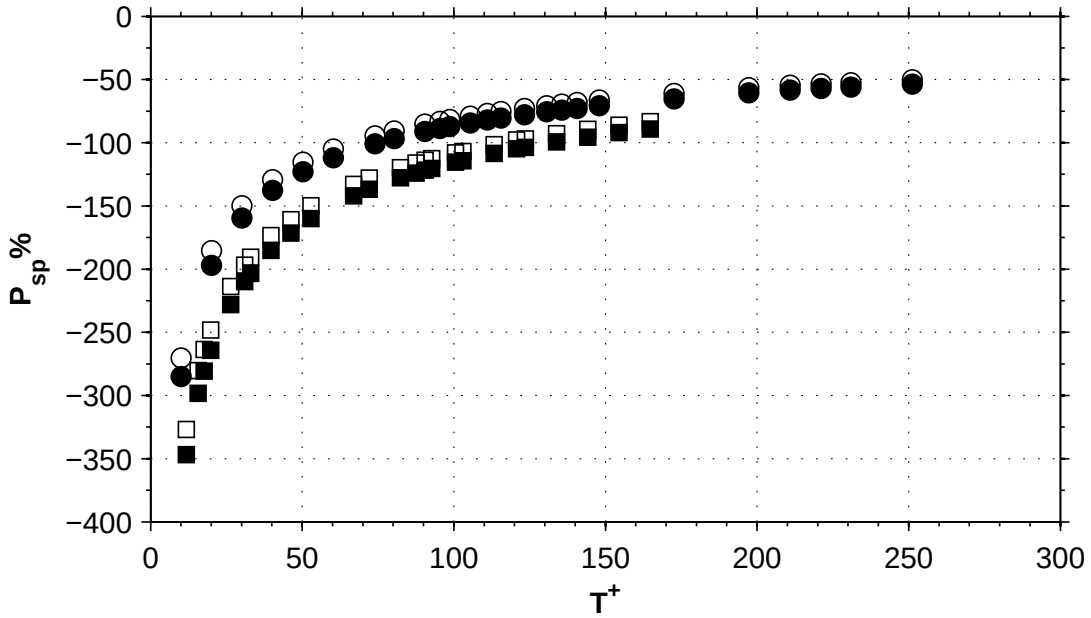

Figure 5.2: Power spent $P_{sp}\%$ versus period of wall oscillation T^+. ∘: MFU at $Re_p = 4760$ and $L_z^+ = 497$; □: MFU at $Re_p = 29500$ and $L_z^+ = 459$. White symbols: regenerative effect accounted; Black Symbols: no regenerative effect.

5.2 Power spent

Power Budget data presented in table 5.1 are shown in figure 5.2, against period of wall oscillation T^+, for both $Re_p = 4760$ and $Re_p = 29500$. The monotonic well-known behavior of $P_{sp}\%$ is well reproduced by the MFU and, most important, Power Spent increases as Reynolds number increase. Near maximum $DR\%$, at $T^+ \approx 110$, the increase in Power Spent is of about 24% of pumping power. At low frequencies this increase is even bigger, reaching the value of 44% at $T^+ = 40$.

Figure 5.3 shows that a linear correlation between DR and $P_{sp}\%$ exists up to the maximum DR for periods of wall oscillation smaller than T^+_{opt}. In this region, $P_{sp}\%$ decrease linearly with DR, with a steeper slope at $Re_p = 29500$ than $Re_p = 4760$. After the maximum, the two curves decrease with roughly the same slope.

Power Spent is represented in figure 5.2 and 5.3 both considering (blank symbols) or neglecting (filled symbols) the Collaborative Power $P_{sp}(+)\%$. Accounting for Collaborative Power does not produce significant effects at $T^+ \geq T^+_{opt}$, while for longer periods the decrease in Power Spent can be of about 15%. Unfortunately, in this region of high frequency, DR is very low and $P_{sp}\%$ very high, countering the benefical effect of a higher $P_{sp}(+)\%$.

The Collaborative effect could be very hard to exploit practically with a sensitive actuator, capable of a instantaneous tune of control power, according to $P_{sp}\%$. Such a small positive contribution to Power Spent at high DR, and low $P_{sp}\%$, is desirable, since special (and maybe expensive) actuators are not needed to reach higher performance in the region of forcing periods $T^+ \geq T^+_{opt}$.

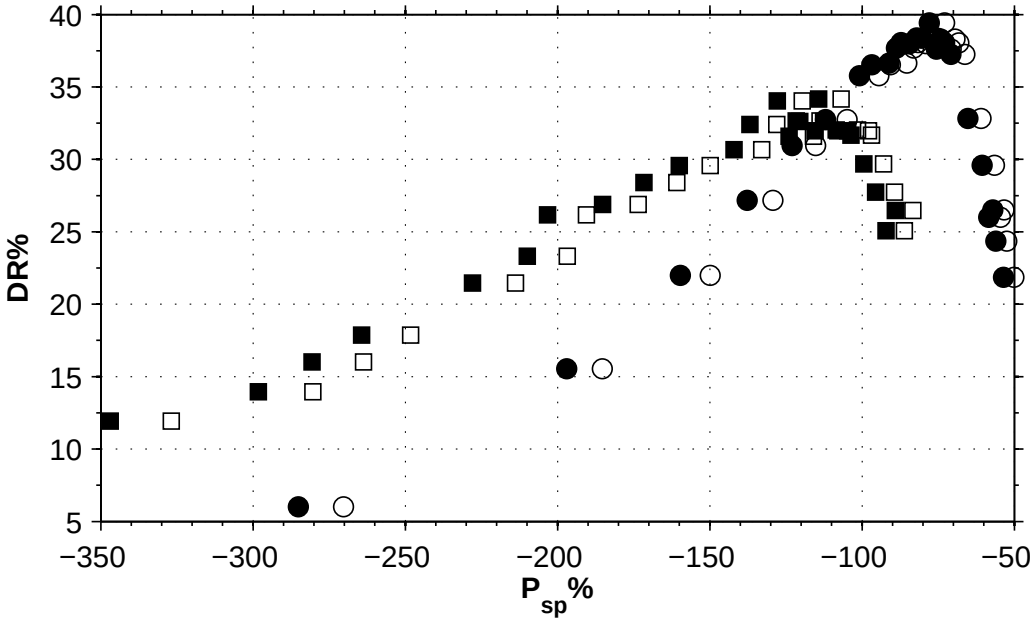

Figure 5.3: Power spent $P_{sp}\%$ versus Drag Reduction $DR\%$. ○: MFU at $Re_p = 4760$ and $L_z^+ = 497$; □: MFU at $Re_p = 29500$ and $L_z^+ = 459$.

5.2.1 Collaborative contribution

The main scaling parameters of collaborative power $P_{sp}(+)\%$ are now studied. Positive and negative contribution to power spent are proportional, as can be clearly seen in figure 5.4. The proportionality seems to be lost for $T^+ \leq 25$, suggesting an asymptotic behavior for very low T^+. The proportionality constant is Reynolds number independent, as a clear collapse of data can be observed at $T^+ > 25$ for different Re_p. A higher $P_{sp}(+)\%$ reached at $Re_p = 29500$ is due to the increased $P_{sp}(-)\%$. Again, collaborative power decreases, as power spent decreases, where its contribution would be more useful: near the maximum of DR, in order to reach a net energy saving, where it varies from 5% at $Re_p = 4670$ to 7.5% at $Re_p = 29500$.

The proportionality constant, i.e. the ratio between $P_{sp}(+)\%$ and $P_{sp}(-)\%$ is shown in figure 5.5 as function of T^+. A constant, Reynolds independent, proportionality coefficient exists for $T^+ \geq 90$ and is ≈ 0.065. At lower periods, the ratio drops, suggesting the existence of a maximum $P_{sp}(+)\%$.

5.3 Net Power Saving

No net Power Saving can be reached for both Reynolds number of $Re_p = 4760$ and $Re_p = 29500$ at $A^+ = 12$, as shown in figure 5.6. This result, already achieved at $Re_\tau = 200$ for a full DNS by [40], is here confirmed at $Re_p = 29500$.

As already shown, the increase of Re_p result in a smaller achievable DR, while $P_{sp}\%$ grows. Consequently to this combined effect, Net Power Saving is significantly reduced at high Reynolds number. As a matter of fact, at $Re_p = 4760$ and $T^+ = 105$, Power Spent is 41%, while at $Re_p = 29500$ and the same period is 76%, showing a 31% growth.

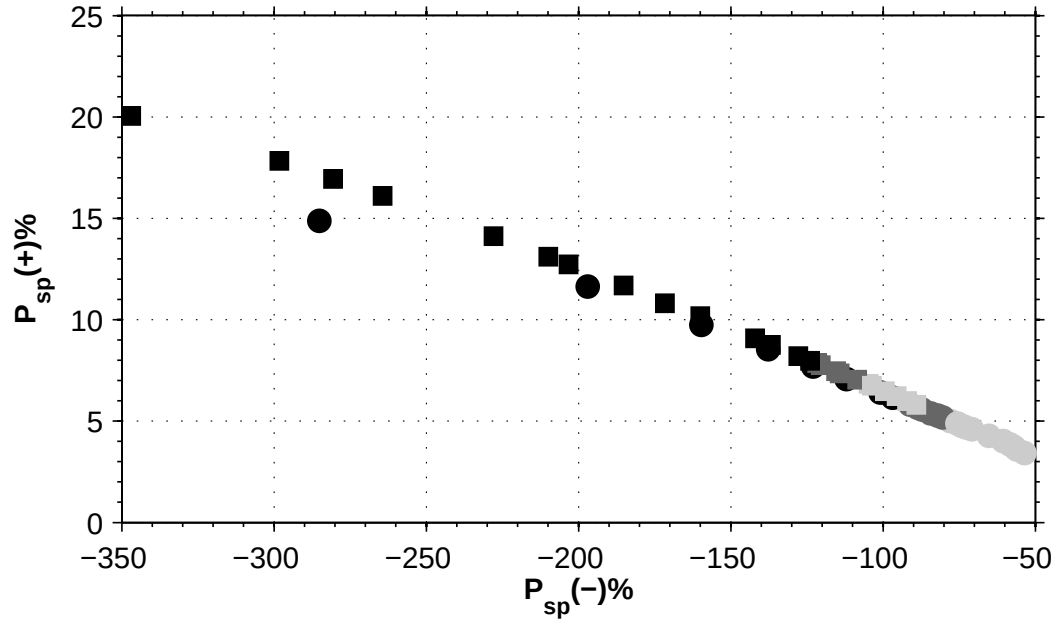

Figure 5.4: Collaborative Power $P_{sp}(+)\%$ versus Power spent $P_{sp}(-)\%$. ∘: MFU at $Re_p = 4760$ and $L_z^+ = 497$; □: MFU at $Re_p = 29500$ and $L_z^+ = 459$. Black symbols: $T^+ < 90$, Dark gray: $90 \leq T^+ \leq 120$, Light Gray $T^+ > 120$.

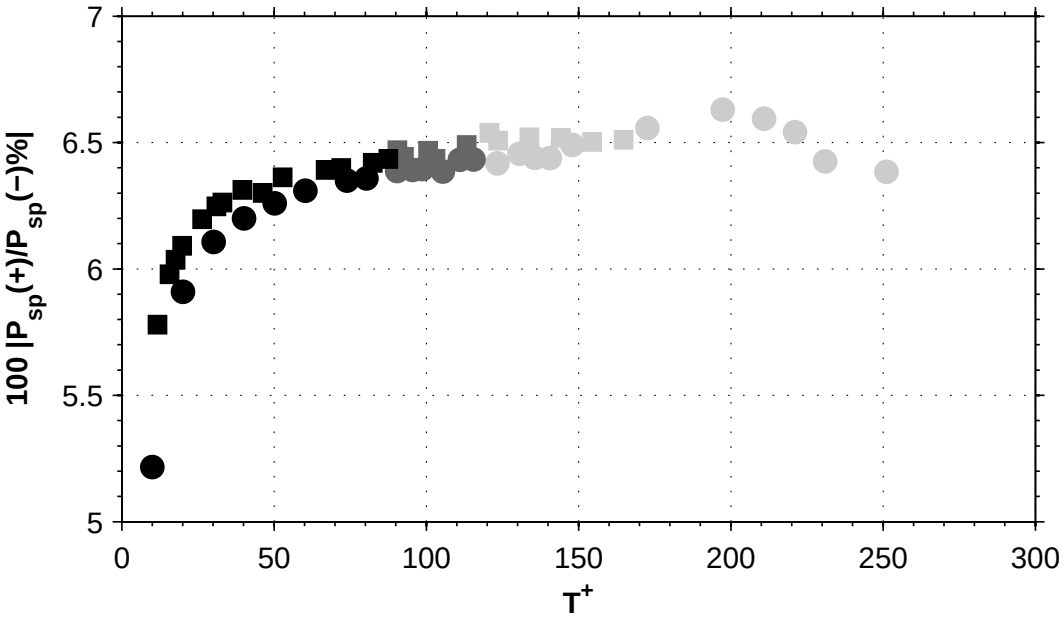

Figure 5.5: Ratio of Collaborative Power $P_{sp}(+)\%$ to Power spent $P_{sp}(-)\%$ versus Period of wall oscillation T^+. ∘: MFU at $Re_p = 4760$ and $L_z^+ = 497$; □: MFU at $Re_p = 29500$ and $L_z^+ = 459$. Black symbols: $T^+ < 90$, Dark gray: $90 \leq T^+ \leq 120$, Light Gray $T^+ > 120$.

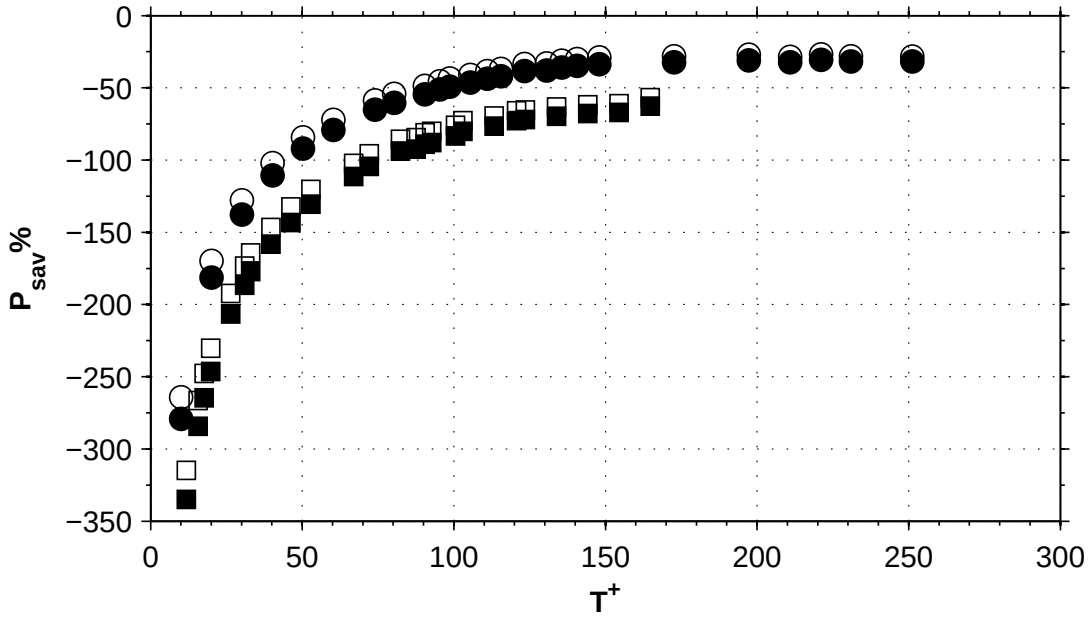

Figure 5.6: Power saved $P_{sav}\%$ versus period of wall oscillation T^+. ∘: MFU at $Re_p = 4760$ and $L_z^+ = 497$; □: MFU at $Re_p = 29500$ and $L_z^+ = 459$; White symbols: regenerative effect accounted; Black symbols: no regenerative effect.

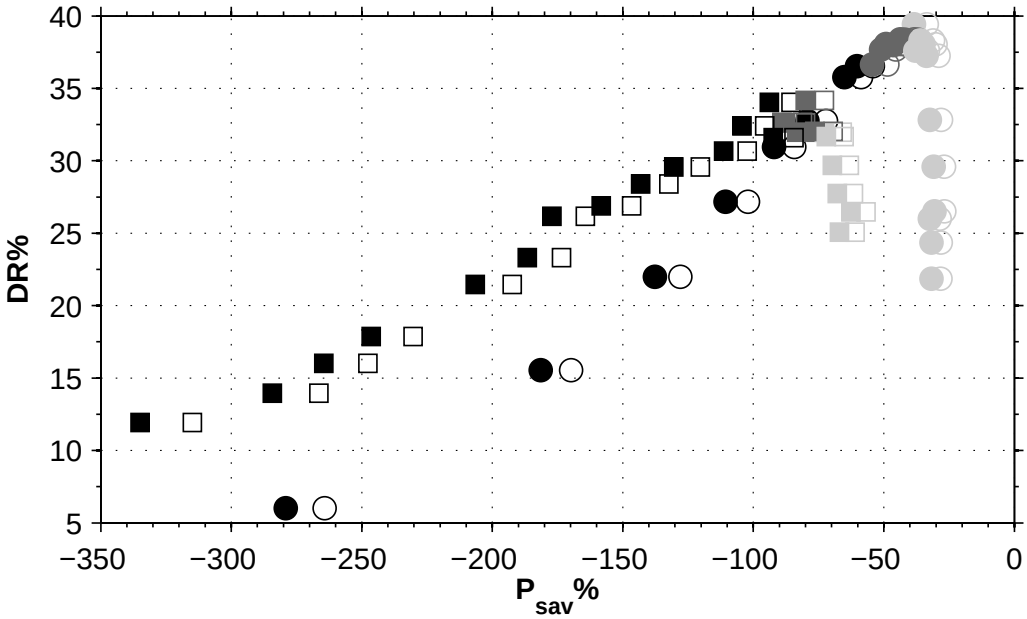

Figure 5.7: Power saved $P_{sav}\%$ versus Drag Reduction $DR\%$. ∘: MFU at $Re_p = 4760$ and $L_z^+ = 497$; □: MFU at $Re_p = 29500$ and $L_z^+ = 459$. Black symbols: $T^+ < 90$, Dark gray: $90 \leq T^+ \leq 120$, Light Gray $T^+ > 120$. Filled symbols: no regenerative effect; Blank symbols: regenerative effect accounted.

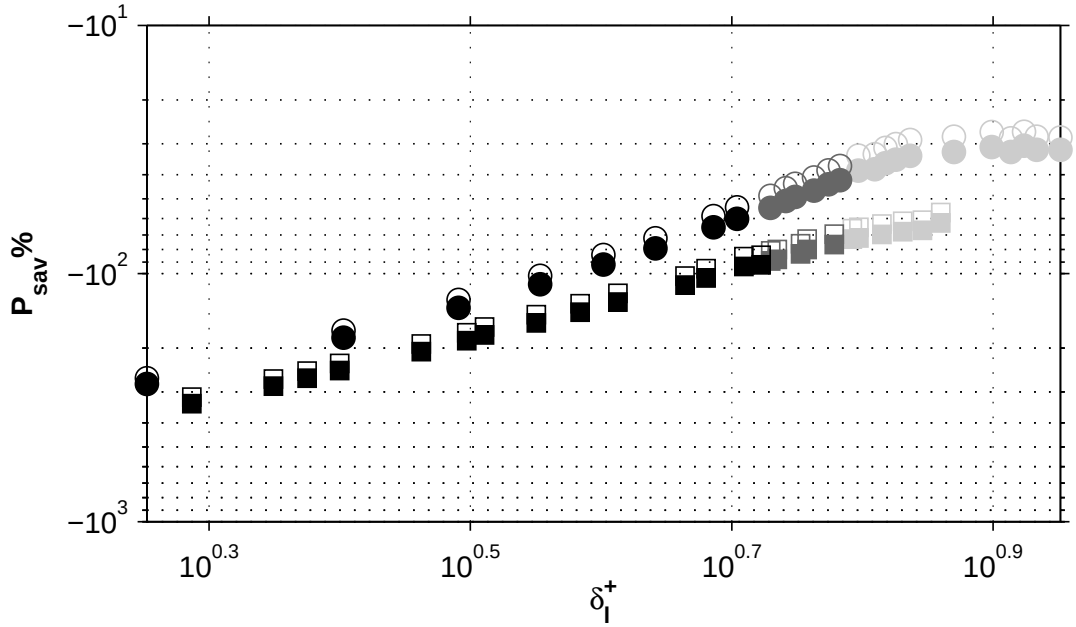

Figure 5.8: Power saved $P_{sav}\%$ versus Stokes Layer Thickness δ_l^+. ∘: MFU at $Re_p = 4760$ and $L_z^+ = 497$; □: MFU at $Re_p = 29500$ and $L_z^+ = 459$. Black symbols: $T^+ < 90$, Dark gray: $90 \leq T^+ \leq 120$, Light Gray $T^+ > 120$. Filled symbols: no regenerative effect; Blank symbols: regenerative effect accounted.

In [40] has been demonstrated that a net energy saving is attainable at $Re_\tau = 200$. We now expect that, for each (T^+,A^+) couple that lead to a net energy saving, a sufficiently high Reynolds number exist, that results in a null power budget. No limiting Reynolds number have been found at $A^+ = 12$, since no positive $P_{sav}\%$ can be reached for every T^+.

A linear relationship between $DR\%$ and $P_{sav}\%$ exists up to $T^+ = 105$, as shown in figure 5.7. The diagram of figure 5.8 exhibit a less-than-linear power-law relationship between $P_{sav}\%$ and the Stokes layer thickness δ_l^+ up to $\delta_l^+ \approx 6.5$. This value is demonstrated to correspond to maximum DR in [41]. In the same paper, the possibility of both a linear or $\sqrt{\delta_l^+}$ law for DR were given. It seems now clearer that a power law $DR\% = a(\delta_l^+)^b$ exists, with $b < 1$ function of the Reynolds number. Actually, because of the linear relationship (at suboptimal periods) between $DR\%$ and $P_{sav}\%$, if a linear law existed between $DR\%$ and δ_l^+, this would imply linearity also between $P_{sav}\%$ and δ_l^+.

5.3.1 Collaborative contribution

As its definition suggests, Collaborative contribution to Power Saved $P_{sav}(+)\%$ is clearly the same of $P_{sp}(+)\%$. Now, it is related to $P_{sav}(-)\%$, the power saved when only negative contribution to power spent is taken into account. Figure 5.9 shows a clearly non linear dependency between the two, that conversely holds between $P_{sp}(+)\%$ and $P_{sp}(-)\%$. Nevertheless, a nice collapse of data exists between different Reynolds numbers for periods greater than ≈ 25. The non proportionality is confirmed in figure 5.10, where the ratio $P_{sav}(+)\%/P_{sav}(-)\%$ is drawn against $P_{sav}(-)\%$.

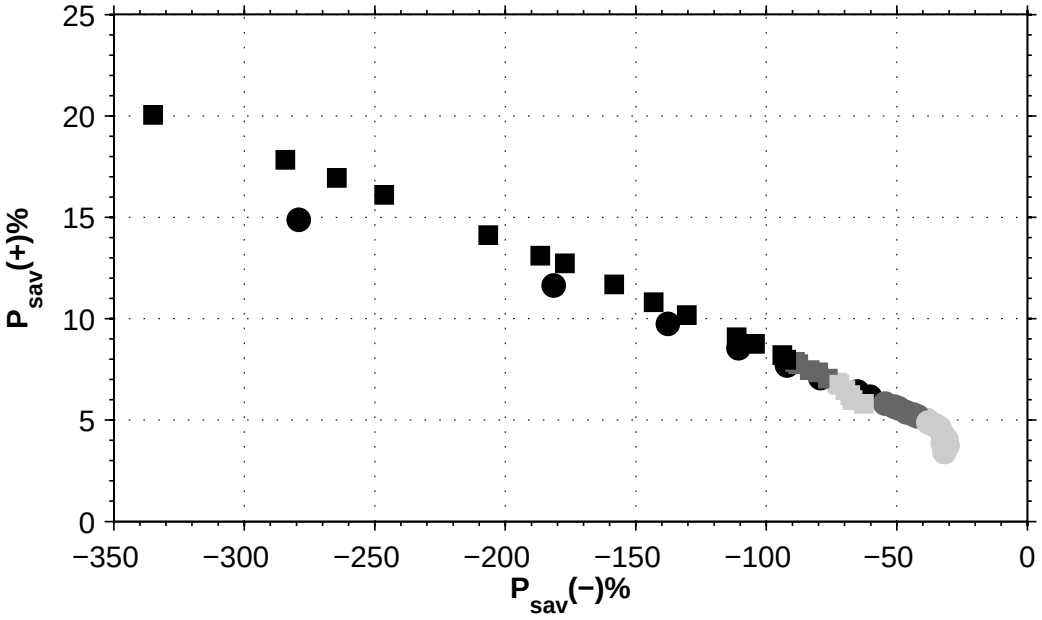

Figure 5.9: Collaborative power $P_{sav}(+)\%$ versus Power Saved $P_{sav}(-)\%$. ∘: MFU at $Re_p = 4760$ and $L_z^+ = 497$; □: MFU at $Re_p = 29500$ and $L_z^+ = 459$. Black symbols: $T^+ < 90$, Dark gray: $90 \leq T^+ \leq 120$, Light Gray $T^+ > 120$.

Again, collaborative contribution to power saved is not significant in the region of high DR and low power spent. At maximum DR, power saved could be 12% or 9% increased at $Re_p = 4760$ or $Re_p = 29500$ respectively, leading to a an increase of net saving of about 8% or 5% of the pumping power. This demonstrate also that a bigger $P_{sav}(+)\%$ at higher Reynolds number is only due to the growth of $P_{sp}(-)\%$ and not to a growth of the collaborative contribution itself.

5.4 Reynolds effect

Figure 5.11 show the trend of DR with Reynolds for two different periods: $T^+ = T^+_{opt}$ (Black) and $T^+ = 40$ (Red). As done by [6], a power law between Re_τ and DR is proposed, showing a $DR\%_{max} \sim Re_\tau^{-0.0879}$ decay for the maximum DR. The DR decrease is reduced at lower period (i.e. higher frequencies): at $T^+ = 40$, DR is nearly constant between $Re_\tau \approx 200$ and 1000.

Nonetheless, [6] suggested the far steeper decay of $DR \sim Re_\tau^{-0.2}$, studing Reynolds numbers between $Re_\tau \approx 200$ to 400.

Such a difference can be due to the lack of predictive power of the minimal flow unit for DR in case of the oscillating wall, to the high uncertainty of the results or to the wider range of Reynolds studied, if compared to [6].

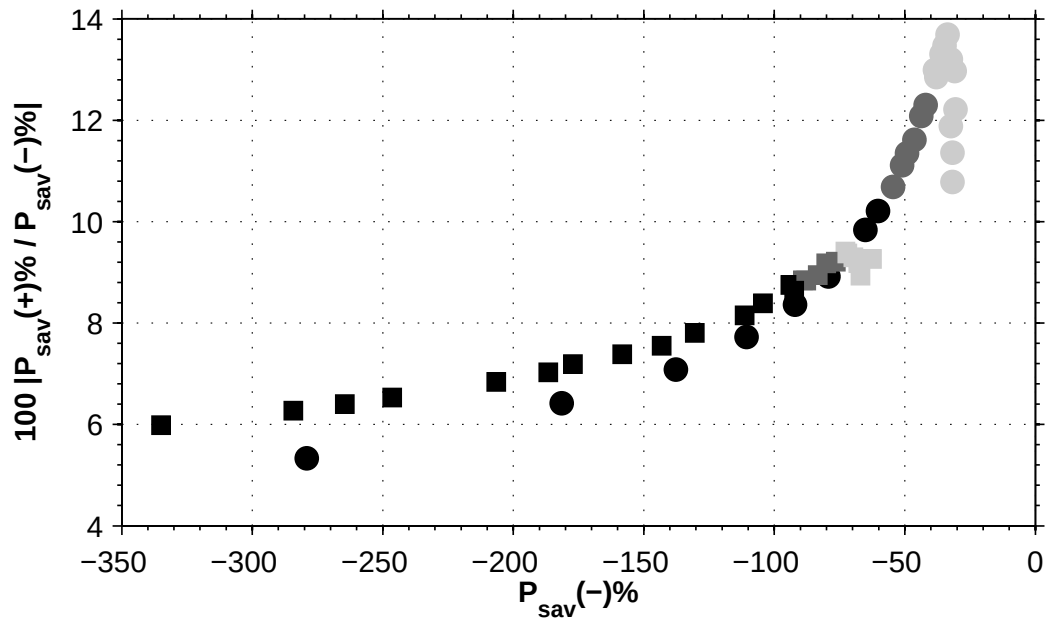

Figure 5.10: Ratio of Collaborative Power $P_{sav}(+)\%$ to Power saved $P_{sav}(-)\%$ versus Power saved. ○: MFU at $Re_p = 4760$ and $L_z^+ = 497$; □: MFU at $Re_p = 29500$ and $L_z^+ = 459$. Black symbols: $T^+ < 90$, Dark gray: $90 \leq T^+ \leq 120$, Light Gray $T^+ > 120$.

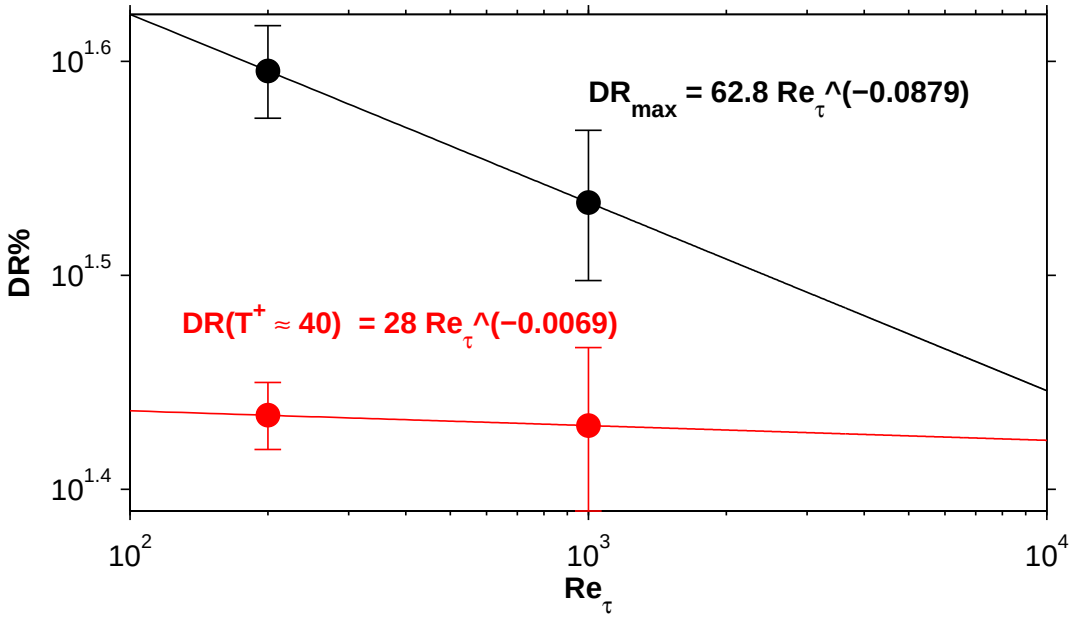

Figure 5.11: Drag Reduction $DR\%$ versus Re_τ for wall oscillating at $A^+ = 12$. ○: MFU data; Solid line: exponential-law fit. Red: $T^+ = 40$; Black: $T^+ = T^+_{opt}$

Chapter 6

Traveling Waves

In this chapter main results concerning streamwise traveling waves of spanwise velocity as a predetermined flow-control technique are presented and discussed, making use of the parameters defined in the previous chapter to evaluate control effectiveness.

In the next sections, Drag Reduction $DR\%$ obtained at $Re_p = 4760$, $Re_p = 29500$ and $Re_p = 73000$ is presented, as well as Power Required $P_{sp}\%$ to actuate the control and the Net Power budget $P_{sav}\%$.

In the last section, the effect of Reynolds number on the drag reduction, the power spent and saved is discussed.

Further results, equally interesting but not focused on the main topic of this work, the Reynolds effect, can be found in the Appendix B. The scaling of uncertainty and drag reduction is assessed and the effects of the control on the mean and punctual wall-shear spectrum are studied.

6.1 Drag Reduction

The whole set of simulations is documented in tables 6.1, 6.2 and 6.3, respectively at $Re_p = 4760$, $Re_p = 29500$ and $Re_p = 73000$, in terms of the parameters of the oscillation, κ_x, ω^+ and A^+, and the power budget.

Drag reduction results of the three Reynolds numbers are represented in figure 6.1 at $A^+ = 12$, which is a very common value of wave amplitude in literature, and especially in [42], and $\kappa_x = 0.005$, that has been proven to be the streamwise wavenumber that leads to the highest peak of DR, at an optimal ω [42].

A maximum $DR\%$ of 49.0 has been obtained (Case 62) at $Re_p = 4760$ at $\omega+ = 0.012$, for a wave slowly traveling forward at $c^+ \approx 2$. The peak of maximum DR is well captured by MFU. If compared to DNS at the same Reynolds number from [42], the point of highest DR is located at the same ω^+, but only $DR\% = 46.6$ is reached. As it happens for oscillating wall, DR is overestimated, particularly near the point of maximum DR, where it appears 2.4% higher.

The DI region range from $c^+ = 9$ to $c^+ = 16$ and is well reproduced by MFU, which locates the point of maximum DI (case 66) at $\omega = 0.062$ and $c^+ = 12$, the same identified in [42]. When DI is obtained, c^+ approaches $\mathcal{U}_w^+ = 10$, the mean convective velocity of near wall-structures. Obviously, different turbulent structures are convected with their own typical velocity and $\mathcal{U}_w^+ = 10$ is only an average value, that is why the region of DI extends

Case	A^+	κ_x^+	ω^+	c^+	$T_i U_P/h$	P_{sp}	P_{sav}	$DR\%$	$\Delta DR\%$
8	12	0.0063	0.020	3	270	−27.2	22.8	50.0	3.661
9	12	0.0063	0.302	48	80	−178.0	−162.2	15.9	1.158
10	12	0.0063	0.106	17	24	−96.9	−90.7	6.2	1.411
11	12	0.0063	0.042	7	96	−41.4	−28.2	13.2	1.062
12	12	0.0063	−0.106	-17	194	−109.9	−78.1	31.8	1.065
13	12	0.0063	−0.020	-3	200	−59.3	−15.5	43.8	0.970
14	12	0.0063	0.022	3	238	−26.9	21.9	48.8	3.253
15	12	0.0063	0.000	0	308	−42.4	6.0	48.4	1.075
16	12	0.0063	0.010	2	290	−34.1	15.4	49.5	1.577
17	12	0.0063	0.211	33	109	−147.0	−126.0	21.0	1.111
50	12	0.0063	0.080	13	50	−79.9	−92.1	−12.2	1.204
51	12	0.0063	0.030	5	480	−30.1	2.6	32.7	1.741
52	12	0.0063	0.149	24	85	−121.8	−95.4	26.3	0.954
53	12	0.0063	−0.299	-47	95	−181.3	−165.4	15.8	1.180
54	12	0.0063	−0.050	-8	80	−79.6	−40.0	39.6	1.172
55	12	0.0063	0.040	6	85	−38.8	−22.6	16.2	1.062
56	12	0.0063	0.129	20	70	−112.2	−86.8	25.4	1.124
58	12	0.0050	−0.202	-40	255	−148.3	−126.1	22.3	0.762
59	12	0.0050	−0.050	-10	255	−78.3	−39.3	39.0	0.796
60	12	0.0050	0.000	0	345	−38.9	9.8	48.7	1.631
61	12	0.0050	0.006	1	500	−33.7	14.1	47.8	1.865
62	12	0.0050	0.012	2	255	−28.3	20.8	49.0	3.940
63	12	0.0050	0.018	4	284	−25.9	19.4	45.3	4.276
64	12	0.0050	0.043	9	70	−45.6	−43.2	2.4	0.776
65	12	0.0050	0.056	11	80	−61.8	−68.4	−6.6	0.811
66	12	0.0050	0.062	12	50	−68.9	−78.8	−9.9	0.806
67	12	0.0050	0.075	15	70	−78.0	−88.0	−10.0	0.969
68	12	0.0050	0.082	16	95	−82.0	−85.1	−3.1	0.965
69	12	0.0050	0.100	20	190	−97.0	−76.1	20.9	1.000
70	12	0.0050	0.131	26	112	−113.7	−85.5	28.2	0.804
71	12	0.0050	0.178	36	144	−134.5	−109.2	25.3	0.816
72	12	0.0050	0.297	59	75	−176.5	−160.1	16.4	0.835
73	12	0.0050	0.015	3	205	−26.5	21.9	48.4	3.783
74	12	0.0050	0.009	2	205	−31.0	17.2	48.2	2.764
75	12	0.0050	0.023	5	460	−28.1	4.0	32.0	1.905
76	12	0.0050	0.059	12	40	−65.6	−73.9	−8.3	0.797
77	12	0.0050	0.125	25	105	−110.8	−82.1	28.7	0.797

Table 6.1: Power budget data for different traveling wave parameters, namely wavenumber κ_x^+, frequency ω^+ and phase speed $c^+ = \omega^+/\kappa_x^+$ at $Re_p = 4760$.

Case	A^+	κ_x^+	ω^+	c^+	T_iU_P/h	P_{sp}	P_{sav}	$DR\%$	$\Delta DR\%$
14	16	0.0205	0.020	1	18	−76.5	−37.9	38.7	2.051
15	16	0.0205	0.297	14	17	−227.5	−222.5	5.0	4.275
16	16	0.0205	0.104	5	20	−88.5	−61.3	27.2	2.519
17	16	0.0205	0.042	2	20	−61.9	−20.5	41.4	2.056
18	16	0.0205	−0.104	-5	20	−158.6	−130.9	27.7	2.893
19	16	0.0205	−0.020	-1	20	−105.3	−70.1	35.2	2.087
20	16	0.0205	0.021	1	20	−75.6	−37.3	38.4	2.042
21	16	0.0205	0.000	0	20	−91.4	−55.3	36.1	2.378
22	16	0.0205	0.009	0	20	−83.8	−45.8	38.0	2.242
23	16	0.0205	0.208	10	5	−178.4	−182.0	−3.6	3.516
42	16	0.0205	0.068	3	25	−57.6	−13.8	43.8	1.867
43	16	0.0205	0.248	12	1	−199.9	−210.4	−10.5	4.064
45	16	0.0049	−0.190	-39	33	−186.9	−164.0	22.8	2.699
46	16	0.0049	−0.047	-10	23	−99.8	−64.9	34.9	1.877
47	16	0.0049	0.000	0	40	−52.8	−14.3	38.6	2.544
48	16	0.0049	0.006	1	50	−46.1	−6.3	39.8	2.291
49	16	0.0049	0.011	2	24	−41.8	−6.5	35.2	2.994
50	16	0.0049	0.017	3	26	−41.1	−15.4	25.7	2.426
51	16	0.0049	0.040	8	17	−59.8	−56.0	3.8	2.602
52	16	0.0049	0.053	11	7	−78.9	−80.0	−1.1	2.829
53	16	0.0049	0.058	12	9	−87.0	−91.3	−4.3	3.086
54	16	0.0049	0.071	15	6	−99.5	−97.6	1.9	3.023
55	16	0.0049	0.083	17	12	−110.2	−99.4	10.8	3.998
56	16	0.0049	0.095	19	20	−120.7	−104.7	16.0	2.998
57	16	0.0049	0.123	25	25	−142.9	−116.7	26.1	2.921
58	16	0.0049	0.168	34	18	−169.4	−144.4	24.9	2.323
59	16	0.0049	0.280	57	26	−221.9	−205.3	16.6	2.392
61	16	0.0050	0.012	2	35	−41.0	−3.9	37.1	2.294
62	16	0.0050	0.082	16	5	−108.3	−99.1	9.2	4.027
63	12	0.0050	0.130	26	13	−146.8	−120.0	26.8	2.035
64	12	0.0050	0.064	13	4	−93.5	−93.1	0.4	3.178
65	12	0.0050	−0.189	-38	10	−109.2	−88.5	20.7	2.276
66	12	0.0050	−0.047	-9	11	−58.5	−24.7	33.8	1.780
67	12	0.0050	0.000	0	11	−31.4	5.1	36.5	2.477
68	12	0.0050	0.006	1	27	−28.0	6.9	34.9	2.526
69	12	0.0050	0.011	2	27	−25.0	8.0	33.0	3.009
70	12	0.0050	0.017	3	24	−23.7	3.6	27.3	2.943
71	12	0.0050	0.040	8	11	−34.0	−26.8	7.2	3.060
72	12	0.0050	0.052	10	10	−45.7	−43.8	1.9	2.790
73	12	0.0050	0.058	12	6	−50.7	−50.5	0.2	2.709
74	12	0.0050	0.070	14	7	−57.6	−56.1	1.5	2.583
75	12	0.0050	0.082	16	14	−63.6	−57.2	6.4	4.726
78	12	0.0050	0.094	19	14	−69.9	−57.7	12.1	4.328
77	12	0.0050	0.122	24	23	−83.0	−61.9	21.0	2.448
78	12	0.0050	0.167	33	24	−98.7	−75.5	23.2	2.448
79	12	0.0050	0.278	55	14	−129.5	−113.4	16.1	2.285
80	12	0.0050	0.012	2	64	−25.0	6.3	31.3	2.669
81	12	0.0050	0.082	16	18	−63.4	−56.3	7.1	3.019
82	12	0.0050	0.130	26	20	−86.2	−62.6	23.6	2.844
83	12	0.0050	0.064	13	10	−54.8	−55.5	−0.7	2.594
84	12	0.0050	0.144	29	24	−91.1	−68.3	22.8	2.640

Table 6.2: Power budget data for different traveling wave parameters, namely wavenumber κ_x^+, frequency ω^+ and phase speed $c^+ = \omega^+/\kappa_x^+$ at $Re_p = 29500$.

Case	A^+	κ_x^+	ω^+	c^+	T_iU_P/h	P_{sp}	P_{sav}	$DR\%$	$\Delta DR\%$
1	12	0.0047	−0.005	-1	28	−29.6	−0.4	29.2	4.172

Table 6.3: Power budget data for different traveling wave parameters, namely wavenumber κ_x^+, frequency ω^+ and phase speed $c^+ = \omega^+/\kappa_x^+$ at $Re_p = 73000$.

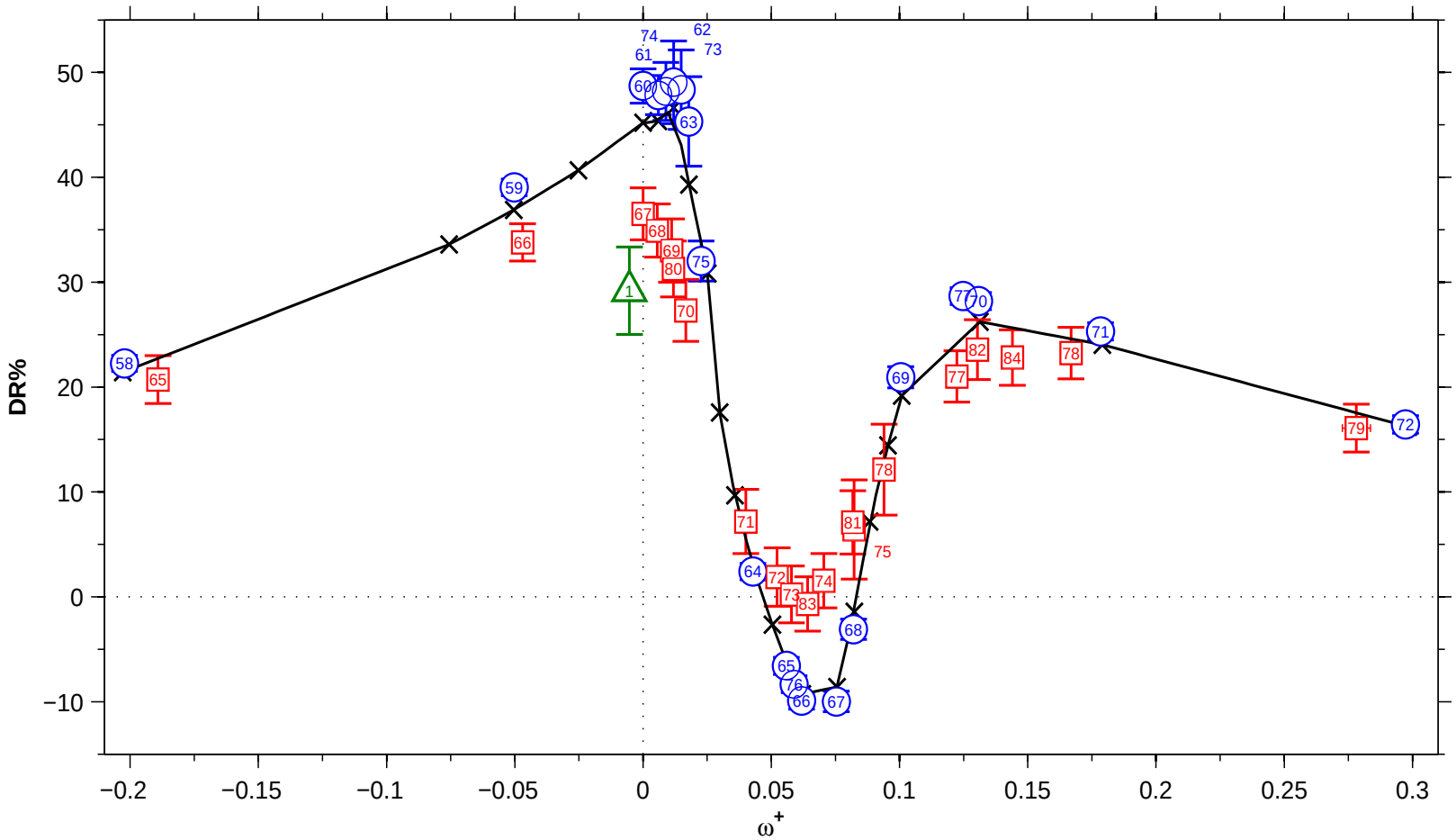

Figure 6.1: $DR\%$ versus ω^+ for traveling waves at $\kappa_x^+ = 0.005$ and $A^+ = 12$. Solid line and $\times$: DNS at $Re_P = 4760$ from [42]; $\circ$: MFU at $Re_p = 4760$; $\square$: MFU at $Re_p = 29500$; $\triangle$: MFU at $Re_p = 73000$. Error bars at 95% Confidence level.

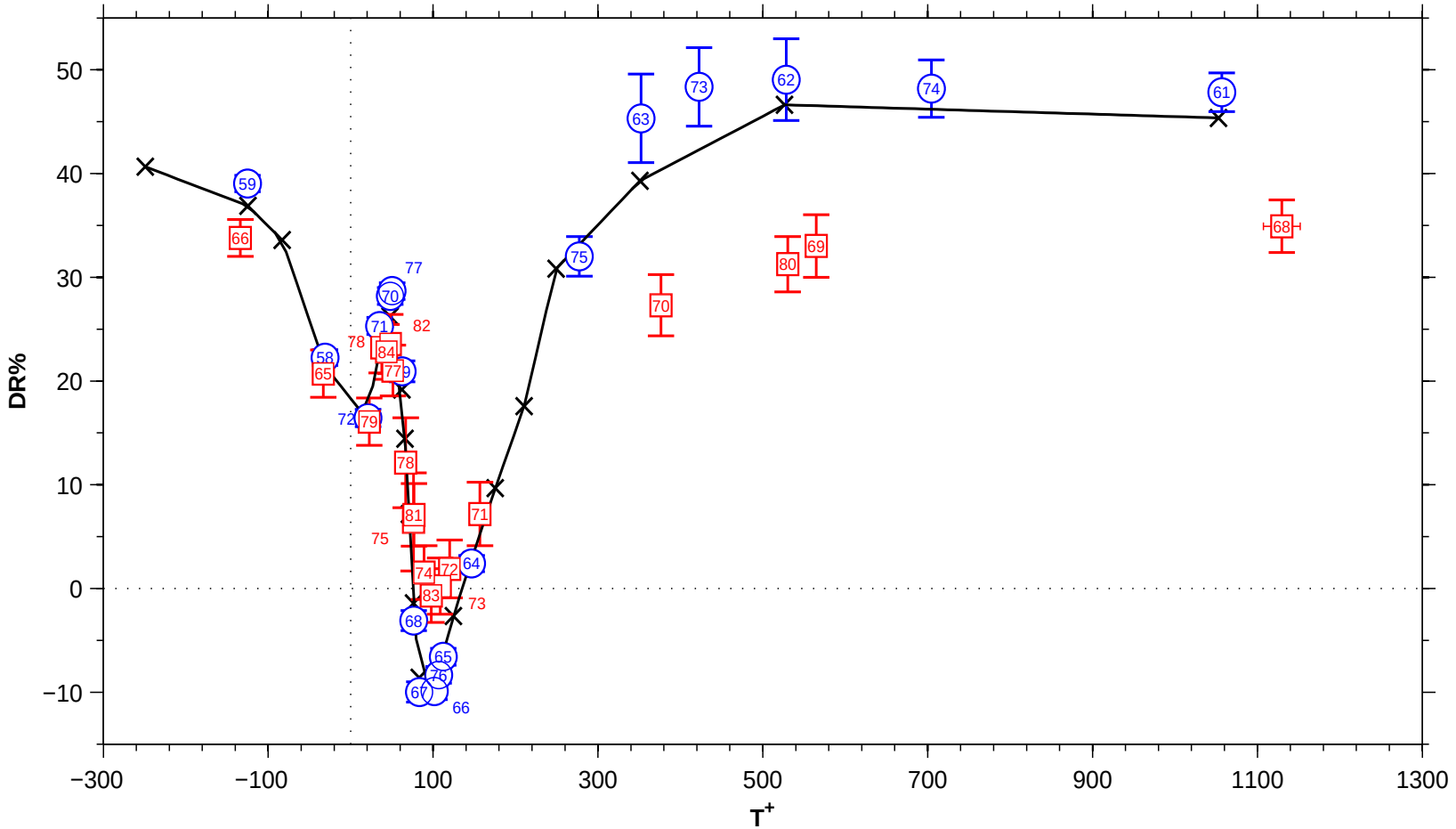

Figure 6.2: $DR\%$ versus T^+ for traveling waves at $\kappa_x^+ = 0.005$ and $A^+ = 12$. Solid line and ×: DNS at $Re_P = 4760$ from [42]; ○: MFU at $Re_p = 4760$; □: MFU at $Re_p = 29500$; △: MFU at $Re_p = 73000$. Error bars at 95% Confidence level.

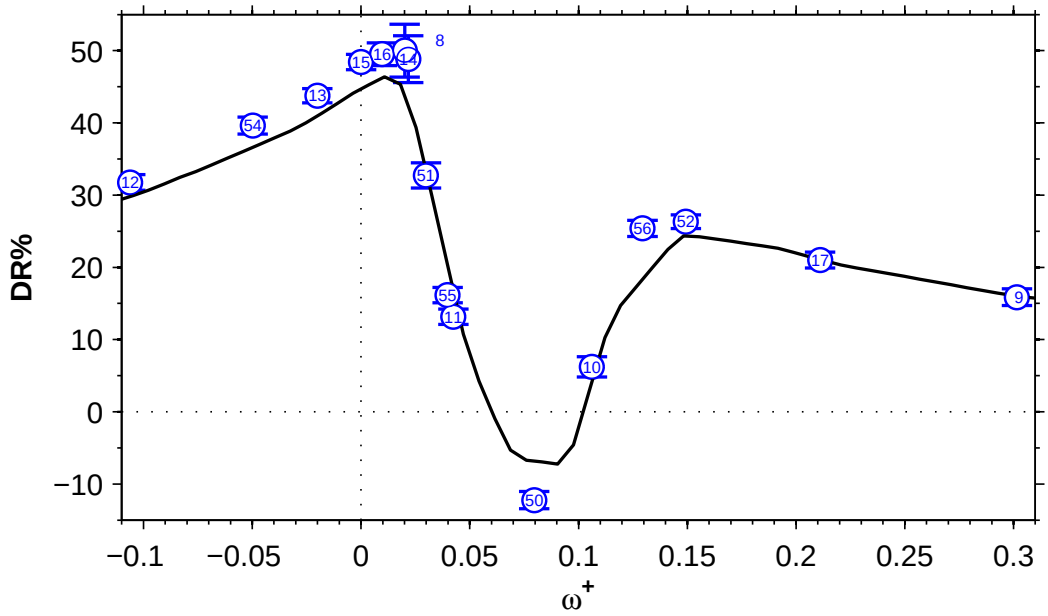

Figure 6.3: $DR\%$ versus ω^+ for traveling waves at $\kappa_x^+ = 0.0063$ and $A^+ = 12$. Black solid line : DNS Results at $Re_P = 4760$ from [42]; ○: MFU at $Re_p = 4760$. Error bars at 95% Confidence level.

over a range of c^+. When DI occurs, turbulent structures are cyclically tilted in the spanwise direction by the wall forcing, which is stationary if observed in a reference frame convecting with the structures.

When the drag-increasing lock-in effect is ceased, a local maximum of $DR = 28.7$ (case 77) can be observed at $\omega^+ = 0.125$, for a wave traveling at $c^+ = 25$. When compared to the DNS of [42], a slight overestimation and shift of this peaks appear in figure 6.1. The effect is only apparent and due to the very sparse DNS point near the maximum. It is realistic that MFU has correctly located the point of local maximum.

MFU gives very accurate predictions on DR for all backward traveling waves and forward traveling waves with $\omega > 0.012$, that is after the absolute maximum of DR. Within this open range, overestimation of friction reduction is limited and accurate predictions of peaks are obtained.

At $Re_p = 29500$ the maximum DR achievable trough spanwise velocity waves (case 67) with $\kappa_x^+ = 0.005$ is 36.5 for a standing wave with $\omega^+ = 0$. If compared with the DNS from [42], a 10% reduction of maximum DR is verified. The shift in the point of maximum is here noteworthy and possibly due to the high uncertainty, rather than a bias error of MFU. The lack of shift for the same Reynolds but $A^+ \approx 15$ enforces the supposition (figure 6.4).

Even the peak of DI is reduced and drops from -9.9 at $Re_p = 4760$ to -0.7 at $Re_p = 29500$, while no shift in the point of maximum DI can be observed, being located at $\omega^+ = 0.064$ (case 83), leading to a wave traveling at $c^+ = 12$.

The interval of c^+ that leads to DR has become strongly narrower, being the point at $c^+ = 12$ the only one that exhibit small DI. Other points in the neighborhood shows a slight DR. Considering the lock-in mechanism causing DI, this means that convective velocity $\mathcal{U}_w^+$

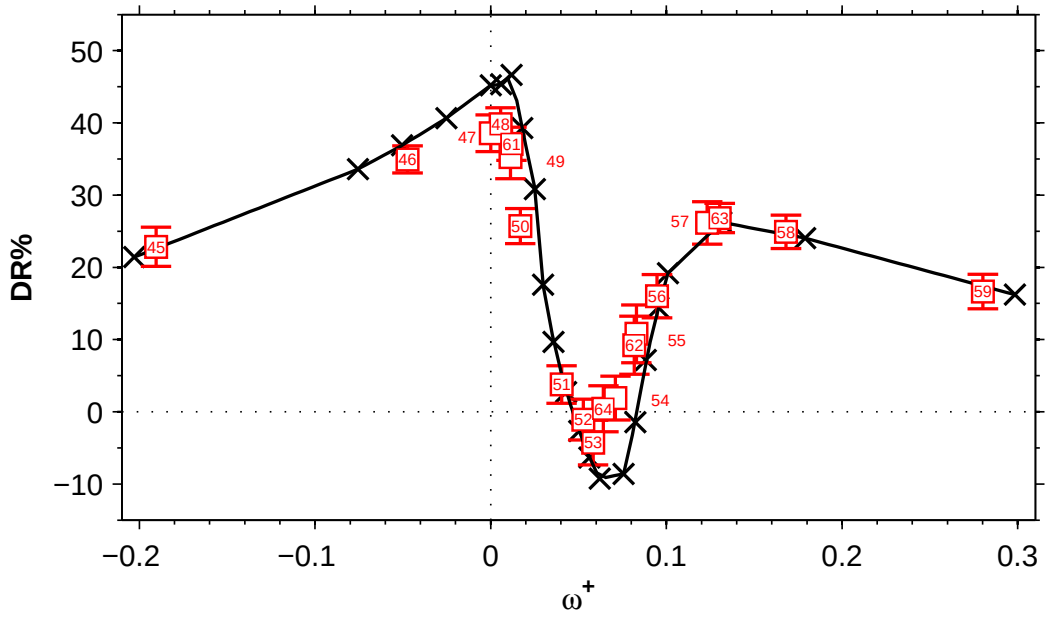

Figure 6.4: $DR\%$ versus ω^+ for traveling waves at $\kappa_x^+ = 0.005$ and $A^+ = 15.6$. Black solid line : DNS Results at $Re_P = 4760$ from [42]; □: MFU at $Re_p = 29500$. Error bars at 95% Confidence level.

remained substantially unchanged but the interaction mechanism between the generalized stokes layer and turbulent structures has changed, possibly due to changes in low-Re turbulent structures at the wall or to increase of turbulent fluctuations turbulent structures are overimposed to, that weakens the lock-in effect. Further studies are indeed necessary.

The second local maximum of DR is located at $\omega^+ = 0.130$ (case 82, $c^+ = 26$) and a friction reduction of 23.6 found, no shift in the peak is observed if comared to DNS data from [42]. A decrease DR of 5% is visible, increasing Re_p to 29500.

The loss of effectiveness in DR at $Re_p = 29500$, even if still present, is less significant where $|\omega^+| > 0.125$, that is if $|c^+| > 26$ at $\kappa_x^+ = 0.005$.

Only one point at $Re_p = 73000$ and $\omega^+ = -0.005$ has been computed and is represented in figure 6.1, a 29.2 DR has been obtained. Reasonably supposing DR rate does not change significantly from $\omega^+ = 0.005$ to $\omega^+ = 0$, we compare the results with maximum DR at $Re_p = 29500$ and $\omega^+ = 0$: a further decrease in friction reduction of 7.3% is computed.

A look at figure 6.2, where DR is represented against T^+ instead of ω^+, offers a better view on the decrease in DR near its maximum at low frequencies and a clearer comparison on the differences between oscillating wall and traveling waves.

Figure 6.3 compare MFU and DNS results for traveling waves at $\kappa_x^+ = 0.0063$ and $A^+ = 12$. Previous remarks are confirmed: local maxima of DR and DI are well captured, even if slight overestimation of DR is present. Very good agreement exists between MFU and DNS data at $\omega^+ < 0.1$ and $\omega^+ > 0.025$.

Drag reduction remains substantially unchanged, varying Reynolds number, in the range $|\omega^+| > 0.1$, as shown in figure 6.4 at $\kappa_x^+ = 0.005$, if wave amplitude A is kept constant in outer units and equal to $A = 0.5042$, which corresponds to $A^+ = 15$ at $Re_p = 29500$. Nevertheless,

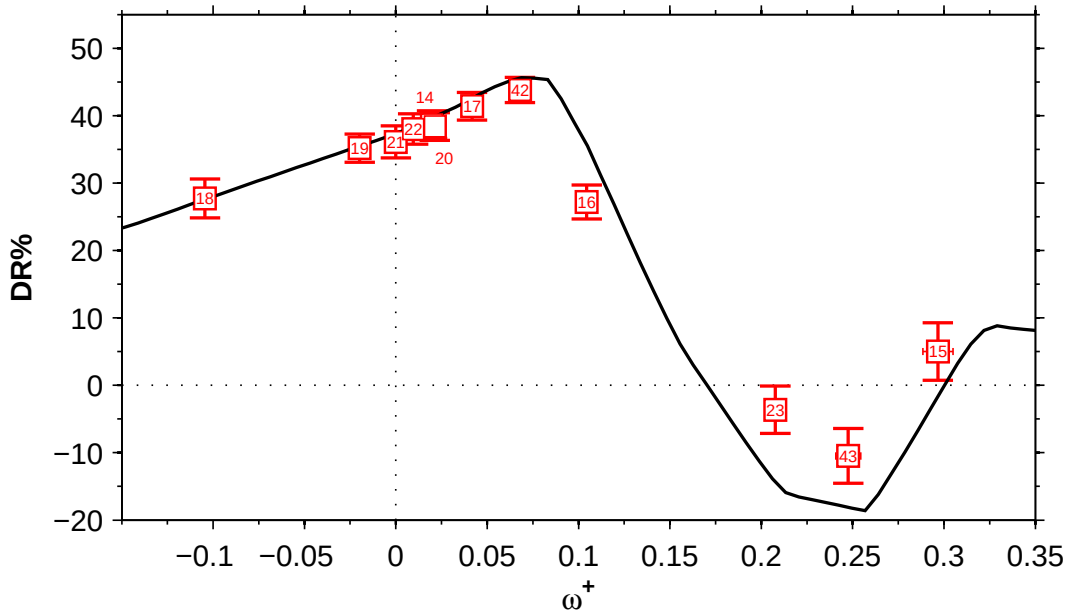

Figure 6.5: $DR\%$ versus ω^+ for traveling waves at $\kappa_x^+ = 0.02$ and $A^+ = 15.6$. Black solid line : DNS Results at $Re_P = 4760$ from [42]; □: MFU at $Re_p = 29500$. Error bars at 95% Confidence level.

sensible drop of DR is observed near its maximum at $\omega^+ \approx 0.01$, in spite of the increase of A^+.

Except the flattening of the DI peak, very small differences can be observed in figure 6.5 between the DNS at $Re_p = 4760$ and $Re_p = 29500$ at $\kappa_x^+ = 0.02$, if $A = 0.5042$ is kept constant in outer units, leading to $A^+ = 15$ at $Re_p = 29500$.

Comparing figures 6.4 and 6.5, the decrease in DR with Re_p is suggested to be function not only of DR itself but also of the (κ_x, ω) couple, at fixed A^+. Thus, a parametric numerical campaign is required in the whole wave parameters plane to clarify the dependency. If the sensitivity to Reynolds number could be different according to the region of the (κ_x, ω) plane, a relatively unaffected region could exist even at $Re_p = 29500$. In this sense, the optimal (κ_x, ω) couple can vary with Reynolds. In our case, we studied a fixed value of $\kappa_x = 0.005$ and therefore no shift in the optimal point for DR appears.

6.2 Power spent

Figure 6.6 shows power spent $P_{sp}\%$ against wave frequency ω^+ at $A^+ = 12$and $\kappa_x^+ = 0.005$. The most noteworthy feature of traveling waves, in contrast to oscillating wall, is the decrease of $P_{sp}\%$ with Reynolds number. The decrease is subtle near $\omega^+ \approx 0.02$, where DR is high, and significant at large frequencies. Even the single $Re_p = 73000$ point confirms the positive trend. It could be possible to reach net power saving at high Reynolds numbers with high frequency forcing: high frequencies are less affected by the decrease of DR with Re, while power required decrease sensibly with Re.

Comparing MFU results at $Re_p = 4760$ with DNS results from [42] at the same Reynolds,

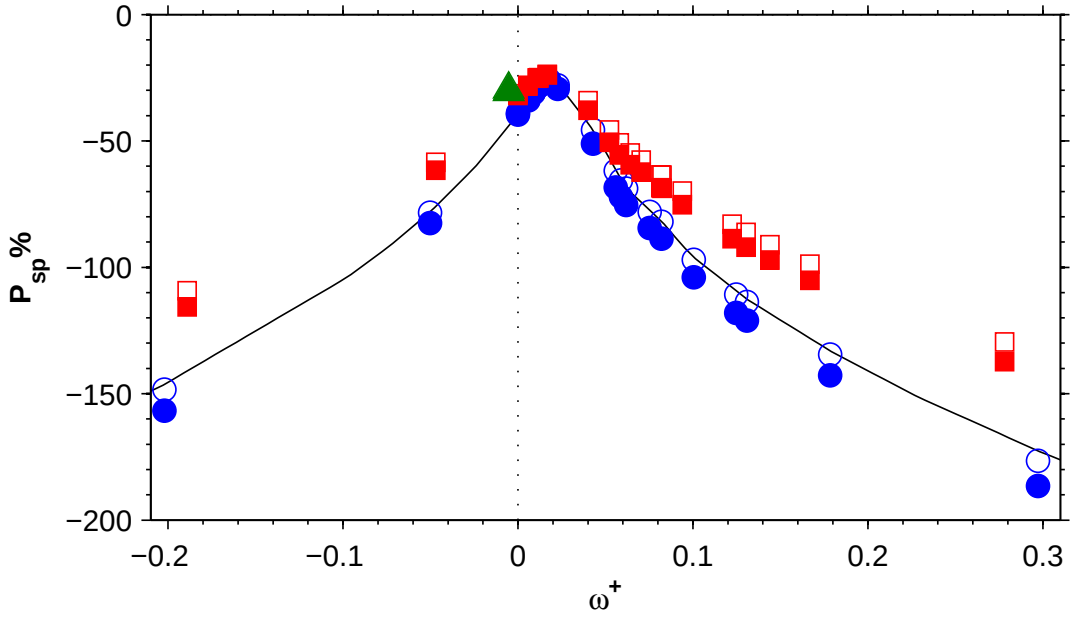

Figure 6.6: Power spent $P_{sp}\%$ versus wave frequency ω^+ at $\kappa_x^+ = 0.005$ and $A^+ = 12$. Black solid line : DNS Results at $Re_P = 4760$ from [42]; ○: MFU at $Re_p = 4760$ and $L_z^+ = 497$; □: MFU at $Re_p = 29500$ and $L_z^+ = 459$; △: MFU results at $Re_p = 73000$. Filled symbols: regenerative effect not accounted.

a very nice agreement can be appreciated. The point of minimum $P_{sp}\%$ is also well located by the MFU. As demonstrated for the oscillating wall, even narrow channels can predict $P_{sp}\%$ very well, due to the similarity between the GSL that develops in a turbulent channel and the laminar solution found in [41].

Power spent is plotted against DR in figure 6.7. A linear trend is discernible in the upper part of the curves, until maximum DR is reached. Here linearity is lost and DI is reached in the lower part. Linearity is recovered as DR increase again, once the local maximum being reached, in the leftmost part of the figure. Minimum power spent is clearly reached at maximum DR.

6.2.1 Collaborative contribution

The regenerative contribution to power spent $P_{sp}(+)\%$ decay as the maximum of DR is approached, as can be clearly seen in figures 6.6 and 6.7. The behavior can be both desirable or not. Obviously, it would be positive if Collaborative effect were high at maximum DR, in order to reach a positive power budget. However, to exploit $P_{sp}(+)\%$ a spanwise-friction sensitive actuator is necessary. Such an actuator could be difficult, or expensive, to build and operate. Thus, the possibility to reach a net power saving without the collaborative effect is a very positive feature.

Figure 6.8 show that $P_{sp}(+)\%$ and $P_{sp}(-)\%$ are proportional up to $T^+ < 90$. The proportionality constant does not vary with Reynolds number. If $90 < T^+ < 160$ an increase of $P_{sp}(+)\%$ can be observed, while points at $T^+ > 160$ show a sudden reduction of the collaborative effect.

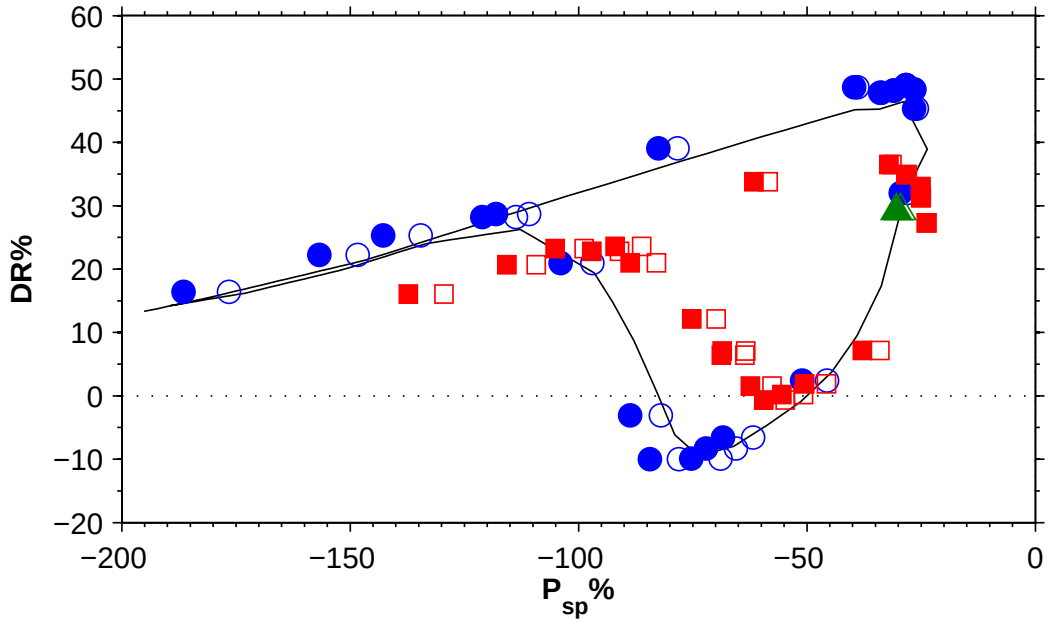

Figure 6.7: Drag Reduction $DR\%$ versus Power Spent $P_{sp}\%$ at $\kappa_x^+ = 0.005$ and $A^+ = 12$. Black solid line : DNS Results at $Re_P = 4760$ from [42]; ∘: MFU at $Re_p = 4760$ and $L_z^+ = 497$; □: MFU at $Re_p = 29500$ and $L_z^+ = 459$; △: MFU results at $Re_p = 73000$. Filled symbols: regenerative effect not accounted.

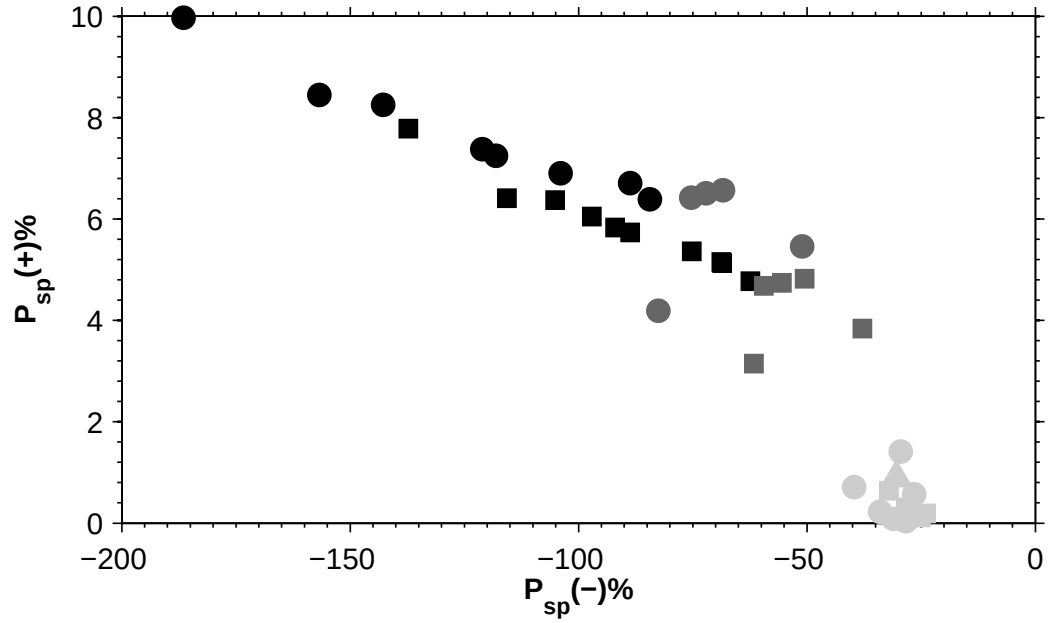

Figure 6.8: Collaborative Power $P_{sp}(+)\%$ versus Power Spent $P_{sp}(-)\%$ at $\kappa_x^+ = 0.005$ and $A^+ = 12$. ∘: MFU at $Re_p = 4760$ and $L_z^+ = 497$; □: MFU at $Re_p = 29500$ and $L_z^+ = 459$; △: MFU results at $Re_p = 73000$. Black symbols: $T^+ < 90$, Dark gray: $90 \leq T^+ \leq 160$, Light Gray $T^+ > 160$.

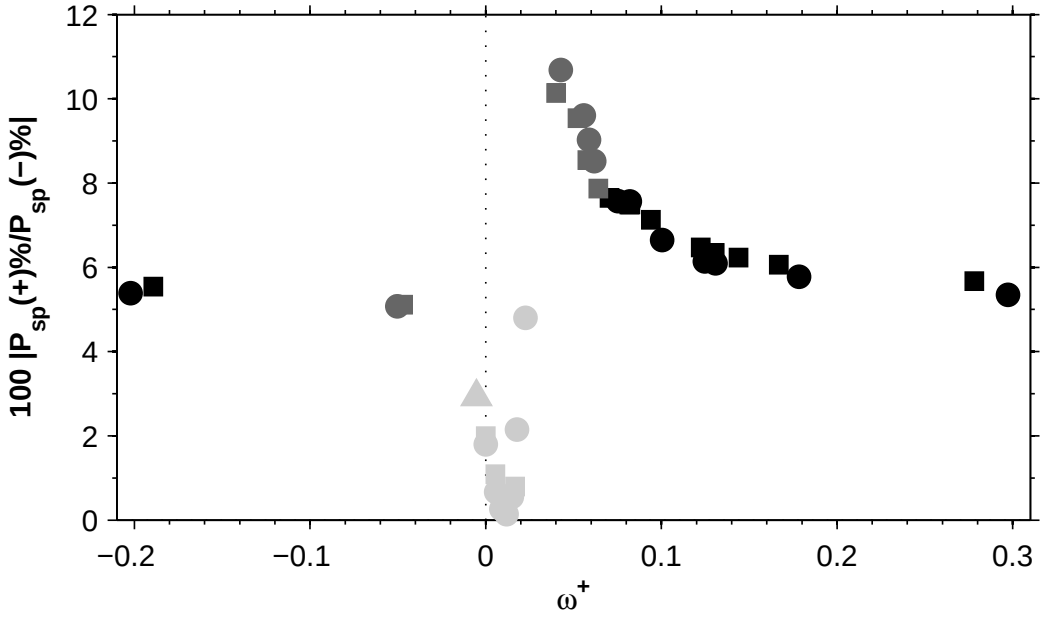

Figure 6.9: Ratio of Collaborative Power $P_{sp}(+)\%$ to Power Spent $P_{sp}(-)\%$ versus wave frequency ω^+ at $\kappa_x^+ = 0.005$ and $A^+ = 12$. ∘: MFU at $Re_p = 4760$ and $L_z^+ = 497$; □: MFU at $Re_p = 29500$ and $L_z^+ = 459$; △: MFU results at $Re_p = 73000$. Black symbols: $T^+ < 90$, Dark gray: $90 \leq T^+ \leq 160$, Light Gray $T^+ > 160$.

Figure 6.9 confirms the remarks and enriches the scenario. The coefficient $k = P_{sp}(+)/P_{sp}(-)$ is constant for $|\omega^+| > 0.1$ and equals 0.06. In this range of wave frequencies $P_{sp}(+)\%$ is constantly 6% of $P_{sp}(-)\%$. The ratio k exhibit a minimum at $\omega^+ = 0.012$, that is when maximum DR is reached, due to the corresponding peak of $P_{sp}(-)\%$. An unexpected local maximum of k is reached at $\omega^+ = 0.04$, that is at $c^+ = 8$. It is quite near the mean turbulent convective velocity $\mathcal{U}_w^+ \approx 10$, but not so near to be related to the lock-in effect for sure. Actually the DI region begins at $c^+ = 9$ and maximum DI is located at $c^+ \approx 12$. Thus, other interaction mechanisms affect $P_{sp}(+)\%$ and causes its maximum at $\omega^+ = 0.04$.

6.3 Net Power Saving

Positive net power saving can be reached at both $Re_p = 4760$ and $Re_p = 29500$, with $\kappa_x = 0.005$ and $A^+ = 12$. A positive power budget of 21.9 can be reached (case 73) at $Re_p = 4760$ with wave frequency $\omega^+ = 0.015$ and wave speed $c^+ = 3$. The overestimation of DR near its maximum due to MFU results in a slight overestimation of net power saving in the range $0 \leq \omega^+ \leq 0.012$. As a result, MFU-predicted $P_{sav}\%$ is 3.9% greather than that computed in [42]. At $Re_p = 29500$ a net saving of 8% can be attained, at $\omega^+ = 0.011$ and $c^+ = 2$: a reduction of about 13.9% is obtained.

The only point at $Re_p = 73000$ is a non-optimal backward-traveling wave with frequency $\omega^+ = -0.005$ and $c^+ = -1$. No net saving is obtained for this wave, which leads instead to a small negative power budget of $P_{sav}\% = -0.4$. The distance of this point from the optimal $\omega^+ \approx 0.001$ is small and thus, if a net saving could be achieved, it would be small, on the

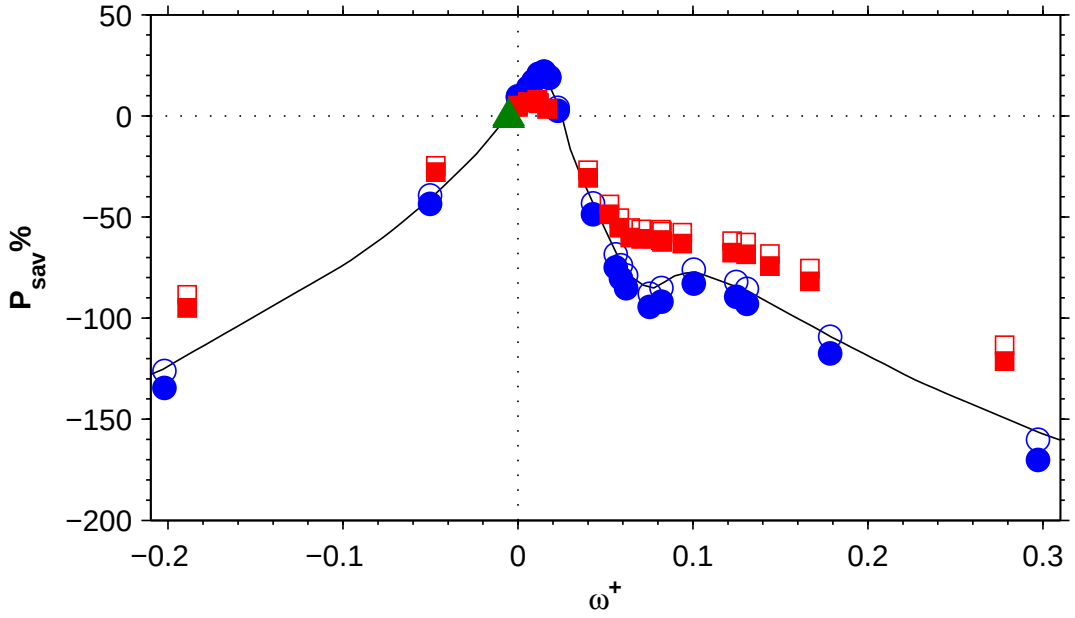

Figure 6.10: Power saved $P_{sav}\%$ versus wave frequency ω^+ at $\kappa_x^+ = 0.005$ and $A^+ = 12$. Black solid line : DNS Results at $Re_P = 4760$ from [42]; ○: MFU at $Re_p = 4760$ and $L_z^+ = 497$; □: MFU at $Re_p = 29500$ and $L_z^+ = 459$; △: MFU results at $Re_p = 73000$. Filled symbols: regenerative effect not accounted.

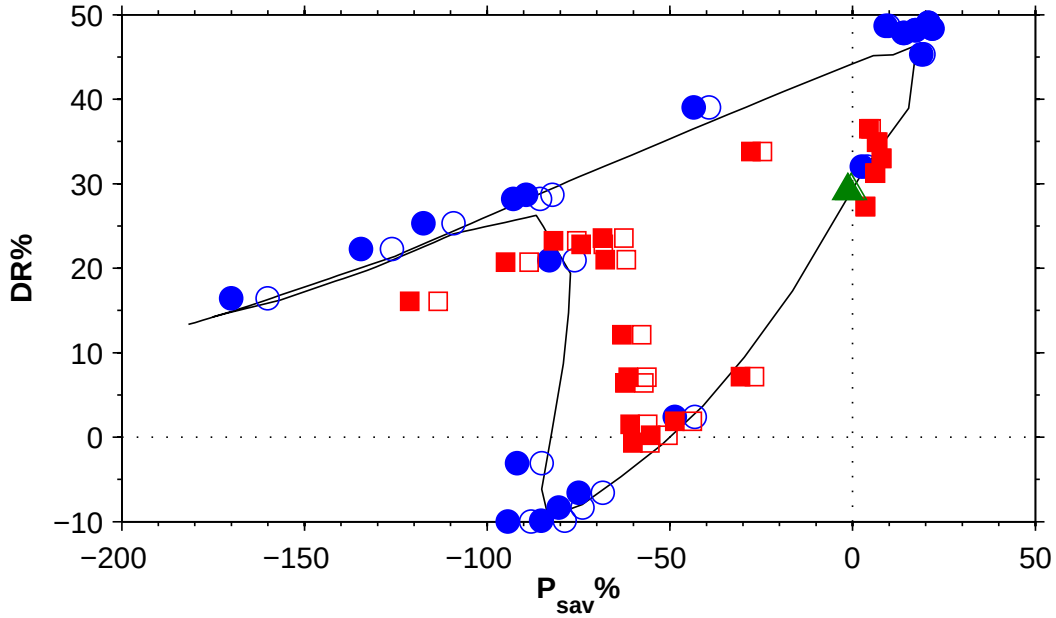

Figure 6.11: Drag Reduction $DR\%$ versus Power caved $P_{sav}\%$ at $\kappa_x^+ = 0.005$ and $A^+ = 12$. Symbols as in 6.6.

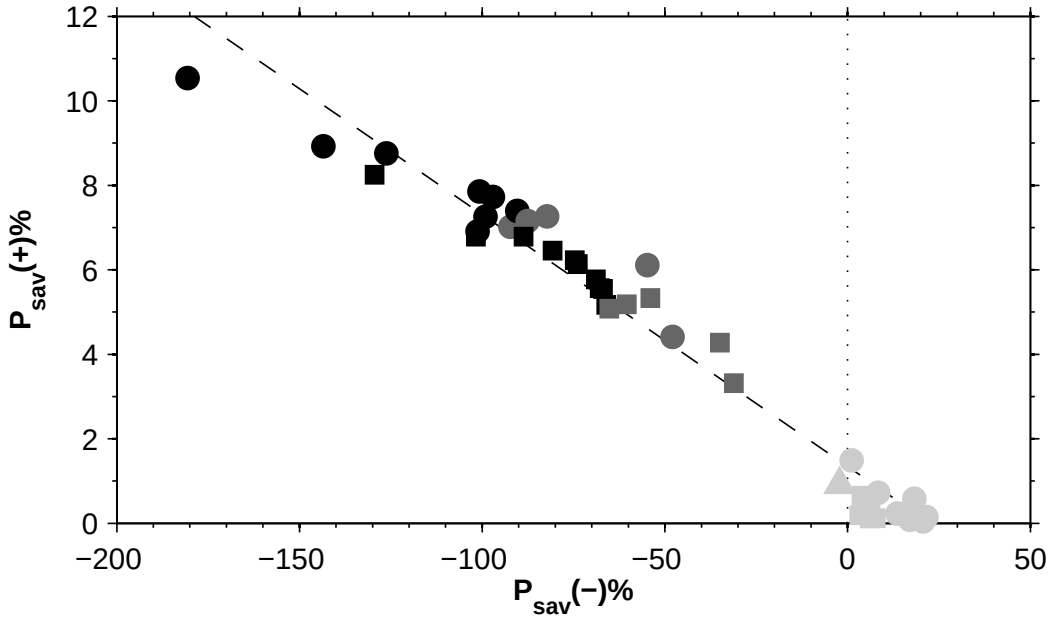

Figure 6.12: Collaborative Power $P_{sav}(+)\%$ versus Power Saved $P_{sav}(-)\%$ at $\kappa_x^+ = 0.005$ and $A^+ = 12$. Symbols as in 6.9.

order of unity.

Figure 6.10 clearly shows that a net power saving can be reached in the neighborhood of the point of maximum DR, where $P_{sp}\%$ experiences a minimum. Elsewhere the budget is considerably negative but a increasing trend with Re is confirmed. The decrease in power spent with Re is greater than that of DR away from the point of maximum DR, leading to a greater $P_{sav}\%$. However, at least at $\kappa_x = 0.005$, the reduction of maximum DR is far greater than the decrease of $P_{sp}\%$, producing a drop of maximum $P_{sav}\%$ at $Re_p = 29500$.

Figure 6.11 represents the relationship between DR and $P_{sav}\%$. The leftmost part of the curves exhibits linear correlation between $P_{sav}\%$ and DR. The slope of the linear part of the curve does not change when Re_p is varied, but it is shifted toward bigger $P_{sav}\%$. When observed at constant DR, the increase in $P_{net}\%$ due to Reynolds number appears even greater than at constant ω^+. Since the green point at $Re_p = 73000$ is backward-traveling wave, it should belong to the right end of the linear part of the $DR - P_{sav}$ curve which is not represented, due to the lack of point. Nevertheless, since the slope does not change sensibly with Re, a further increase in P_{sav}, in the linear part of the curve is obtained. In the upper-right corner of the figure, where DR reaches its maximum, the opposite trend with Re occurs: $P_{sav}\%$ decreases, because the decrease in DR exceeds that of $P_{sp}\%$.

6.3.1 Collaborative contribution

Again, positive contribution to power spent vanishes as a positive $P_{net}(-)\%$ is attained. Linearity holds between $P_{sp}(+)\%$ and $P_{sp}(-)\%$, except for few point at $|\omega^+| > 0.3$. The linear law is Reynolds independent.

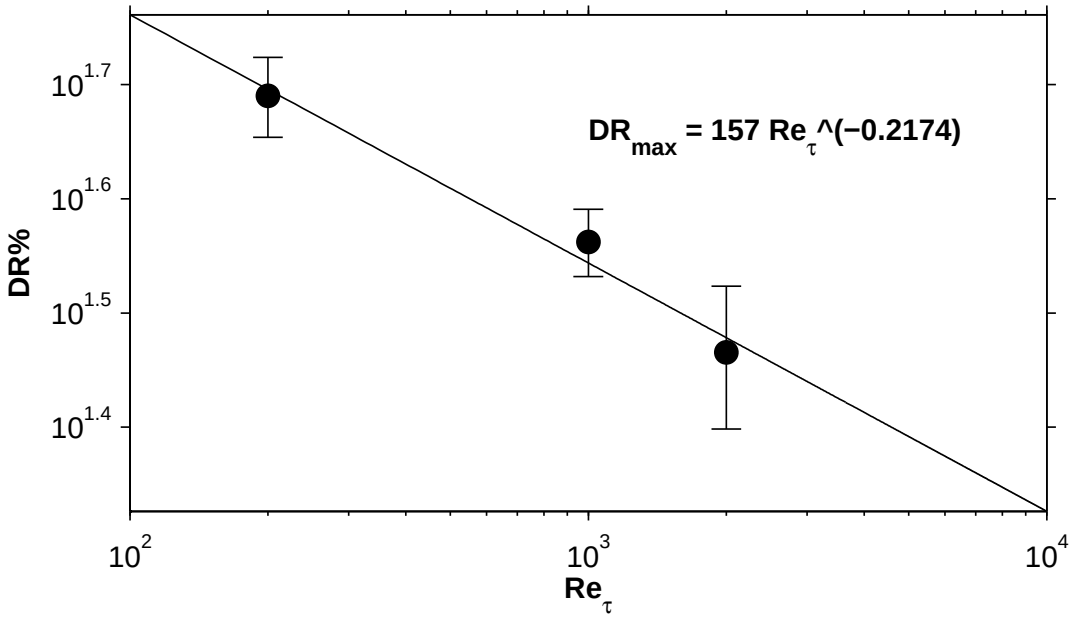

Figure 6.13: Maximum drag reduction $DR_{max}\%$ versus Re_τ for traveling waves with $\kappa_x = 0.005$ and $A^+ = 12$. ∘: MFU data; Solid line: exponential-law fit.

6.4 Reynolds effect

The trend of the maximum DR versus Reynolds number is presented in figure 6.13 for a Reynolds number up to $Re_p = 73000$, corresponding to $Re_\tau \approx 2000$. The following power lawholds between the two:

$$DR\%_{max} \sim Re_\tau^{-0.217} \tag{6.1}$$

which is surprisingly near the exponent -0.2 proposed by [6]. If this law were valid even for very high Reynolds numbers, a 10% DR is obtained for Reynolds up to $Re_\tau \approx 3 \times 10^5$.

The decay of DR turns out to be different for different wave frequencies ω^+, as shown in figure 6.14. At $\omega^+ = 0.0012$ (Black), the point of maximum DR ar $Re_p = 4760$, the dacay shows an exponent very closed to 6.1, yet slightly bigger, because the maximum DR at $Re_p = 29500$ takes place at $\omega^+ = 0$, i.e. for a steady forcing.

More interesting is the very low decrease in DR with Re_τ at $\omega^+ = -0.2$, where the following empirical law holds:

$$DR\%(\omega^+ = -0.2) \sim Re_\tau^{-0.0463} \tag{6.2}$$

with this exponent a 10% DR is obtained at $Re_\tau = 6.6 \times 10^9$.

The power sent for the control decreses with Re_τ, as also documented in [45]. The trend is confirmed by the present work but the decrease exponent is dependent on the wave parameters. As clearly represented in figure 6.15, the power spent keeps approximately constant at $\omega^+ = 0.0012$ (Black), while is proportional to $\sim Re_\tau^{-0.19}$ at $\omega^+ = -0.2$. If these trend were confirmed even at very high Re, a $P_{sav}\% > 1$ holds up to $Re_\tau = 5153.6$ at $\omega^+ = 0.0012$, while to reach a net saving at $\omega^+ = -0.2$, a $Re_\tau > 10^8$ is required.

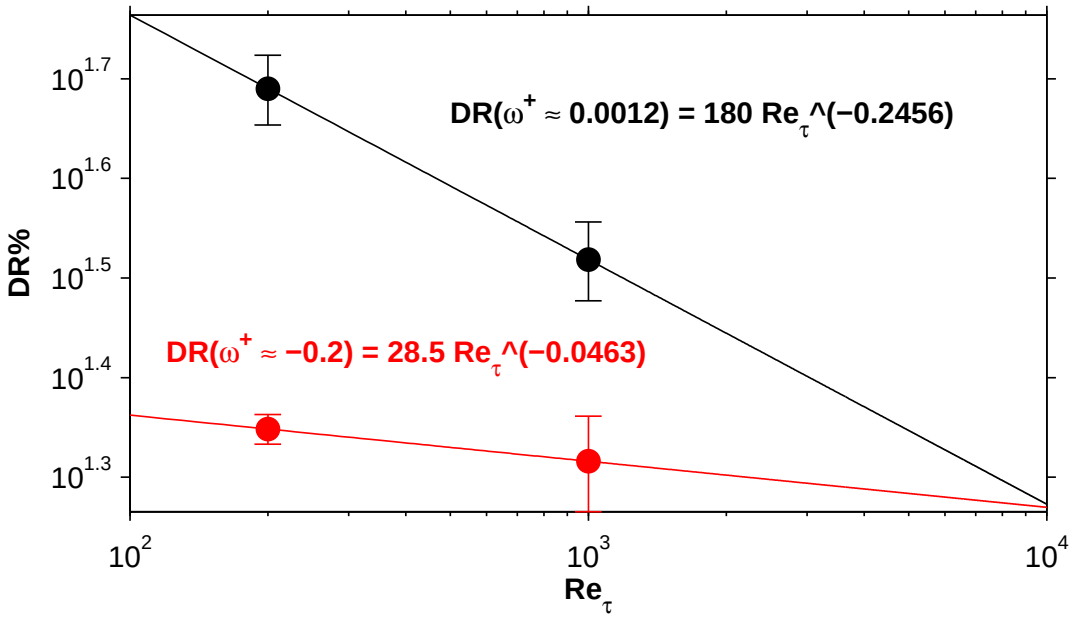

Figure 6.14: Drag Reduction $DR\%$ versus Re_τ for traveling waves with $\kappa_x = 0.005$ and $A^+ = 12$. ○: MFU data; Solid line: exponential-law fit. Red: $\omega^+ = -0.2$; Black: $\omega^+ = 0.0012$

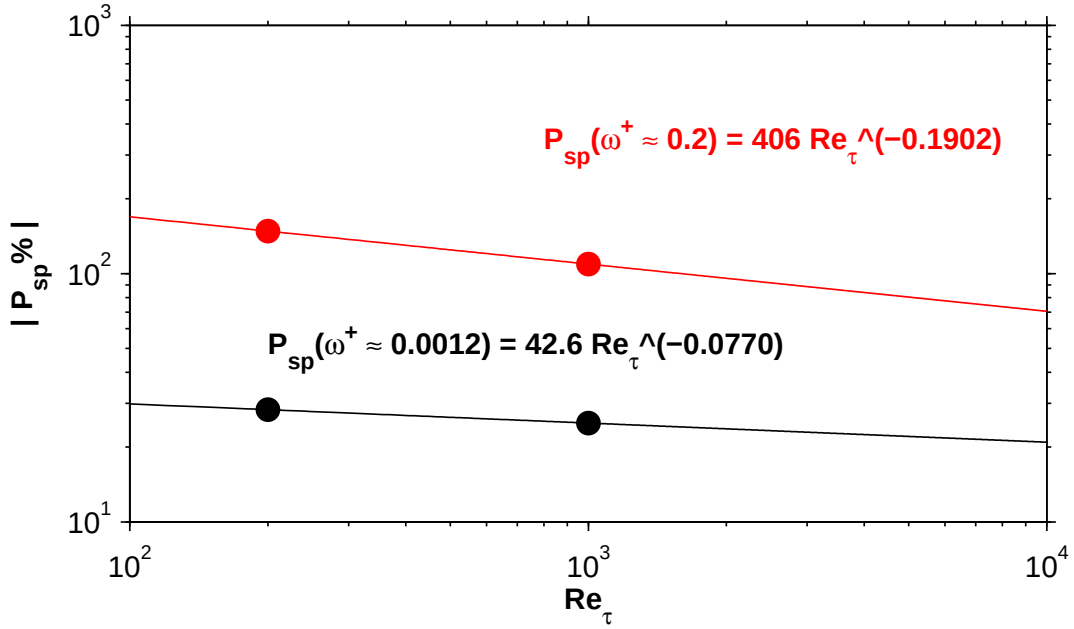

Figure 6.15: Powr spent $P_{sp}\%$ versus Re_τ for traveling waves with $\kappa_x = 0.005$ and $A^+ = 12$. Symbols as in 6.14.

Chapter 7

Conclusions and Future Work

This work has described the response of a turbulent channel flow, at values of the Reynolds number up to 73000, to sinusoidal waves of spanwise velocity applied at the wall and traveling along the streamwise direction. The effect of increasing the Reynolds number upon the drag reduction and the consequent potential net energy savings has been studied trough Direct Numerical Simulations. To increase Re while keeping the computational costs affordable, we have employed computational domains of reduced extension. Though they are much larger than the MFU, the Minimal Flow Unit that guarantees a sustained turbulence, their limited size requires special care to interpret results that are indeed slightly dependent upon the box size. A special procedure has been developed to instrument the DNS results with an error bar, that is related to the finite averaging time.

A domain size of $L_x^+ \times L_z^+ \approx 500 \times 1000$ has been proved to be appropriate and led to accurate results, showing a slight overestimation of DR, that never exceeded 4% (based on the reference wall shear), and was significant only in a limited potion of the parameter space. A precise estimation of power requirements for the control has also been obtained by our simulations. In conclusion, our small-box drag reduction estimation led to nice agreement with the most accepted literature in the field of spanwise velocity waves [40] [42] [17] [41] [43].

We succeeded in investigating Reynolds numbers up to $Re_\tau \approx 2000$, as far as we know the highest at which spanwise wall forcing has been tested. The maxima of DR achieved in this work are compared to the available results and represented as a function of Re_τ in figure 7.1. The behavior in the range $200 \leq Re_\tau \leq 2000$ is unveiled and the following dependency of maximum DR upon Reynolds is proposed:

$$DR_{max}\% \sim Re_\tau^{-0.217} \tag{7.1}$$

very similar to the one proposed by [6], who used DR data up to $Re_\tau = 400$ for the oscillating wall. If the law held even for very high Reynolds numbers, a 10% DR would be still achievable at $Re_\tau \approx 3 \times 10^5$.

Potential net power saving might be reached at very high Reynolds number trough the control with non-optimal wave parameters. At high frequencies, far away from optimal values, the power spent for the control decreases much faster than DR: the following empirical laws are proposed at $\kappa_x^+ = 0.005$:

$$DR\% \sim Re_\tau^{-0.046} \qquad P_{sp}\% \sim Re_\tau^{-0.190} \qquad (|\omega^+| = 0.2) \tag{7.2}$$

which gives the hope to reach a unit net saving $P_{net}\%$ at $Re_\tau \approx 10^8$.

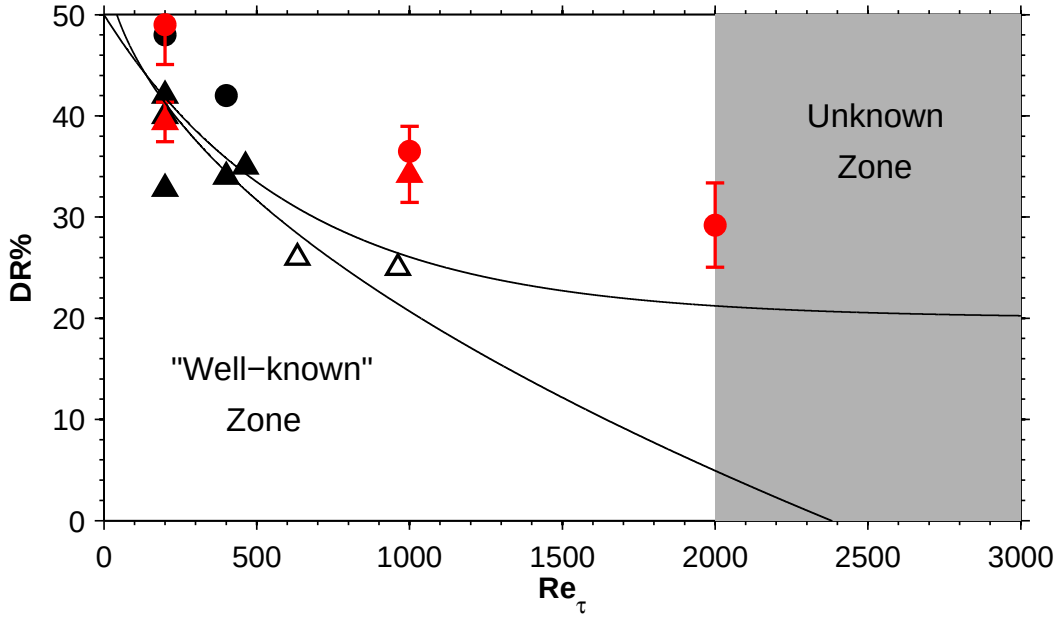

Figure 7.1: Drag Reduction as a function of the Reynolds number Re_τ for few experimental (blank symbols) or numerical (filled symbols) studies. ○: traveling waves, △: oscillating wall. Red Markers are results from the present study.

The position of the optimal point $(\kappa_x^+, \omega^+, A^+)_{opt}$ in the wave parameter space is constant, revealing the inner scaling. Nonetheless, the heterogeneous sensitivity of DR upon Re suggests its slow drift toward higher frequencies at higher Re. It is hard to draw ultimate conclusions from the small amount of wavenumbers studied in this work, but Re has proven to be less influent on DR at $\kappa_x^+ = 0.02$ than $\kappa_x = 0.005$, suggesting that a region on the plane (κ_x^+, ω^+) could exist, that is more resistant to the Reynolds effect, causing the shift in $\kappa_{x,opt}$ and giving the hope to reach significant DR even at high Re.

Finally we are not able to answer *conclusively* the question whether traveling waves can be used at high Re to reach a net power saving or not. However, thanks to our experiments that enrich the available database of new data at moderately high Reynolds numbers, we can claim that the possibillity of a positive net power budget is still standing. Two are the regions of the plane ω^+, κ_x^+ where this might happen: the former is obviously near the optimal point $(\kappa_x^+, \omega^+)_{opt}$, the latter is at high frequencies, where the value taken by κ_x becomes less significant.

The results of the present study suggest several pathways for future research. The whole ω^+, κ_x^+ plane should be investigated, in order to understand the variation in DR sensitivity upon Re. Then, higher Reynolds numbers should be simulated, to verify the pertinence of the power law between DR and Re. A further comprehension of the mechanisms at the basis of DR are necessary to improve our modeling ability and discover RANS turbulence models or LES suitable for the drag reduction estimation.

Appendix A

Error-estimation strategies

Most of flow and control statistics presented in Chapter 3 require a spatial average over walls to be computed, thus, their time history fluctuations are proportional to $(L_x \times L_z)^{-1}$. The small domain of MFU and the intermittency of $\mathrm{d} < u > /\mathrm{d}y$ (See Chap.2.3) cause high fluctuations of spatially-averaged statistics. Hence, it is fundamental to choose good error-estimate strategies, in order to obtain reliable data and quantify the statistical error.

We have put to the test two different error-estimate strategies. The first follows a more classical approach to turbulent flow statistic and requires the computation of the autocorrelation function for the random variable whose statistical error on the mean is needed. The second adopts a different approach, which can be applied to both flow and other statistics. It exploit the well-known results for white-noise to give an estimate for a generic signal statistical error. This second method is proposed and descripted in [34].

A.1 The autocorrelation function

Assumptions This method is based on the assumption that statistical data are single realizations, equally spaced in time, of a continuous stationary (ergodic) random processes. Strong stationarity specifies that all statistical moments are time-invariant. Implicit in this is also the assumption that the signals are free of initial transient.

Definitions Being $x(t)$ a continuous random ergodic signal, a mean value of $x(t)$ can be defined as:

$$\mu =< x(t) > \tag{A.1}$$

where μ does not depend on time, due to ergodicity. Equally, the autocorrelation $R(\tau)$ is:

$$R(\tau) =< x(t)x(t+\tau) > \tag{A.2}$$

where $< \bullet >$ is the expected value. The autocorrelation is a measure of how distinct realization of x, distant τ in time, are correlated each other. Due to the ergodicity hypothesis, R depends only on the separation τ and not on time t.

Population mean value μ and autocorrelation R are unobservable, since a infinite sample length is required to compute them exactly. Thus, they are replaced by their best estimate: the sample mean $\overline{x}$ and the sample autocorrelation $\overline{R}$. They can be computed as:

$$\overline{x} = \frac{1}{T}\int_0^T x(t)\mathrm{d}t \qquad \overline{R}(\tau) = \frac{1}{T}\int_0^T x(t)x(t+\tau)\mathrm{d}t \tag{A.3}$$

where T is the length of the sample. Both $\overline{x}$ and $\overline{R}$ are random variables on their own.

Given an autocorrelation R, an autocorrelation function $\rho(\tau)$ can be defined as:

$$\rho(\tau) = \frac{R}{\sigma_x^2} \tag{A.4}$$

where σ_x^2 is the variance of the signal x. Once again, this unobservable statistic will be substituted by its best estimate the sample variance s^2.

We define $\sigma_{\overline{x}}$ as the standard deviation of the random variable 'sample mean' $\overline{x}$. This is the statistical quantity to be found in order to quantify the random error on the estimate of μ.

Formulation of the method Each sample x_j belong to the same realization of the signal $x(t)$. Thus, two different sample x_i and x_j are not statistically independent. This means that their cross-covariance $< x_i, x_j > \neq 0$.

It can be easily seen that the standard deviation of the sample mean can be related to the autocorrelation function $\rho(\tau)$. Actually,

$$\sigma_{\overline{x}}^2 = \left\langle (\overline{x} - \mu)^2 \right\rangle \tag{A.5}$$

Substituting the definition of sample mean $\overline{x}$, one obtains:

$$\sigma_{\overline{x}}^2 = \left\langle \left(\frac{1}{T} \int_0^T x(t) \mathrm{d}t \, - \mu \right)^2 \right\rangle \tag{A.6}$$

Defining as $x^{'}(t)$ the signal subtracted the mean, Eq.A.6 becomes:

$$\sigma_{\overline{x}}^2 = \left\langle \left(\frac{1}{T} \int_0^T x^{'}(t) \mathrm{d}t \right)^2 \right\rangle \tag{A.7}$$

The autocorrelation R can be shown by splitting the square of the integral above, leading to:

$$\sigma_{\overline{x}}^2 = \frac{1}{T^2} \int_0^T \int_0^T \left\langle x^{'}(t) x^{'}(s) \right\rangle \mathrm{d}t \mathrm{d}s \tag{A.8}$$

where in $\left\langle x^{'}(t) x^{'}(s) \right\rangle$ we recognise the $R(s-t)$. If we call $\tau = s - t$, and with the definition of autocorrelation function, Eq.A.8 turns into:

$$\sigma_{\overline{x}}^2 = \frac{\sigma^2}{T^2} \int_0^T \int_{-t}^{T-t} \rho(\tau) \mathrm{d}\tau \mathrm{d}t \tag{A.9}$$

By integrating in τ, we finally obtain the desired variance of the mean, dependent on ρ:

$$\sigma_{\overline{x}}^2 = \frac{2\sigma^2}{T} \int_0^T \rho(\tau) \left(1 - \frac{|\tau|}{T} \right) \mathrm{d}t \tag{A.10}$$

If $T >> \tau_{max}$, hence the sample length is bigger than the maximum time separation we want to describe in the autocorrelation, Eq. A.10 reduces to:

$$\sigma_{\overline{x}}^2 = \frac{2\sigma^2}{T} \mathcal{T} \tag{A.11}$$

where $\mathcal{T} = \int_0^T \rho(\tau)\mathrm{d}\tau$.

The central limit theorem, which states that $\overline{x}$ has a Gaussian probability density function, allow us to find a confidence interval for μ:

$$\overline{x} - \gamma\sigma_{\overline{x}} \leq \mu \leq \overline{x} - \gamma\sigma_{\overline{x}} \tag{A.12}$$

where $\gamma = z_{\alpha/2}$ is the standardized confidence interval of a normalized Gaussian PDF and depends on the desired confidence level.

A.2 The equivalent white noise

Assumptions Also this method requires the signal to be ergodic, thus, statistically stationary and free from initial transient.

Definitions The random error $\sigma_{\overline{x}}$ on the estimate $\overline{x}$ of the mean value μ of a random variable $x(t)$ is defined as:

$$\sigma_{\overline{x}} = \sqrt{<\overline{x}^2> - <\mu>^2} \tag{A.13}$$

where $<\bullet>$ is the expected value operator. It is convenient to define the normalized random error ε as:

$$\varepsilon = \frac{\sigma_{\overline{x}}}{\mu} \tag{A.14}$$

Both A.13 and A.14 contain μ, which is unobservable in practice, since an infinite sample length would be needed to compute it precisely. Thus, μ have to be replaced by its best estimate $\overline{x}_T$, obtained with a sample of length T.

Hence, due to the dependence on $\overline{x}_T$, normalized random error ε becomes a function of T.

Formulation of the method This method implies three main steps:

1. An estimation of the dependency of random error ε on sample length T is computed
2. This estimation is used to find the worst-case random error through a comparison with analytical results of bandwidth-limited Gaussian white-noise
3. Central limit theorem is used to recover a confidence interval at a certain confidence level

This steps are now discussed in detail.

Step 1 The signal $x(t)$, observed for a length T, is divided into a series of N_w windows of length T_w. For $T_w \ll T$ the random statistical error can be estimated by:

$$\varepsilon(T_w) \approx \frac{\sqrt{\left\langle \left(\overline{x}_{T_w} - \overline{x}_T\right)^2 \right\rangle_{N_w}}}{\overline{x}_T} \tag{A.15}$$

where $<>_{N_w}$ stands for the averaging over all the available windows. By varying the window size, the error trend as a function of sample length can be estimated. The estimate becomes decreasingly accurate as T_w tends to T, since the number of available windows decrease. Thus, unless long time-resolved benchmark signals are available (e.g. from comparable experiments), the usefulness of this method alone is therefore limited.

Step 2 A further component is introduced, which enables both an error estimate for the available sample length as well as a prognosis of the error development for still longer samples. Analytical expressions for the error of various statistical quantities as a function of sample length can be derived for the special case of bandwidth-limited Gaussian white noise (of bandwidth B). By integrating the corresponding autocovariance function, the following formulae for the error on the mean of a bandwidth-limited Gaussian white noise is:

$$\varepsilon(T) \approx \frac{1}{\sqrt{2BT}} \left(\frac{\sigma_x}{\mu_x} \right) \tag{A.16}$$

where σ_x and μ_x are the standard deviation and mean of the random signal $x(t)$. By again replacing the unobservable quantities μ_x and σ_x with the best available estimates, $\overline{x}$ and s, the parameter B becomes the only unknown in A.16. B is treated as a curve-fitting parameter: the smallest B is chosen so that the curve A.16 intersect the curve of relation A.15. In this way, the curve-fit is as conservative as possible, since the lowest B means the highest ε. Assuming that the error behaviour for long sample lengths can be approximated by that of white noise is equivalent to assuming that the autospectral density function, $\Phi_{xx}(\omega)$ is flat in the bandwidth B, especially at lowest (and most poorly resolved) frequencies. In this sense, the approximation of the random error with that of the white noise is a conservative choice and lead always to its overestimation.

Step 3 The central limit theorem ensures that the probability density function (PDF) of $\overline{x}_{T_w}$, as $N_w \gg 1$, tends to be a Gaussian, disregarding the PDF of $x(t)$. This means that the quantified error can be used to establish confidence intervals for the unknown true values of the statistical quantities, namely:

$$\frac{\overline{x}_T}{1+\gamma\varepsilon} \leq \mu \leq \frac{\overline{x}_T}{1+\gamma\varepsilon} \tag{A.17}$$

where $\gamma = z_{\alpha/2}$ is the standardized confidence interval of a normalized Gaussian PDF and depends on the desired confidence level.

In this manner, estimates of the random statistical error magnitude and the probability distributions of statistical quantities from unsteady simulations can be obtained, with the simulated time series as the sole input.

A.3 Uncertainty on Drag Reduction

These two procedures have been used to obtain the standard deviation σ of the wall shear $< \mathrm{d}u/\mathrm{d}y >$ in case of uncontrolled and controlled flows. Then, uncertainty on Drag Reduction is computed with the RSS with the following procedure.

Starting from the expression of Drag Reduction, already given in Chapter 3, i.e.

$$DR\% = 100 \frac{C_{f,0} - C_f}{C_{f,0}} \tag{A.18}$$

where $C_f = 2\tau_w/(\rho U_b^2)$, depends only on τ_w since U_b is constant for constant-Q simulations. The definition A.18 can be conveniently rewritten expliciting the wall shear $< \mathrm{d}u/\mathrm{d}y >$, which comes out from $\tau_w = \rho\nu < \mathrm{d}u/\mathrm{d}y >$, obtaining:

$$DR\% = 100 \left(1 - \frac{< \mathrm{d}u/\mathrm{d}y >}{< \mathrm{d}u/\mathrm{d}y > |_0} \right) \tag{A.19}$$

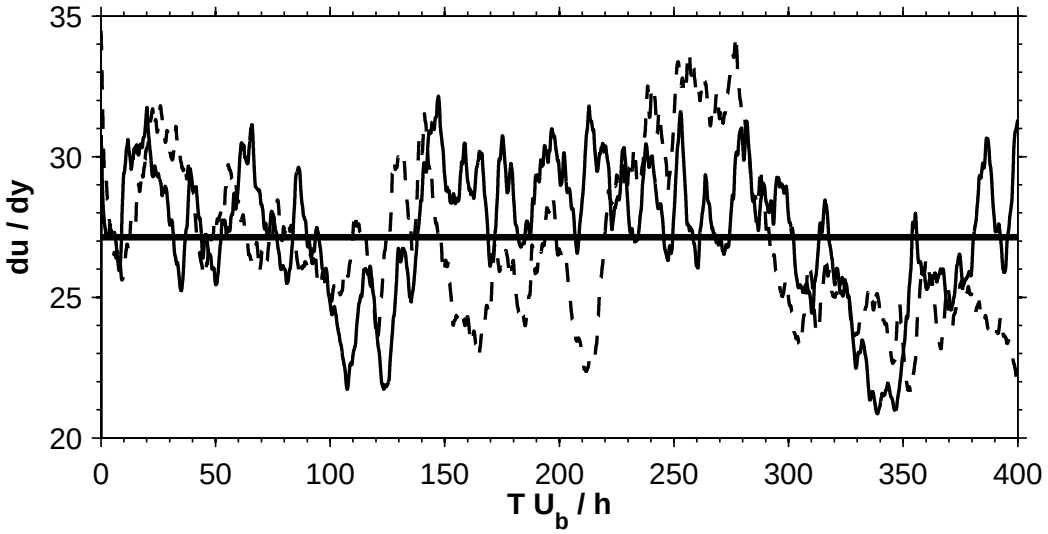

Figure A.1: Time history of wall shear, case 55 at $Re_p = 29500$. Thin solid line: Top wall; dashed line: bottom wall; thick line: time-averaged wall shear.

where $< \mathrm{d}u/\mathrm{d}y > |_0$ is the wall shear of the reference uncontrolled case. We call it Ω, for simplicity, in this paragraph.

Thus, $DR\%$ is a function of values taken by Ω_0 and Ω. Deriving A.19 by both its independent variables leads to:

$$\frac{\partial DR\%}{\partial \Omega_0} = 100\frac{\Omega}{\Omega_0^2} \qquad \frac{\partial DR\%}{\partial \Omega} = -100\frac{1}{\Omega_0} \tag{A.20}$$

These are the sensitivities of the statistical error on $DR\%$ to errors on both the reference (left) and controlled (right) wall shear. The standard deviation of the DR can be now written as:

$$\sigma_{DR\%} = 100\sqrt{\left(\frac{\Omega}{\Omega_0^2}\right)^2 \sigma_{\Omega_0}^2 + \left(\frac{1}{\Omega_0}\right)^2 \sigma_{\Omega}^2} \tag{A.21}$$

The central limit theorem allows to estimate a confidence interval for DR, once a confidence level has been chosen. The expected value of $DR\%$ lies in the interval:

$$DR\% - \gamma\sigma_{DR} \leq < DR\% > \leq DR\% + \gamma\sigma_{DR} \tag{A.22}$$

A.4 Comparison

In table A.1, confidence interval for $DR\%$ is computed with both methods mentioned above for several simulations at $Re_p = 4760$, $Re_p = 29500$ and $Re_p = 73000$, where a DR has been achieved through travelling waves. As regards the forcing, $\kappa_x^+ = 0.005$ and $A^+ = 12$, while ω^+ is changes. Uncertainties predicted by the two methods are very similar. Slightly bigger values are obtained for high Drag Reduction with the white-noise comparison method. Both methods loose partially their reliability at high DR, where the $\mathrm{d}u/\mathrm{y}$ exhibits very high fluctuations. Figure A.1 refers to the case 55 at $Re_p = 29500$. Sharp and high peaks of

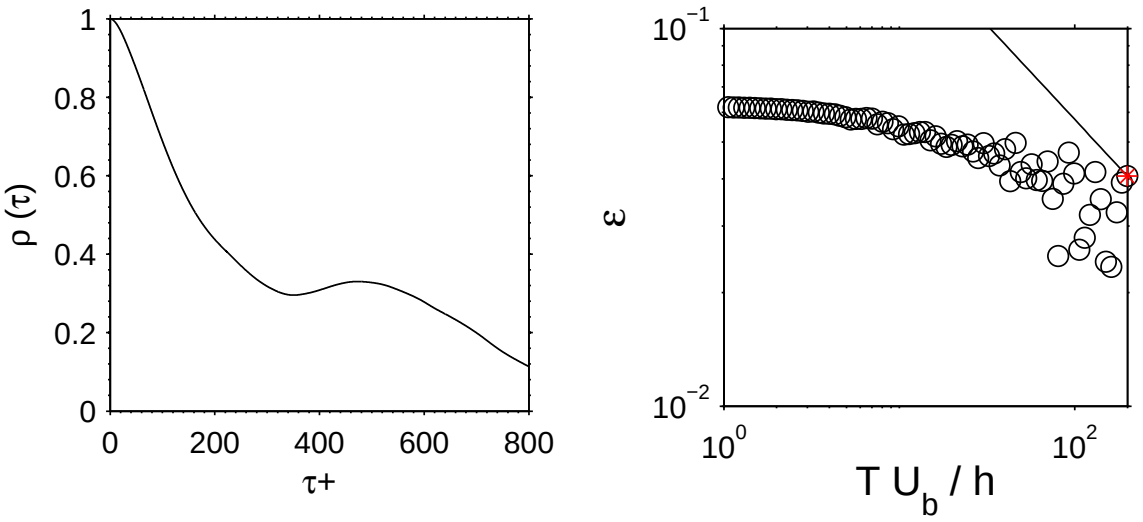

Figure A.2: On the left: autocorrelation function for the case 55 at $Re_p = 29500$ (left), a lack of decay to zero is visible. On the right: the normalized random error ε as function of T_w, spurious oscillations affect the result.

wall shear are visible, as well as a long period fluctuation of the order $tU/h \approx 200$. These fluctuations would require a very long and prohibitive sample time to be adequately resolved and influence negatively both the autocorrelation and the normalized random error $\varepsilon(T_w)$.

Figure A.2a shows the autocorrelation function for the same case as before. While for small separations τ it shows a deterministic behaviour, when separation increases chaotic fluctuations cause the lack of a clear decay to zero. It is then difficult to define the integral time $\mathcal{T}$, which is in this case defined as the point where $\rho(\tau)$ takes its minimum value.

Figure A.2b represents the normalized error on the wall shear ε as a function of the sample size T_w. Straight line represent the fitted law for a comparable bandwidth-limited white noise. Even here, stochastic fluctuations of ε are present for large T_w, due to the reduced number of sample windows.

Both methods reduce their precision when the need of a good estimate of $\Delta DR\%$ would be necessary: near the maximum of Drag Reduction. Nevertheless the white-noise method seems to overestimate the error, due to very high fluctuations of ε. Thus, we preferred the autocorrelation method, which, among all, does not need the introduction of fitting coefficients and other unusual elements.

Therefore, we should observe that in both methods the estimated error is proportional to $T^{-1/2}$, thus doubling the sample time will, at least, reduce the error of a factor $\sqrt{2}/2$. The reduction in random error will be actually bigger, because the stochastic effect of fluctuations reduces with sample size.

Case	ω^+	$DR\%$	ΔDR_A	ΔDR_{WN}	Case	ω^+	$DR\%$	ΔDR_A	ΔDR_{WN}
		$Re_p = 4760$					$Re_p = 29500$		
58	-0.20	22	0.76	0.76	45	-0.19	20.71	2.28	2.42
59	-0.05	39	0.80	0.80	46	-0.05	33.80	1.78	1.61
60	0.00	49	1.63	1.62	47	0.00	36.51	2.48	2.88
61	0.01	48	1.86	2.31	48	0.01	34.92	2.53	2.12
62	0.01	49	3.94	5.10	49	0.01	33.01	3.01	3.58
63	0.02	45	4.28	3.93	50	0.02	27.31	2.95	2.98
64	0.04	2	0.78	0.73	51	0.04	7.18	3.06	2.94
65	0.06	-7	0.81	0.82	52	0.05	1.88	2.79	3.10
66	0.06	-10	0.81	0.80	53	0.06	0.22	2.71	2.77
67	0.08	-10	0.97	0.97	54	0.07	1.54	2.59	2.70
68	0.08	-3	0.97	0.85	55	0.08	6.42	4.73	5.55
69	0.10	21	1.00	0.92	56	0.09	12.12	4.33	4.11
70	0.13	28	0.80	0.82	57	0.12	21.00	2.45	2.68
71	0.18	25	0.82	0.78	58	0.17	23.24	2.45	2.49
72	0.30	16	0.84	0.85	59	0.28	16.09	2.29	3.14
73	0.01	48	3.78	4.33	61	0.01	31.26	2.67	2.93
74	0.01	48	2.76	3.54	62	0.08	7.10	3.02	3.51
75	0.02	32	1.90	1.89	63	0.13	23.57	2.85	3.16
76	0.06	-8	0.80	0.81	64	0.06	-0.68	2.60	2.41
77	0.12	29	0.80	0.80	65	0.14	22.81	2.64	2.64
		$Re_p = 73000$							
01	0.01	29	4.17	4.41					

Table A.1: Confidence interval, at 95% confidence level, for Drag Reduction. ΔDR_A is computed with autocorrelation method, while ΔDR_{WN} with equivalent white noise. Simulation for travelling waves with $A^+ = 12$ and $\kappa^+ = 0.005$

Appendix B

Further Results

Further results, equally interesting but not strictly related to the effect of Re on DR, the main topic of the present work, are presented in this appendix.

In the first two sections we present a brief search of the scaling parameters of both confidence interval on $DR\%$ and the initial transient length.

In the third section the spectrum of the mean wall-shear stress is computed and the effect of the control on it studied, confirming the prediction of [17] in the oscillating wall case.

In the fourth section two punctual wall-shear correlations and spectra are computed for the sole case of traveling waves, owing to computational cost. An interesting modulation of the punctual wall-shear is found and discussed.

B.1 Uncertainty scaling

Uncertainty on drag reduction, $\Delta DR\%$ is an essential parameter to consider when DR results come from MFU simulations. It is interesting to study the main parameters that affects uncertainty on DR, when the domain area S^+, expressed in wall units, is kept constant. The dependency of uncertainty on DR with domain size has been already discussed in section 4.2.2.

Particular care should be taken, trying to find a scaling parameter for $\Delta DR\%$, since, as discussed in chapter A.3, it is obtained with error propagation techniques from uncertainty on Ω_0 and Ω, that is on the mean wall shear of reference and controlled case respectively.

Due to its compound nature, $\Delta DR\%$ depends both on the reference case and controlled case uncertainties and thus it scales both with forcing parameters, namely T^+ and A^+, and with reference parameters, such as Re_p.

In following figures, both methods for computing uncertainty, described in A.3, are compared. Both lead to similar results but the equivalent white-noise method exhibits a bigger scattering in uncertainty esteem.

B.1.1 Oscillating wall

Uncertainty vs DR and T^+

Uncertainty on DR is related to the value of DR itself, and generally increases as maximum DR is approached (figure B.1). Nevertheless, a uncertainty growth can be observed even for very low values of DR and great scattering of uncertainty values near maximum DR is

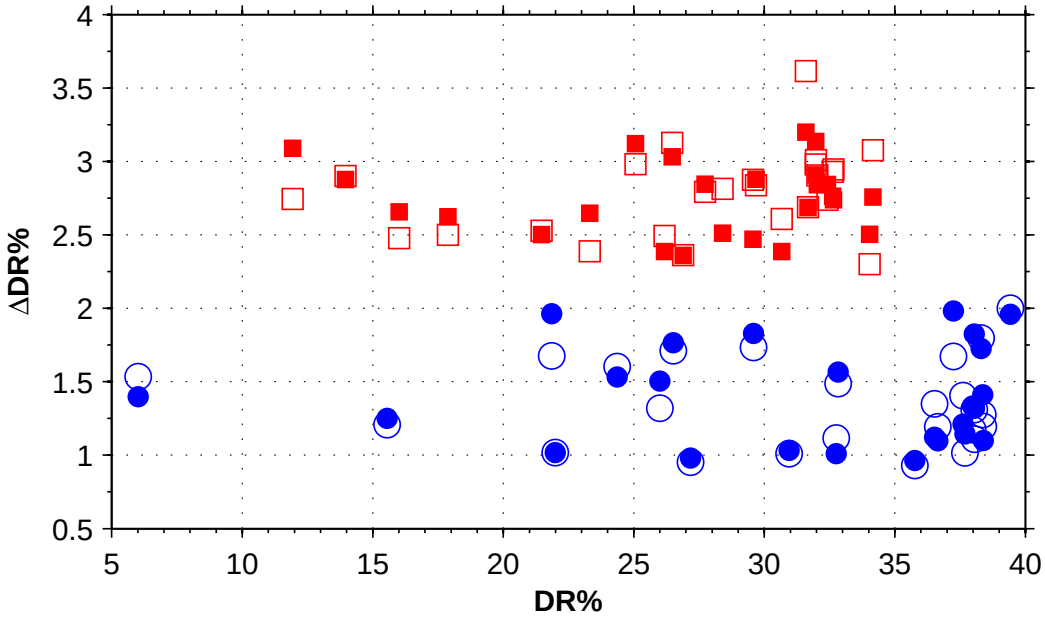

Figure B.1: Drag Reduction Uncertainty $\Delta DR\%$ versus Drag Reduction $DR\%$. ○: MFU at $Re_p = 4760$ and $L_z^+ = 497$; □: MFU at $Re_p = 29500$ and $L_z^+ = 459$. Filled symbols: Autocorrelation method; Blank symbols: Equivalent White Noise method.

observed. Values near the minimal uncertainty are present even at high DR. A lower bound for $\Delta DR\%$, which reaches a minimum at $DR\% \approx 22$, can be seen for both $Re_p = 4760$ and $Re_p = 29500$. Here, also abruptly higher value of $\Delta DR\%$ can be seen.

Comparing uncertainty with T^+ reveals, figure B.2, a clear minimum of uncertainty on DR at $T^+ \approx 50$. Uncertainty both grows for ascending or descending T^+ with respect of the local minimum We can now state that maximum uncertainty is not reached when $T^+ = T^+_{opt}$.

Uncertainty vs Power

The monotonically ascending relationship between $P_{sp}\%$ and T^+ result in a trend between $\Delta DR\%$ and $P_{sp}\%$ as the one of figure B.3. Minimum of uncertainty is reached, right before a sudden increase, at low values of $P_{sp}\%$. Uncertainty grows with a softer slope as $P_{sp}\%$ increases.

Same consideration can be done comparing uncertainty to power saved $P_{sav}\%$, as shown in figure B.4

Uncertainty vs Stokes Layer thickness

Stokes layer thickness is defined as $delta_l = \sqrt{T^+/\pi}$. Thus, Uncertainty is expected to behave similarly against T^+ and δ_l^+ (figure B.5). A local minimum can be observed at $\delta_l^+ \approx 4$ and slightly higher values of uncertainty correspond to $\delta_l^+ \approx \delta^+_{l,opt}$. Again, uncertainty increases for both thicker or thinner Stokes layers.

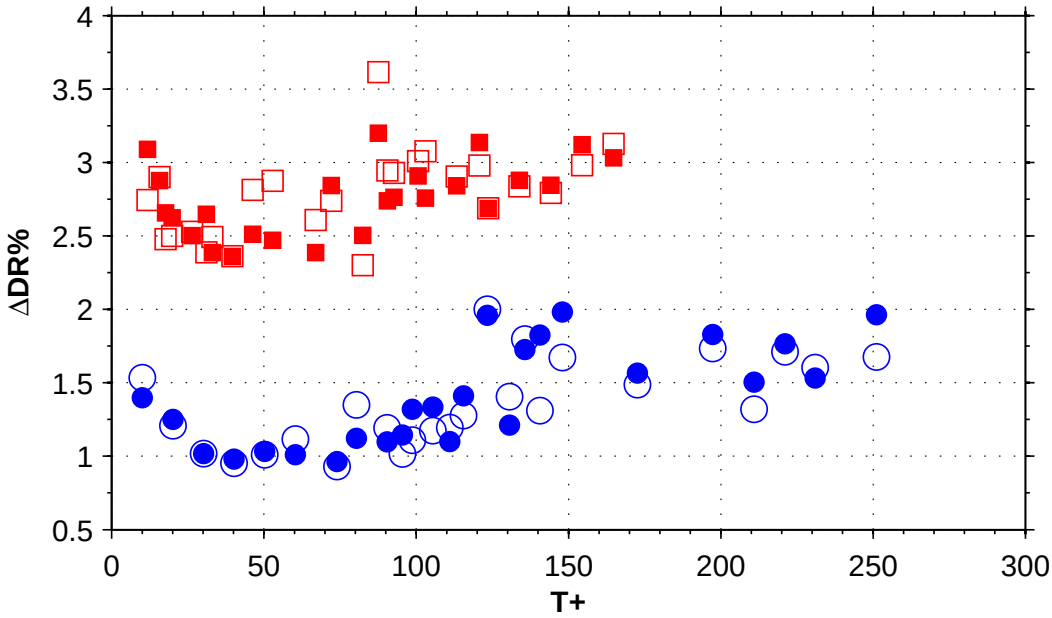

Figure B.2: Drag Reduction Uncertainty $\Delta DR\%$ versus Period of wall oscillation T^+. ○: MFU at $Re_p = 4760$ and $L_z^+ = 497$; □: MFU at $Re_p = 29500$ and $L_z^+ = 459$. Filled symbols: Autocorrelation method; Blank symbols: Equivalent White Noise method.

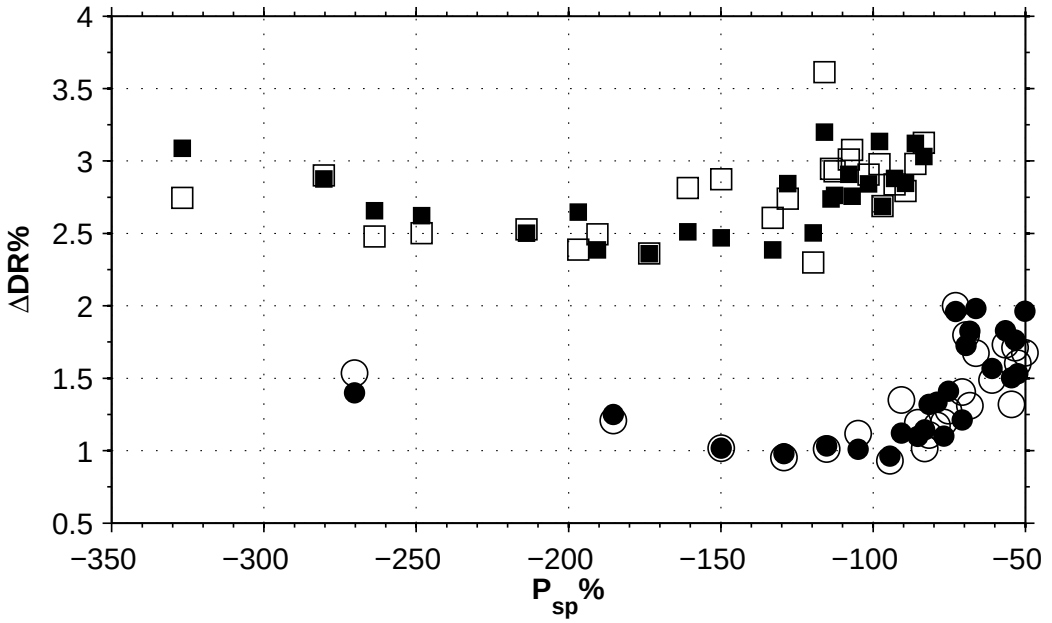

Figure B.3: Drag Reduction Uncertainty $\Delta DR\%$ versus Power Spent $P_{sp}\%$. ○: MFU at $Re_p = 4760$ and $L_z^+ = 497$; □: MFU at $Re_p = 29500$ and $L_z^+ = 459$. Filled symbols: Autocorrelation method; Blank symbols: Equivalent White Noise method.

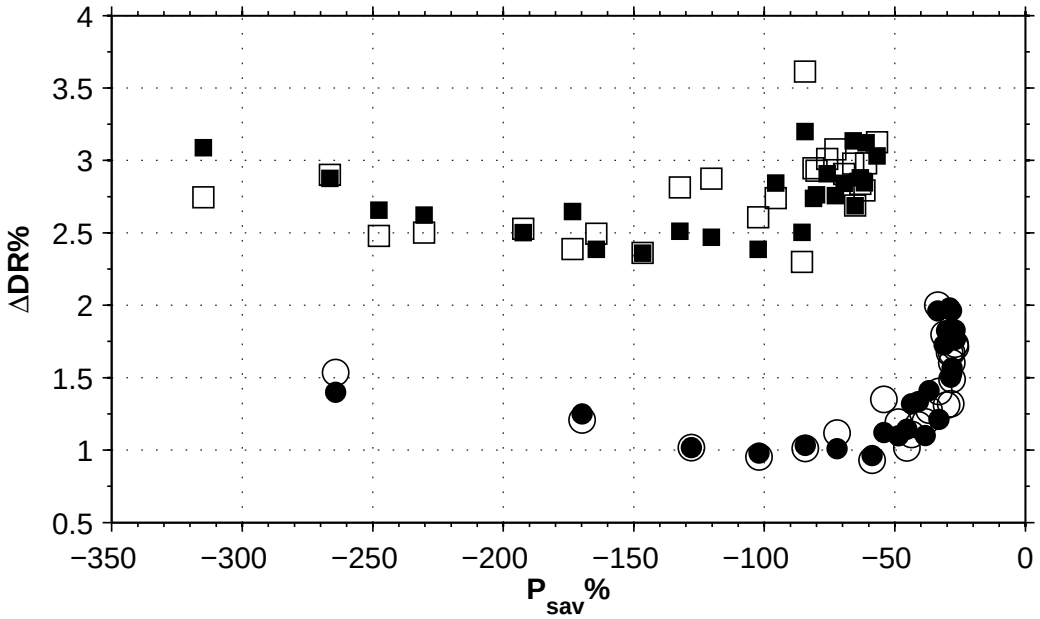

Figure B.4: Drag Reduction Uncertainty $\Delta DR\%$ versus Power Saved $P_{sav}\%$. ○: MFU at $Re_p = 4760$ and $L_z^+ = 497$; □: MFU at $Re_p = 29500$ and $L_z^+ = 459$. Filled symbols: Autocorrelation method; Blank symbols: Equivalent White Noise method.

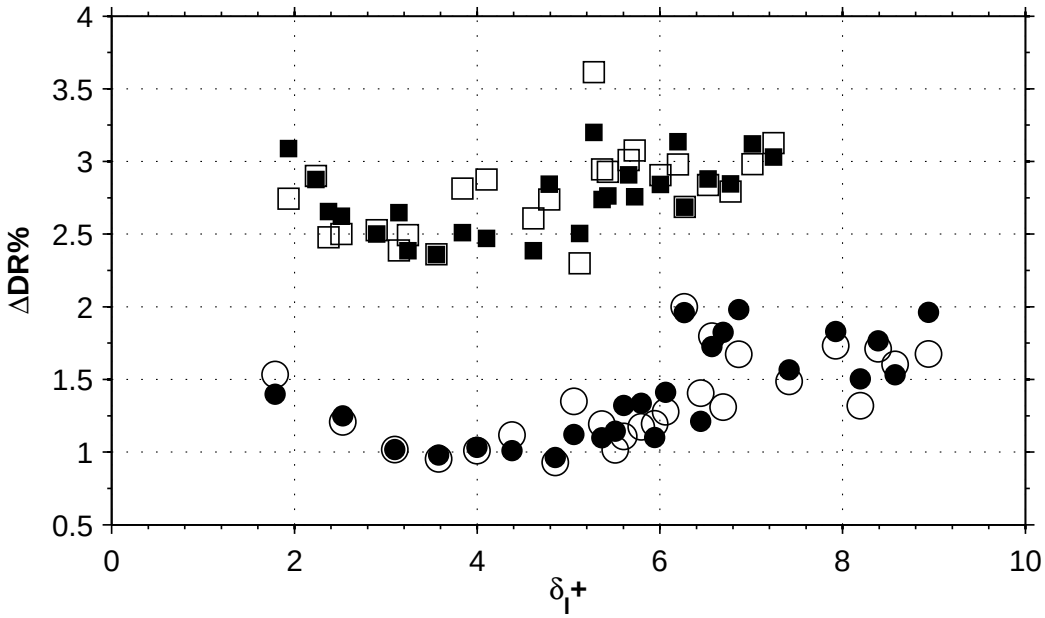

Figure B.5: Drag Reduction Uncertainty $\Delta DR\%$ versus Stokes Layer Thickness δ_l^+. ○: MFU at $Re_p = 4760$ and $L_z^+ = 497$; □: MFU at $Re_p = 29500$ and $L_z^+ = 459$. Filled symbols: Autocorrelation method; Blank symbols: Equivalent White Noise method.

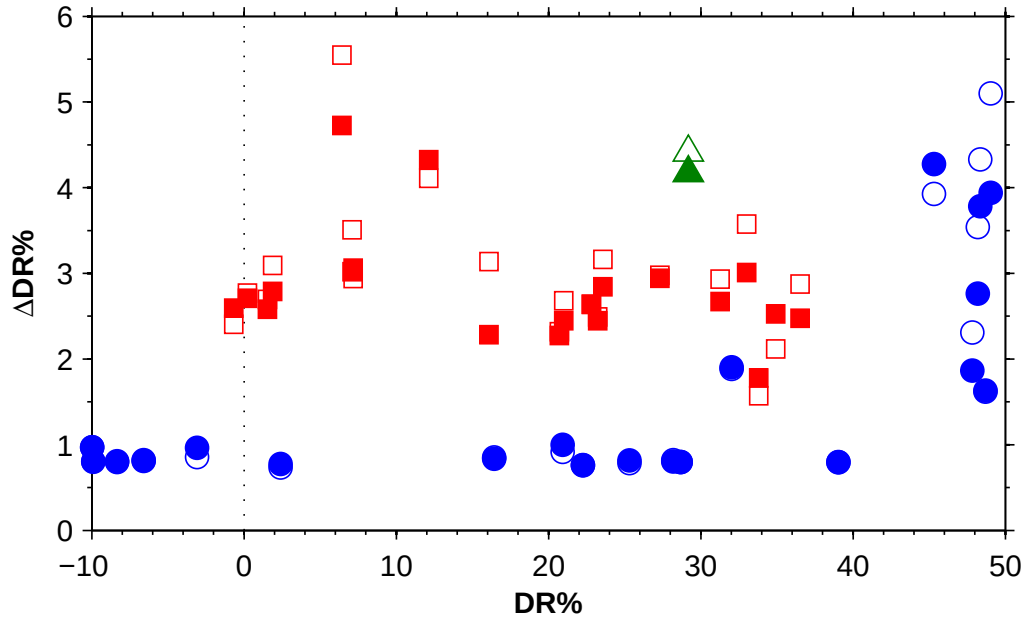

Figure B.6: Drag Reduction Uncertainty $\Delta DR\%$ versus Drag Reduction $DR\%$ at $\kappa_x^+ = 0.005$ and $A^+ = 12$. ◯: MFU at $Re_p = 4760$; □: MFU at $Re_p = 29500$; △. Filled symbols: Autocorrelation method; Blank symbols: Equivalent White Noise method.

B.1.2 Traveling waves

Uncertainty vs DR and ω^+

Differently from oscillating wall, the uncertainty on DR $\Delta DR\%$ appears to be more scattered and less sensitive to wave parameters. In figure B.6 uncertainty on DR is compared to DR itself. At $Re_p = 4760$ maximum uncertainty is reached together with the highest DR, while $\Delta DR\%$ remains quite constant and equals 1% in the whole DR range. At $Re_p = 29500$ the highest uncertainty is located at lower DR than before. Figure B.7 place the maximum $\Delta DR\%$ at $\omega^+ \approx 0.9$, that is where DR increase again after the lock-in DI region. Even at $Re_p = 29500$, the uncertainty keeps constant elsewhere and approximately 2,75%. No trend can be inferred from the only one point at $Re_p = 73000$, from which we can only notice the further increase of $\Delta DR\%$ to the value of ≈ 4.

Both peaks of uncertainty at $Re_p = 4760$ and $Re_p = 29500$ reach a maximum $\Delta DR \approx 4.5$, meaning that the uncertainty jump is bigger at low Reynolds and reduces as Re increases.

Uncertainty vs Power

Comparing DR uncertainty to Power spent or saved does not offer further information on its scaling, thus only the relationsip with the former is presented in figure B.8. At low values of $P_{sp}\%$, where DR is high, uncertainty reaches its highest values. The behavior is not confirmed at $Re_p = 29500$, where uncertainty maximum is reached for lower values of $P_{sp}\%$.

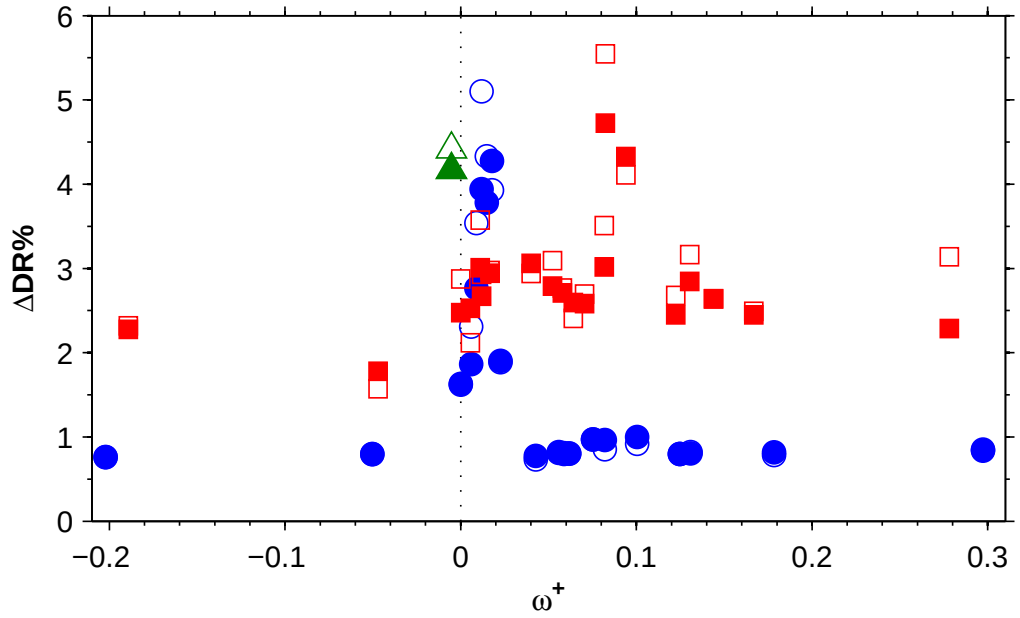

Figure B.7: Drag Reduction Uncertainty $\Delta DR\%$ versus wave frequency ω^+ at $\kappa_x^+ = 0.005$ and $A^+ = 12$. ◯: MFU at $Re_p = 4760$; □: MFU at $Re_p = 29500$; △: MFU results at $Re_p = 73000$. Filled symbols: Autocorrelation method; Blank symbols: Equivalent White Noise method.

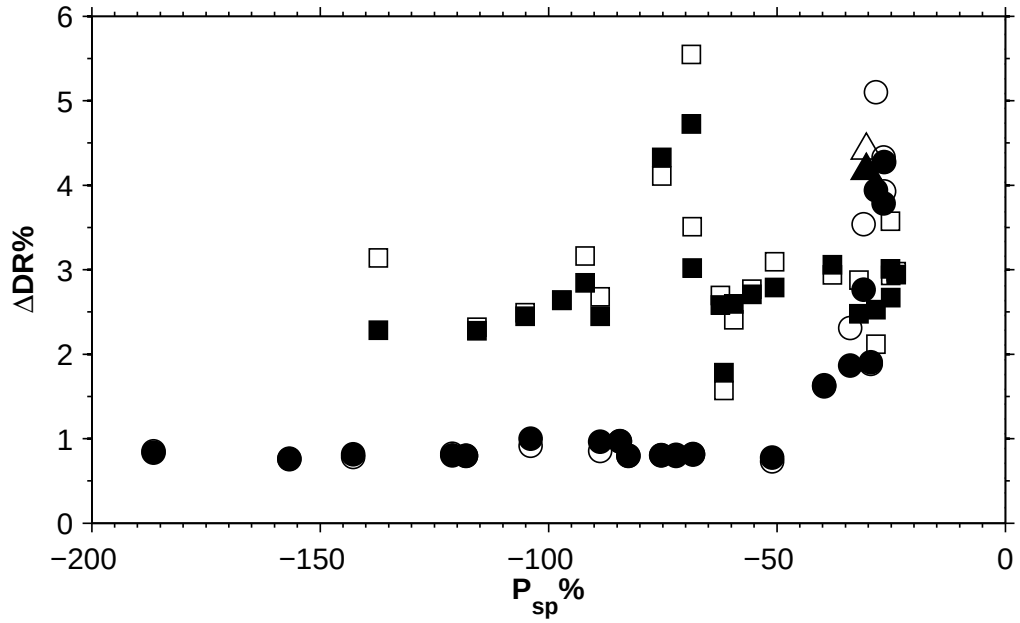

Figure B.8: Drag Reduction Uncertainty $\Delta DR\%$ versus Power Spent $P_{sp}\%$ at $\kappa_x^+ = 0.005$ and $A^+ = 12$. ◯: MFU at $Re_p = 4760$; □: MFU at $Re_p = 29500$; △: MFU results at $Re_p = 73000$. Filled symbols: Autocorrelation method; Blank symbols: Equivalent White Noise method.

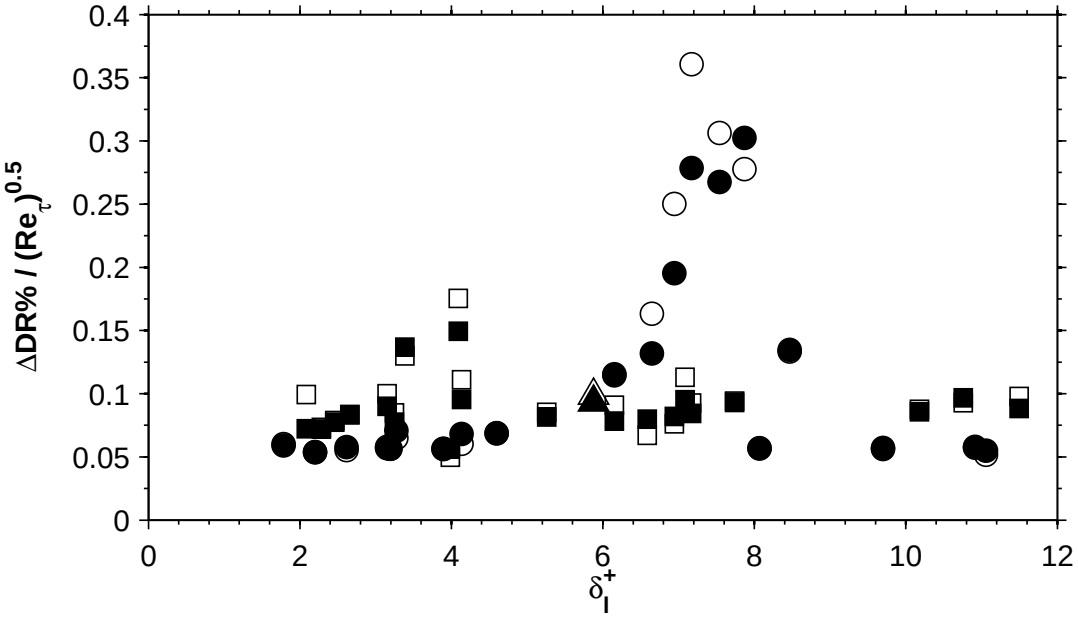

Figure B.9: Drag Reduction Uncertainty $\Delta DR\%/\sqrt{Re_\tau}$ versus Generalized Stokes Layer δ_l^+ at $\kappa_x^+ = 0.005$ and $A^+ = 12$. ◯: MFU at $Re_p = 4760$; □: MFU at $Re_p = 29500$; △: MFU results at $Re_p = 73000$. Filled symbols: Autocorrelation method; Blank symbols: Equivalent White Noise method.

Uncertainty versus GSL thickness

Finally, DR uncertainty is represented against GSL thickness in figure B.9. A collapse of data at different Re_p is found, if $\Delta DR\%$ is scaled with $\sqrt{Re_\tau}$, or equivalently with u_τ/ν. The scaling is maybe due to the choice of a constant domain area S^+ in wall units, that is, the domain gets smaller as Re_p increase.

The peaks of DR uncertainty are located at $\delta_l^+ = 7$ at $Re_p = 4760$ and at $\delta_l^+ = 4$ at $Re_p = 29500$. As it could be expected, the value of maximum $\Delta DR\%$ does not scale with $\sqrt{Re_\tau}$, because it is due to traveling wave-related effects.

B.2 Initial transient scaling

Initial transient (IT) length at different Reynolds numbers has been found to scale possibly both with viscous time unit or with the inner-outer time scale L_x/U_b. The latter scaling leads to a slightly better agreement than the former, but further explanation are required. If initial transient scaled with L_x/U_b, a dependency of its length on domain size would be implied, but [39] have proved that IT is not L_x-dependent. New meaning can be given to the L_x/U_b scaling if one considers that L_x^+ is kept constant among simulations at different Reynolds number. Thus, such a time scale is equivalent to δ_ν/U_b and, recalling the definition of δ_ν, to $\nu/(u_\tau U_b)$ or $\sqrt{\nu\, t_\nu/U_b}$.

The two different scaling can be seen in figures B.10 and B.11, where IT length is represented against DR. A slightly better collapse exists with L_x/U_b scaling, but a wider range of

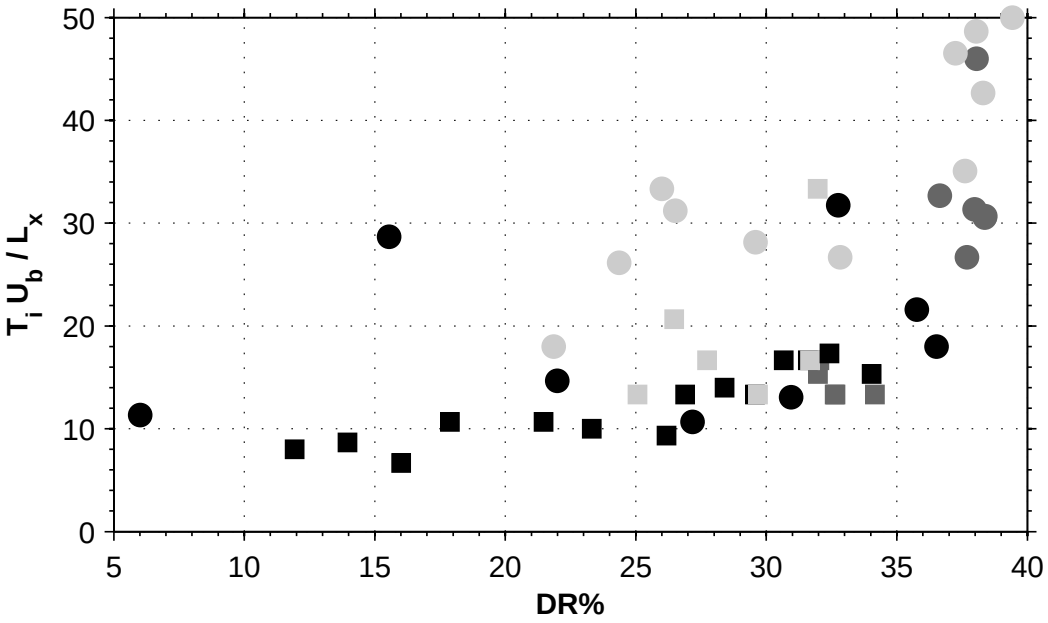

Figure B.10: Initial transient length $T_i U_b/L_z$ versus Drag Reduction $DR\%$. ∘: MFU at $Re_p = 4760$ and $L_z^+ = 497$; □: MFU at $Re_p = 29500$ and $L_z^+ = 459$. Black symbols: $T^+ < 90$, Dark gray: $90 \leq T^+ \leq 120$, Light Gray $T^+ > 120$.

Reynolds numbers should be investigated to precisely state which is the right scaling.

B.2.1 Oscillating wall

IT versus DR

IT transient length remains substantially unchanged with DR (figures B.10 and B.11), being only moderately lengthened as DR increase, up to the neighborhood of maximum DR, where, at $Re_p = 4760$, it grows abruptly. The sudden growth at $Re_p = 29500$ has not been observed. Such a discrepancy can be explained as a low-Re effect: at low Reynolds numbers, when a highly drag-reducing control is activated turbulent flow experience a phenomenon similar to transition, after an initial fast reduction of turbulent fluctuations.

IT versus Power

Figures B.12 and B.13 show a quasi-linear relationship of IT length with $P_{sp}\%$ at $Re_p = 29500$. The only exception are light gray points, due to the high values of DR exhibit a higher IT length. Points at $Re_p = 4760$ are to scattered to make any deduction.

IT versus Stokes Layer thickness

Figures B.14 and B.15 confirms previous results: maximum IT length is observed at $\delta_l^+ \approx \delta_{opt}^+ = 6.2$, where highest DR is reached. While at $Re_p = 4760$ IT reaches its maximum gradually, at $Re_p = 29500$ only one point in the neighborhood of δ_{opt}^+ shows an abrupt jump in IT length.

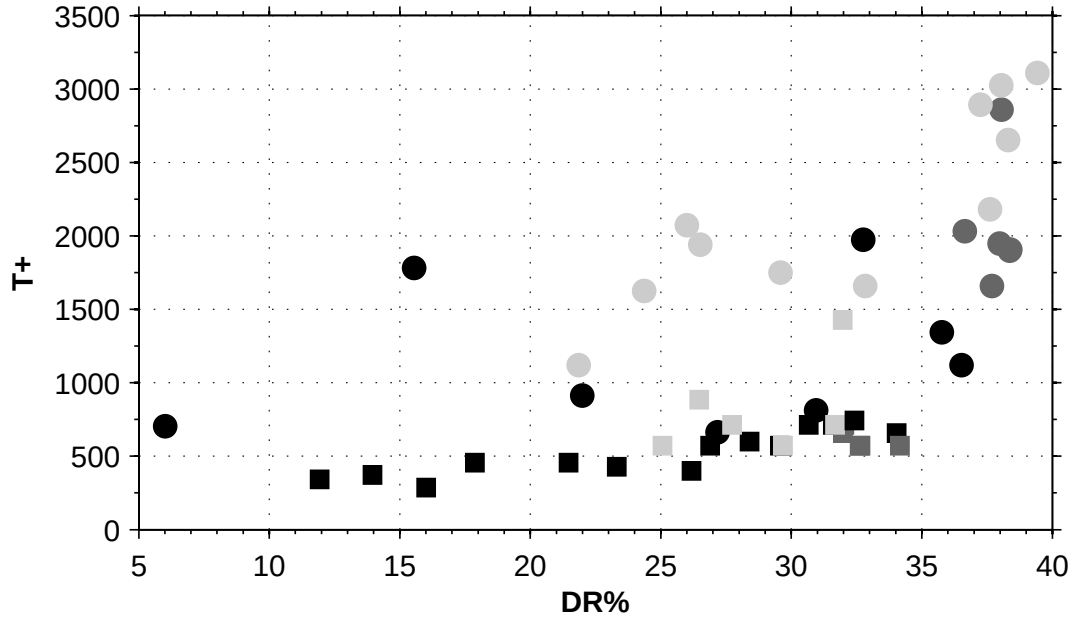

Figure B.11: Initial transient length T_i^+ versus Drag Reduction $DR\%$. ∘: MFU at $Re_p = 4760$ and $L_z^+ = 497$; □: MFU at $Re_p = 29500$ and $L_z^+ = 459$. Black symbols: $T^+ < 90$, Dark gray: $90 \leq T^+ \leq 120$, Light Gray $T^+ > 120$.

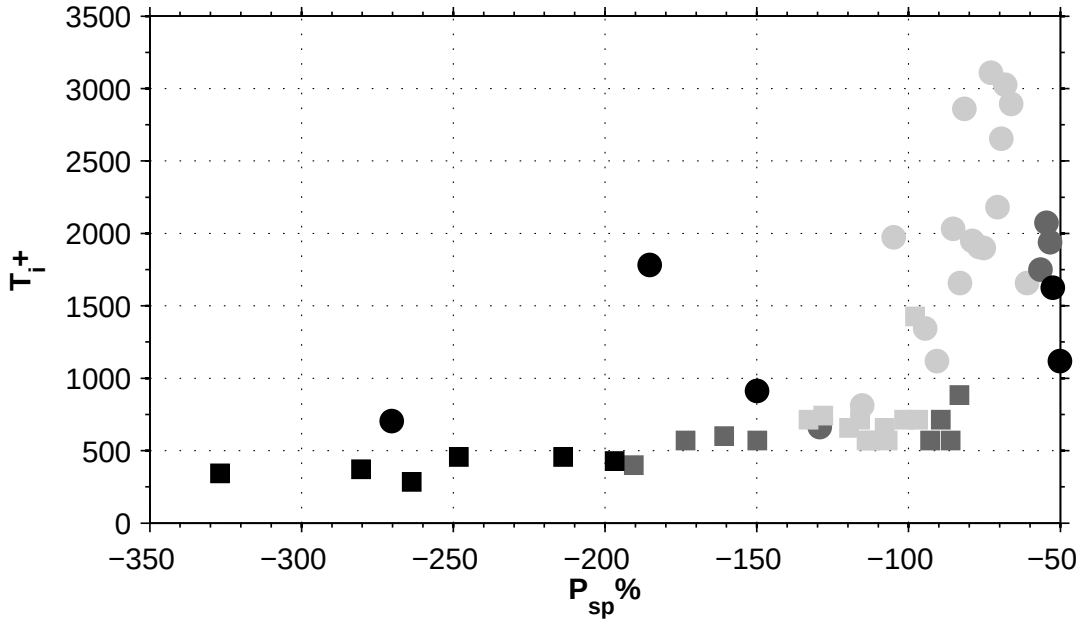

Figure B.12: Initial transient length T_i^+ versus Power Spent $P_{sp}\%$, accounting for regenerative braking. ∘: MFU at $Re_p = 4760$ and $L_z^+ = 497$; □: MFU at $Re_p = 29500$ and $L_z^+ = 459$. Black symbols: $DR\% < 25$, Dark gray: $25 \leq DR\% \leq 30$, Light Gray $DR\% > 30$.

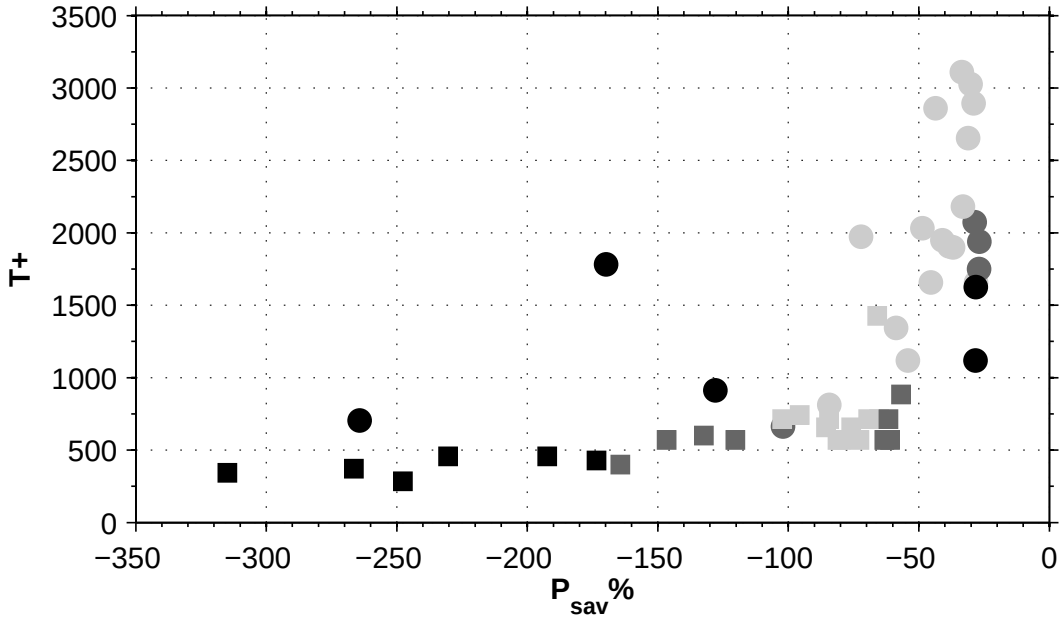

Figure B.13: Initial transient length T_i^+ versus Power Saved $P_{sav}\%$, accounting for regenerative braking. ∘: MFU at $Re_p = 4760$ and $L_z^+ = 497$; □: MFU at $Re_p = 29500$ and $L_z^+ = 459$. Black symbols: $DR\% < 25$, Dark gray: $25 \leq DR\% \leq 30$, Light Gray $DR\% > 30$.

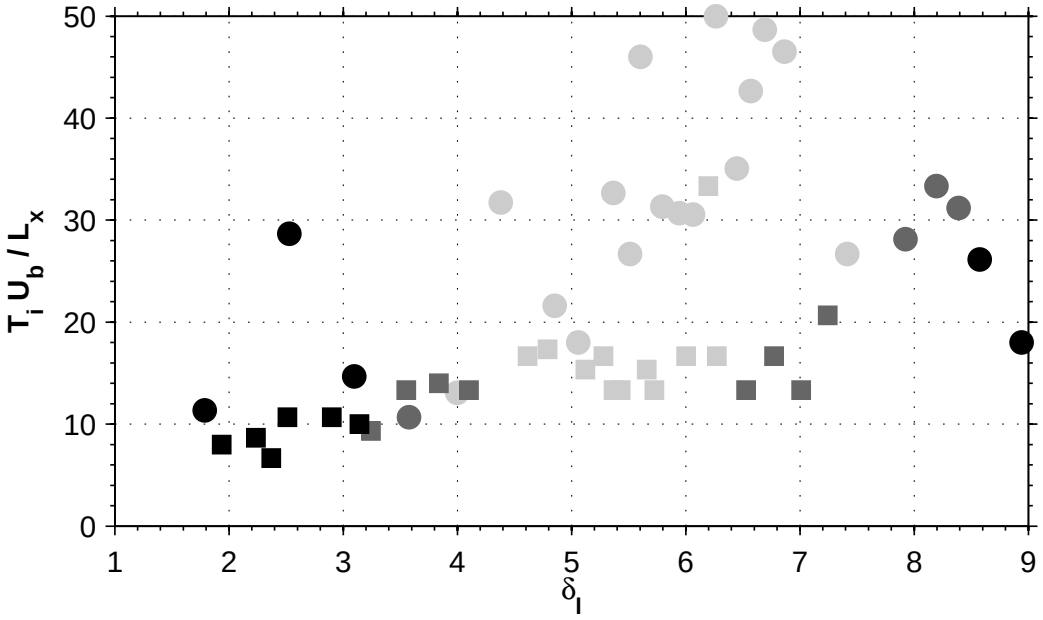

Figure B.14: Initial transient length $T_i\, U_b/L_z$ versus Stokes Layer Thickness δ_l, accounting for regenerative braking. ∘: MFU at $Re_p = 4760$ and $L_z^+ = 497$; □: MFU at $Re_p = 29500$ and $L_z^+ = 459$. Black symbols: $DR\% < 25$, Dark gray: $25 \leq DR\% \leq 30$, Light Gray $DR\% > 30$.

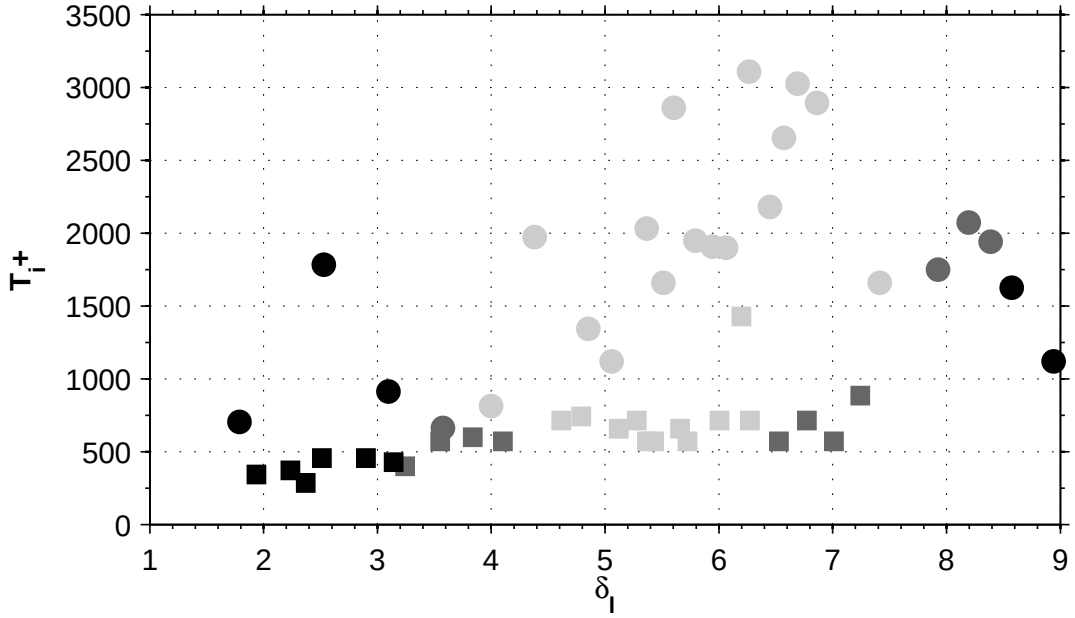

Figure B.15: Initial transient length T_i^+ versus Stokes Layer Thickness δ_l, accounting for regenerative braking. ∘: MFU at $Re_p = 4760$ and $L_z^+ = 497$; □: MFU at $Re_p = 29500$ and $L_z^+ = 459$. Black symbols: $DR\% < 25$, Dark gray: $25 \leq DR\% \leq 30$, Light Gray $DR\% > 30$.

It should also be observed that, even if at $Re_p = 4760$ DR optimal period is not very accurately predicted, the maximum IT is clearly located at δ_{opt}^+, again suggesting that the shift in the point of maximum DR was due to high uncertainty in DR data.

B.2.2 Traveling waves

Since slight differences can be appreciated between the t_ν and the δ_ν/U_b in the previous chapter, we report here only the more classic choice of viscous time length.

IT versus DR

IT transient lengthens as DR grows especially near the highest DR, where it can become even 4 times longer. When DR is less than 25%, transient length is scarcely influenced by DR as remains practically unchanged, as visible in figure B.16.

IT versus Power

Transient length correlates well with $P_{sp}\%$, being lengthened at high $P_{sp}\%$, as visible in figure B.17. A local minimum is located for both $Re_p = 4760$ and $Re_p = 29500$ at $P_{sp} \approx -50\%$. After this minimum, for descending values of power required, IT length experiences a sudden increase.

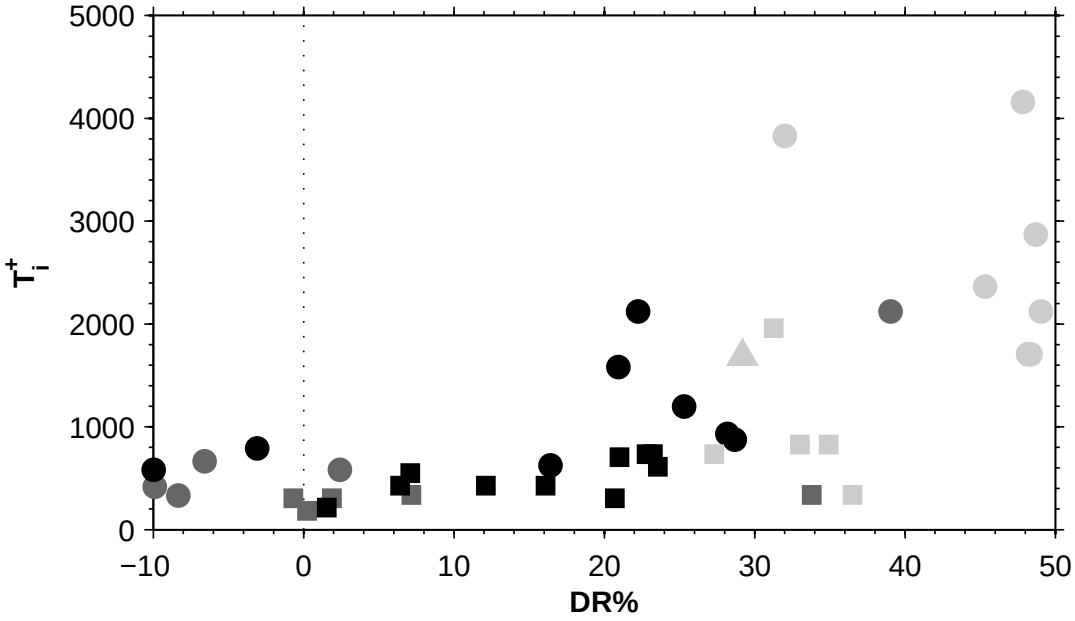

Figure B.16: Initial Transient length T_i^+ versus Drag Reduction $DR\%$ at $\kappa_x^+ = 0.005$ and $A^+ = 12$. ◯: MFU at $Re_p = 4760$; □: MFU at $Re_p = 29500$; △: MFU results at $Re_p = 73000$. Black symbols: $T^+ < 90$, Dark gray: $90 \leq T^+ \leq 160$, Light Gray $T^+ > 160$.

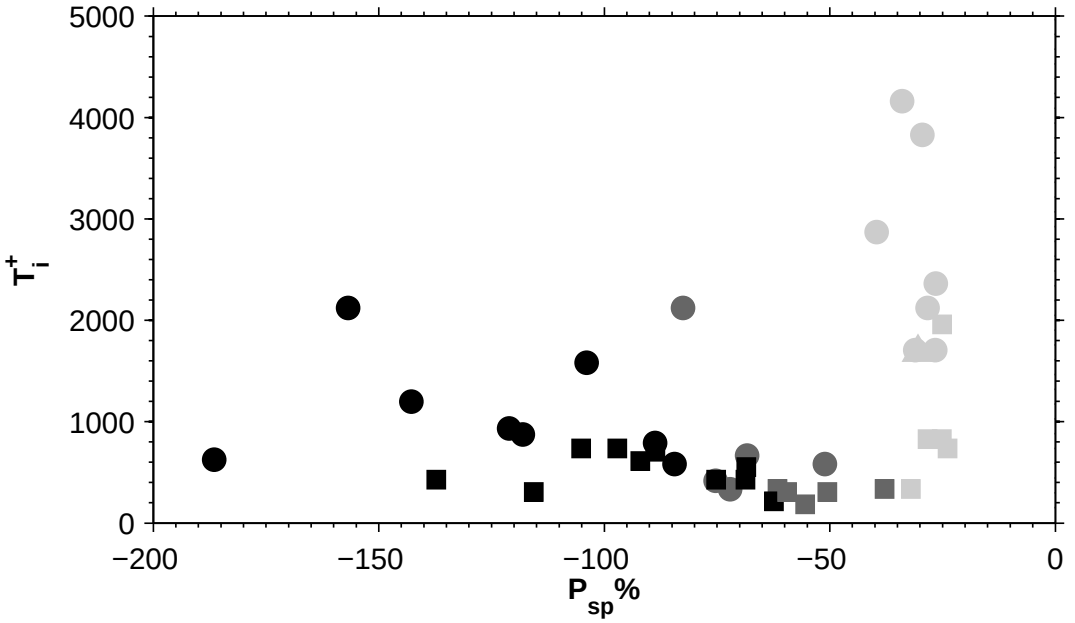

Figure B.17: Initial Transient length T_i^+ versus Power Spent $P_{sp}\%$ at $\kappa_x^+ = 0.005$ and $A^+ = 12$. ◯: MFU at $Re_p = 4760$; □: MFU at $Re_p = 29500$; △: MFU results at $Re_p = 73000$. Black symbols: $T^+ < 90$, Dark gray: $90 \leq T^+ \leq 160$, Light Gray $T^+ > 160$.

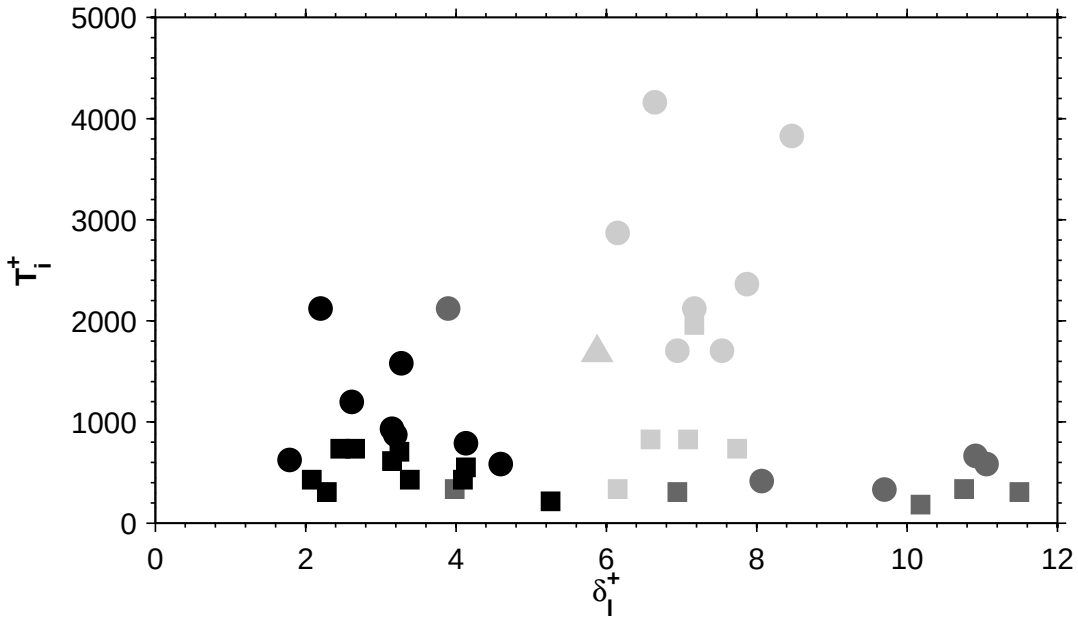

Figure B.18: Initial Transient length T_i^+ versus Generalized Stokes Layer thickness δ_l^+ at $\kappa_x^+ = 0.005$ and $A^+ = 12$. ◯: MFU at $Re_p = 4760$; □: MFU at $Re_p = 29500$; △: MFU results at $Re_p = 73000$. Black symbols: $T^+ < 90$, Dark gray: $90 \leq T^+ \leq 160$, Light Gray $T^+ > 160$.

IT versus GSL thickness

Long IT can be found in the range $6 \leq \delta_l^+ \leq 8$, where high DR is also reached. Few points near $\delta_l^+ \approx 3$ exhibit longer initial transients.

B.3 Space-averaged wall-shear spectrum

Space-averaged wall-shear spectra are computed for both traveling waves and oscillating wall for the whole dataset, interesting results on space-averaged shear modulations are found, confirming predictions of [17], in case of oscillating wall, and posing further interesting questions.

B.3.1 Oscillating wall

Spectra of the space-averaged wall shear have been computed from the time histories of $\mathrm{d}u/\mathrm{d}y$ at walls. Figures B.19 and B.20 compare two mean shear spectra at $Re_p = 29500$ for a reference and a controlled case at $T^+ = 101$ and $A^+ = 12$. A clear peak of energy is associated to a frequency $\omega = 2\omega_f$, where $\omega_f = 2\pi/T$ is the forcing frequency.

A possible explanation is given in [17]: when the wall moves it generates a sheet of streamwise vorticity, negative when the wall is moving towards positive z, positive on the contrary. When wall oscillation is made in a turbulent boundary layer, the sheet of streamwise vorticity is tilted into the spanwise direction opposite to the wall movement, generating in both leftward and rightward phase of the cycle negative spanwise vorticity. Consequently,

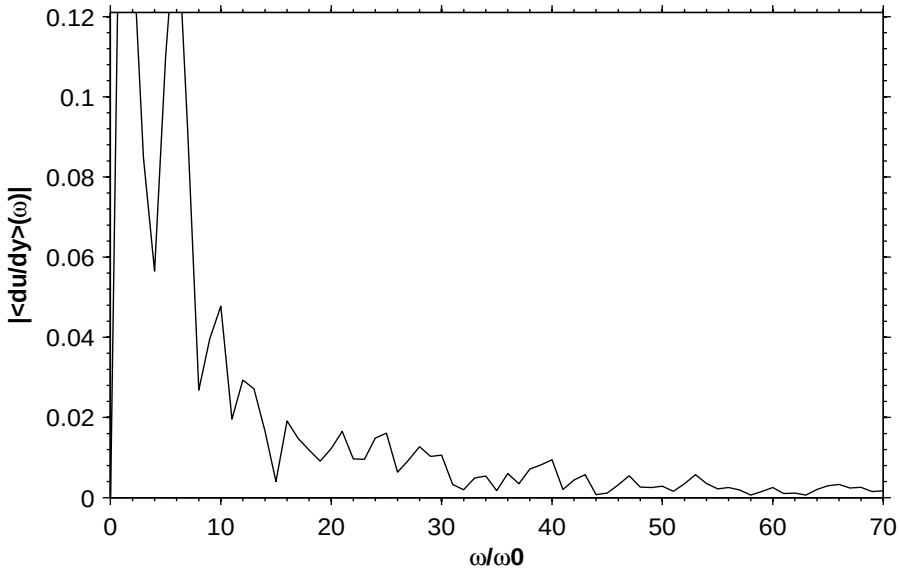

Figure B.19: Spectrum of mean wall shear stress $< du/dy >(\omega)$ versus frequency ω at $Re_p = 29500$, case 0a. $\omega_0 = 0.063$.

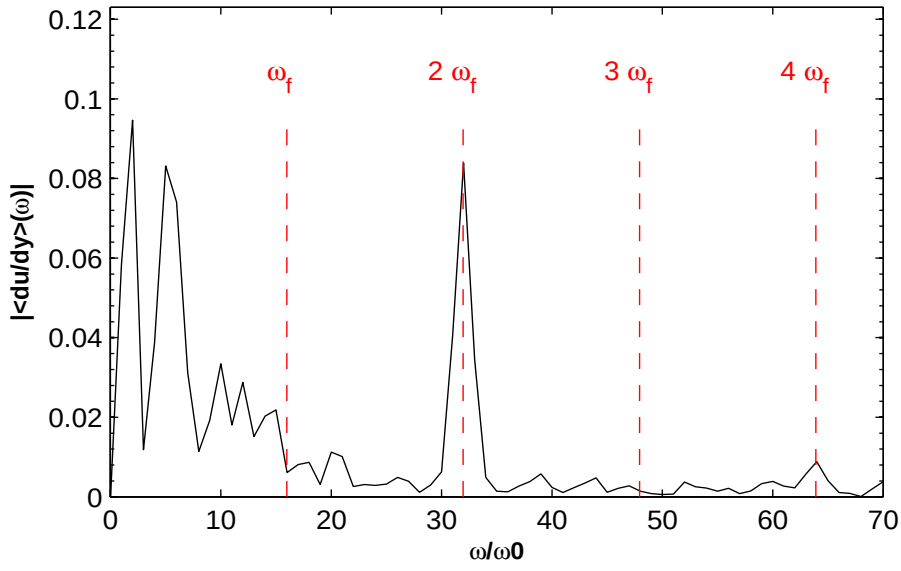

Figure B.20: Spectrum of mean wall shear stress $< du/dy >(\omega)$ versus frequency ω at $Re_p = 29500$, case 38, i.e. $T^+ = 101$. Frequencies multiple of the forcing frequency ω_f are highlighted in red. $\omega_0 = 0.068$.

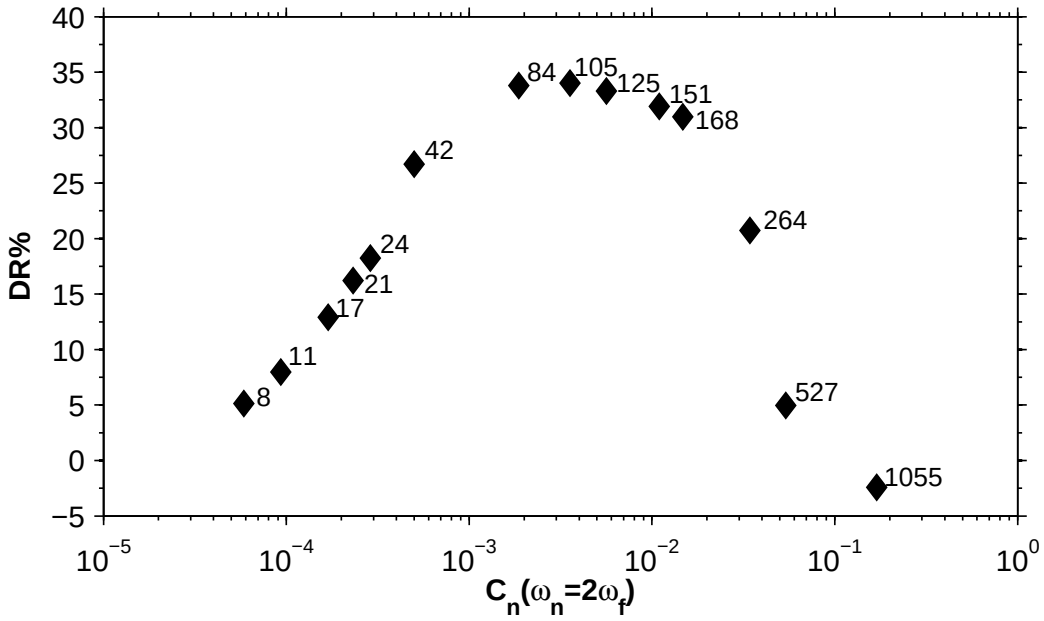

Figure B.21: Drag Reduction $DR\%$ versus amplitude of the Fourier coefficient associated to the second forcing wave $C_n(\omega_n = 2\omega_f)$ at $Re_p = 4760$. $\diamond$: Full Channel DNS from Quadrio's database, labels stand for period of wall oscillation T^+

the streamwise velocity in the near wall region is periodically reduced, with a frequency $2\omega_f$. This result in the space averaged wall shear spectrum as a modulation of the same frequency.

Even if the mechanism have been already described in [17], it is confirmed by the evidence of the peak in space averaged wall shear at $2\omega_f$, evidence that has not been documented before.

The amplitude of the peak is mildly affected by the type of signal windowing adopted. In order to highlight the peak at $2\omega_f$, after discarding the initial transient, the wall shear time history has been divided into shorter subsignals. These subsignal have been windowed with a hanning window and their spectra averaged. This cut the lower frequencies that does not interest this study and smoothen the spectrum but reduces the resolution. Therefore the peak-amplitude should be read as a indication of its order of magnitude rather than an absolute value.

Power density associated to the 2nd forcing wave $C_n(\omega_n = 2\omega_f)$ is plotted in figure B.21 against DR for DNS data at $Re_p = 4760$ from [42]. A linear correlation seems to hold for DR up to 20, while from $T^+ \approx 160$, around $C_n(2\omega_f) \approx 10^{-2}$ DR exhibit a more rapid decay but the peak amplitude continue to grow.

As a matter of fact, peak amplitude and T^+ appear to be related by a power law $C_n(2\omega_f) = a(T^+)^b$, with $b \approx 1$ even at very low forcing frequency, where DI is obtained (figure B.22).

The energy content of the space-averaged wall shear associated to $2\omega_f$ has been computed also for MFU at $Re_p = 29500$. Higher oscillations of wall shear due to the narrow channel cause more scattering of data, compared to DNS. Even at $Re_p = 29500$ the same result as for DNS at lower Reynolds is obtained in figure B.23, where peak amplitude against DR is represented. Slightly higher values of energy than those of DNS at $Re_p = 4760$ are

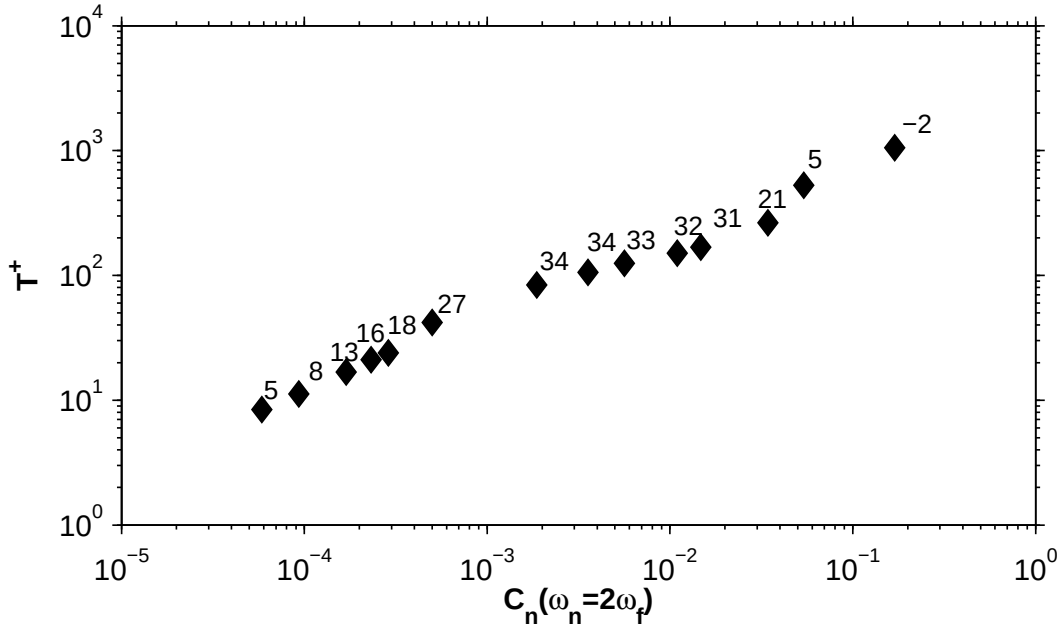

Figure B.22: Period of wall oscillation T^+ versus amplitude of the Fourier coefficient associated to the second forcing wave $C_n(\omega_n = 2\omega_f)$ at $Re_p = 4760$. $\diamond$: Full Channel DNS from Quadrio's database, labels stand for Drag Reduction $DR\%$.

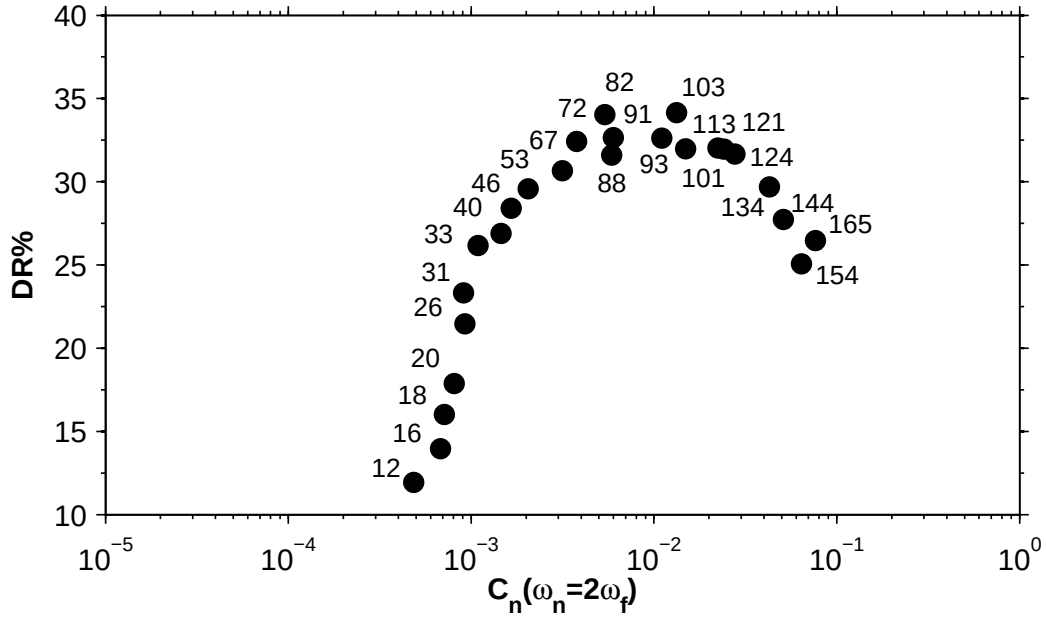

Figure B.23: Drag Reduction $DR\%$ versus amplitude of the Fourier coefficient associated to the second forcing wave $C_n(\omega_n = 2\omega_f)$ at $Re_p = 29500$. $\circ$: MFU results, labels stand for period of wall oscillation T^+

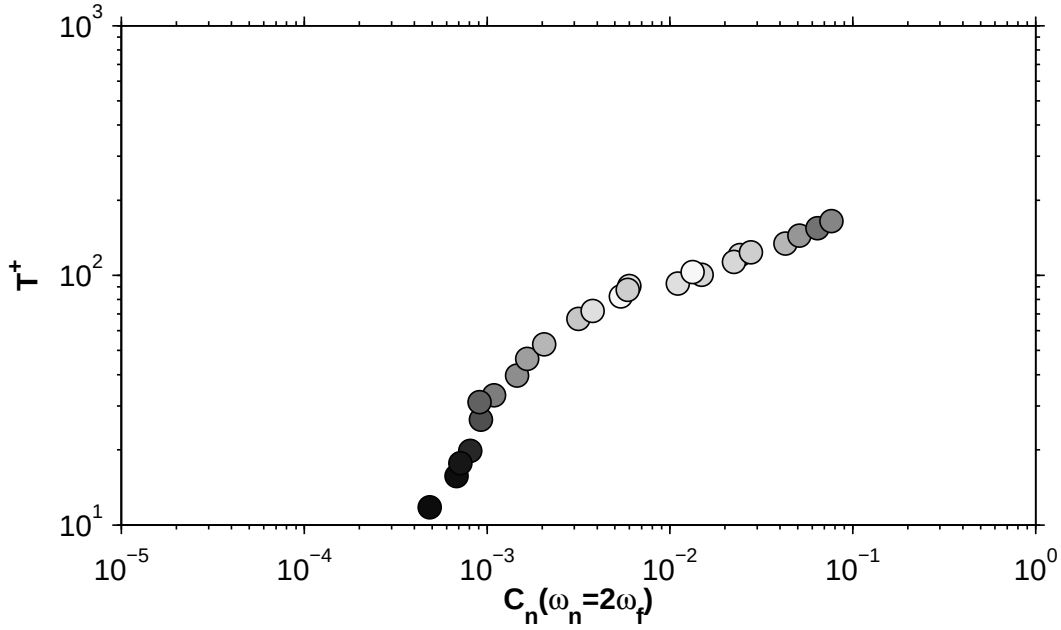

Figure B.24: Period of wall oscillation T^+ versus amplitude of the Fourier coefficient associated to the second forcing wave $C_n(\omega_n = 2\omega_f)$ at $Re_p = 29500$. ∘: MFU results. Colors are from black $DR\% = 0$ trough gray $DR\% = 25$ to white $DR\% = 35$.

obtained. Nevertheless, the more rapid decay of DR with $C_n(2\omega_f)$ begins at a peak amplitude of $\approx 2 \times 10^{-2}$.

No power law holds at $Re_p = 29500$ between T^+ and $C_n(2\omega_f)$, even if the monotonic trend is preserved. If a power-law really held, this would mean an underestimation of the peak amplitude at high value of DR, i.e. for $90 \leq T^+ \leq 120$.

An optimal peak amplitude of $C_n(2\omega_f) \approx 0.01$ leads to the maximum DR for both $Re_p = 4760$ ad $Re_p = 29500$. Even if a deep analysis of vorticity field is not addressed in this work, it could be interesting to bridge our observations and those made in [17]. If they were right, an optimal oscillation in spanwise vorticity (and hence in the streamwise velocity) could exist. The importance of a unifying vision with the studies on the Stokes layer in a turbulent channel made in [41] is underlined.

B.3.2 Traveling waves

The space-averaged wall shear stress undergo a periodic modulation of frequency $\omega = 2\omega_f$, if the wall is oscillated periodically in the spanwise direction. The vorticity tilting mechanism involved in the modulation is described in [17] and produced visible peaks in the mean wall shear spectrum, as seen in the previous chapter.

Theoretically, the modulation in space-averaged wall shear could be observed even when traveling waves are imposed at walls. The vorticity is actually tilted by wall motion in the negative spanwise direction both whether the wall is moving leftward or rightward, thus, in principle, the fact that at any time the spanwise flow rate is null should not make the difference.

Nevertheless, figures B.25a and B.25b show no significant peak in the space-averaged wall

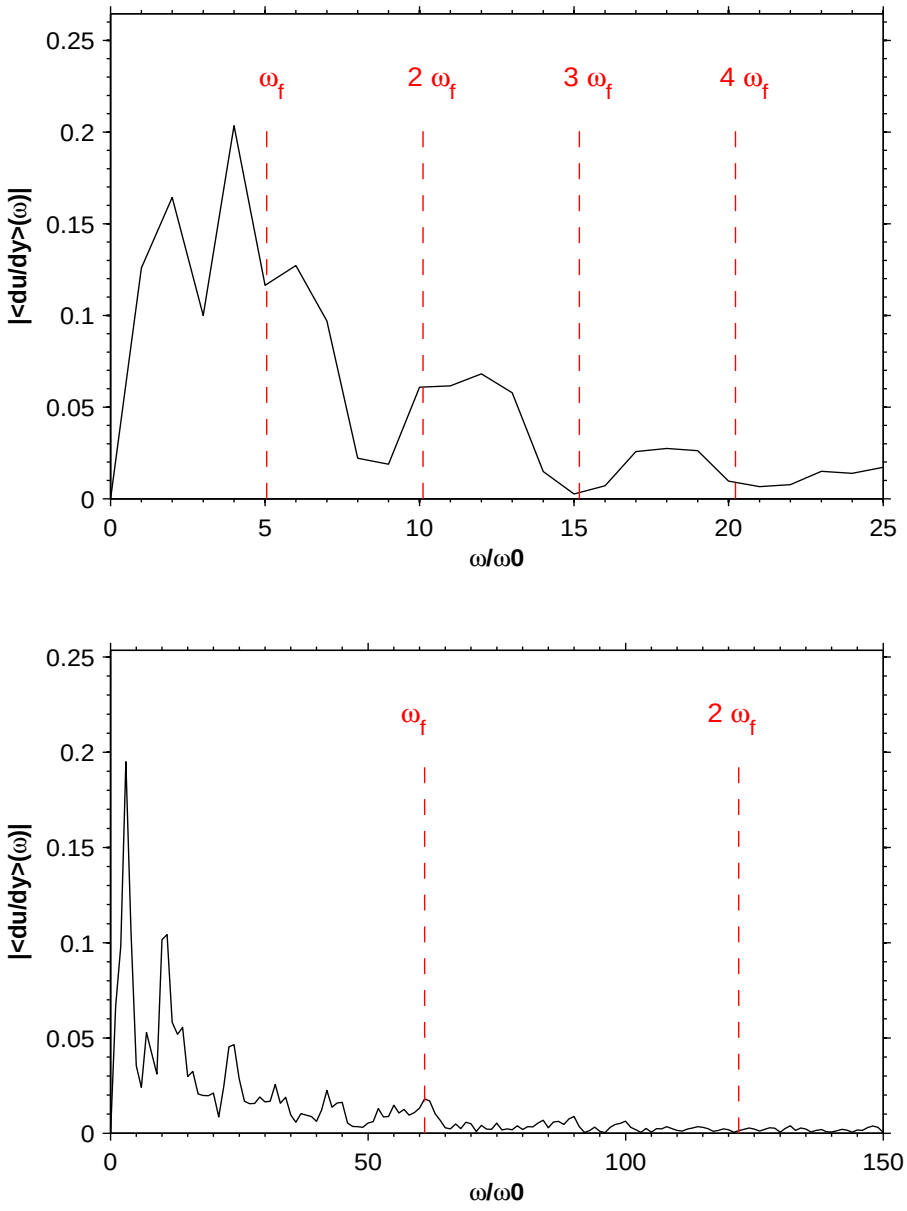

Figure B.25: Spectrum of mean wall shear stress $< du/dy > (\omega)$ versus frequency ω/ω_0 at $Re_p = 29500$, $\omega_0 = 0.032$, $\kappa_x^+ = 0.005$ and $A^+ = 12$. Top: case 68 at high $DR\%$; Bottom: case 83 at high DI

shear spectrum. At all Reynolds numbers and wave frequencies studied, no modulation of wall shear were visible. The lack of modulation in space-averaged wall shear does not surprise: traveling waves are a space- and time-dependent forcing. The space average sums up spanwise wall slices at different phases of the forcing cycle and no modulation appears in it.

B.4 Punctual Wall Shear

Space-averaged wall shear is not suitable to see whether periodic alterations of streamwise wall shear occur, when $k_x \neq 0$ and flow is controlled trough waves traveling at a finite speed.

Punctual wall shear is then studied, in search of footprints of the vorticity tilting mechanism in both temporal autocorrelation function and its Fourier transform, the power spectral density.

For this purpose, a spanwise "rake" of 96 wall probes have been placed at both walls at the same streamwise location, giving a total of 192 wall shear probes. The computation of punctual wall shear requires the calculation of the wall-normal derivative of the streamwise velocity and an additional inverse FFT of the two wall slices of the flow field. A large amount of memory is required to store 192 wall probes at each timestep, thus only two simulation for each Reynolds number underwent these additional calculations.

B.4.1 Traveling Waves

Autocorrelation function

Temporal autocorrelation functions have been computed for two cases at $Re_p = 4970$ and $Re_p = 29500$ and are shown in figure B.26. The uncontrolled reference cases are shown as solid line, circles refer to $Re_p = 4760$, while squares to $Re_p = 29500$.

The autocorrelations of uncontrolled channels show a similar behavior, with local maxima of different amplitude, according to Re, placed at $\tau^+ \approx 100$. As discussed in [38], periodic boundary conditions can explain the phenomenon. Turbulent structures are conveyed at a speed $\mathcal{U}_w^+ \approx 10$. When they exit the channel, due to periodic boundary condition, rappears at the beginning of it and eventually travel again over the same point. Hence, same structures periodically travel over the same point after a finite time which depends on domain streamwise length and turbulent convective speed, namely $L_x^+/\mathcal{U}_w^+$.

In [38] a turbulent convective speed of $\mathcal{U}_w^+ \approx 10$ has been computed and an increase in the value for narrow channels proven. Considering the length of the channel $L_x^+ = 1256$ and the "return" time of $T^+ = 100$, a $\mathcal{U}_w^+$ of 12.5 is approximately computed, confirming the increase of $\mathcal{U}_w^+$ for narrow channels.

The two controlled cases are backward-traveling waves at $\omega^+ = -0.202$ and $\kappa_x^+ = 0.005$, thus giving $c^+ = -40.4$. The local maximum at $T^+ \approx 100$ is still present but a more evident modulation in the temporal correlation is visible. Some kind of interaction between the spanwise flow and vorticity field at walls reflects into the longitudinal wall shear autocorrelation function.

Power Spectral Density

The PSD of the punctual wall shear (figures B.27 and B.28) confirms that the wall shear is modulated with frequency ω_f, the forcing frequency, in contrast to what we discovered for the oscillating wall, where the modulation frequency was $2\omega_f$.

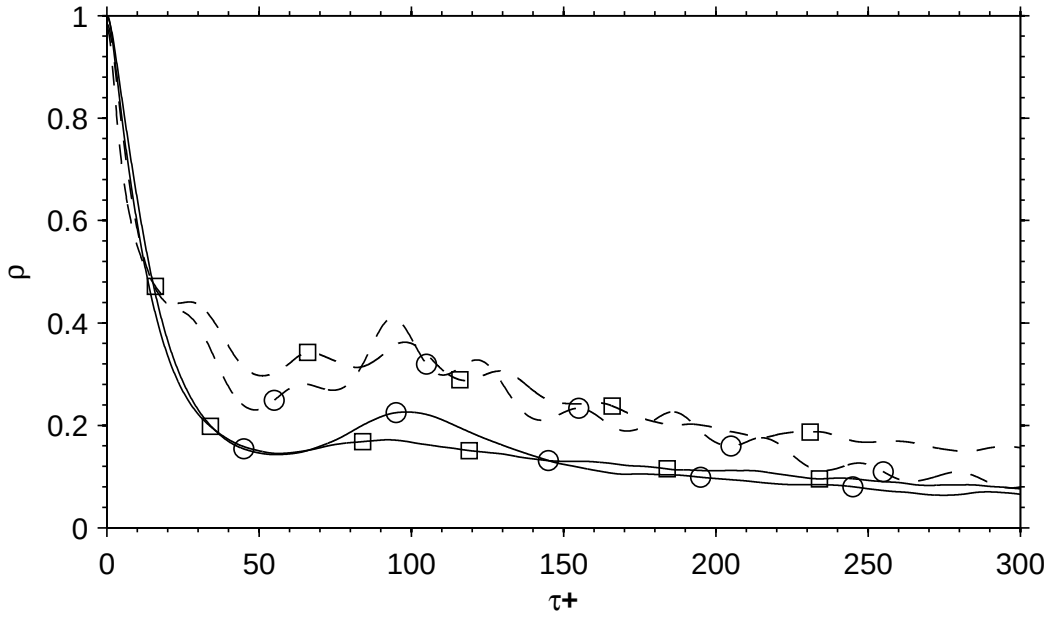

Figure B.26: Autocorrelation function ρ of the punctual wall shear stress as function of separation time τ^+, expressed in viscous units. ◯: MFU at $Re_p = 4760$, $\omega^+ = -0.202$, $\kappa_x^+ = 0.005$, $A^+ = 12$; □: MFU results at $Re_p = 29500$, $\omega^+ = -0.190$, $\omega^+ = -0.202$, $\kappa_x^+ = 0.005$, $A^+ = 15$. Solid line: Reference uncontrolled cases; Dashed line: controlled cases.

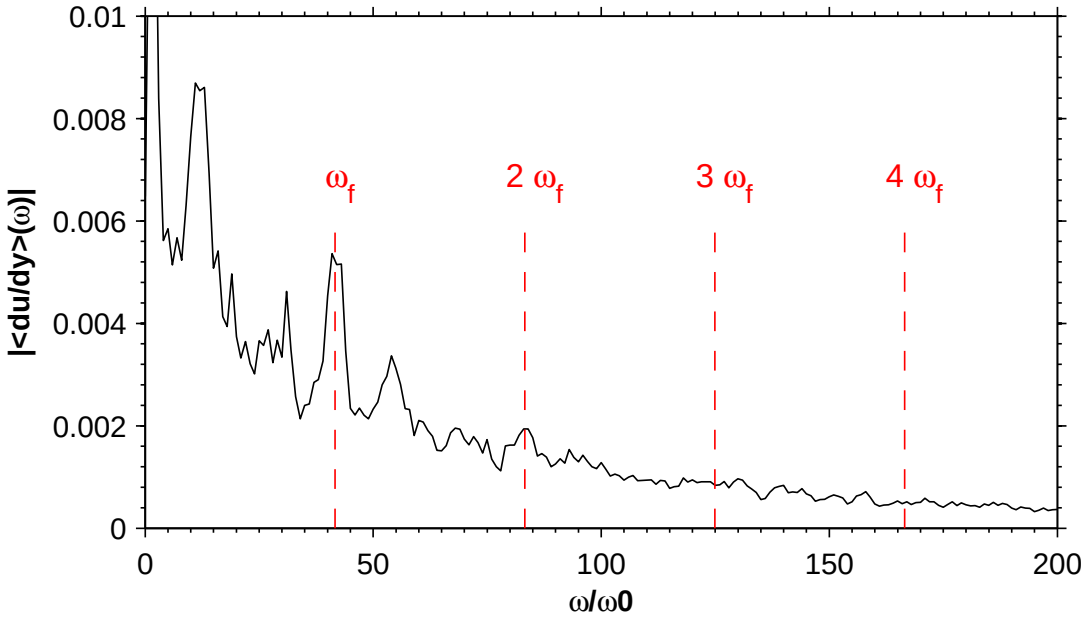

Figure B.27: Power Spectral Density of the punctual wall shear stress $|du/dy(\omega)|$ versus frequency ω/ω_0 at $Re_p = 4760$, case 58 with $L_z = 2\pi$, $\omega_0 = 0.0404$. Forcing parameters are the same as B.26

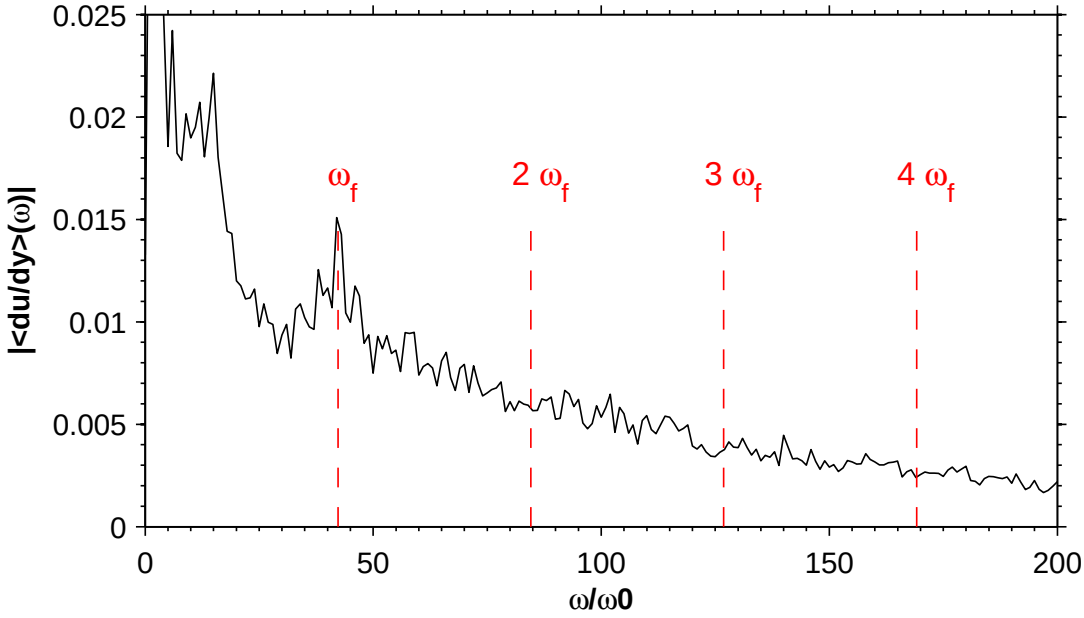

Figure B.28: Power Spectral Density of the punctual wall shear stress $|du/dy(\omega)|$ versus frequency ω/ω_0 at $Re_p = 29500$, case 45 with $L_z = 1.32$, $\omega_0 = 0.1370$. Forcing parameters are the same as B.26.

The interaction mechanisms described in [17], true for the oscillating wall, may change if wave traveling at a finite speed are considered. On the other hand, completely ignoring the spatial dimension may cause the loss of basic information, necessary to understand what interactions the flow undergoes.

Moreover, if the equivalent wave period $\mathcal{T}^+ = \lambda_x^+/(c^+ - \mathcal{U}_w^+)$ is computed, the value of $\mathcal{T}^+ = 25$ is obtained. At this period, if oscillating wall were used, a peak value of ≈ 0.0005 would be found in the spectrum of the mean wall shear at $2\omega_f$. If this value could be acceptable even for traveling waves, it would be less than, or near to, the noise level at $2\omega_f$, then a peak could exist, but cannot be observed at such a low period.

Nevertheless, it should be considered that no peak can be observed in the spectrum at ω_f for oscillating wall, thus something changes when traveling waves are used.

Such a small database of punctual wall shear is not enough to clarify the whole scenario of traveling waves. At least spatial information is needed to understand the interaction between the GSL, the sheet of streamwise vorticity it generates, the tilting of vorticity and its influence on the streamwise velocity.

Differently from the oscillating wall, when $k_x \neq 0$ the GSL generates a sheet of streamwise vorticity which is spatially modulated, this potentially influence the vorticity tilting mechanism when c^+ is not very large.

Anyway, further studies are needed to give a unified vision of both traveling waves nd oscillating wall, understanding well what drag reducing interactions happen at walls.

Ringraziamenti

Ringrazio anzitutto Maurizio per avermi permesso di lavorare con lui a questo progetto, che ci è costato più di 800 mail e ore di conversazione su skype. Non solo senza il suo aiuto questo lavoro non sarebbe stato possibile, ma durante questi mesi i suoi preziosi consigli mi hanno permesso di imparare molto. Grazie per la fiducia che ha riposto in me e nelle mie capacità.

Ringrazio inoltre l'Università di Salerno per aver concesso l'uso del sistema dedicato di calcolo che ci ha permesso di portare a termine questo lavoro.

Herzlichen Dank an Bettina fuer die Gelegenheit die Sie mir gegeben hat: es ist einen Antrieb gewesen, die Uni am besten zum beenden.

Un sentito grazie anche a Luigi, per aver stimolato la mia curiosità e avermi fatto appassionare alla Fluidodinamica e alla Matematica.

Ringrazio la mia famiglia che mi ha supportato e sopportato assieme in questi anni di studio, non sempre facili. Grazie per aver creduto in me e non avermi fatto pressione fino all'ultimo. Grazie alla Ele e perché condivide la camera con me, non è facile, e per averci portato dentro il buon umore.

Ringrazio tutte le persone che in questi anni hanno dovuto patire la mia assenza durante i periodi più duri dell'Università. La vostra vicinanza, anche quando ero molto impegnato, è stata fondamentale per arrivare sano e salvo alla fine.

Grazie a tutti i miei amici e colleghi della Bovisa, gran posto, con cui ho condiviso grasse e grosse risate in questi cinque anni. Grazie per avermi fatto ridere immaginando Morino che non sa fare l'esame di Aeroservo perché gli è capitato il metodo a pistoni. Siete stati davvero importanti, mi avete aiutato negli ultimi esami e verrà per tutti il momento della Grande Baldoria :). Niente più Two More Years!

Ringrazio Andrea, Susanna, Gully, Minno, Valentina, Paolo, Domenico, Paola, Diego e Davide perché gli ultimi mesi sarebbero stati impossibili senza di voi. E'stato davvero divertente disperarci assieme e ridere delle nostre ultime fatiche!

Ringrazio anche il mio porto, da dove sempre parto e dove sempre voglio approdare, dopo aver fatto un gran casino. Uno stimolo immenso a diventare grande.

Ringrazio l'Anni perché ha dato utilissimi consigli, perché la gita a Houston è stata davvero fantastica e perché è una fonte di ispirazione.

Ringrazio la Rossi per i dolori al malleolo, alla valvola del cuore, perché dice di essere timida e sono tutte frottole, perché ha lo sguardo timido, perché ha gli occhi verdi e per tante altre cose leggere e vaganti.

Ringrazio anche tutti coloro che non sono in questo elenco e fanno parte di me e della mia vita e che hanno contributito in qualsiasi modo a questo lavoro. Grazie!

Bibliografia

[1] M.S. Acarlar and C.R. Smith. A Study of Hairpin Vortex in a Laminar Boundary Layer. Part I. Hairpin Vortex Generated by a Hemisphere Protuberance. *J. Fluid Mech.*, 175:1–41, 1987.

[2] F. Auteri, A. Baron, M. Belan, G. Campanardi, and M. Quadrio. Experimental assessment of drag reduction by traveling waves in a turbulent pipe flow. *Phys. Fluids*, 22(11):115103/14, 2010.

[3] T. Bewley, P. Moin, and R. Temam. DNS-based predictive control of turbulence: an optimal benchmark for feedback algorithms. *J. Fluid Mech.*, 447:179–225, 2001.

[4] T. R. Bewley and S. Liu. Optimal and robust control and estimation of linear paths to transition. *J. Fluid Mech.*, 365:305–349, 1998.

[5] H. Choi, P. Moin, and J. Kim. Active turbulence control for drag reduction in wall-bounded flows. *J. Fluid Mech.*, 262:75–110, 1994.

[6] J.-I. Choi, C.-X. Xu, and H. J. Sung. Drag reduction by spanwise wall oscillation in wall-bounded turbulent flows. *AIAA J.*, 40(5):842–850, 2002.

[7] K-S. Choi and M. Graham. Drag reduction of turbulent pipe flows by circular-wall oscillation. *Phys. Fluids*, 10(1):7–9, 1998.

[8] Milton Van Dyke. Album of fluid motion. 1982.

[9] Oscar Florez and Javier Jiménez. Hierarchy of minimal flow units in the logarithmic layer. *Phys. Fluids*, (22), 2010.

[10] B. Ganapathisubramani, E.K. Longmire, and I. Marusic. Experimental investigation of vortex properties in a turbulent boundary layer. *Phys. Fluids*, 18:055105, 2006.

[11] Bharathram Ganapathisubramani, ELLEN K. Longmire, and IVAN Marusic. Characteristics of vortex packets in urbulent boundary layers. *Journal of Fluid Mechanics*, 478:35–46, 2003.

[12] S. Hoyas and J. Jimenez. Scaling of the velocity fluctuations in turbulent channels up to $Re_\tau = 2003$. *Phys. Fluids*, 18(011702):4, 2006.

[13] Nicholas Hutchins and Ivan Marusic. Large-scale influences in near-wall turbulence. *Philosophical Transactions of the Royal Society A: Mathematical, Physical and Engineering Sciences*, 365(1852):647–664, 2007.

[14] K. Iwamoto, K. Fukagata, N. Kasagi, and Y. Suzuki. Friction drag reduction achievable with near-wall manipulation at high Reynolds numbers. *Phys. Fluids*, 17(011702):4, 2005.

[15] J. Jiménez and P. Moin. The minimal flow unit in near-wall turbulence. *J. Fluid Mech.*, 225:213–240, 1991.

[16] S.S. Joshy, J.L. Speyer, and J. Kim. A system theory approach to the feedback stabilization of infinitesimal and finite-amplitude perturbations in plane Poiseuille flow. *J. Fluid Mech.*, 332:157–184, 1997.

[17] G.E. Karniadakis and K.-S. Choi. Mechanisms on transverse motions in turbulent wall flows. *Ann. Rev. Fluid Mech.*, 35:45–62, 2003.

[18] N. Kasagi, Y. Hasegawa, and K. Fukagata. Towards cost-effective control of wall turbulence for skin-friction drag reduction. In Eckhardt B., editor, *Advances in Turbulence XII*, volume 132, pages 189–200. Springer, 2009.

[19] J. Kim and F. Hussain. Propagation velocity of perturbations in turbulent channel flow. *Phys. Fluids A*, 5(3):695–706, 1993.

[20] J. Kim, P. Moin, and R. Moser. Turbulence statistics in fully developed channel flow at low Reynolds number. *J. Fluid Mech.*, 177:133–166, 1987.

[21] H.-P. Kreplin and E. Eckelmann. Propagation of perturbations in the viscous sublayer and adjacent wall region. *J. Fluid Mech.*, 95(2):305–322, 1979.

[22] L. Cortelezzi and J. Speyer. Robust reduced-order controller of laminar boundary layer transition. *Phys. Rev. E*, 1998.

[23] C. Lee, J. Kim, D. Babcock, and R. Goodman. Application of neural networks to turbulence control for drag reduction. *Phys. Fluids*, 9:1740–1747, 1997.

[24] K.H. Lee, L. Cortelezzi, J. Kim, and J. Speyer. Application of reduced-order controller to turbulent flows for drag reduction. *Phys. Fluids*, 13(5), 2001.

[25] T. Lee, M. Fisher, and W. H. Schwarz. Investigation of the effects of a compliant surface on boundary-layer stability. *Journal of Fluid Mechanics*, 288:37–58, 1995.

[26] S.K. Lele. Compact Finite Difference Schemes with Spectral-like Resolution. *J. Comp. Phys.*, 103:16–42, 1992.

[27] P. Luchini. Viscous sublayer analysis of riblets and wire arrays. *Appl. Sci. Res.*, 50:255–266, 1993.

[28] P. Luchini and M. Quadrio. A low-cost parallel implementation of direct numerical simulation of wall turbulence. *J. Comp. Phys.*, 211(2):551–571, 2006.

[29] J. Lumley. Drag reduction in two-phase and polymer flows. *Physics of Fluids*, 20(10):64, 1977.

[30] J. L. Lumley. Drag reduction in turbulent flow by polymer additives. *Journal of Polymer Science: Macromolecular Reviews*, 7(1):263–290, 1973.

[31] H. Luo and T.R. Bewley. Accurate simulation of near-wall turbulence over a compliant tensegrity fabric. In *SPIE Paper 5757-17.*, 2005.

[32] K. Mahesh. A Family of High Order Finite Difference Schemes with Good Spectral Resolution. *J. Comp. Phys.*, 145(1):332–358, 1998.

[33] F. Martinelli. *Feedback control of turbulent wall flows.* PhD thesis, Politecnico di Milano, 2009.

[34] C. Mockett, T. Knacke, and F. Thiele. Detection of initial transient and estimation of statistical error in time-resolved turbulent flow data. Technical report, Institute of Fluid Mechanics and Engineering Acoustics, Technische Universitaet Berlin, 2010.

[35] S.B. Pope. *Turbulent Flows.* Cambridge University Press, Cambridge, 2000.

[36] M. Quadrio. Drag reduction in turbulent boundary layers by in-plane wall motion. *Phil. Trans. R. Soc. A*, 369(1940):1428–1442, 2011.

[37] M. Quadrio, F. Auteri, A. Baron, M. Belan, and A. Bertolucci. Experimental assessment of turbulent drag reduction by wall traveling waves. In B. Eckhardt, editor, *Advances in Turbulence XII, Proc. 12th EUROMECH Eur. Turbulence Conf., Marburg (D), Sept. 2009. ISBN 978-3-642-03084-0*, volume 132 of *Springer Proceedings in Physics*, pages 657–660. Springer Berlin Heidelberg, 2009.

[38] M. Quadrio and P. Luchini. Integral time-space scales in turbulent wall flows. *Phys. Fluids*, 15(8):2219–2227, 2003.

[39] M. Quadrio and P. Ricco. Initial transient of a turbulent boundary layer with spanwise oscillations. Technical report, Dipartimento di Ingegneria Aerospaziale – Politecnico di Milano – DIA-SR 02-14, 2002.

[40] M. Quadrio and P. Ricco. Critical assessment of turbulent drag reduction through spanwise wall oscillation. *J. Fluid Mech.*, 521:251–271, 2004.

[41] M. Quadrio and P. Ricco. The laminar generalized Stokes layer and turbulent drag reduction. *J. Fluid Mech.*, 667:135–157, 2011.

[42] M. Quadrio, P. Ricco, and C. Viotti. Streamwise-traveling waves of spanwise wall velocity for turbulent drag reduction. *J. Fluid Mech.*, 627:161–178, 2009.

[43] M. Quadrio, C. Viotti, and P. Luchini. Skin-friction drag reduction via steady streamwise oscillations of spanwise velocity. In J.M.L.M. Palma and Silva Lopes A., editors, *Advances in Turbulence XI*, Advances in Turbulence XI, pages 659–661. Springer, Berlin, 2007.

[44] O. Reynolds. An experimental investigation on the circumstances which determine whether the motion of water shall be direct or sinuous, and the law of resistance in parallel channels. *Proc. R. Soc. London A*, 35:84, 1883.

[45] P. Ricco and M. Quadrio. Wall-oscillation conditions for drag reduction in turbulent channel flow. *Intl J. Heat Fluid Flow*, 29:601–612, 2008.

[46] P. Ricco, M. Quadrio, and C. Viotti. Modification of turbulent friction drag by streamwise-traveling waves of spanwise velocity. In *European Drag Reduction and Flow Control Meeting - EDRFCM 2008 - Ostritz-St.Mariental (D), September 8–11, 2008*, 2008.

[47] S. K. Robinson. Coherent motions in the turbulent boundary layer. *Ann. Rev. Fluid Mech.*, 23:601–639, 1991.

[48] P.J. Schmid and D.S. Henningson. *Stability and Transition in Shear Flows*. Springer, 2001.

[49] W. Schoppa and F. Hussain. Coherent structure generation in near-wall turbulence. *J. Fluid Mech.*, 453:57–108, 2002.

[50] G. Schrauf. Key Aerodynamic Technologies for Aircraft Performance Improvement. In 5th Community Aeronautics Days, 2006.

[51] C. R. Smith and S. P. Metzler. The characteristics of low-speed streaks in the near-wall region of a turbulent boundary layer. *Journal of Fluid Mechanics*, 129:27–54, 1983.

[52] L.H. Thomas. The stability of plane Poiseuille flow. *Phys. Rev.*, 91(4):780–783, 1953.

[53] S.M. Trujillo, D.G. Bogard, and K.S. Ball. Turbulent Boundary Layer Drag Reduction using an Oscillating Wall. *AIAA Paper 97-1870*, 1997.

[54] G. Vittori and R. Verzicco. Direct simulation of transition in an oscillatory boundary layer. *Jounal of Fluid Mechanics*, 371:207–232, 1998.

[55] F. Waleffe. Exact coherent structures in channel flow. *J. Fluid Mech.*, 435:93–102, 2001.